



TECHNISCHE UNIVERSITÄT MÜNCHEN

Lehrstuhl für Lebensmittelverpackungstechnik

**Influence of substrate roughness and hygroexpansion on defects and electrical resistivity
of aluminum coated paper**

Martina Lindner

Vollständiger Abdruck der von der Fakultät Wissenschaftszentrum Weihenstephan für Ernährung, Landnutzung und Umwelt der Technischen Universität München zur Erlangung des akademischen Grades eines

Doktors der Naturwissenschaften (Dr. rer. nat.)

genehmigten Dissertation.

Vorsitzende: Prof. Dr. Natalie Germann

Prüfer der Dissertation: 1. Prof. Dr. Horst-Christian Langowski
2. Prof. Dr. Rainer Brandt

Die Dissertation wurde am 07.06.2019 bei der Technischen Universität München eingereicht und durch die Fakultät Wissenschaftszentrum Weihenstephan für Ernährung, Landnutzung und Umwelt am 01.10.2019 angenommen.

*I seem to myself like a child playing on the seashore, and diverting myself in
now and then finding a smoother pebble or a prettier shell than ordinary,
whilst the great ocean of truth lay all undiscovered before me.*

Sir Isaac Newton

Danksagung

Die vorliegende Arbeit entstand während meiner Tätigkeit als wissenschaftliche Mitarbeiterin am Fraunhofer-Institut für Verfahrenstechnik und Verpackung und am Lehrstuhl für Lebensmittelverpackungstechnik des Wissenschaftszentrums Weihenstephan für Ernährung, Landnutzung und Umwelt der Technischen Universität München in Freising. Ich möchte mich bei denjenigen bedanken, die mich in dieser herausfordernden, aber auch ungemein lohnenden Phase meiner akademischen Laufbahn begleitet haben.

Ganz besonders danken möchte ich meinem Doktorvater Prof. Dr. Horst-Christian Langowski, der sowohl mit seinem immensen fachlichen Wissen, als auch mit seiner konstruktiven Kritik diese Arbeit begleitet hat. Tiefer Dank gilt auch meinem Mentor Dr. Matthias Reinelt, der mir während vieler intensiver Diskussionen die Möglichkeiten und Grenzen der Dateninterpretation aufzeigte. Meinem Zweitprüfer Prof. Dr. Rainer Brandt danke ich herzlichst für die Motivation zur Promotion, sein Vertrauen in mich und die Abnahme der Prüfung. Ihm sowie der Prüfungsvorsitzenden Prof. Dr. Natalie Germann danke ich für die Übernahme des jeweiligen Amtes.

Bei Dr. Cornelia Stramm, Dr. Klaus Noller und Dr. Sven Sänglerlaub bedanke ich mich aufrichtig für die Möglichkeit, die Arbeit in der Abteilung Materialentwicklung des Fraunhofer-Instituts für Verfahrenstechnik und Verpackung IVV anfertigen zu können.

Bei Florian Höflsauer, Julia Heider und Tobias Gilch bedanke ich mich für die hilfreichen Beiträge, die sie im Rahmen ihrer Masterarbeiten geleistet haben.

Vielen Dank auch an alle meine Kolleginnen und Kollegen in der Abteilung Materialentwicklung: Danke für Eure Hilfsbereitschaft, die vielen Lackier- und Beschichtungstage, den freundschaftlichen Umgang und die lustigen und aufmunternden Gespräche auf der Feuertreppe. Egal wo es mich einmal hin verschlagen wird, ich hoffe immer solche Kollegen wie Euch um mich herum zu haben.

Von ganzem Herzen danke ich Prof. Dr. Markus Schmid, Andreas Stäbler und Monika Haas dafür, dass sie mir in schwierigen Zeiten eine große Stütze waren.

Mein wärmster Dank gilt meiner Familie für ihre endlose, bedingungslose Liebe und unablässige Unterstützung.

Scientific publications

Peer reviewed papers which are part of this thesis

- 1) Lindner, M. Factors affecting the hygroexpansion of paper. Journal of Material Science 2017.
- 2) Lindner, M.; Schmid, M. Thickness measurement methods for physical vapor deposited aluminum coatings in packaging applications: A review. Coatings 2017.
- 3) Lindner, M.; Höflsauer, F.; Heider, J.; Reinelt, M.; Langowski, H.-C. Comparison of thickness determination methods for physical-vapor-deposited aluminum coatings in packaging applications. Thin Solid Films 2018.
- 4) Lindner, M.; Heider, J.; Reinelt, M.; Langowski, H.C. Hygroexpansion and surface roughness cause defects and increase the electrical resistivity of physical vapor deposited aluminum coatings on paper. Coatings 2019.
- 5) Lindner, M.; Gilch, T.; Reinelt, M.; Langowski, H.C. Hygroexpansion, surface roughness and porosity affect the electrical resistance of EVOH-aluminum-coated paper. Coatings 2019.

Further peer reviewed papers

- 1) Coltelli, M.-B.; Wild, F.; Bugnicourt, E.; Cinelli, P.; Lindner, M.; Schmid, M.; Weckel, V.; Müller, K.; Rodriguez, P.; Staebler, A. State of the art in the development and properties of protein-based films and coatings and their applicability to cellulose based products: An extensive review. Coatings 2015.
- 2) Lindner, M.; Rodler, N.; Jesdinszki, M.; Schmid, M.; Sänglerlaub, S. Surface energy of corona treated PP, PE and PET films, its alteration as function of storage time and the effect of various corona dosages on their bond strength after lamination. Journal of Applied Polymer Science 2017.
- 3) Müller, K.; Bugnicourt, E.; Latorre, M.; Jorda, M.; Echegoyen Sanz, Y.; Lagaron, J.M.; Miesbauer, O.; Bianchin, A.; Hankin, S.; Bölz, B.; Pérez, G.; Jesdinszki, M.; Lindner, M.; Scheuerer, Z.; Castelló, S.; Schmid, M. Review on the processing and properties of polymer nanocomposites and nanocoatings and their applications in the packaging, automotive and solar energy fields. Nanomaterials 2017.

- 4) Lindner, M.; Bäumlner, M.; Stäbler, A. Inter-correlation among the hydrophilic–lipophilic balance, surfactant system, viscosity, particle size, and stability of candelilla wax-based dispersions. Coatings 2018.
- 5) Metzger, C.; Sanahuja, S.; Behrends, L.; Sänglerlaub, S.; Lindner, M.; Briesen, H. Efficiently extracted cellulose nanocrystals and starch nanoparticles and techno-functional properties of films made thereof. Coatings 2018.
- 6) Senturk Parreidt, T.; Lindner, M.; Rothkopf, I.; Schmid, M.; Müller, K. The development of a uniform alginate-based coating for cantaloupe and strawberries and the characterization of water barrier properties. Foods 2019 (handed in for publication).

Oral presentations with first authorship

- 1) Lindner, M. Transparent and high barrier biodegradable film and sheet for customised modified atmosphere food packaging. Empack. Madrid, Spain 2015.
- 2) Lindner, M. Metallization of paper for food packaging. Science meets Industry / Industry meets Science, Kenniscentrum Papier en Karton (KCPK). Arnhem, Netherlands 2016.
- 3) Lindner, M. Thickness measurement methods for physical vapor deposited aluminum coatings in packaging applications: A comparison. Symposium on Packaging, International Association of Packaging Research Institutes (IAPRI). Lausanne, Switzerland 2017.
- 4) Lindner, M. Barrier coatings for paper and board. Paper and Board Innovation event, Kenniscentrum Papier en Karton (KCPK). Arnhem, Netherlands 2017
- 5) Lindner, M. Thickness determination of evaporated aluminum coatings on polymer webs. Polymer Testing and Analysis, AMI. Berlin, Germany 2018.
- 6) Lindner, M. Development of recyclable bio-based materials with antimicrobial and antioxidant functionalities to improve food shelf life. Chemplast Expo. Madrid, Spain, 2018.
- 7) Lindner, M. Hygroexpansion and surface roughness cause defects and increase the electrical resistivity of aluminium PVD coatings on paper. Innovative Material Science & Nanotechnology conference. Valencia, Spain 2018.

- 8) Lindner, M.; Noller, K. Development of barrier properties on papers on the basis of biopolymeric coatings. Specialty Papers Conference. Cologne, Germany 2018.
- 9) Lindner, M. Development of recyclable bio-based materials with antimicrobial and antioxidant functionalities to improve food shelf life. Specialty Papers conference. Berlin, Germany 2019.
- 10) Lindner, M. Nachhaltige Barrierebeschichtungen für Papierverpackungen. Solpack 3.0. Hamburg, Germany 2019.
- 11) Lindner, M. Hygroexpansion, lacquer coating and surface roughness affect the electrical resistivity and gas barrier of physical vapor deposited aluminum coatings on paper. Symposium on Packaging, International Association of Packaging Research Institutes (IAPRI). Twente, Netherlands 2019.

Poster presentations with first authorship

- 1) Lindner, M. Thickness measurements of nano-scale aluminum layers on PET films. Symposium on Packaging, International Association of Packaging Research Institutes (IAPRI). Lausanne, Switzerland 2017.
- 2) Lindner, M.; Sangerlaub, S. Bio-based mineral oil barrier coatings for paper. European PLACE 2019 Conference, TAPPI. Porto, Portugal 2019.

Content

DANKSAGUNG..... I

SCIENTIFIC PUBLICATIONS..... II

PEER REVIEWED PAPERS WHICH ARE PART OF THIS THESIS..... II

FURTHER PEER REVIEWED PAPERS II

ORAL PRESENTATIONS WITH FIRST AUTHORSHIP..... III

POSTER PRESENTATIONS WITH FIRST AUTHORSHIP..... IV

CONTENT V

KURZFASSUNG..... VII

ABSTRACT..... VII

1. GENERAL INTRODUCTION 1

**1.1. PHYSICAL VAPOR DEPOSITION-COATED PAPER SUBSTRATES AS
PACKAGING MATERIALS..... 1**

1.2. SCIENTIFIC QUESTIONS AND RESEARCH APPROACH..... 2

1.3. FACTORS LEADING TO DEFECTS IN INORGANIC COATINGS..... 4

**1.3.1. VACUUM DURING THE PVD PROCESS AND PAPER
HYGROEXPANSION..... 5**

**1.3.2. ALUMINUM LAYER GROWTH AND SUBSTRATE SURFACE: EFFECT
OF DEBRIS, PORES AND ROUGHNESS 6**

1.3.3. INTRINSIC AND EXTERNAL STRESSES..... 8

1.3.4. MECHANICAL PROPERTIES AND FRACTURE MECHANISMS 11

1.3.5. EFFECTS OF ALUMINUM COATING THICKNESS..... 11

1.3.6. CONCLUSION..... 12

1.4. CHAPTER BIBLIOGRAPHY 14

2.	REVIEW:	
	FACTORS AFFECTING THE HYGROEXPANSION OF PAPER.....	16
3.	REVIEW:	
	THICKNESS MEASUREMENT METHODS FOR PHYSICAL VAPOR DEPOSITED	
	ALUMINUM COATINGS IN PACKAGING APPLICATIONS: A REVIEW	43
4.	RESEARCH PAPER:	
	COMPARISON OF THICKNESS DETERMINATION METHODS FOR PHYSICAL-VAPOR-	
	DEPOSITED ALUMINUM COATINGS IN PACKAGING APPLICATIONS.....	76
5.	RESEARCH PAPER:	
	HYGROEXPANSION AND SURFACE ROUGHNESS CAUSE DEFECTS AND INCREASE	
	THE ELECTRICAL RESISTIVITY OF PHYSICAL VAPOR DEPOSITED ALUMINUM	
	COATINGS ON PAPER	87
6.	RESEARCH PAPER:	
	HYGROEXPANSION, SURFACE ROUGHNESS AND POROSITY AFFECT THE	
	ELECTRICAL RESISTANCE OF EVOH-ALUMINUM-COATED PAPER	107
7.	DISCUSSION, OUTLOOK AND CONCLUSION	123
7.1.	FACTORS LEADING TO DEFECTS IN ALUMINUM COATINGS.....	123
7.2.	DETECTION OF DEFECTS VIA ELECTRICAL RESISTIVITY	124
7.3.	REDUCTION OF DEFECT-TRIGGERING FACTORS AND THEIR	
	INTERACTIONS	125
7.3.1.	MODIFICATION OF PAPER HYGROEXPANSION.....	125
7.3.2.	EFFECT OF SUBSTRATE HYGROEXPANSION ON ELECTRICAL	
	RESISTANCE OF ALUMINUM	126
7.3.3.	REDUCTION OF SUBSTRATE SURFACE ROUGHNESS AND	
	SUBSTRATE POROSITY.....	126
7.3.4.	EFFECT OF INCREASING ALUMINUM THICKNESS ON THE AREA	
	NUMBER DENSITY OF DEFECTS IN ALUMINUM COATINGS.....	127
7.4.	CONCLUSION: MAIN FACTOR LEADING TO DEFECTS IN ALUMINUM	
	COATINGS.....	128
7.5.	CHAPTER BIBLIOGRAPHY	130
8.	SUMMARY.....	131
	CURRICULUM VITAE.....	133

Kurzfassung

Das Verhalten Nanometer-dünner Aluminiumschichten auf un- und polymerbeschichtetem Papier wurde untersucht. Die Defekt-Flächendichte in der Aluminiumbeschichtung wurde indirekt durch deren effektiven elektrischen Widerstand beschrieben, welcher mit steigender Aluminiumdicke abnahm, und mit der Hygroexpansion und Rauheit des Papiers stieg. Die Hygroexpansion nahm durch eine Polymer-Vorbeschichtung zu und führte zu Rissen in der Aluminiumschicht. Nur auf polymerbeschichteten Papieren, deren Oberfläche nicht porös ist, konnten Aluminiumschichten (>35nm) der Hygroexpansion standhalten.

Abstract

This study addresses the behavior of thin (nanoscale) aluminum coatings on uncoated and polymer coated papers. The area number density of defects in the aluminum coating was described indirectly by the effective electrical resistivity, which increased with thinner aluminum coatings, hygroexpansion and greater substrate paper roughness. Hygroexpansion was promoted by polymer pre-coating, and caused cracks in the aluminum. Aluminum coatings (>35 nm thick) could withstand hygroexpansion only on polymer pre-coated (non-porous) substrates.

1. General introduction

1.1. Physical vapor deposition-coated paper substrates as packaging materials

As fossil based resources decline, biobased materials are gaining more importance. One large market for fossil-based polymers is packaging, particularly flexible packaging materials combining low costs and low material usage [1]. Packaging must also fulfil other requirements, such as containment, convenience, communication and, most importantly, protection. For example, packaging must protect goods against permeating gases that could reduce the shelf life of the product. This protection can be achieved by combining different polymers that build a physical barrier against different gases (Figure 1a, b). One efficient strategy to increase the performance of a gas barrier is by applying nanoscale thickness inorganic silicon oxide, aluminum oxide or aluminum coatings by physical vapor deposition (PVD) onto polymeric substrate films (Figure 1c). Such coatings can increase the gas barrier by approximately two orders of magnitude as long as the coatings are virtually defect-free [2]. However, in real applications, such inorganic coatings always contain some defects, which allow the permeation of small quantities of gas (Figure 1d).

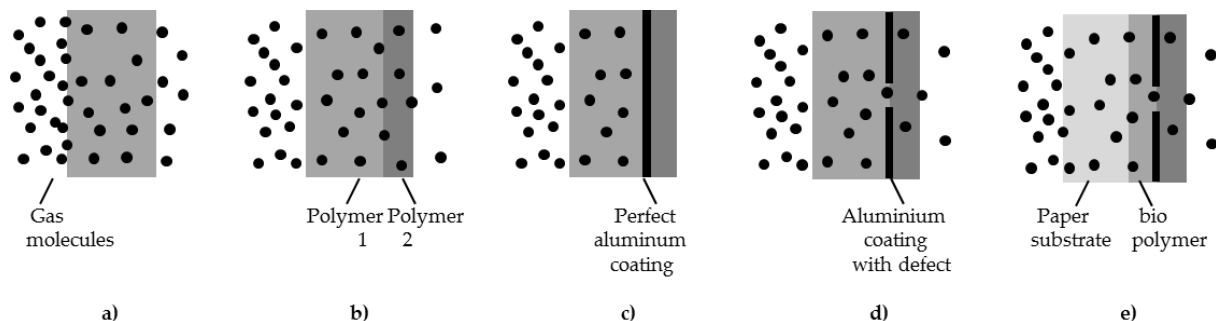


Figure 1: Permeation through organic and inorganic materials (adapted from [2]): a) pure polymer; b) bilayer material comprising two different polymers; c) multilayer material with additional, idealized inorganic coating; d) realistic aluminum coating with defect; e) part of the base polymer is replaced by a paper substrate.

The concept of biobased packaging materials, in which paper replaces the fossil-based polymer substrates for PVD, has existed for decades. In this approach, paper is pre-coated with a thin layer of polymer that smoothens the paper surface (Figure 1e). Indeed, PVD is already widely used with paper substrates, but only for decorative purposes [3]. Gas barrier improvement is not achieved when applying a coating to paper by PVD, and **the reasons for this have yet to be understood** [4].

1.2. Scientific questions and research approach

Reasons for the lack of barrier performance of PVD inorganic coatings on paper have yet to be investigated in detail, in order to find suitable approaches for overcoming this challenge. What is known thus far is that the barrier performance of aluminum coatings on polymers is dependent on the aluminum's chemical composition, the microstructure and area number density of defects [5,6]. The chemical composition is affected mainly by the nature of the aluminum raw material and the residual oxygen content in the evaporation chamber (recipient). Given that both are kept constant, any investigation of the lack of barrier performance must focus on the **microstructure of the coating and the area number density of defects**.

Despite efforts to minimize the area number density of defects, it is not yet possible to produce a defect-free inorganic coating even on the best available polymer substrates by PVD according to the current state of the art [7]. Such defects increase gas permeability and thus limit the applications of the coated polymer as a barrier packaging material. The mechanisms by which gases permeate through inorganic coatings on polymer substrates depend on the defect size [8]. The major mechanism is diffusion through macroscopic defects (>100 nm), where permeation continues just as it would in the absence of a coating [9]. For technically relevant substrate thicknesses and defect sizes, permeation through defects in inorganic coatings can be modeled approximately using Equation (1) [10]. Herein, the permeability of the substrate with the inorganic coating $Q_{sub+coat}$ depends only on the permeability coefficient (P) of the polymeric substrate, the number of defects per unit area (n_d) and the effective average defect area (a) [11].

$$Q_{sub+coat} \approx 2 \cdot P \cdot n_d \cdot \sqrt{a} \quad (1)$$

This equation emphasizes the negative influence of defects in the aluminum coating, when a gas barrier is required. Thus far it remains unclear which factors influence the defect density in the aluminum when a paper substrate is used. Moreover, no method is yet available to quickly gain information about the area number density of defects in the aluminum on paper based substrates due to the opacity of the paper in contrast to transparent polymer substrates. In order to **reduce the quantity of these defects** and produce more effective packaging materials, the **following scientific questions** have to be answered.

1) Which key factors influence the extent of defects in the inorganic coating?

To answer this question, the converting process was screened for key parameters, revealing that aluminum thickness, hygroexpansion and paper roughness are critical factors. This work is described in Chapter 1, Section 1.3.

2) How can such defects in an aluminum coating be detected?

In the case of polymeric substrates, defects in the aluminum coating can be detected by microscopy. This is not the case for paper substrates due to massive light scattering of paper substrates. The electrical resistance and effective resistivity were identified as suitable parameters to describe the appearance of defects indirectly. The electrical resistance is the property of a substance to resist the flow of current through it, whereas the electrical resistivity is the electrical resistance per unit length and per unit of cross-sectional area of the substance. Both values describe defects indirectly because defects reduce the electrical conductance and increase the resistance of aluminum coatings. This work is described in Chapter 3.

3) How can factors that cause defects in an aluminum coating be influenced?

The roughness of the paper substrate can be reduced by adding a polymer coating and the aluminum thickness can easily be controlled during PVD, so these approaches were tested as potential strategies to reduce the area number density of defects (Chapters 5 and 6). In the case of hygroexpansion, influencing factors remain unclear. Therefore, several potential triggers were evaluated, revealing that hygroexpansion is affected by polymer pre-coatings and chemical treatments such as grafting (Chapter 2).

4) What is the effect of different combinations of aluminum thickness, hygroexpansion and paper roughness on the area number density of defects and electrical resistance of aluminum coatings?

Greater hygroexpansion and substrate roughness were expected to lead to more defects in the aluminum coating and thus to a higher electrical resistance. Moreover, the following was found: When an exceptionally thin aluminum coating is applied on an exceptionally rough surface, this combination enhances the effect of hygroexpansion on the area number density of defects and thus on electrical resistance (Chapters 5 and 6).

5) What is the main factor leading to defects in the aluminum coating?

In order to most effectively reduce the number and extent of defects in the aluminum coatings, it was necessary to determine the relative importance of the different critical parameters. The most important factor was found to be substrate roughness, followed by hygroexpansion and aluminum thickness (Chapters 5, 6 and 7).

1.3. Factors leading to defects in inorganic coatings

In order to determine the factors that lead to defects in the inorganic coating, the converting process was screened for critical parameters that might affect the area number density of defects. This density of defects of aluminum applied to paper was found to be mainly affected by paper roughness, aluminum thickness and paper hygroexpansion (Figure 2). Each factor is addressed in turn in Sections 1.3.1–1.3.5 and the effects of these factors are summarized in Section 1.3.6.

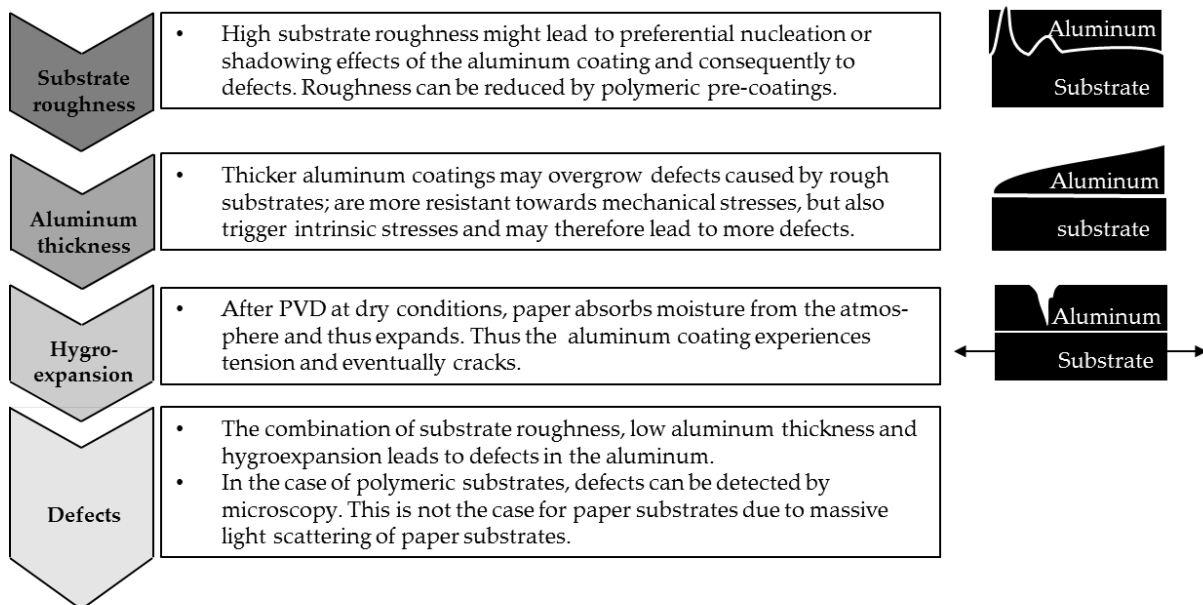


Figure 2. Accumulation of effects that might trigger defects in PVD aluminum coatings on paper during the converting process: substrate roughness, aluminum thickness and hygroexpansion.

1.3.1. Vacuum during the PVD process and paper hygroexpansion

PVD is a vacuum-based coating process, in which the evaporated material, such as aluminum, aluminum oxide or silicon oxide, is physically heated before it condenses on the cooler substrate, which is passed by unwinding and rewinding using the equipment shown in Figure 3 [12]. Given that only aluminum is used in the present study, the treatment of metal oxides and ceramics is excluded from the discussion below.

A high vacuum is needed because it increases the mean free path length and enhances the quality of the aluminum coating [3]. This is because high stoichiometric purity and high aluminum coating quality can only be achieved by a low particle collision rate in the interval between the evaporator and substrate. A high residual gas concentration leads to a higher inter-atomic collision rate and the formation of undesirable molecules. The vacuum avoids the scattering of aluminum atoms and their reaction with gas atoms or molecules (e.g. with oxygen to form aluminum oxide). Therefore, a minimal vacuum pressure must be ensured in order to avoid a heterogeneous aluminum coating.

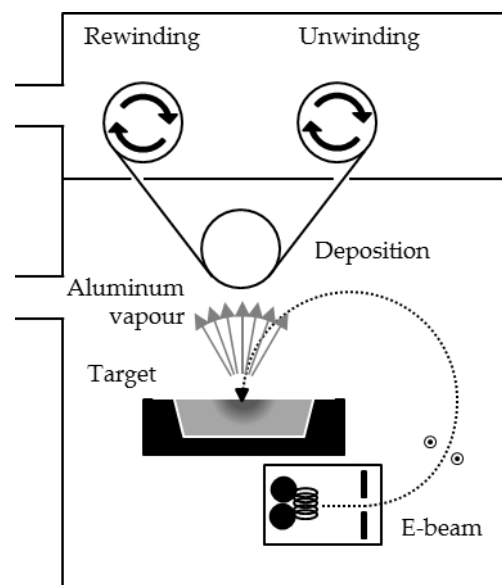


Figure 3: Physical vapor deposition vacuum chamber (schematic).

Although the **vacuum increases the quality of the aluminum coating** on polymeric substrates, it is **also a hindrance** during the formation of closed aluminum layers on hygroscopic substrates such as paper. As described in Chapter 2, paper absorbs moisture from the atmosphere and thus expands. Consequently, it also shrinks under vacuum, as the moisture content is released. The aluminum is then evaporated and deposited on the

shrunken paper. Once the process is finished, the paper is removed from the vacuum chamber and re-humidified, undergoing $\sim 1\text{-}2\%$ **re-expansion**. The aluminum coating thus experiences tension and **eventually cracks**. The effect of aluminum cracking was described earlier for aluminum-coated polymers, where the area number density of defects and gas permeability increased due to mechanical stretching [13]. The effect of hygroexpansion is described in more detail in Section 1.3.3.

1.3.2. Aluminum layer growth and substrate surface: effect of debris, pores and roughness

After evaporation, aluminum condenses on the cooler substrate (Figure 3). Layer growth starts with the first nuclei of condensed atoms that are deposited on the surface, and these define the subsequent layer structure. The arriving atoms lose kinetic energy, and are loosely bound as adatoms on the surface. Those adatoms predominantly bind to existing material clusters or to other energetically favorable sites, such as steps, edges or cavities in the surface topography. If the residual energy is sufficient, the atoms can diffuse across the substrate surface, allowing single adatoms to form stable or metastable clusters [5,14].

Three models have been proposed covering a variety of potential interactions between substrate and adatoms (Figure 4), with the models in (a) and (c) representing the extremes and (b) a combination of them [5,14-16]. In the model of Frank-van der Merwe (Figure 4a), the cohesion between adatoms is weaker than their adhesion to the substrate. A monolayer grows, which is fully closed, before the next layers grow. The Stranski-Krastanov model (Figure 4b) begins in a similar manner, but islands start to appear on the initially closed monolayer. In contrast, the Volmer-Weber model (Figure 4c) goes to the other extreme and assumes that cohesion between adatoms is stronger than their adhesion to the substrate. Following the nucleation of small clusters, these grow to form small three-dimensional islands. A closed coating is achieved only when the layer grows [16-19] to more than two atomic monolayers [17].

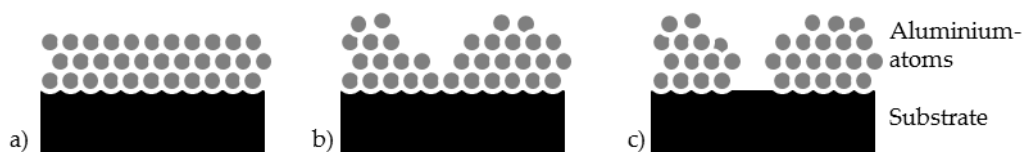


Figure 4. Models for layer growth: a) Frank-van der Merwe; b) Stranski-Krastanov; c) Volmer-Weber. Black shape = substrate; gray shape = aluminum.

The exact process of layer growth and thus the appearance of defects in the aluminum coatings is dependent on many factors including the evaporation and substrate temperature, the pressure during PVD and the substrate morphology [20]. The substrate surface morphology is characterized by three main parameters, which can affect the integrity of the aluminum coating (Figure 5).

Parameter 1 (Figure 5a): Macroscopic defects may appear due to contamination with dust before the PVD process. These dust particles can stick to the substrate surface while they are coated with aluminum but may fall off afterwards because they are only loosely bound, leaving a defect in the coating. Such debris can be removed using hydrostatic web cleaning devices [21].

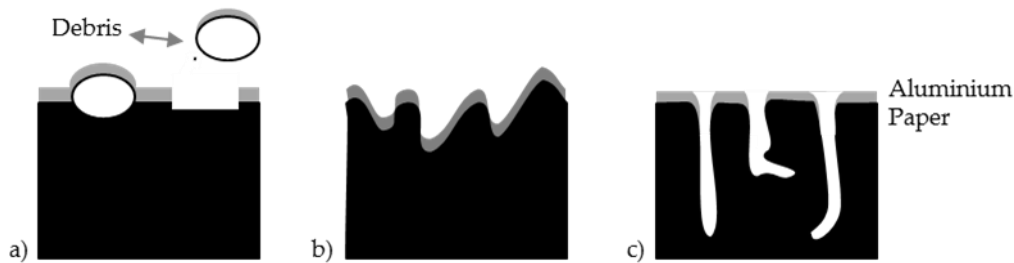


Figure 5. Factors affecting surface morphology: a) dust on the substrate surface; b) rough surfaces; c) porous surfaces. Black shape = paper; gray shape = aluminum.

Parameter 2 (Figure 5b): Imperfections might appear due to substrate roughness. Given that roughness may exist simultaneously on several size scales, the aluminum coatings exhibit superimposed shadow growth boundaries, each associated with a size scale of substrate roughness [22]. For rough substrates, three film growth processes have been described (Figure 6). First, valleys in the surface will lead to preferential nucleation and epitaxy because these valleys are energetically favorable for aluminum atoms (Figure 6a).

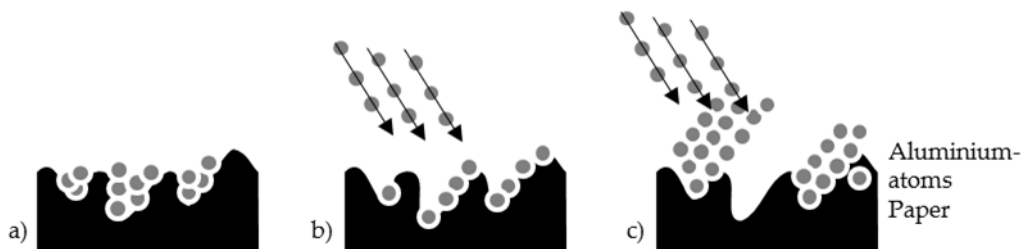


Figure 6. Possible effects of substrate roughness on thin film growth. Black shape = paper; gray shape = aluminum.

Second, shadows cast by nuclei during the early stage of film deposition inhibit growth in the projected source direction (Figure 6b) [23]. Third, the roughness itself casts a shadow, which leads to slower-growing areas in the shadow (Figure 6c). If the deposition time is short, the shadowed areas may not form a fully-closed surface, thus leaving defects in the aluminum coating.

Parameter 3 (Figure 5c): Porous substrates emphasize the shadowing effect. The shadowing effect becomes even more pronounced because little of the aluminum vapor will flow into the pores during the PVD timeframe. It is more likely that aluminum deposits on the surface and pores will remain uncoated.

On polymeric and paper substrates, parameter 1 (i.e. dust on the surface) can be addressed by cleaning. Parameter 2 (roughness) can be reduced to the nanometer scale by the biaxial orientation of polymer films such as biaxially oriented polyethylene terephthalate (boPET). Substrate roughness has been shown to increase the area number density of defects and thus the gas permeability [24]. Parameter 3 (substrate porosity) is not relevant on polymeric substrates. However, it is important to consider the impact of **both roughness and substrate porosity of paper substrates** because they are present at the **micrometer scale**, can affect coating integrity [12], and can only be reduced partially by polymeric coating. However, **the extent to which these two factors affect the appearance of defects in aluminum coatings on paper is not year clear** (see Chapters 5 and 6).

1.3.3. Intrinsic and external stresses

In addition to the built-in defects discussed above, the integrity of aluminum coatings is also threatened by stress that may lead to defects in the form of cracks. The forms of stress that affect inorganic coatings on polymer substrates have been investigated, but this is not the case for paper substrates. Known sources of stress for aluminum coatings on polymer substrates are summarized in the first and second columns of Table 1 and their potential effect on aluminum coatings on paper substrates is inferred in the third column.

External stresses are expected to vanish once the load is removed, both for paper and polymer films. But in the case of tensions due to expansion mismatch and intrinsic tensions, the substrate material is expected to play a major role.

Stresses due to expansion mismatch can appear due to **thermal expansion** and contraction of aluminum and polymers during and after aluminum deposition. The thermal expansion coefficients of polymers and aluminum differ by a factor of 10 ($23 \cdot 10^{-6}/^{\circ}\text{C}$ at 20°C , $37 \cdot 10^{-6}/^{\circ}\text{C}$ at 627°C for aluminum [25]; $10 \cdot 10^{-5}/^{\circ}\text{C}$ at $20\text{--}60^{\circ}\text{C}$ for polypropylene [26]). Assuming a temperature change of $0\text{--}30^{\circ}\text{C}$ for a 1 m wide sheet of metallized polypropylene film, this leads to a difference in expansion between polypropylene and aluminum of 0.3% vs. 0.07%, or 2.3 mm over the width of the sheet. The influence is likely to be negligible because a strain of up to 6% could be tolerated without the formation of defects in the aluminum layers in laminated PVD coated films [13]. The thermal expansion of pure cellulose is in the same range as aluminum ($4.3 \cdot 10^{-5}/^{\circ}\text{C}$ [27]). However, this value is valid only for pure cellulose, not taking into account hemicellulose, lignin and the adverse effect of humidity. In literature no values were found for the thermal expansion of cellulose fibers or paper.

Table 1: Major forms of stress in PVD coatings on polymer and paper substrates.

	Polymeric substrates	Paper substrates
External stresses	Common for both types of substrates: Applied forces such as web tension during conversion lead to deformation and thus to external stresses [28,29].	
Expansion mismatch	Temperature changes and different coefficients of thermal expansion in the coating and substrate material lead to an expansion mismatch [30].	Hygroexpansion of the paper substrate stresses the aluminum coating (see Chapter 2).
Intrinsic stresses	The accumulation of crystallographic flaws that are built into the coating during deposition leads to intrinsic stresses [31].	Crystallographic flaws are triggered by increased substrate roughness (Section 1.3.2).

In the case of paper, the major expansion appears as **hygroexpansion**, which refers to moisture-induced dimensional changes. Hygroexpansion is critical because PVD takes place under a high vacuum of $\sim 10^{-6}$ mbar (Section 1.3.1) so the water evaporates in the course of the process and the **paper shrinks. After metallization**, the paper is transferred to humid air

and subsequently **expands** by ~1–2% as water enters from the uncoated side. Again assuming a 1 m wide sheet of metallized paper, this leads to a difference in expansion of 2% versus 0%, or 2 cm over the width of the sheet. Due to this high expansion mismatch, the **aluminum coating is strained and is expected to crack.**

Intrinsic stresses are present in a body when no external tensions or expansion mismatch are applied. They can arise due to crystallographic flaws and defects. In the case of crystallographic flaws, some extra atoms are introduced midway through a crystal, distorting nearby planes of atoms (Figure 7). These extra atoms break existing bonds and form new ones, leading to local compression and tension. Such flaws are triggered by factors such as nanoscale substrate surface roughness. In the case of polymers, inorganic coatings are applied onto very smooth, partially biaxial-oriented, stretched polymeric films, which are characterized by nanoscale roughness. In contrast, paper substrates are characterized by nanoscale and microscale roughness. Flaws cannot be fully avoided in either case, but the microscale roughness of paper further triggers defects in the aluminum coating such as those as described in Section 1.3.2. Such defects lead to local stress concentrations that encourage localized damage and lead to crack initiation and propagation (Figure 7b, Figure 8b) [32,33]. These factors indicate that even more flaws and heterogeneities are present in aluminum on paper substrates, thus the **intrinsic stress on paper substrates is expected to be much higher.**

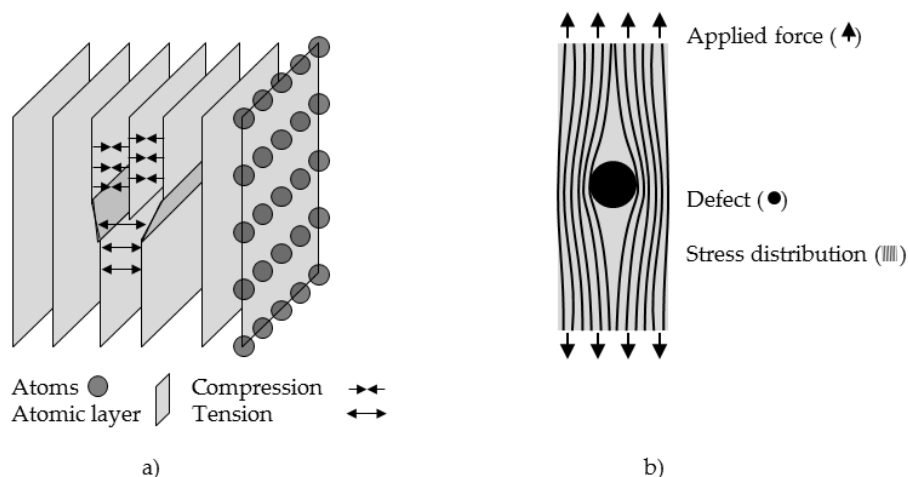


Figure 7. a) Crystallographic flaws. b) Stress distribution around defects in aluminum coatings.

Whether these stresses ultimately lead to cracks depends on the mechanical properties of the aluminum coating. This factor is described in the next chapter.

1.3.4. Mechanical properties and fracture mechanisms

The **mechanical properties** of metals such as aluminum differ from those of ceramics and polymers. Metals are more ductile than ceramics, but more brittle than polymers. Thus, aluminum has a higher fracture stress but a lower fracture strain than polymers (Figure 8a). In comparison to brittle PVD materials such as silicon oxide or aluminum oxide, more ductile materials such as aluminum become thinner or form necks when strained beyond the yield point. At higher strains, these thinned regions become cracks (Figure 8b). The fracture stress of inorganic materials can be extremely high when they are pure and possess a perfect inner structure, such as pure crystals. However, the fracture stress declines rapidly in the presence of crystalline flaws or defects. In the case of paper substrates, **roughness and substrate porosity can increase the area number density of defects** in the aluminum coatings as described in Sections 1.3.2 and 1.3.3. Those defects may lead to local stress concentrations and thus **reduce the mechanical stability of the aluminum, which is particularly critical during hygroexpansion**.

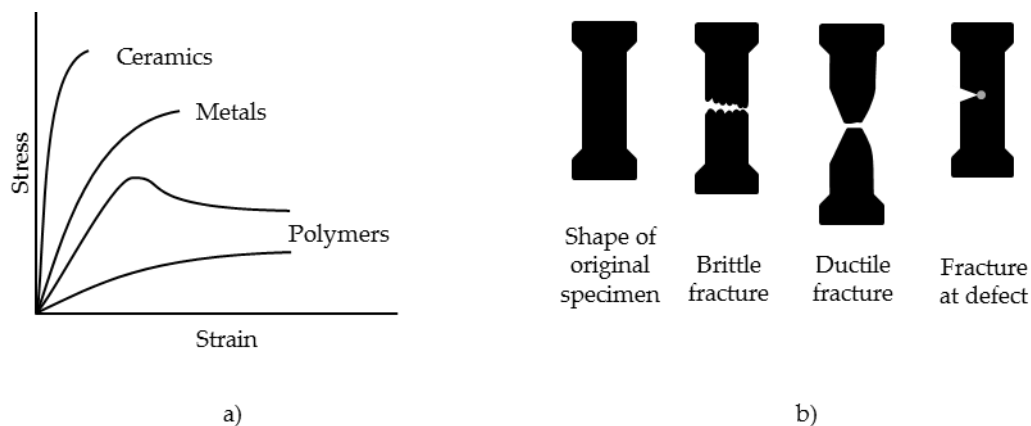


Figure 8. a) Comparison of the mechanical properties of metals, polymers and ceramics. b) Visualization of different fracture modes.

1.3.5. Effects of aluminum coating thickness

Thicker aluminum coatings are more resistant towards mechanical deformation [34], which is especially relevant with respect to the stresses caused by hygroexpansion. Moreover, thicker aluminum coatings could presumably also overgrow defects in the coatings caused by substrate roughness (Section 1.3.2). However, thicker aluminum coatings also increase the intrinsic stress due to the increased probability of lattice mismatches [35,36] and can thus lead to cracks, when those stresses exceed adhesion forces. The critical

thickness at which a thin film starts to crack due to intrinsic stress can be as low as several tens of nanometers [31], which is the thickness of typical aluminum PVD coatings.

Concluding, **it is unclear whether thicker layers could help to overcome the causes of defects in aluminum coatings**, namely the defects due to substrate roughness, intrinsic stresses, or expansion mismatch.

1.3.6. Conclusion

This chapter summarized the factors responsible for defects in inorganic coatings, such as aluminum. The following parameters were found to be most critical (Figure 9).

- 1) **Aluminum thickness:** Thicker aluminum coatings are more resistant towards mechanical stresses, but also trigger intrinsic stresses and may therefore lead to more defects.
- 2) **Hygroexpansion of the paper:** A high vacuum is necessary during the PVD process which leads to drying and shrinkage of the paper. When the PVD process is finished, the paper is re-humidified and thus re-expands, and the aluminum on top eventually cracks.
- 3) **Substrate roughness:** Substrate roughness induces defects in the aluminum coating itself and also reduces the mechanical stability of the aluminum coating during hygroexpansion.

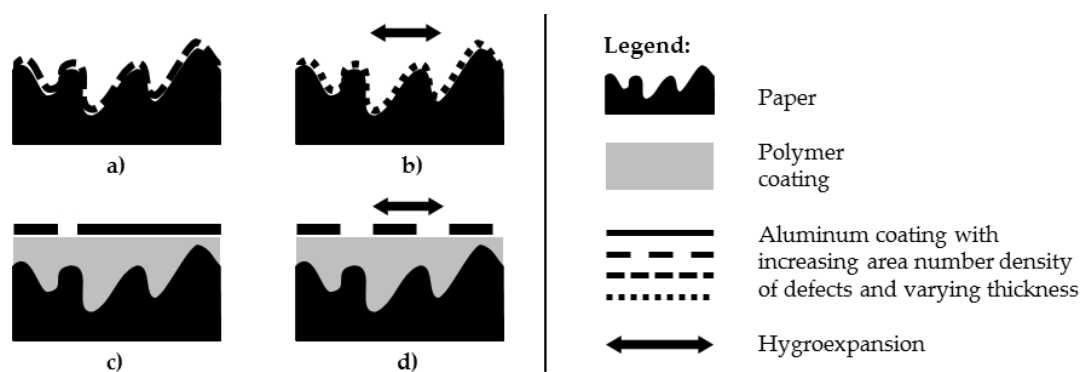


Figure 9: a) Paper with aluminum coating and a high area number density of defects in the aluminum. b) Increasing defect density due to hygroexpansion. c) Paper with polymer pre-coating and aluminum coating, with few defects. d) Increasing defect density due to hygroexpansion.

Based on this conclusion, the remaining questions were elaborated as described in Table 2.

Table 2: Overview over scientific questions and the relevant publications.

1) Which key factors influence the extent of defects in the inorganic coating?		
Chapter 1	page 12	Conclusion
2) How can such defects in an aluminum coating be detected?		
Chapter 3	page 43	Review: Thickness measurement methods for physical vapor deposited aluminum coatings in packaging applications: A review.
3) How can factors that cause defects in an aluminum coating be influenced?		
Chapter 2	page 16	Review: Factors affecting the hygroexpansion of paper
Chapter 5	page 87	Research paper: Hygroexpansion and surface roughness cause defects and increase the electrical resistivity of physical vapor deposited aluminum coatings on paper
Chapter 6	page 107	Research paper: Hygroexpansion, surface roughness and porosity affect the electrical resistance of EVOH-aluminum-coated paper
4) What is the effect of different combinations of aluminum thickness, hygroexpansion and paper roughness on the area number density of defects and electrical resistance of aluminum coatings?		
Chapter 5	page 87	Research paper: Hygroexpansion and surface roughness cause defects and increase the electrical resistivity of physical vapor deposited aluminum coatings on paper
Chapter 6	page 107	Research paper: Hygroexpansion, surface roughness and porosity affect the electrical resistance of EVOH-aluminum-coated paper
5) What is the main factor leading to defects in the aluminum coating?		
Chapter 5	page 87	Research paper: Hygroexpansion and surface roughness cause defects and increase the electrical resistivity of physical vapor deposited aluminum coatings on paper
Chapter 6	page 107	Research paper: Hygroexpansion, surface roughness and porosity affect the electrical resistance of EVOH-aluminum-coated paper
Chapter 7	page 123, page 128	Discussion, outlook and conclusion

1.4. Chapter bibliography

1. *Europa: Hohe Nachfrage nach flexiblen Verpackungen.* Euwid 2019.
2. Piringer, O.G.; Baner, A.L. *Plastic Packaging: Interactions with Food and Pharmaceuticals.* Wiley: 2008.
3. Bishop, C. *Vacuum deposition onto webs, films and foils.* William Andrew: 2011.
4. Eckl, J.; Lindner, M.; Förster, F. *Abschlussbericht: Innovative papierbasierte Packstoffe durch Barrierefunktionalisierung mit nanoskaligen Schichten zum Ersatz von erdölbasierten Rohstoffen und Folienverbunden - Paper4Barrier.* Technische Informationsbibliothek Hannover 2015.
5. Neugebauer, A. *Condensation, Nucleation, and Growth of Thin Films.* In Handbook of thin film technology, Maissel, L.I.; Glang, R., Eds. McGraw-Hill: New York, 1970.
6. Kaßmann, M. *Grundlagen der Verpackung: Leitfaden für die fächerübergreifende Verpackungsausbildung.* Beuth Verlag: 2014.
7. Lohwasser, W. *Not only for Packaging,* 43rd Annual Technical Conference of the Society of Vacuum Coaters, 2000.
8. Langowski, H.-C.; Utz, H. *Dünne anorganische Schichten für Barrierepackstoffe.* Internationale Zeitschrift für Lebensmittel-Technik, Marketing, Verpackung und Analytik 2002, 9, 522.
9. Roberts, A.P.; Henry, B.M.; Sutton, A.P.; Grovenor, C.R.M.; Briggs, G.A.D.; Miyamoto, T.; Kano, M.; Tsukahara, Y.; Yanaka, M. *Gas permeation in silicon oxide/polymer (SiO₂/PET) barrier films: role of oxide lattice, nano-defects and macrodefects.* Journal of Membrane Science 208 2002, 75 – 88.
10. Prins, W.; Hermans, J.J. *Theory of Permeation through Metal Coated Polymer Films.* The Journal of Physical Chemistry 1959, 63, 716-720.
11. Miesbauer, O.; Schmidt, M.; Langowski, H.-C. *Stofftransport durch Schichtsysteme aus polymeren und dünnen anorganischen Schichten.* Vakuum in Forschung und Praxis 2008, 20, 32-40.
12. G. Kienel; Sommerkamp, P. *Aufdampfen im Hochvakuum.* In Vakuum-Beschichtung 2, VDI Verlag: Düsseldorf, 1992; pp 20-26.
13. Moosheimer, U. *Vacuum coating of polymer films for packaging and technical applications.* Final Research Report, funding nr BRRT985091, European Commission 2001.
14. Haefler, R.A. *Oberflächen- und Dünnschicht-Technologie.* Springer: 1987.
15. Kienel, G.; Frey, H. *Dünnschichttechnologie.* VDI Verlag: 1987; Vol. 506.
16. Vook, R.W. *Structure and growth of thin films.* International Metals Reviews 1982, 27, 209-245.
17. Reichelt, K.; Jiang, X. *The preparation of thin films by physical vapour deposition methods.* Thin Solid Films 1990, 191, 91-126.
18. Kern, R.; de Lay, G.; Metois, J.J. *Basic mechanisms in the early stage of epitaxy.* E. Kaldis (Hrsg.), Current topics in material science 1979, 3, 135-419.
19. Stoyanov, S. *Nucleation theory for high and low supersaturations.* Current topics in material science 1979, 3, 421-462.
20. Thornton, J.A. *Influence of apparatus geometry and deposition conditions on the structure and topography of thick sputtered coating.* Journal of vacuum science and technology 1974, 11, 666-670.

21. Wandres GmbH micro-cleaning. *Effiziente Oberflächenreinigung für Kartonage-, Papier- und Folienbahnen*. 2019, product brochure.
22. Thornton, J.A. *High rate thick film growth*. Annual review of materials science 1977, 7, 239-260.
23. Bishop, C.A. *Vacuum Deposition onto Webs, Films and Foils*. 2nd ed.; Elsevier: 2011.
24. Müller, K.; Schönweitz, C.; Langowski, H.-C. *Thin Laminate Films for Barrier Packaging Application - Influence of Down Gauging and Substrate Surface Properties on the Permeation Properties*. Packaging Technology and Science 2012, 25, 137-148.
25. Hatch, J.E.; Association, A.; Metals, A.S. *Aluminum: Properties and Physical Metallurgy*. American Society for Metals: 1984.
26. Tripathi, D. *Practical Guide to Polypropylene*. RAPRA Technology: 2002.
27. Wada, M. *Lateral thermal expansion of cellulose I β and III polymorphs*. Journal of Polymer Science Part B: Polymer Physics 2002, 40, 1095-1102.
28. Bunshah, R.F. *Handbook of deposition technologies for films and coatings: science, technology, and applications*. William Andrew: 1994.
29. Dribinskiy, S.; Fluß, D. *Aufgedampfte SiO $_x$ Barrierschichten unter monoaxialem Stress*. Vakuum in Forschung und Praxis 2014, 26, 32-33.
30. Raghuram, A.; Bunshah, R. *The effect of substrate temperature on the structure of titanium carbide deposited by activated reactive evaporation*. Journal of vacuum science and technology 1972, 9, 1389-1394.
31. Thornton, J.A.; Hoffman, D. *Stress-related effects in thin films*. Thin Solid Films 1989, 171, 5-31.
32. Li, P.; Lee, P.; Maijer, D.; Lindley, T. *Quantification of the interaction within defect populations on fatigue behavior in an aluminum alloy*. Acta Materialia 2009, 57, 3539-3548.
33. Kirsch, C. *Die Theorie der Elastizität und die Bedürfnisse der Festigkeitslehre*. Zeitschrift des Vereines Deutscher Ingenieure 1898, 42, 797-807.
34. Cordill, M.J.; Taylor, A.A.; Schmidegg, K. *Thickness effects on the fracture of chromium films on polyethylene terephthalate*. BHM Berg- und Hüttenmännische Monatshefte 2011, 156, 434-437.
35. Klokholm, E.; Berry, B. *Intrinsic stress in evaporated metal films*. Journal of The Electrochemical Society 1968, 115, 823-826.
36. Flötotto, D. *Mechanisms of intrinsic stress formation in thin film systems*. Dissertation, Universität Stuttgart, Stuttgart, 10.2013.

2. Review:

Factors affecting the hygroexpansion of paper

Paper is a network of fibers, and hygroexpansion is therefore influenced by the swelling behavior of individual fibers as determined by their polymer composition and ultrastructure. The three main polymers in fibers are cellulose, hemicellulose and lignin, among which hemicellulose shows the highest increase in volume. The polymers form 4–5 hollow, concentric structures stabilized by microfibrils that wind around them. A steeper winding angle of the microfibrils in fibers and the presence of curled fibers in paper increases the degree of hygroexpansion of paper.

Because the swelling of paper depends on the absorbance of water by single fibers, the swelling can be influenced by altering the chemical composition of the fiber surface. Chemical treatments such as poly-electric multilayers, crosslinking, grafting and the addition of lignin and fillers can reduce hygroexpansion.

During pulp and paper production, the different pulp fractions, processes like beating, refining and drying can have an effect on paper sheet hygroexpansion. Moreover, hygroexpansion is higher in the cross-machine direction but lower in the machine direction, reflecting the degree of fiber orientation in a paper sheet. Although more inter-fiber contacts promote hygroexpansion, the effect of paper density (pore volume and fiber content) is disputed. Only one study was found¹ dealing with the effect of polymeric coatings on the hygroexpansion of paper, and it concluded that coating paper with polyethylene reduces hygroexpansion in the machine direction.

In summary, hygroexpansion is mainly influenced by the processing and chemical and morphological structure of the paper, which can be adjusted during paper production only. In processes following the paper production, these factors cannot be influenced and only methods like grafting, corona treatment, and coating with polymers can subsequently be applied to affect paper hygroexpansion.

Author contributions: Martina Lindner: writing, outline, editing, revision, visualization.

¹ Paunonen, S. Influence of moisture on the performance of polyethylene coated solid fiberboard and boxes. Dissertation, Norwegian University of Science and Technology, Trondheim, 2010.



Factors affecting the hygroexpansion of paper

Martina Lindner^{1,2,*}

¹TUM School of Life Sciences Weihenstephan, Chair of Food Packaging Technology, Technical University of Munich, Weihenstephaner Steig 22, 85354 Freising, Germany

²Fraunhofer-Institute for Process Engineering and Packaging IVV, Giggenhauser Straße 35, 85354 Freising, Germany

Received: 3 April 2017

Accepted: 5 July 2017

© The Author(s) 2017. This article is an open access publication

ABSTRACT

Paper is a widely used packaging material and is nowadays regaining importance, e.g., as bio-based and biodegradable material. Moreover, new technologies such as polymer–fiber composites, printed electronics and the deep drawing of paper are developing. The process stability and also the resulting quality of paper converting processes such as coating, metallization, printing, and the printing of electronics are highly affected by the hygroexpansion of paper. In order to reduce production instability and to choose and develop paper substrates with ideal characteristics, critical parameters need to be known. This paper offers an extensive overview of those parameters, starting at a molecular and microscopic level with the effect of the constituents and morphology of single fibers, before moving on to paper contents, chemical modifications and additives and finally concluding with paper production and fiber network modification. It was found that the major influences are single fiber sorption, inter-fiber contacts, microfibril angle, fiber morphology (length, width, curliness) and fiber orientation. This review gives new ideas and insights for technologists working in research, development and production optimization of paper-based products.

Introduction

Since 1960 paper production has increased in Europe [1]. In 2015, 106,496 thousand tons of paper was produced in Europe and 407,595 thousand tons worldwide, of which 6% were produced for newsprint, 25% for other graphic applications, 57% for packaging, 9% for hygiene, sanitary and household use and 4% for other applications [2]. In the field of packaging, paper fulfills different purposes. It is used for the protection of the goods (for example, when used as single material for food wrapping), in laminates (for example for

carton board liquid packaging), and for secondary packaging (for example boxes). Apart from that, it is used to improve rationalization, by being formed into small load carriers or being used as bar code labels. Moreover, it serves as a tool for communication and marketing, for example as a substrate for printing or printed electronics [3]. In all cases, the performance can be influenced by the hygroexpansion of paper. Hygroexpansion is the dimensional change due to fluctuations of the relative humidity of the surrounding atmosphere which affects the moisture content of the paper [4]. Due to hygroexpansion, laminates and labels

Address correspondence to E-mail: martina.lindner@ivv.fraunhofer.de

can separate, wrinkle or curl, the distance between printing fiducial marks can be altered and the noble appearance of metallized paper can be diminished. As paper is a network of single fibers, the sheet hygroexpansion is mainly influenced by single fiber hygroexpansion. The hygroexpansion here in turn is determined by the polymers that make up the fiber and the ultrastructure of the fiber. This review therefore starts with the effect of the smallest unit—the polymers—before advancing to the fiber, chemical modification and the treatment of fibers during production and concluding with the formation of the fiber network, the effect of paper laminates and an overview of expansion models. Examples of references are given on each structural level.

Scope, aim and demarcation

In this paper, only natural fibers, which are not incorporated into a matrix such as plastics, concrete or else, are taken into account. Creep, curling, wrinkling etc. are mostly excluded. However, they are mentioned where this might help give readers some new ideas or where these properties are somehow related to hygroexpansion (e.g., shrinking [5], wet strength [6], hydroexpansion [7] or creep [8]). Effects related to humidity and dimensional stability have already been partially reviewed [9, 10]. Also, hygroexpansion measurement techniques have been presented [11]. This present review focuses on the factors which trigger hygroexpansion along the production chain, starting from at a molecular level. Regarding expansion coefficients, it has to be taken into account that these coefficients were measured using different methods for different wood species and relate to different factors (e.g., transverse, circumferential, longitudinal strain in relation to moisture content, relative humidity) in fibers or paper sheets. Therefore, expansion coefficients can vary widely and only limited comparisons can be made. In cases where no actual numbers were given in publications, values were estimated from graphs where possible.

Measurement of single fiber and paper sheet hygroexpansion

For the measurement of single fiber hygroexpansion, atomic force microscopy (AFM) [12, 13] and light microscopy [14] in combination with specially

designed software for fiber analysis [15, 16] were used to acquire images of fibers and cellulose fibrils. Even 3D images can be obtained by microtomography [17, 18]. In each case, the images were used to measure the fiber dimensions under varying relative humidity, from which the expansion coefficients were calculated. The measurements were mostly done manually or via software.

In principle, the hygroexpansion of single fibers is different in the transversal and longitudinal direction. Additionally, fibers are anisotropically oriented in paper sheets. Consequently, the expansion of paper sheets is higher in the cross direction (CD) than in the machine direction (MD) (see section “Fiber orientation”). Apart from this, paper sheets of course also expand in the out-of-plane direction. In general, measurement techniques for hygroexpansion can be divided into mechanic and optical techniques.

One example of a mechanical system is the Nee-nah-type hygroexpansimeter. Here, a paper strip is fixed between two clamps, one of which is movable. The contraction and expansion of the sample causes a displacement of the movable clamp. This displacement is monitored via a micrometer, or in newer versions by a linear variable differential transformer [19–21] or a laser scanning position sensor [11, 22, 23]. The disadvantage is that the movable clamp needs to apply some load in order to stretch the sample. If the load is too high, this can falsely increase the measured expansion values.

An optical approach is the scanning of paper samples with commercially available high-resolution scanners (1200 dpi). The paper sheets are placed on the scanner and ideally weighed down in order to flatten the sample. After scanning the samples at different humidities, the dimensions can be measured and the expansion calculated [24]. Digital correlation techniques are also used to monitor sheet hygroexpansion [25]. Here, a speckle pattern is applied, for example by spraying color on the paper surface (Fig. 1) [26]. At different relative humidities, images are taken of the paper surface and the varying distances between distinctive points are determined by investigation of the statistical resemblance between two groups of pixel data [27]. This method has the disadvantage that cockling and curling can negatively influence the accuracy of the test method.

A similar method was used by Viguie et al. [29], where 3D maps of the paper sample were obtained by X-ray synchrotron microtomography. The gray

Fig. 1 Schematic illustration of speckle pattern [28].

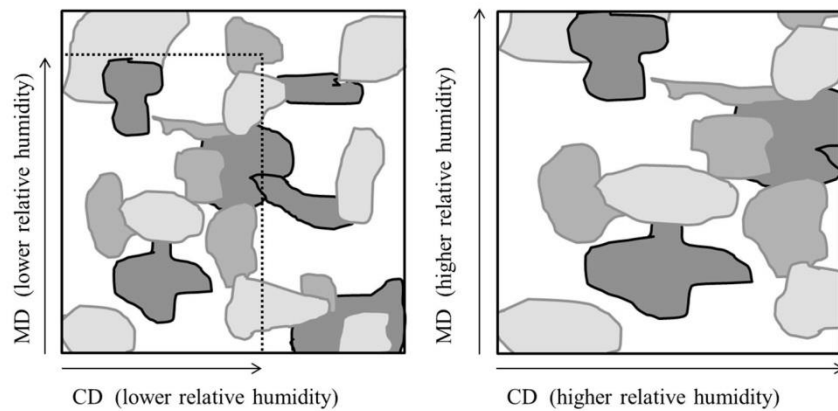


Table 1 Overview of values and units used to describe hygroexpansion

Denomination	Referred to as	Explanation	Formula	Units
Dimensional change	exp	Ratio between the length* variation (Δl) and the initial length* (l_0) of the specimen	$\text{exp} = \frac{\Delta l}{l_0}$	–
Percent dimensional change	% exp	Percentage ratio between the length* variation (Δl) and the initial length* (l_0) of the specimen	$\% \text{exp} = \frac{\Delta l}{l_0} \cdot 100\%$	%
Percent volumetric change	% vol	Percentage ratio between the volume variation (ΔV) and the initial volume (V_0) of the specimen	$\% \text{vol} = \frac{\Delta V}{V_0} \cdot 100\%$	%
Moisture content	m.c.	Ratio between mass of water (m_w) and dry paper (m_{dry})	$\text{mc} = \frac{m_w}{m_{\text{dry}}}$	–
Percentaged moisture content	% m.c.	Percentage ratio between mass of water (m_w) and dry paper (m_{dry})	$\text{mc} = \frac{m_w}{m_{\text{dry}}} \cdot 100\%$	%
Relative humidity	r.h.	Ratio between the absolute humidity (a.h.) and the maximum humidity (m.h.)	$\text{r.h.} = \frac{\text{a.h.}}{\text{m.h.}}$	–
Percent relative humidity	% r.h.	Percentage ratio between the absolute humidity (a.h.) and the maximum humidity (m.h.)	$\text{r.h.} = \frac{\text{a.h.}}{\text{m.h.}} \cdot 100\%$	%

* Length can also be replaced by width or thickness, too

shadings of the visible fibrous and porous phases were used as a speckle pattern, based on which the expansion was then calculated as described before. Out-of-plane hygroexpansion can be measured by common thickness measurement methods using, for example, micrometers or profilometers [30].

Measurement values generally relate the hygroexpansion to a certain relative humidity or to a moisture content of the paper. The values can have the units presented in Table 1.

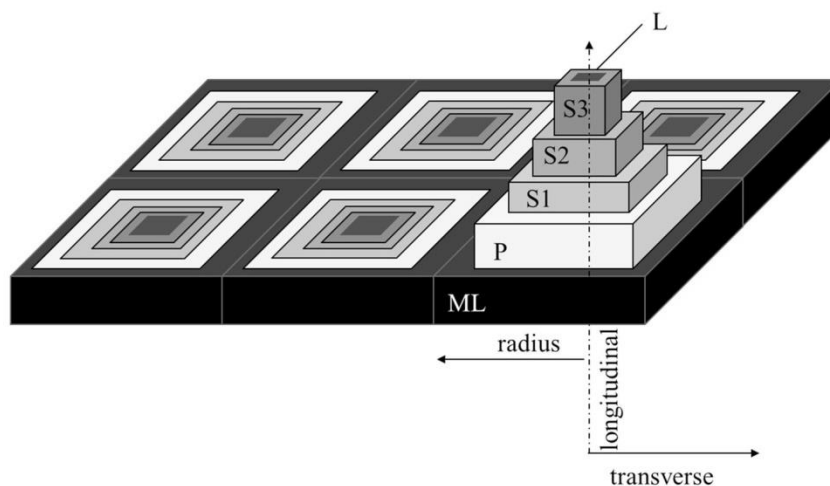
Impacts on the hygroexpansion of the single fibers

Wood fibers have lengths of roughly 1–3 mm and widths of 10–50 μm , with a fiber wall thickness of 1–5 μm [31]. They are assumed to appear as hollow

concentric structures comprising the cell wall and the lumen (L) inside [32, 33]. As illustrated in Fig. 2, the cell wall consists of four, and sometimes five, different layers [34]. These layers are commonly called the primary cell wall (P) and the secondary wall consisting of an outer layer (S1), a middle layer (S2) and an inner layer (S3). The middle lamella (ML) surrounds every single wood fiber and strongly binds the fibers to each other. It is hence not perceived as a cell wall layer. The task of the middle lamella is to provide the connection between the cells for transport of biochemicals between the cells [35].

However, the shape of real fibers deviates from this ideal situation. According to their task, cells can be divided into those having a mechanical function, a conducting function and a storing function. In softwood, those functions are fulfilled in the same sequence by latewood tracheids, earlywood tracheids

Fig. 2 Schematic illustration of the cell wall layer of soft wood fiber (adapted from [34]) [28]. *ML* middle lamella, *P* primary cell wall, *L* lumen.



and parenchyma cells. In hardwood those are libriform, sklerenchym cells for mechanical stability, tracheids as conducting cells and parenchyma cells for storing. Accordingly, they vary in shape and size. For papermaking, the tracheids of softwood and libriform cells of hardwood are useful, as they support the mechanical stability of paper due to their length and length-to-width-ratio [36]. Additionally, latewood fibers are shorter, but the cell wall thickness is greater than in earlywood fibers. When fibers are extracted for the paper making process, their shape is additionally altered. Lignin and hemicelluloses are removed, so that the outer surface structure of chemical pulp resembles that of the S1 layer [31]. Apart from that, the lumen collapses during pulping, sheet making and beating of the fibers [32, 37]. This leads to a flattening of the fibers [38], and so sometimes they are modeled as a laminate [37]. More information about the effect of such fiber shape variations can be found in sections “Fiber morphology” “Effect of wood species, parts of the plant, age and compression wood” “Pulp fractions and hornification” “Beating and refining” and “Inter-fiber contact”.

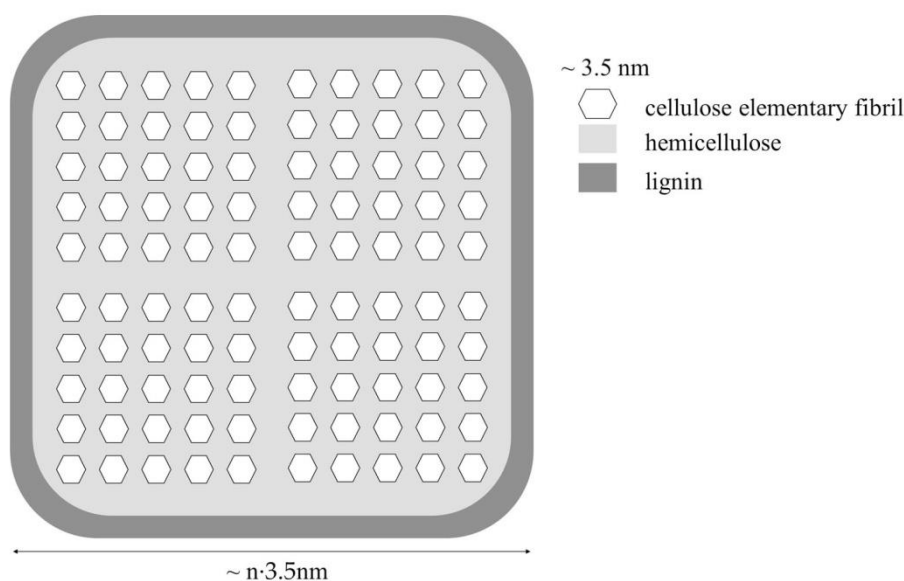
Cell walls are composed of three main polymers: cellulose, hemicelluloses and lignin (see Fig. 3). Cellulose is arranged as lamellar membranes, which are stepwise subdivided into macrofibrils, microfibrils (diameter roughly a multiple of ~ 3.5 nm), elementary fibrils (~ 40 cellulose chains, diameter of ~ 3.5 nm, values highly depending on the specie and measurement technique [39–43]), and the cellulose molecules [39, 40, 44]. (These divisions are, however, not used in a stringent manner in the literature.) As Fig. 3 shows, the microfibril aggregates are assumed

to consist of elementary fibrils, which are coated with hemicelluloses and then framed with lignin. However, those polymers are not distributed equally within the cell wall layers. The S layers contain a higher amount of cellulose and hemicelluloses than the P layers. The lignin content is approximately equal among the S layers [34]. The local arrangement of the polymers can be explained as follows based on their chemical affinity [45]: As the more hydrophilic lignin is not compatible with cellulose, hemicelluloses acts like a surfactant, which reduces the free energy and works as an “interfacial boundary region”. For example acetylated side groups turn toward the lignin, whereas hydroxylated side groups orient themselves toward the cellulose (due to having similar solubility parameters, “*simulus sub solvuntur*”). The steric overlapping of side groups between the layers can lead to an “interpenetrating polymer network [...] of diffuse character” [45]. The importance or unimportance of this inter-layer for the hygroelastic properties is addressed by Wang et al. [46] and Derome et al. [47] as well as in section “Microfibril angle”. The following subsections discuss the effect of the single polymers (cellulose, hemicelluloses and lignin), the microfibril angle, the fiber morphology and sorption on the hygroexpansion of single fibers and paper sheets.

Effects of the polymers in the fiber

As mentioned previously, fibers are constructed out of cellulose, hemicellulose and lignin. The relative amounts and the exact composition of each polymer depend on the plant, specie and part of the plant [48].

Fig. 3 Ultrastructural organization of elementary fibrils, hemicelluloses and lignin within the microfibril (adapted from [34]) [28].



Cells generally consist out of approximately 40–50% cellulose, 5–20% lignin, 5–20% hemicelluloses and 8–12% moisture [36, 49]. For wood, average values amount to 45% cellulose, 27% lignin and 23% hemicellulose [50]. The approximate weight fraction of the polymers in the S1/S2/S3 layer is 43/20/14% for lignin, 30/33/36% for hemicellulose and 27/47/50% for cellulose [51].

Taking different sources into account, the moisture contents are about 2.5–7.5% for lignin, 5–10% for cellulose and 10–20% for hemicellulose [52–55]. Other sources state that the amount of absorbed water in a fiber is divided between the hemicellulose, cellulose and lignin in the ratio of 2.6:0:1 [56, 57]. Accordingly, the effect of hemicellulose on the elastic properties is the highest, whereas the impact of lignin and cellulose is only of medium influence [46, 58].

Apart from the weight fraction and the sorption mechanism of the different polymers, the molecular arrangement is reported to play a significant role [45, 59]. Whereas a high concentration of covalent bonds in the cross section of an oriented polymer leads to high stiffness, a high concentration of hydrogen bonds transverse to the polymer backbone leads to a high swelling capacity [34]. This is in line with the description of swelling as “the transport of the swelling agent through a system of pores and channels, leading to some splitting of hydrogen bonds of the cellulose dense, but accessible (meaning most of the time amorphous) regions” [60].

In order to give a better insight into the swelling mechanisms in the single polymers, scientific results on the expansion and water adsorption of cellulose, hemicellulose and lignin are summarized in the following section. Interested readers can find more information about the elastic properties of the single polymers as well as the softening effect of water elsewhere [58, 61, 62].

Hereinafter, findings about the swelling and adsorption of the different polymers are presented, starting with the hemicellulose, followed by cellulose before coming to lignin.

Hygroexpansion of hemicellulose

The exact composition of hemicellulose differs for different plants and parts of plants. Chemically, its main fractions are mannose, xylose, glucose, galactose and arabinose. Compared to cellulose, hemicellulose is branched and has short polymers with a degree of polymerization of only 200 [63, 64]. It has already been mentioned that hemicellulose absorbs the highest amount of water and thus shows the most extensive swelling among the fiber polymers. As swelling is related to the solubility of the constituent in a solvent, the Hansen solubility parameters [65] can be taken into account to estimate the swelling behavior [45]. Due to the high solubility parameters of hemicellulose side groups, it absorbs more water.

Hygroexpansion of cellulose

Cellulose is a hydrophilic glucan polymer, consisting of chains of 1,4- β -bonded anhydroglucose units with a degree of polymerization of 300–10000. These chains enclose alcoholic hydroxyl groups, building intramolecular and intermolecular bonds as well as bonds with ambient hydroxyl groups [48, 66] (see Fig. 4). Cellulose can be subdivided into cellulose I and II as well as α and β conformations, of which cellulose I in the native form. Whereas cellulose I molecular chains are arranged in parallel, cellulose II appears with antiparallel chains. Cellulose I α and I β are composed of extended chains, aligned with the microfibril axis. The α -form has only a single chain with a triclinic unit, and the β -form has two chains in monoclinic arrangement. Cellulose II is the most stable form [66, 67]. Consequently, the high density and ordered supramolecular structure reduce the swelling capacity, although it is highly hygroscopic. Apart from the crystallinity, the chemical surrounding of the cellulose and the processing has influences on the water sorption.

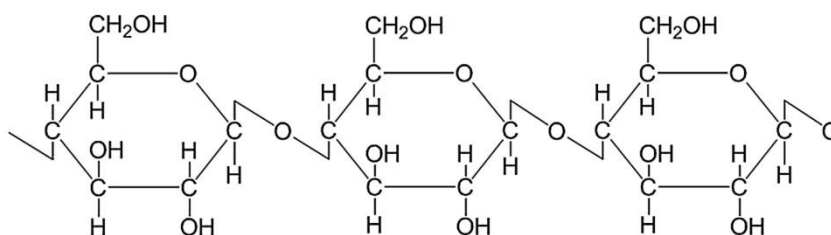
The crystallinity of cellulose appears in different orders, and even amorphous regions (without any order) exist [60, 68]. The exact relative amount of crystalline and amorphous cellulose depends on the species [69]. Compared to lignin and hemicellulose, cellulose is a rather crystalline material and therefore its swelling capability—determined by the amorphous regions—is low and sometimes neglected when talking about fiber hygroexpansion [46, 70, 71] or homogenized with the swelling capability of hemicelluloses [47]. However, only 60–70% of the cellulose in cell wall layers exists in a crystalline form. Thirty to forty percent is amorphous and affected by water molecules [72]. Kocherbitov et al. evaluated the hydration of microcrystalline cellulose (cellulose I and II) and amorphous cellulose. They found that the water sorption increases from cellulose I to cellulose II to amorphous cellulose [73]. During the process of water absorption by amorphous

cellulose, water molecules are first of all bound to the O6 and O2 hydroxyl groups of cellulose. Only at higher moisture contents O3 hydroxyl groups and the acetal oxygens attract water molecules. Progressively, the water molecules built clusters before filling capillary channels. The estimated volume hygroexpansion (% vol) of amorphous cellulose was 0.0097% for 0–36% hydration level (m.c.) [74]. Similar is found for different microcrystalline celluloses where a higher crystallinity led to a lower moisture content below 75% r.h. At 75% r.h. crystallinity indexes of 45–95% led to moisture contents of 12–6% m.c., respectively. Above 75% r.h., a rapid increase in moisture content was observed for highly crystalline cellulose powders [55]. However, microfibrillated and whiskered cellulose showed the same sorption isotherm even though they had different crystallinities and morphologies [53]. Contrary to expectations, no clear correlation between the crystallinity index and the hygroexpansion of paper could be found [69]. This might be related to the adverse effects that are reported for cellulose such as expansion during drying and shrinkage during water absorption [75–77].

The expansion and sorption of cellulose not only depend on the crystallinity but also on the surroundings of the cellulose molecules. Counter ions are reported to have a huge effect on the moisture sorption of cellulosic materials containing sulfate and carboxylic groups in different ionic forms [78]. Additionally, the swelling dynamics of cellulose depend on the applied solvents [45, 79]. Moreover, it was observed that the swelling was non-uniform along the fibers and showed some “ballooning” for different solvents [60]. One explanation might be that when the fibrils in the secondary wall swell transversely, the primary wall bursts at distinct spots. In these areas “ballooning” is visible, namely non-uniform swelling along the fibers [80].

Apart from the crystallinity and the chemical surroundings of the cellulose molecules, the processing

Fig. 4 Structure of cellulose.



and the general fiber constitution may have an effect. Such has been shown by Fahlén and Salmén [81], who observed thermally triggered reorganization of cellulose molecules (temperatures between 0 and 225 °C) leading to swelling of cellulose aggregates (18 nm diameter in unprocessed wood, 23 nm in processed wood). Moreover, a decreasing hemicelluloses content is reported to lead to a higher average fibril aggregate size (diameter of 17.9–22.2 nm) due to coalescence of the cellulose microfibrils [82].

Hygroexpansion of lignin

Lignin is a phenolic compound, consisting of the monomers p-coumaryl, coniferyl, and sinapyl alcohols. Lignin gives fibers mechanical stability [48, 83]. As lignin is commonly removed from the fibers in order to reduce paper yellowing, few publications deal with the swelling of lignin.

The sorption isotherm for lignin is very strong dependent on the extraction method. The moisture content at 50% r.h. is ~5% for dioxane lignin, ~9.5% for Klason lignin and ~10% for periodate lignin [84]. Lignin from conifer cuticles is reported to have moisture contents of 2 and 6% at 50% r.h. during adsorption and desorption, respectively [54]. The solubility and swelling of lignin is lowest in water and increases from benzene to methanol, ether and acetone. Constituents of lignin with a lower molecular weight are soluble in a wider range of solvents [85]. Moreover, the fiber swelling increases, as soon as the softening temperature (60–75 °C) has been reached possibly due to movement or flow of the lignin [86]. It was reported that the use of different lignin derivatives (aminated lignin, manganese(III) + lignin, suberin-like lignin) reduces the hygroexpansion of paper from 0.29 to 0.26% (for change of relative humidity from 33 to 66% r.h.) [87]. Apart from the chemical composition, the impact of lignin on the hygroexpansion depends on the microfibril angle in the S2 layer [46]. The combination of a higher lignin content and small microfibril angles in the S2 layer reduces the transverse fiber hygroexpansion [70].

Microfibril angle

The microfibril angle (MFA) is commonly defined as the angle between the longitudinal axis and the microfibril [88] (see Fig. 5). Microfibrils wind helically within the secondary layers. However, the

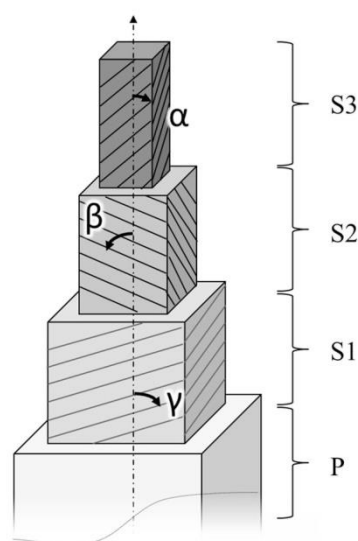


Fig. 5 Winding of microfibrils in layer S1, S2 and S3 (adapted from [34]) [28].

winding direction of the microfibrils differs: usually S1 and S3 wind in the opposite direction of S2 [89]. Microfibrils in S1 and S3 show progressive change of winding direction toward and away from S2, respectively.

In the primary cell wall, there is a random orientation of cellulose microfibrils. In the S1 layer, MFAs of 50°–70° are common, whereas in the S2 layer the MFA is only approximately 5°–30°. In the S3 layer, the MFA is again much higher at around 70° [35]. The MFAs for different species and cell wall layers have been studied in detail [50, 89, 90, 91, 92, 93]. Within their winding direction, microfibrils show a secondary structure. Microfibrils in S1 and S2 appear as a Z-helix or S-helix, whereas in the S2 layer the microfibrils are arranged in a Z-helix [89, 94]. Although the plant species has an influence, the location of growing does not seem to affect the MFA [95]. However, the fiber treatment during paper production is reported to have an effect. Beating increased the MFA from 3°–15° to 12°–32°, whereas drying increased it further to 39°–48° [95].

The effect of the MFA in each layer depends on the thickness of each layer. Some 90% of the mass is concentrated in the S2 layer [96]. For this reason, the S2 layer defines the swelling properties of normal wood to a major degree [93]. The S1 and S3 layers can be thin and therefore have less influence [90]. Consequently, quite often only the S2 layer is taken into

account. Marklund and Varna [52] even went one step further and replaced the S1, S2, and S3 layers with one single layer in the analytical model. This did not majorly affect the expansion in the longitudinal and transverse direction at different MFAs. However, Bergander and Salmén [58] evaluated the influence of the MFA depending on the layer thickness of S1 and S3. In the transverse direction, the effect of the layer thickness of S1 and S3 is distinct: by doubling the layer thickness of the S1 layer, the transverse elastic modulus increased by 20% at an MFA of 70°. This shows how important it is to take S1, its thickness, and its MFA into account.

Generally, all publications agree that a higher MFA leads to higher hygroexpansion in the longitudinal direction and lower hygroexpansion in the transverse direction of the fiber [47, 52, 97, 98, 99, 100]. For small MFAs (<30°), the longitudinal shrinkage is a lot smaller (<1%) than the transverse shrinkage (7–9%), but in the region of extremely large MFAs (40°–50°) this relation switches and the longitudinal shrinkage (<8%) is larger than the transverse shrinkage (<4%) [71]. Similarly, Neagu and Gamstedt [34] reported an increase in expansion in the longitudinal direction from about 0–0.3 (exp.) and a decrease from 0.4 to 0.2 (exp.) in the transverse direction for MFAs of 0°–50°. At a higher abstraction level, it is proven that a lower MFA leads to lower shrinkage of paper sheets [101, 96]. For in-plane isotropic sheets, a reduction from ~0.007 to ~0.004 (exp.) for MFAs of ~40° to ~23° was observed, respectively [96].

Apart from the layer thickness and the microfibril angle itself, the effect of the MFA is somewhat constrained by external factors. Likewise, the chemical characteristics of the fiber seem to have an influence on the effect of the MFA, as compression wood showed lower tangential shrinkage (5.94%) than juvenile wood (8.37%) at the same MFA (14.2°) [91]. Also, the degree of fiber restraining appears to have an effect. It was reported that for non-restrained fibers which can rotate freely (compression wood) the longitudinal expansion increased from approximately 0.025–0.4 (exp.) for MFAs of 0°–50°, whereas for restrained fibers (normal wood) the expansion coefficient stays approximately zero for MFAs of 0°–30° and only increases up to ~0.27 for MFAs of 30°–50° [70].

Although the MFA itself is constrained by external factors, it may also actively constrain other processes. Likewise, the contributions of the hemicelluloses and

lignin are dependent on the MFA in S2. In the longitudinal direction, both polymers contribute equally until the MFA reaches 20°. In the MFA range from 20° to 40°, the hemicellulose dominates, whereas at MFAs higher than 40°, lignin dominates. In the transverse direction, both polymers contribute equally until the MFA reaches 30°. At higher MFAs, hemicelluloses dominates [46].

Fiber morphology

In general, the ratios of the different geometrical dimensions of fibers are related to paper properties as follows [14] (see Fig. 6):

- Runkel ratio (ratio of fiber cell wall thickness to its lumen): a high ratio leads to stiff fibers with low bonding ability, and to voluminous paper. The ratio should be about 1.
- Coefficient of flexibility (ratio of lumen width to its fiber diameter): relates to the bonding strength, tensile strength and bursting properties.
- Relative fiber length (ratio of the fiber length to diameter): correlates with the tearing resistance of paper.

Fiber length and width and cell wall layer thickness

Fiber lengths of different species were determined by Ververis et al. [102] and varied between 0.74 and 2.32 mm. The dimensions also depend on the growing conditions with a lack of watering even improving paper pulp properties [103].

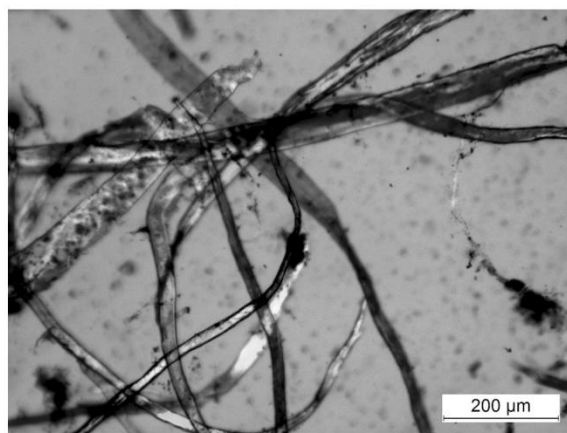


Fig. 6 Microscopic image of fibers [28].

Higher fiber widths lead to higher hygroexpansion (0.12 and 0.20% expansion for a width of 20 and 35 μm , respectively; direction of measurement not indicated) [23]. Uesaka and Moss [101] observed that longer fibers lead to reduced paper hygroexpansion (expansion of ~ 0.05 to $0.12\% \text{exp}/\% \text{m.c.}$ for fiber lengths of 2.57–0.40 mm, respectively, direction of measurement not indicated). Similarly, Kijima and Yamakawa [104] observed an inverse correlation: they measured an expansion of 0.28 and 0.14% for hardwood fiber lengths of 0.93 and 1.09 mm, respectively. For softwood pulps, the expansions were 0.23 and 0.17% for fiber lengths of 1.88 and 2.62 mm, respectively. This observation was closely linked to the amount of inter-fiber contacts, as described in section “Inter-fiber contact”.

Conversely, a positive correlation between the addition of fines and hygroexpansion was reported (4.4 and 9.6% fines giving an expansion coefficient of 0.13 and $0.165\%/\% \text{r.h.}$, respectively) [105]. As mentioned in the previous sections, the polymers present in the cell wall and also the MFA affect the expansion of the cell wall layer. However, the importance of the thinner S1 and S2 layer is often questioned. Whereas some researchers emphasize the importance of S1 and S2 [58], or even introduce additional inter-layers between S1/S2 and S2/S3, respectively [46, 106], others even homogenize these layers into one single layer [52] (see section “Microfibril angle”). A correlation between fiber wall thickness and hygroexpansion has been reported to be negative (expansion of ~ 0.1 to $0.06\% \text{exp.}/\% \text{m.c.}$ for fiber wall thicknesses of 2.25–4 μm) [15] or depend on the wall thickness distribution. It was found that a more peaked and wider distribution of fiber wall thickness leads to a higher hygroexpansion [107]. Pulkkinen et al. [15] found that sheet hygroexpansion is higher for fibers with thin walls at low relative humidities (10–50% r.h.) and lower at higher relative humidities (50–90% r.h.).

Fiber curl and twist

Curl often occurs due to mechanical treatments during pulp processing [108] and depends on the relative humidity [17] and plant species [15]. Fiber curl can be described by the curl factor and the shape factor. The curl factor (f) is the ratio between the fiber contour length (c) and the longest dimension of the fiber (d) ($f = c/d$) (some authors subtract 1 from that value). The shape factor (s) is the ratio

between the longest dimension (d) and fiber contour length (c) ($s = d/c$). Curled fibers, namely having low shape factors of, for example 94.4 and 89.75%, lead to higher hygroexpansion of 0.12 and 0.225%, respectively (approximated values). However, this effect is reduced when the sheets are dried under restraint. This is explained by the reduction of inter-fiber contacts during restrained drying (see section “Density, fiber content and porosity”) [23]. These findings are in accordance with other studies [16, 105]. For different curl factors of 1.17 and 1.37, an increase in expansion of up to $\sim 0.001\%/\% \text{r.h.}$ was found [105].

Effect of wood species, parts of the plant, age and compression wood

Depending on the specie, plant part, age, and growing conditions, fibers have different sorption isotherms [109, 110] and suitability for papermaking [14, 38, 102, 111]. As mentioned in the previous section, the paper properties are related to the ratios of the different geometrical dimensions of the fibers [14]. These dimensions (fiber length, diameter, and wall thickness) are in turn dependent on the plant watering. If poorly watered, the fiber length, diameter, wall thickness, and Runkel ratio were found to be reduced (except in the bark) [103]. Therefore, it is not surprising that paper sheet hygroexpansion depends on the tree species. In cross direction (CD), values of 0.48 and 0.54% for a humidity increase of 10% r.h. to 90% r.h. were found for different species [15]. Generally, hardwood pulps seem to show lower hygroexpansion than softwood pulp ($\sim 0.23\%$ expansion for softwood, 0.13% for hardwood, paper density of $\sim 680 \text{ kg/m}^3$) [23]. The longitudinal and transverse expansion coefficients are reported to be 0.5–2.7 and 4–8% for compression wood, 1–2 and 5–8% for juvenile wood and 1–1.5 and 6–12% for mature wood [91]. Similarly, Joffre et al. [70] found distinct differences between normal and compression wood tracheids, which can be related to the MFA, lignin content and the cylindrical structure.

Water sorption of single fibers

Paper shows an S-shaped sorption isotherm, indicating multilayer adsorption, and also a hysteresis effect between adsorption and desorption [10]. The moisture

content of fibers fluctuates between ~5 and 10% at 50% r.h. [49]. For example, jute, coir and Sitka spruce have higher moisture contents than fibers containing less lignin such as hemp, flax, and cotton [112]. The water uptake of fibers can be explained by various theories such as the surface adsorption theory, solid solution theory, capillary condensation theory, two-phase mechanism, and the pore-size distribution mechanism [113]. However, the exact sorption kinetics as well as the moisture content depends on the species [114], the fiber extraction method, the exact wood constituents, the temperature, the mechanical stress, the previous history of the fibers [113], and on ambient conditions such as the pH, electrolyte concentration, and valency of the counter-ion [115]. Additionally, the swellability of fibers is affected by the charge (water retention values of ~90 and 170% for charges of 50 and 125 $\mu\text{eq/g}$, respectively, for hardwood pulp). Strongly hydrated nonionic polymers and also the number of anionic groups on the fiber wall affect the swellability of the cell wall layers and the quantity of water entering the fiber [116]. For fibers, it was shown that moisture is adsorbed in the form of clusters to the same relative degree on hydroxyl and carboxyl sites in cellulose and hemicellulose [117]. Ways of influencing the moisture content and moisture sorption kinetics are reviewed below.

Different chemical treatments that influence the sorption isotherms of the fibers have been reported [69, 112, 118, 119, 120]. The treatment of flax fibers with acetic anhydride and styrene reduced the water uptake, whereas silane and maleic anhydride do not have such a positive effect [118]. In contrast, maleic anhydride, acetylation, acrylic acid, and styrene showed a positive effect on the water sorption (i.e. a reduction of the water uptake) for Alfa (*Stipa tenacissima*) fibers [119]. Crosslinking by periodate slows down the moisture sorption kinetics (m.c. of 9 and 6.5% at 50% r.h. for carbonyl contents per gram fiber of 0 and 1.2 mmol/g, respectively), which leads to a higher dimensional stability [121, 122]. The relevant research teams were able to simulate the sorption isotherms using Langmuir models, Henry's law and clustering, the Guggenheim–Anderson–de Boer (GAB) model or the Hailwood Horrobin model. Another method that has been found to alter the surface tension—and thereby the water sorption kinetics of fibers and paper—is chemical grafting. This is further described in section “Grafting”.

Chemical modification and additives

The previous section focused on effects that are inherent to the pure fibers. Once the fibers have been extracted, chemical modifications (polyelectrolyte multilayers, crosslinking) or the use of additives (lignin, fillers) can improve the pulp formulation. After paper sheet formation, the main chemical modifications are undertaken by grafting and corona treatment.

Polyelectrolyte multilayers (PEM) and crosslinking

The inter-fiber contact actively influences the wet tensile strength and sheet hygroexpansion (see section “Inter-fiber contact”). The contact area can be altered at a molecular level by polyelectrolyte multilayers (PEM) and crosslinking. Crosslinking can be achieved by oxidation of the fiber and also by a whole range of other reactions.

PEMs are commonly created using a layer-by-layer technique, where cationic and anionic solutions are alternately applied to a surface. These coatings are self-organizing [123]. PEMs made of polyallylamine hydrochloride and polyacrylic acid applied to wood fibers were reported to lead to an increase in the number of fiber–fiber joints and in the number of covalent bonds in the contact area [124]. However, for sheets dried under restraint, the PEM does not have a large influence on hygroexpansion. For sheets dried without restraint, the dimensional change was higher for virgin fibers (~0.5%) than for PEM-treated fibers (~0.35%) for a moisture content of 10%, although the moisture uptake was lower for virgin fibers at a given relative humidity. This was explained by the different dimensions of the contact area in restraint-dried and freely dried sheets and its development under humidity uptake [20, 21]. Another approach was to use dextran as an electrolyte, as its chemical structure is also made up of glucose molecules, just like cellulose. In this process, the cationic acetal dextran is adsorbed on the fiber surface. Then, it is hydrolyzed to convert the acetal groups into reactive aldehyde groups. The crosslinking step is the reaction of aldehyde groups with hydroxyl groups during paper drying. This is shown to have a positive effect on the tensile strength; however, the hygroexpansion was not studied [125].

Apart from the application of PEMs, oxidation is a common method for crosslinking fibers. Almgren et al. [126] measured the hygroexpansion of composites containing crosslinked and non-crosslinked fibers. They found that crosslinking reduced the transverse hygroexpansion from 0.28 to 0.12/% r.h.. A similar reduction was achieved by the application of periodates. Sodium metaperiodate was used to cleave the C2–C3 bond of 1,4-glucans. Consequently, two reactive aldehyde groups are formed and react with other parts of the fiber, for example by hemiacetal linkages. The water sorption and thus the hygroexpansion was reduced by approximately 28% (when the relative humidity was increased from 20 to 85%) [122]. While using the same chemical on kraft fibers, higher hydroexpansion was observed [127]. Similarly, Gimåker lowered the moisture sorption kinetics and reduced the hygroexpansion from 0.34 to 0.22% (for an increase in relative humidity from 50 to 90% r.h.) by periodate oxidation [121]. On Korean traditional paper (Hanji), the application of citric acid was reported to lead to higher dimensional stability [128].

Similarly, Larsson and Wågberg [7] combined a periodate crosslinking process with subsequent application of PEM, consisting of three layers of polyallylamine hydrochloride and two layers of polyacrylic acid. The hydroexpansion under liquid water was observed. It was found that capillary absorption was prevented, but these hydrophobic sheets showed greater expansion. This could be related to the higher moisture content in the upper fiber layers, as all the water is accumulated there.

Apart from oxidation, crosslinking can be achieved by a wide range of chemicals. The crosslinking of fibers with formaldehyde was reported to increase the dimensional stability, but the dimensional stabilization decreased with increasing reaction time [129–131]. Moreover, formaldehyde, maleic acid (also in combination with glycerol), acetylation, etherification, the use of polyethylene glycol and other methods were compared for reducing the swelling of wood fibers. In this study, polyethylene glycol showed the highest anti-swelling efficiency, followed by acetylation and formaldehyde [131] (see also [132, 133]). Alternatives to formaldehyde can be found in the cotton cellulose industry, for example, butanetetracarboxylic acid [134, 135]. The application of diepoxides, dialdehydes, polyacetals, cyclic ethylene ureas was found to reduce hygroexpansion but also the mechanical strength [136]. An increase in

inter-fiber bonds thereby increasing wet web strength by 70% was achieved by the following procedure: The fibers were first treated with carboxymethylcellulose. Then, the 1-ethyl-3-[3-(dimethylaminopropyl)] carbodiimide-assisted reaction of carboxyl and amine groups was triggered and finally adipic dihydrazide was used as the crosslinking agent [137]. Elegir et al. [6] used laccase, an enzyme which oxidizes free phenolic lignin moieties. This allowed the crosslinking of lingo-cellulosic fibers and positively affected the wet tensile strength.

Grafting

As mentioned in section “Impacts on the hygroexpansion of the single fibers”, the swelling of the paper sheet and also of the single fibers depends on the water absorbance of the single fibers. By altering the chemical composition of the fiber surface, the water absorbance can be reduced. The chemical composition can be altered by grafting, namely the covalent attachment of monomers to a surface. Two grafting processes are distinguishable [138]: (a) the surface is functionalized with immobilized initiators followed by polymerization with monomers; (b) functionalized monomers react with the backbone of the polymers. In each case it must be kept in mind that only the surface of the fiber or paper sheet is treated, not the bulk. Below is a summary of publications, where different kinds of grafting were used to reduce hygroexpansion, change the water sorption isotherm, or at least increase the water repellency. Interested readers will find in-depth information about the surface treatments of paper in the extensive review by Samyn [139].

A typical application of type a) process is the corona treatment of polymer surfaces to increase the surface tension and substrate wettability. This technique uses corona discharge which forms a highly reactive gas that reacts with polymer surfaces primarily by breakage of H–C bonds [140, 141]. Consequently, polar groups, such as carbonyl and carboxyl groups are produced [141–151]. When this method was applied to paper, aldehyde groups but not carboxyl groups were formed and surprisingly the water sorption decreased slightly. The treatment seemed to trigger the formation of strong bonds which reduced the penetration of water into the paper sheet [152].

An example of type b) process is treatment of the fibers by acetylation or with styrene, acrylic acid, or maleic anhydride. These methods drastically reduced

the water sorption (from ~ 7.5 to 6% at 50% r.h. for styrene treatment) [119]. Similar studies were performed by Alix et al. [118] who tested the effect of maleic anhydride, acetic anhydride, silane and styrene on flax fibers. Once again, styrene treatment showed the strongest effect. In another study, vinyltrimethoxysilane and g-methacryloxypropyltrimethoxysilane were grafted onto paper sheets by cold-plasma discharge. This treatment reduced the surface tension from about 29.3 to almost 0 mN/m [153]. Similar results were achieved by grafting fatty acids (C16, C18, C22) [154]. A reduction of the polar/dispersive part of the surface tension from $20/28$ to $3/27$ mJ/m² was reported for a 6 h treatment with C18 [155]. By grafting methyl methacrylate onto fibers of *Agave Americana* L., the presence of accessible $-OH$ groups was altered, leading to a reduction in moisture uptake from ~ 7 to $\sim 4\%$ for a graft yield of 0 and 13.6% , respectively, at a relative humidity of 55% . Simultaneously, the swelling was reduced by $\sim 65\%$ [156].

Lignin

Lignin is often removed from the fibers in order to reduce the yellowing of paper. It is then burnt in a recovery boiler to produce steam. However, this process is rather expensive. Therefore, its use as an additive in paper production was tested. It was found that the mechano-sorptive creep can be decreased and wet strength increased [87, 157]. Not only the wet strength but also the hygroexpansion of paper was reduced from 0.29 to 0.26% (for a change in relative humidity of 33 to 66% on in-plane isotropic sheets) by the addition of manganese (III)-lignin and suberin-like lignin derivatives. However, when pulps with increasing lignin contents were used (3 – 14%), this led to increased hygroexpansion (~ 0.2 to $\sim 0.23\%$). This is explained by the simultaneous relative decrease in the amount of cellulose which helps to fixate the fibrous network (see section “Hygroexpansion of cellulose”) [158]. Moreover, a new hydrophobic coating has been developed which consists of lignin with vegetable oil and attains a contact angle with water of 120° [159].

Fillers

Fillers tend to decrease the hygroexpansion due to the inhibition or reduction of inter-fiber bonds [160].

Accordingly, Figueiredo et al. [161] found that the wet expansion under tension is strongly affected by the filler content. The excessive addition of inorganic fillers reduced the paper web dimensional stability in the cross direction (expansion of ~ 2.4 to $\sim 2.75\%$ for ash contents of ~ 23 to $\sim 36\%$). In contrast, Laurell Lyne et al. [160] found that a filler content of 40% reduced the hygroexpansion by 20% in CD, but no difference was observed between clay and chalk. In the machine direction (MD), the expansion was almost the same for filled and unfilled sheets.

Pulp and paper production

The sections “Fiber morphology”, “Effect of wood species, parts of the plant, age and compression wood” and “Water sorption of single fibers” summarized the effects of different wood species. The fiber origin—and the relevant connected chemical composition and morphology of the fibers—play important roles. Other factors that can influence the hygroexpansion are the extraction process, reuse, and mechanical treatment.

Pulp fractions and hornification

When bleached kraft pulp is replaced by high yield pulp, hygroexpansion increases from ~ 0.074 to $\sim 0.08\%/%$ m.c. at replacements of $\geq 20\%$ (direction of measurement (MD or CD) not indicated) [27]. Bleached chemo-thermomechanical (BCTM) fibers—which are a type of high yield pulp—were reported to expand more in the transverse direction than kraft pulp (5.4 and 4.1% , respectively, for r.h. in the range of 50 – 90% r.h.). However, when BCTMP was added to kraft pulp, the paper showed lower expansion. This is explained by the interaction with other factors such as the sheet density, structure, and inter-fiber bonding [162].

In contrast, the addition of up to 20% microfibrillated cellulose increased the hygroexpansion of freely dried sheets from ~ 0.9 to $\sim 1.8\%$ (for a humidity increase from 33 to 84%). The effect was less pronounced for restraint-dried sheets. The fineness of the additive did not have a major influence [24].

Another fiber fraction that might gain importance in coming years is recycled fiber. In order to reduce the negative environmental impact, the use of recycled fibers is being promoted. However, infinite reuse

is not possible [163]. The drying of fibers causes the fibers to shrink and collapse, and the fiber walls even partially coalesce. This process reduces the accessibility for water molecules during absorption. As these surfaces absorb less water, the initial volume and softness cannot be recovered. This process is also considered as “hornification” [164, 165]. Accordingly, there is a linear correlation between the water retention value and the degree of hornification [166]. A detailed insight into the chemical processes during hornification has been given [165, 167]. The collapsing of the fiber and the reduction in water absorbance leads to a decrease in hygroexpansion when such hornified fibers are added to the pulp. The expansion coefficient in the machine direction (MD) was 0.104%/ % r.h. for virgin fibers and 0.096%/ % r.h for fibers that had undergone hornification. These observations were, however, dependent on the drying conditions (freely or under restraint) [20, 127] (see section “Density, fiber content and porosity”).

Beating and refining

Beating and refining are mechanical processes that are used to adjust the fiber morphology for the paper-making processes. While the word beating is rather used for laboratory scale or older processes, the word refining is used for modern mill equipment. The aim of the process is the straightening, shortening, and/or flexibilization of the fibers. Refining reduces the length, width, and coarseness of the fibers.

Lower fiber coarseness gives a higher contact area between the fibers in the paper sheet [23]. This can be related to the collapse of the lumen, the resulting flattening of the fiber, and the subsequent increase in the contact area (see section “Inter-fiber contact”). Furthermore, it was reported to increase the paper sheet density [168–171]. Both factors led to higher hygroexpansion (see sections “Density, fiber content and porosity” and “Inter-fiber contact”). In contrast, Pulkkinen et al. [107] reported a negative effect of refining on hygroexpansion due to alteration of the fiber wall thickness. Salmén et al. [105] took two effects into account: The production of fines during beating led to a higher hygroexpansion of freely dried sheets. Additionally, reduced coarseness and curl led to a lower shrinkage during production and thus to lower hygroexpansion. When sheets with curled fibers were dried under restraint, the hygroexpansion was reduced.

Drying

The drying process in the paper machine consists of three different sections, namely the wire section, press section and drying section. The important factor concerning the hygroexpansion is the drying restraints, which are in turn influenced by process parameters such as stretching, drying, and web tension [172].

Concerning the machine parameter side, the three-dimensional deformation of paper sheets during water absorption was shown to be affected by the non-stable drying conditions in the cross direction. The drying shrinkage was found to be higher at the outer sides ($\sim 0.8\%$ in CD) and lower in the middle of the web ($\sim 0.5\%$ in CD) [25]. A higher shrinkage during drying also leads to higher subsequent hygroexpansion [5, 25, 173]. This can in turn lead to the three-dimensional deformation of the paper web. Such imperfections induce residual stresses in the paper web which must not be neglected when modeling the three-dimensional deformation of paper sheets [174].

Moreover, the web tension during drying was found to influence the hygroexpansion. The lower the moisture content is, until when the paper is dried under restraint, the lower the observed hygroexpansion. For example, the hygroexpansion was ~ 0.3 , ~ 0.2 and $\sim 0.15\%$, when the sheet was dried under restraint down to a relative humidity of 90, 50 and 16%, respectively [175]. This was also confirmed by other researchers. The higher the degree of restraining during drying, the lower is the hygroexpansion (e.g., 2.11% for unrestrained sheets, 0.73% when 4% shrinkage was allowed during drying, for an increase in relative humidity from 30 to 90%, direction of measurement not indicated). When the web was additionally stretched in cross direction, hygroexpansion was further reduced. [173]. Apart from stretching during drying, the drying itself also plays an important role. When paper was dried with superheated steam at 320 °C, the hygroexpansion coefficient was reduced by 15%. This was reasoned as being due to the thermal softening of lignin [176].

Fiber network

The dimensional stability of fiber networks is directly and/or indirectly related to the effect of moisture content. As already described, the changes in the

dimensions of single fibers are basically due to their physicochemical interaction with water [12]. In addition, the expansion of the whole fiber network depends on the interaction of the fibers with each other.

Single fiber hygroexpansion

As explained in section “Measurement of single fiber and paper sheet hygroexpansion”, fibers show higher expansion in the transverse direction due to the longitudinal orientation of the polymer chains. Moreover expansion coefficients of the polymers were summarized. The dimensions of the whole fiber were found to increase by 0.10 to 0.15/ % m.c. in the transverse direction [30], by 0.17strain/%r.h. in transverse direction and 0.014strain/%r.h. in longitudinal direction [18], by 1.9–3.3% in the transverse direction, by 2.3–3.2% in the longitudinal direction, by 14.5–18.2% in area and by 12.4–17.3% in height in humidity cycles of 50–78–21% [13]. Apart from the arrangement of the polymers, another explanation for the anisotropic swelling of fibers was the “reinforced matrix hypothesis” [71, 177, 178]. In this hypothesis, the lignin-hemicellulosic matrix is assumed to shrink isotropically and to work like a skeleton in the secondary wall, whereas the cellulose microfibrils are assumed not to shrink during desorption. As a result, the shrinking of the whole fiber is assumed to be anisotropic. In order to link the single fiber hygroexpansion to the sheet hygroexpansion, Heyden, Gustafsson [179] and Uesaka [4] introduced stress transfer factors that describe the efficiency of stress transfer in the network. Simulations successfully reproduced the measured hygroexpansion values. They observed that the expansion in the cross

direction (CD) depends on the fiber orientation, stress transfer, and thus on inter-fiber bonding. In contrast, the expansion in the machine direction (MD) is largely determined by the expansion of the single fibers in the longitudinal direction [4]. An additional effect worth mentioning is that the external surface area of the paper decreases between 0 and 65% r.h. when the fibers expand, most probably due to relaxation processes of the fibers [180].

Fiber orientation

Fiber orientation influences many important properties of fiber-based materials. Techniques for fiber orientation measurement have been proposed [181, 182], and the mechanical properties as a function of the fiber direction have been evaluated [183, 184].

Due to the sheet production process, fibers are mostly aligned in the machine direction (MD) (Fig. 7). As already explained, the expansion of single fibers is higher in the transverse direction than in the longitudinal direction. The expansion of paper in cross direction (CD) is up to 7 times higher than in the machine direction (MD) [25, 161, 185, 186]. However, fibers are not 100% parallel in reality and the orientation is determined by several variables of the papermaking process. This is why the hygroexpansion increases in the cross direction (CD) and decreases in the machine direction (MD) with increasing degree of orientation [4, 179]. In cases where there is no orientation, namely the fiber orientation is in-plane isotropic, the sheet hygroexpansion correlates with the transverse fiber expansion in both directions [5].

Apart from the sheet hygroexpansion, the fiber orientation also affects the three-dimensional

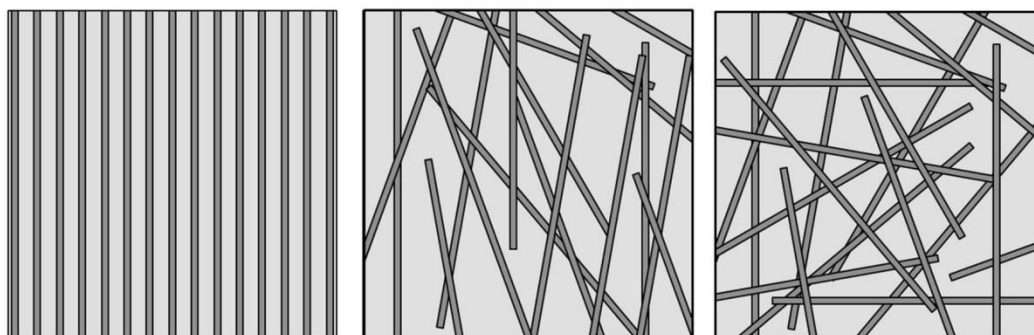


Fig. 7 Perfectly parallel fibers (*left*), mostly parallel fibers (*middle*) and in-plane isotropic fibers (*right*) [28, 187].

deformation of paper. Depending on the fiber orientation, samples show a larger twist when they are cut in the cross direction (CD) than in the machine direction (MD) [188]. Additionally, irregularities in fiber orientations which can arise due to cross flows of the jet from the head box in the paper machine can result in waviness (wavelengths 4–5 cm) [189]. Likewise, a higher disorder of local fiber orientation leads to more cockling [190, 191].

Density, fiber content and porosity

Basically, the three parameters density, fiber content and porosity describe each other. The more fibers are present in a defined volume, the higher the density and the lower the porosity.

Concerning the effect of pores on hygroexpansion, different models have been proposed. For low density sheets, it is reported that pores partially compensate the expansion of the fibers, namely the fibers use the empty space for expansion, so that the pore volume decreases while the fiber volume increases. Thus, the overall volume of the paper sheet is affected only to a minor degree. For high density sheets, the fibers seem to expand, whereas the voids between the fibers stay constant [29]. On the other side, one theory states that voids do not keep their size but seem to expand during water uptake (just like voids in metal expand during thermal treatment) and thus enhance hygroexpansion in freely dried paper. For papers dried under restraint, the void expansion is reported to be equal to the overall expansion [76].

A higher density is generally reported to increase hygroexpansion. This was stated as being due to the increased inter-fiber contact (see section “Inter-fiber contact”) and the effects of pore volume [23, 29, 105, 192, 193]. However, the effect of the density is greater in freely dried sheets than in sheets dried under restraint [105]. Additionally, the hygroexpansion is more affected by drying restraints when the solid content is high [175]. For dry solid contents from 55 to 100%, an increase in hygroexpansion from ~ 0.04 to ~ 0.16 for softwood freely dried pulp was reported [193].

Inter-fiber contact

Inter-fiber bonds are contact areas between different fibers (see Fig. 8) and can be observed by X-ray microtomography [194]. When fibers swell due to moisture absorption, stresses arise at inter-fiber bonds

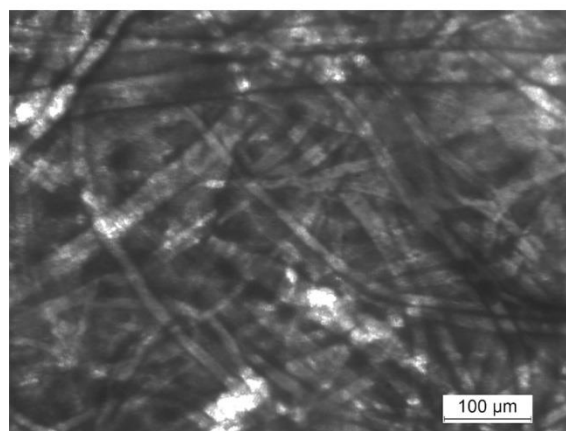


Fig. 8 Fibrous network [28].

[195, 196]. This topic has relevance to sections “Fiber curl and twist”, “Polyelectrolyte multilayers (PEM) and crosslinking”, “Fillers”, “Beating and refining”, and “Fiber orientation” because contact areas are typically dependent on fiber orientation, fiber geometry, and also on the fiber content, namely the density of the material [197]. Also, the contact area can be increased by the application of humidity/wetness and pressure. With higher humidity, the hardness of fibers decreases and thus fiber bond formation via hydrogen bonds increases. To maintain this in the dry state, the fibers need to deform plastically [198, 199]. This can be achieved by the collapse of the fiber lumen during beating [32]. Apart from wetting and softening, the interaction between fibers can be increased by hornification, crosslinking or oxidation (addressed in sections “Chemical modification and additives” and “Pulp and paper production”).

Marulier et al. [197] found up to 45 inter-fiber contacts/mm for fiber lengths of 0–0.5 mm. For fiber lengths >0.5 mm, the number of contacts decreases to about 30 contacts/mm. A positive, partially almost linear correlation between inter-fiber contact or density and hygroexpansion has been reported [5, 23, 76, 105, 200]. In a non-isotropic fiber network, the hygroexpansion consists of two parts: expansion in the machine direction (MD) and the cross direction (CD). The expansion in the cross direction (CD) is mainly affected by fiber orientation (see section “Fiber orientation”) and increases with the degree of inter-fiber bonding [4, 5, 200]. However, the effect of inter-fiber contacts depends on the fiber orientation and increases depending on the degree of drying restraint [21, 201]. Regarding the assumption that

Table 2 Overview of literature sources dealing with the modeling and simulation of hygroexpansion

Hygroexpansion of ...				
Fiber	Wood	Paper sheet	Multilayer	Matrix
[5, 10, 34, 47, 52, 56–58, 69, 70, 71, 74, 101, 108, 112, 118–120, 177–179, 185, 188, 195, 206–233]	[34, 46, 52, 70, 71, 177, 178, 208, 209, 211, 213]	[4, 5, 174, 179, 183, 188–190, 195, 196, 218, 219, 221, 224, 226, 227, 234–237]	[205, 219, 237]	[52, 126, 135, 207, 214, 225, 230, 238–241]

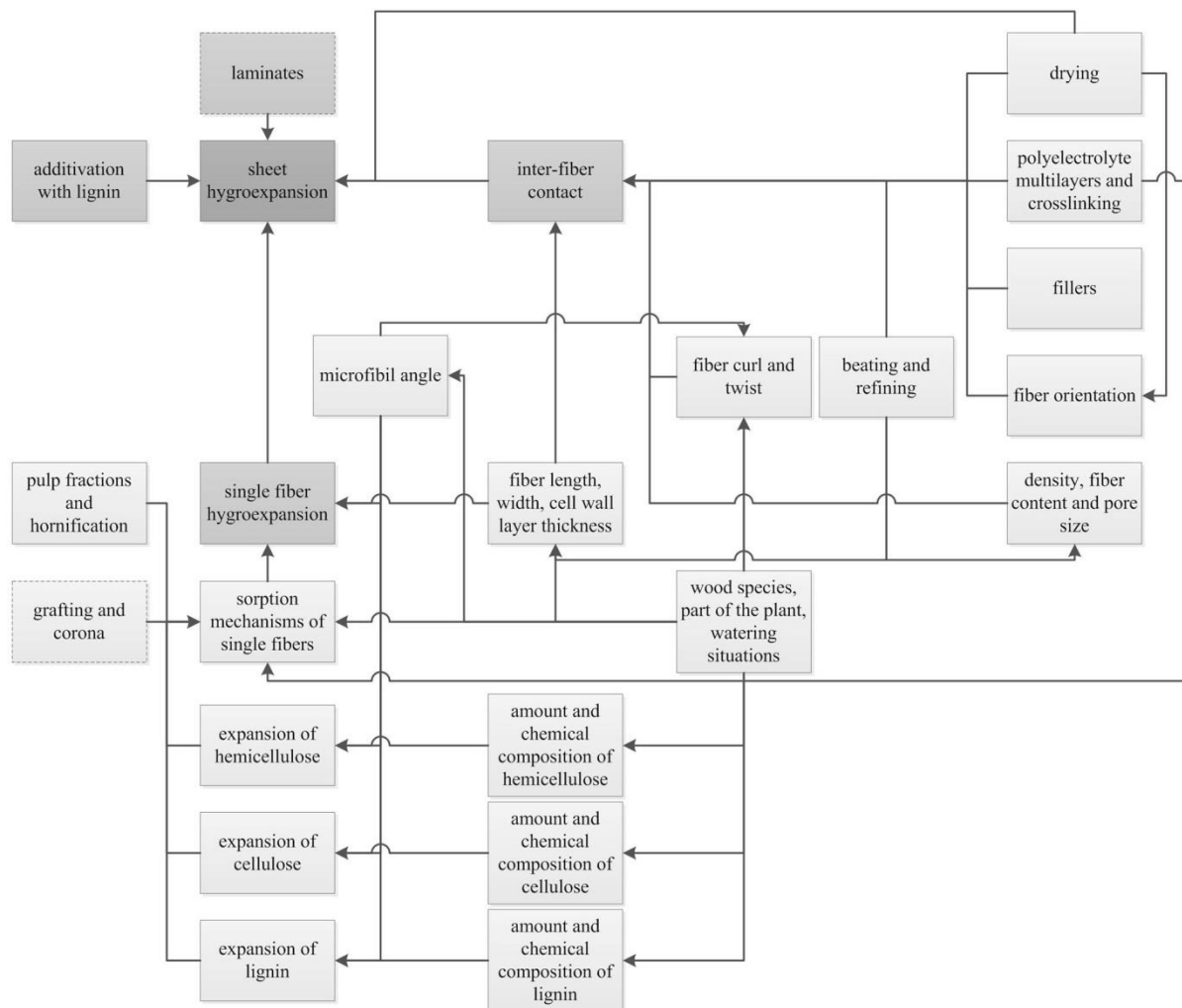


Fig. 9 Interplay of factors affecting hygroexpansion [28].

more inter-fiber contacts lead to a higher hygroexpansion, contrary effects for hydroexpansion have been observed. Sheets of microfibrillated cellulose (i.e. without fiber joints) and ordinary sheets showed

the same expansion. It was concluded that the expansion of the paper sheet is linked to the expansion of the fiber wall and that fiber joints hardly influence the hydroexpansion [7].

Laminates

The term laminate here describes a multilayer material, consisting of paper and one or more additional polymeric layers. Although quite a view patents have been published claiming improved dimensional stability of paper by the application of coatings (see for example [202–204]), only one publication was found, dealing with the effect of polymeric coatings on the hygroexpansion of paper. It was reported that the coating of paper with polyethylene reduces the hygroexpansion in the machine direction (MD) from for example 0.0036%/ % r.h. to 0.0023%/ % r.h. [205].

Models

Lots of work has been put into the development of various models describing the hygroexpansion of fibers, wood, paper sheets, paper polymer multilayers or fibers in a polymer matrix. Some of the conclusions drawn in the relevant publications have been mentioned in the previous sections. It is outside of the scope of this review to compare these models. However, an overview is given of the relevant literature (Table 2).

Conclusions

This review shows that the hygroexpansion of fibers and paper is a property that is affected by and affects many other properties. From the overview in Fig. 9, it can be seen that the main factors are single fiber hygroexpansion and the inter-fiber contacts. For both factors, various methods have been described for influencing the hygroexpansion. These methods are mainly of relevance for paper producers. Only grafting, corona treatment, and coating with polymers (laminates) are of relevance for paper converters. Even the paper producers have little active influence over fiber specific characteristics such as the expansion of the individual polymers, fiber curl and twist, or microfibril angle. The easiest ways to alter the hygroexpansive properties are the drying, the application of polyelectrolyte multilayers, fillers, fiber orientation, density, fiber content and pore size, grafting, and the use of specific pulp fractions such as recycled hornified fibers.

Acknowledgements

I would like to thank Markus Schmid and the reviewers for revision of the manuscript.

Compliance with ethical standards

Conflict of interest The author declares no conflicts of interest.

Open Access This article is distributed under the terms of the Creative Commons Attribution 4.0 International License (<http://creativecommons.org/licenses/by/4.0/>), which permits unrestricted use, distribution, and reproduction in any medium, provided you give appropriate credit to the original author(s) and the source, provide a link to the Creative Commons license, and indicate if changes were made.

References

- [1] European Forest Sector Outlook Study (2005). United Nations Publications
- [2] Papierfabriken VD (2017) Papier 2017, Annual Report
- [3] Tobjörk D, Österbacka R (2011) Paper electronics. *Adv Mater* 23(17):1935–1961. doi:10.1002/adma.201004692
- [4] Uesaka T (1994) General formula for hygroexpansion of paper. *J Mater Sci* 29(9):2373–2377. doi:10.1007/BF00363429
- [5] Sampson WW, Yamamoto J (2011) The drying shrinkage of cellulosic fibres and isotropic paper sheets. *J Mater Sci* 46(2):541–547. doi:10.1007/s10853-010-5006-2
- [6] Elegir G, Bussini D, Antonsson S, Lindström ME, Zoia L (2007) Laccase-initiated cross-linking of lignocellulose fibres using a ultra-filtered lignin isolated from kraft black liquor. *Appl Microbiol Biotechnol* 77(4):809–817. doi:10.1007/s00253-007-1203-6
- [7] Larsson PA, Wågberg L (2010) Diffusion-induced dimensional changes in papers and fibrillar films: influence of hydrophobicity and fibre-wall cross-linking. *Cellulose* 17(5):891–901. doi:10.1007/s10570-010-9433-7
- [8] Considine JM, Stoker DL, Laufenberg TL, Evans JW (1994) Compressive creep-behavior of corrugating components affected by humid environment. *Tappi J* 77(1):87–95
- [9] Uesaka T (1991) Dimensional stability of paper—upgrading paper performance in end use. *J Pulp Pap Sci* 17(2):J39–J46
- [10] Haslach HW (2000) The moisture and rate-dependent mechanical properties of paper: a review. *Mech Time*

- Depend Mater 4(3):169–210. doi:10.1023/A:1009833415827
- [11] Pulkkinen I, Fiskari J, Alopaeus V (2009) The effect of sample size and shape on the hygroexpansion coefficient—a study made with advanced methods for hygroexpansion measurement. *Technical Association of the Pulp and Paper Industry of Southern Africa*, pp 26–33
- [12] Lee JM (2007) An atomic force microscopy study of the local hygro-expansion behavior of cellulose microfibrils. Dissertation, North Carolina State University, Raleigh
- [13] Lee JM, Pawlak JJ, Heitmann JA (2012) Dimensional and hygroexpansive behaviors of cellulose microfibrils (MFs) from kraft pulp-based fibers as a function of relative humidity. *Holzforschung*, pp 66
- [14] Kiaei M, Tajik M, Vaysi R (2014) Chemical and biometrical properties of plum wood and its application in pulp and paper production. *Maderas Ciencia y tecnología* 16(3):313–322. doi:10.4067/S0718-221x2014005000024
- [15] Pulkkinen I, Fiskari J, Alopaeus V (2008) The effect of hardwood fiber morphology on the hygroexpansivity of paper. *BioResources* 4(1):126–141
- [16] Pulkkinen I (2010) From eucalypt fiber distributions to technical properties of paper. Dissertation, Aalto University, Espoo
- [17] Toungara M, Latil P, Dumont PJJ, du Roscoat SR, Orgéas L, Joffré T, Passas R (2014) 3D Observation of the hygroexpansion of wood fibres. In: *MécaMat Grenoble*
- [18] Joffré T, Isaksson P, Dumont PJJ, Roscoat SRd, Sticko S, Orgéas L, Gamstedt EK (2016) A method to measure moisture induced swelling properties of a single wood cell. *Exp Mech* 56(5):723–733. doi:10.1007/s11340-015-0119-9
- [19] Mark RE, Habeger C, Borch J, Lyne MB (2001) *Handbook of physical testing of paper: volume 1, vol I*. CRC Press, Boca Raton
- [20] Larsson PA (2010) Hygro- and hydroexpansion of paper: influence of fibre-joint formation and fibre sorptivity. Dissertation, KTH Royal Institute of Technology, Stockholm
- [21] Larsson PA, Wågberg L (2008) Influence of fibre–fibre joint properties on the dimensional stability of paper. *Cellulose* 15(4):515–525. doi:10.1007/s10570-008-9203-y
- [22] Ikuta S, Hitosugi F (1996) New expansimeter for paper sample. In: *Pulp and paper research conference*, Tokyo, Japan, pp 70–73
- [23] Antonsson S, Mäkelä P, Fellers C, Lindström ME (2009) Comparison of the physical properties between hardwood and softwood pulps. *Nord Pulp Pap Res J* 24(4):409–414. doi:10.3183/NPPRJ-2009-24-04-p409-414
- [24] Manninen M, Kajanto I, Happonen J, Paltakari J (2011) The effect of microfibrillated cellulose addition on drying shrinkage and dimensional stability of wood-free paper. *Nord Pulp Pap Res J* 26(3):297–305
- [25] Mendes AHT, Kim HY, Ferreira PJT, Park SW (2012) The importance of the measurement of paper differential CD shrinkage. *O PAPEL* 73(2):45–50
- [26] Lif JO, Fellers C, Sjö Dahl M (1995) Characterizing the in-plane hygroexpansivity of paper by electronic speckle photography. *J Pulp Pap Sci* 21(9):J302–J308
- [27] Barquin A (2011) Effect of high yield pulp on the dimensional stability of wood-free paper for inkjet printing applications. Master Thesis, University of Toronto, Toronto
- [28] Lindner M (2016) Nutzung des elektrischen Oberflächenwiderstandes zur Abschätzung der Hygroexpansion, Substratraueheit und Gasbarriere von aufgedampften Aluminiumschichten auf Papier und Folie. *Fraunhofer IVV, Freising*
- [29] Viguie J, Dumont PJJ, Mauret E, du Roscoat SR, Vacher P, Desloges I, Bloch JF (2011) Analysis of the hygroexpansion of a lignocellulosic fibrous material by digital correlation of images obtained by X-ray synchrotron microtomography: application to a folding box board. *J Mater Sci* 46(14):4756–4769. doi:10.1007/s10853-011-5386-y
- [30] Neagu RC, Gamstedt EK, Lindström M (2005) Influence of wood-fibre hygroexpansion on the dimensional instability of fibre mats and composites. *Compos A Appl Sci Manuf* 36(6):772–788. doi:10.1016/j.compositesa.2004.10.023
- [31] Chinga-Carrasco G (2011) Cellulose fibres, nanofibrils and microfibrils: the morphological sequence of MFC components from a plant physiology and fibre technology point of view. *Nanoscale Res Lett* 6(1):417. doi:10.1186/1556-276x-6-417
- [32] Yamauchi T (2007) A method to determine lumen volume and collapse degree of pulp fibers by using bottleneck effect of mercury porosimetry. *J Wood Sci* 53(6):516–519. doi:10.1007/s10086-007-0895-7
- [33] Wardrop AB, Preston RD (1947) Organisation of the cell walls of tracheids and wood fibres. *Nature* 160(4078):911–913
- [34] Neagu RC, Gamstedt EK (2007) Modelling of effects of ultrastructural morphology on the hygroelastic properties of wood fibres. *J Mater Sci* 42(24):10254–10274. doi:10.1007/s10853-006-1199-9
- [35] Wiedenhoef AC, Miller RB (2005) Structure and Function of Wood. In: *Wood handbook—wood as an engineering material*. United States Department of Agriculture Forest Service, Madison, Wisconsin, p 9
- [36] Blechschmidt J (2010) *Taschenbuch der Papiertechnik: mit 85 Tabellen*. Hanser

- [37] Salmén L, de Ruvo A (2007) A model for the prediction of fiber elasticity. *Wood Fiber Sci* 17(3):336–350
- [38] Reme PA (2000) Some effects of wood characteristics and the pulping process on mechanical pulp fibres. Dissertation, Norwegian University of Science and Technology, Trondheim
- [39] Heyn A (1969) The elementary fibril and supermolecular structure of cellulose in soft wood fiber. *J Ultrastruct Res* 26(1–2):52–68. doi:10.1016/s0022-5320(69)90035-5
- [40] Meier H (1962) Chemical and morphological aspects of the fine structure of wood. *Pure Appl Chem* 5(1–2):37–52
- [41] Jakob HF, Fratzl P, Tschegg SE (1994) Size and arrangement of elementary cellulose fibrils in wood cells: a small-angle X-ray scattering study of picea abies. *J Struct Biol* 113(1):13–22. doi:10.1006/jsbi.1994.1028
- [42] Jakob H, Fengel D, Tschegg S, Fratzl P (1995) The elementary cellulose fibril in *Picea abies*: comparison of transmission electron microscopy, small-angle X-ray scattering, and wide-angle X-ray scattering results. *Macromolecules* 28(26):8782–8787. doi:10.1021/ma00130a010
- [43] Zhang Y, Chen X, Liu J, Gao P, Shi D, Pang S (1997) Size and arrangement of elementary fibrils in crystalline cellulose studied with scanning tunneling microscopy. *J Vac Sci Technol Microelectron Nanometer Struct Process Meas Phenom* 15(4):1502–1505. doi:10.1116/1.589483
- [44] Muhlethaler K (1960) Die Feinstruktur der Zellosemikrofibrillen. *Beih Z Schweiz Forstver* 30:55–64
- [45] Hansen CM, Björkman A (1998) The ultrastructure of wood from a solubility parameter point of view. *Holzforchung Int J Biol Chem Phys Technol Wood* 52(4):335–344. doi:10.1515/hfsg.1998.52.4.335
- [46] Wang NL, Liu WY, Lai JP (2014) An attempt to model the influence of gradual transition between cell wall layers on cell wall hygroelastic properties. *J Mater Sci* 49(5):1984–1993. doi:10.1007/s10853-013-7885-5
- [47] Derome D, Rafsanjani A, Hering S, Dressler M, Patera A, Lanvermann C, Sedighi-Gilani M, Wittel FK, Niemz P (2013) The role of water in the behavior of wood. *J Build Phys* 36(4):1744259112473926. doi:10.1177/1744259112473926
- [48] Mohanty AK, Misra M, Hinrichsen G (2000) Biofibres, biodegradable polymers and biocomposites: an overview. *Macromol Mater Eng* 276–277(1):1–24. doi:10.1002/(SICI)1439-2054(20000301)276:1<1:AID-MAME1>3.0.CO;2-W
- [49] Saheb DN, Jog JP (1999) Natural fiber polymer composites: a review. *Adv Polym Technol* 18(4):351–363. doi:10.1002/(SICI)1098-2329(199924)18:4<351:Aid-Adv6>3.0.Co;2-X
- [50] Oksman K, Mathew AP, Bismarck A (2014) Handbook of green materials, volume 5: biobased composite materials, their processing properties and industrial applications. World Scientific Publishing Company, Singapore
- [51] Panshin AJ, De Zeeuw C (1980) Textbook of wood technology: structure, identification, properties, and uses of the commercial woods of the United States and Canada, vol Bd. 1. McGraw-Hill, New York
- [52] Marklund E, Varna J (2009) Modeling the hygroexpansion of aligned wood fiber composites. *Compos Sci Technol* 69(7–8):1108–1114. doi:10.1016/j.compscitech.2009.02.006
- [53] Belbekhouche S, Bras J, Siqueira G, Chappey C, Lebrun L, Khelifi B, Marais S, Dufresne A (2011) Water sorption behavior and gas barrier properties of cellulose whiskers and microfibrils films. *Carbohydr Polym* 83(4):1740–1748. doi:10.1016/j.carbpol.2010.10.036
- [54] Reina JJ, Domínguez E, Heredia A (2001) Water sorption-desorption in conifer cuticles: the role of lignin. *Physiol Plant* 112(3):372–378. doi:10.1034/j.1399-3054.2001.1120310.x
- [55] Mihrianyan A, Llagostera AP, Karmhag R, Strømme M, Ek R (2004) Moisture sorption by cellulose powders of varying crystallinity. *Int J Pharm* 269(2):433–442. doi:10.1016/j.ijpharm.2003.09.030
- [56] Persson K (2000) Micromechanical modelling of wood and fibre properties. Lund University, Lund
- [57] Cave I (1978) Modelling moisture-related mechanical properties of wood part I: properties of the wood constituents. *Wood Sci Technol* 12(1):75–86
- [58] Bergander A, Salmén L (2002) Cell wall properties and their effects on the mechanical properties of fibers. *J Mater Sci* 37(1):151–156. doi:10.1023/A:1013115925679
- [59] Salmén L, Olsson AM, Stevanic JS, Simonovic J, Radotic K (2012) Structural organisation of the wood polymers in the wood fibre structure. *BioResources* 7(1):521–532
- [60] Cuissinat C, Navard P (2006) Swelling and dissolution of cellulose part I: free floating cotton and wood fibres in N-methylmorpholine-N-oxide–water mixtures. *Macromol Symp* 244(1):1–18. doi:10.1002/masy.200651201
- [61] Salmén L (2004) Micromechanical understanding of the cell-wall structure. *CR Biol* 327(9–10):873–880. doi:10.1016/j.crv.2004.03.010
- [62] Nakamura KI, Wada M, Kuga S, Okano T (2004) Poisson's ratio of cellulose I β and cellulose II. *J Polym Sci Part B Polym Phys* 42(7):1206–1211. doi:10.1002/polb.10771
- [63] Neville AC (1993) Biology of fibrous composites: development beyond the cell membrane. Cambridge University Press, Cambridge

- [64] Jacobs A, Dahlman O (2001) Characterization of the molar masses of hemicelluloses from wood and pulps employing size exclusion chromatography and matrix-assisted laser desorption ionization time-of-flight mass spectrometry. *Biomacromol* 2(3):894–905
- [65] Hansen CM (2012) Hansen solubility parameters: a user's handbook. CRC Press, Boca Raton
- [66] Credou J, Berthelot T (2014) Cellulose: from biocompatible to bioactive material. *J Mater Chem B* 2(30):4767–4788. doi:10.1039/c4tb00431k
- [67] Mark RE, Borch J (2001) Handbook of physical testing of paper, vol Bd. 1. Taylor & Francis, Milton Park
- [68] Wüstenberg T (2013) Cellulose und Cellulosederivate: Grundlagen, Wirkungen und Applikationen. Behr's Verlag DE, Humberg
- [69] Pulkkinen I, Fiskari J, Alopaeus V (2009) CPMA 13C NMR analysis of fully bleached eucalypt pulp samples: links to handsheet hygroexpansivity and strength properties. *J Appl Sci* 9(22):3991–3998
- [70] Joffre T, Neagu RC, Bardage SL, Gamstedt EK (2014) Modelling of the hygroelastic behaviour of normal and compression wood tracheids. *J Struct Biol* 185(1):89–98. doi:10.1016/j.jsb.2013.10.014
- [71] Yamamoto H, Sassus F, Ninomiya M, Gril J (2001) A model of anisotropic swelling and shrinking process of wood—part 2. A simulation of shrinking wood. *Wood Sci Technol* 35(1–2):167–181
- [72] Alince B (2002) Porosity of swollen pulp fibers revisited. *Nord Pulp Pap Res J* 17(1):71–73. doi:10.3183/NPPRJ-2002-17-01-p071-073
- [73] Kocherbitov V, Ulvenlund S, Kober M, Jarring K, Arnebrant T (2008) Hydration of microcrystalline cellulose and milled cellulose studied by sorption calorimetry. *J Phys Chem B* 112(12):3728–3734. doi:10.1021/jp711554c
- [74] Mazeau K (2015) The hygroscopic power of amorphous cellulose: a modeling study. *Carbohydr Polym* 117:585–591. doi:10.1016/j.carbpol.2014.09.095
- [75] Chen WC, Tejado A, Alam MN, van de Ven TG (2015) Hydrophobic cellulose: a material that expands upon drying. *Cellulose* 22(4):2749–2754. doi:10.1007/s10570-015-0645-8
- [76] Salmén L, Fellers C (1989) The nature of volume hydroexpansivity of paper. *J Pulp Pap Sci* 15(2):J63–J65
- [77] Roseveare WE (1947) Contributions to the physics of cellulose fibres. P. H. HERMANS. Elsevier, New York-Amsterdam, 1946. In English. 221 pp. Price \$4.00. *J Polym Sci* 2(3):354. doi:10.1002/pol.1947.120020321
- [78] Berthold J, Desbrieres J, Rinaudo M, Salmén L (1994) Types of adsorbed water in relation to the ionic groups and their counter-ions for some cellulose derivatives. *Polymer* 35(26):5729–5736
- [79] Uetani K, Yano H (2012) Zeta potential time dependence reveals the swelling dynamics of wood cellulose nanofibrils. *Langmuir* 28(1):818–827. doi:10.1021/la203404g
- [80] Cuissinat C, Navard P (2008) Swelling and dissolution of cellulose, part III: plant fibres in aqueous systems. *Cellulose* 15(1):67–74. doi:10.1007/s10570-007-9158-4
- [81] Fahlén J, Salmén L (2003) Cross-sectional structure of the secondary wall of wood fibers as affected by processing. *J Mater Sci* 38(1):119–126. doi:10.1023/A:1021174118468
- [82] Wan J, Wang Y, Xiao Q (2010) Effects of hemicellulose removal on cellulose fiber structure and recycling characteristics of eucalyptus pulp. *Bioresour Technol* 101(12):4577–4583. doi:10.1016/j.biortech.2010.01.026
- [83] Roberts V, Stein V, Reiner T, Lemonidou A, Li X, Lercher JA (2011) Towards quantitative catalytic lignin depolymerization. *Chem Eur J* 17(21):5939–5948. doi:10.1002/chem.201002438
- [84] Cousins WJ (1976) Elastic-modulus of lignin as related to moisture-content. *Wood Sci Technol* 10(1):9–17
- [85] Schuerch C (1952) The solvent properties of liquids and their relation to the solubility, swelling, isolation and fractionation of lignin. *J Am Chem Soc* 74(20):5061–5067. doi:10.1021/ja01140a020
- [86] Eriksson I, Haglind I, Lidbrandt O, Sahnén L (1991) Fiber swelling favoured by lignin softening. *Wood Sci Technol* 25(2):135–144. doi:10.1007/bf00226813
- [87] Antonsson S (2007) The Use of lignin derivatives to improve selected paper properties. Dissertation, Royal Institute of Technology, Stockholm
- [88] Barnett JR, Bonham VA (2004) Cellulose microfibril angle in the cell wall of wood fibres. *Biol Rev* 79(2):461–472. doi:10.1017/S1464793103006377
- [89] Meylan BA, Butterfield BG (1978) Helical orientation of the microfibrils in tracheids, fibres and vessels. *Wood Sci Technol* 12(3):219–222. doi:10.1007/BF00372867
- [90] Andersson S, Serimaa R, Torkkeli M, Paakkari T, Saranpää P, Pesonen E (2000) Microfibril angle of Norway spruce [*Picea abies* (L.) Karst.] compression wood: comparison of measuring techniques. *J Wood Sci* 46(5):343–349. doi:10.1007/bf00776394
- [91] Leonardon M, Altaner CM, Vihermaa L, Jarvis MC (2010) Wood shrinkage: influence of anatomy, cell wall architecture, chemical composition and cambial age. *Eur J Wood Wood Prod* 68(1):87–94. doi:10.1007/s00107-009-0355-8
- [92] Reiterer A, Jakob HF, Stanzl-Tschegg SE, Fratzl P (1998) Spiral angle of elementary cellulose fibrils in cell walls of *Picea abies* determined by small-angle X-ray scattering.

- Wood Sci Technol 32(5):335–345. doi:10.1007/bf00702790
- [93] Sahlberg U, Salmén L, Oscarsson A (1997) The fibrillar orientation in the S2-layer of wood fibres as determined by X-ray diffraction analysis. Wood Sci Technol 31(2):77–86. doi:10.1007/bf00705923
- [94] Donaldson L, Xu P (2005) Microfibril orientation across the secondary cell wall of Radiata pine tracheids. Trees 19(6):644–653. doi:10.1007/s00468-005-0428-1
- [95] Vainio A, Sirvio M, Paulapuro H (2007) Observations on the microfibril angle of Finnish papermaking fibres. In: 61st Appita annual conference and exhibition, Gold Coast, Australia 6–9 May 2007: Proceedings, 2007. Appita Inc., p 397
- [96] Courchene CE, Peter GF, Litvay J (2006) Cellulose microfibril angle as a determinant of paper strength and hygroexpansivity in Pinus taeda L. Wood Fiber Sci 38(1):112–120
- [97] Burgert I, Frühmann K, Keckes J, Fratzl P, Stanzl-Tschegg S (2004) Structure–function relationships of four compression wood types: micromechanical properties at the tissue and fibre level. Trees 18(4):480–485. doi:10.1007/s00468-004-0334-y
- [98] Eder M, Jungnickl K, Burgert I (2008) A close-up view of wood structure and properties across a growth ring of Norway spruce (*Picea abies* [L.] Karst.). Trees 23(1):79–84. doi:10.1007/s00468-008-0256-1
- [99] Gindl W, Gupta HS, Schöberl T, Lichtenegger HC, Fratzl P (2004) Mechanical properties of spruce wood cell walls by nanoindentation. Appl Phys A 79(8):2069–2073. doi:10.1007/s00339-004-2864-y
- [100] Jäger A, Bader T, Hofstetter K, Eberhardsteiner J (2011) The relation between indentation modulus, microfibril angle, and elastic properties of wood cell walls. Compos A Appl Sci Manuf 42(6):677–685. doi:10.1016/j.compositesa.2011.02.007
- [101] Uesaka T, Moss C (1997) Effects of fibre morphology on hygroexpansivity of paper—a micromechanics approach. Fund Papermak Mater 1:663–679
- [102] Ververis C, Georghiou K, Christodoulakis N, Santas P, Santas R (2004) Fiber dimensions, lignin and cellulose content of various plant materials and their suitability for paper production. Ind Crops Prod 19(3):245–254. doi:10.1016/j.indcrop.2003.10.006
- [103] Ogbonnaya CI, Roy-Macauley H, Nwalozie MC, Annerose DJM (1997) Physical and histochemical properties of kenaf (*Hibiscus cannabinus* L.) grown under water deficit on a sandy soil. Ind Crops Prod 7(1):9–18. doi:10.1016/S0926-6690(97)00034-4
- [104] Kijima T, Yamakawa I (1978) Effect of beating condition on shrinkage during drying. Jpn Tappi J 32(12):722–727
- [105] Salmén L, Boman R, Fellers C, Htun M (1987) The implications of fiber and sheet structure for the hygroexpansivity of paper [curl, shrinkage, beating, fines]. Nordic Pulp Pap Res J (Sweden) 4
- [106] Wang N, Liu W, Peng Y (2013) Gradual transition zone between cell wall layers and its influence on wood elastic modulus. J Mater Sci 48(14):5071–5084. doi:10.1007/s10853-013-7295-8
- [107] Pulkkinen I, Fiskari J, Aittamaa J (2007) The effect of fiber wall thickness distribution on dimensional stability. In: 61st Appita annual conference and exhibition, Gold Coast, Australia 6–9 May 2007: Proceedings, 2007. Appita Inc., p 373
- [108] Gärd J (2002) The influence of fibre curl on the shrinkage and strength properties of paper. M. Sc. thesis, Lulea University of Technology
- [109] Er-ni M (2013) Studies on moisture sorption and hygroexpansion of wood from static condition to dynamic condition. Hubei Agric Sci 21:003
- [110] Skaar C (1988) Hygroexpansion in wood. In: Timell TE (ed) Wood–water relations. Springer, Berlin, pp 122–176. doi:10.1007/978-3-642-73683-4
- [111] Eklund D (1969) Dimensional stability of paper from different types of pulp. PAPER JA PUU-PAPPER OCH TRA 51(2):153
- [112] Hill CAS, Norton A, Newman G (2009) The water vapor sorption behavior of natural fibers. J Appl Polym Sci 112(3):1524–1537. doi:10.1002/app.29725
- [113] Venkateswaran A (1970) Sorption of aqueous and non-aqueous media by wood and cellulose. Chem Rev 70(6):619–637. doi:10.1021/cr60268a001
- [114] Eligon AM, Achong A, Saunders R (1992) Moisture adsorption and desorption properties of some tropical woods. J Mater Sci 27(13):3442–3456. doi:10.1007/bf01151818
- [115] Lindstrom T, Carlsson G (1982) The effect of chemical environment on fiber swelling. Sven Papperstidn 85(3):R14–R20
- [116] Laine J, Stenius P (1997) Effect of charge on the fibre and paper properties of bleached industrial kraft pulps. Pap Puu 79(4):257–266
- [117] Olsson AM, Salmen L (2004) The association of water to cellulose and hemicellulose in paper examined by FTIR spectroscopy. Carbohydr Res 339(4):813–818. doi:10.1016/j.carres.2004.01.005
- [118] Alix S, Philippe E, Bessadok A, Lebrun L, Morvan C, Marais S (2009) Effect of chemical treatments on water sorption and mechanical properties of flax fibres. Bioresour Technol 100(20):4742–4749. doi:10.1016/j.biortech.2009.04.067

- [119] Bessadok A, Marais S, Gouanvé F, Colasse L, Zimmerlin I, Roudesli S, Métayer M (2007) Effect of chemical treatments of Alfa (*Stipa tenacissima*) fibres on water-sorption properties. *Compos Sci Technol* 67(3–4):685–697. doi:10.1016/j.compscitech.2006.04.013
- [120] Sørensen G, Hoffmann J (2003) Moisture sorption in moulded fibre trays and effect on static compression strength. *Packag Technol Sci* 16(4):159–169. doi:10.1002/pts.622
- [121] Gimåker M (2010) Influence of fibre modification on moisture sorption and the mechanical properties of paper
- [122] Larsson PA, Gimåker M, Wågberg L (2008) The influence of periodate oxidation on the moisture sorptivity and dimensional stability of paper. *Cellulose* 15(6):837–847. doi:10.1007/s10570-008-9243-3
- [123] Gribova V, Auzely-Velty R, Picart C (2012) Polyelectrolyte multilayer assemblies on materials surfaces: from cell adhesion to tissue engineering. *Chem Mater Publ Am Chem Soc* 24(5):854–869. doi:10.1021/cm2032459
- [124] Eriksson M, Torgnysdotter A, Wågberg L (2006) Surface modification of wood fibers using the polyelectrolyte multilayer technique: effects on fiber joint and paper strength properties. *Ind Eng Chem Res* 45(15):5279–5286. doi:10.1021/ie060226w
- [125] Horvath AT, Pelton R, Larsson PT, Wågberg L (2010) Effect of cross-linking fiber joints on the tensile and fracture behavior of paper. *Ind Eng Chem Res* 49(14):6422–6431. doi:10.1021/ie100334z
- [126] Almgren KM, Gamstedt EK, Varna J (2010) Contribution of wood fiber hygroexpansion to moisture induced thickness swelling of composite plates. *Polym Compos* 31(5):762–771. doi:10.1002/pc.20858
- [127] Larsson PA, Hoc M, Wågberg L (2009) The influence of grammage, moisture content, fibre furnish and chemical modifications on the hygro-and hydro-expansion of paper. In: 14th Fundamental research symposium on advances in pulp and paper research location: St Annes Coll, Oxford, England, 13–18, 2009, pp 355–388
- [128] Chung YS, Pak P-K (2006) Effect of crosslinking on dimensional stability and dyeability of Korean traditional paper (Hanji) (전통한지의 형태안정성 및 염색성에 미치는 가교의 영향). *Text Sci Eng* 43(2):95–100
- [129] Weatherwax RC, Caulfield DF (1978) The pore structure of papers wet stiffened by formaldehyde crosslinking: I. Results from the water isotherm. *J Colloid Interface Sci* 67(3):498–505
- [130] Cohen W, Stamm A, Fahey D (1959) Dimensional stabilization of paper by cross-linking with formaldehyde. *Tappi* 42(12):934–940
- [131] Norimoto M, Gril J, Rowell RM (1992) Rheological properties of chemically modified wood: relationship between dimensional and creep stability. *Wood Fiber Sci* 24(1):25–35
- [132] Rana AK, Mitra BC, Bannerjee AN (1999) Effect of acetylation on dimensional stability, mechanical, and dynamic properties of jute board. *J Appl Polym Sci* 72(7):935–944. doi:10.1002/(Sici)1097-4628(19990516)72:7<935:Aid-App9>3.0.Co;2-W
- [133] Dekka M, Saikia CN (2000) Chemical modification of wood with thermosetting resin: effect on dimensional stability and strength property. *Bioresour Technol* 73(2):179–181. doi:10.1016/S0960-8524(99)00167-4
- [134] Kang I-S, Yang CQ, Weishu W, Lickfield GC (1998) Mechanical strength of durable press finished cotton fabrics. *Text Res J* 68(11):865–870. doi:10.1177/004051759806801112
- [135] Paunonen S, Gregersen Ø (2010) Effect of polyethylene coating on in-plane hygroexpansion of solid fiberboard. In: Paunonen S (ed) Influence of moisture on the performance of polyethylene coated solid fiberboard and boxes. Norwegian University of Science and Technology, Trondheim
- [136] LeBel RG, Schwartz RW, Sepall O (1968) A novel approach to dimensional stabilization of paper. *Tappi* 51(9):79–84
- [137] Tejado A, Antal M, Liu X, van de Ven TG (2011) Wet cross-linking of cellulose fibers via a bioconjugation reaction. *Ind Eng Chem Res* 50(10):5907–5913. doi:10.1021/ie1023589
- [138] Bhattacharya A, Rawlins JW, Ray P (2008) Polymer grafting and crosslinking. Wiley, New York
- [139] Samyn P (2013) Wetting and hydrophobic modification of cellulose surfaces for paper applications. *J Mater Sci* 48(19):6455–6498. doi:10.1007/s10853-013-7519-y
- [140] Izdebska J (2016) Corona treatment. In: Ebnesajjad S (ed) Printing on polymers. William Andrew Publishing, Chadds Ford, pp 123–142. doi:10.1016/B978-0-323-37468-2.00008-7
- [141] Zhang D, Sun Q, Wadsworth LC (1998) Mechanism of corona treatment on polyolefin films. *Polym Eng Sci* 38(6):965–970. doi:10.1002/pen.10264
- [142] Guimond S, Wertheimer MR (2004) Surface degradation and hydrophobic recovery of polyolefins treated by air corona and nitrogen atmospheric pressure glow discharge. *J Appl Polym Sci* 94(3):1291–1303. doi:10.1002/app.21134
- [143] Zenkiewicz M (2001) Investigation on the oxidation of surface layers of polyolefins treated with corona discharge. *J Adhes Sci Technol* 15(1):63–70. doi:10.1163/156856101743319

- [144] Sun C, Zhang D, Wadsworth LC (1999) Corona treatment of polyolefin films—a review. *Adv Polym Technol* 18(2):171–180. doi:10.1002/(SICI)1098-2329(199922)18:2<171:AID-ADV6>3.0.CO;2-8
- [145] Strobel M, Lyons CS, Strobel JM, Kapaun RS (1992) Analysis of air-corona-treated polypropylene and poly(ethylene terephthalate) films by contact-angle measurements and X-ray photoelectron spectroscopy. *J Adhes Sci Technol* 6(4):429–443. doi:10.1163/156856192X00764
- [146] Sapięha S, Cerny J, Klemberg-Sapięha JE, Martinu L (1993) Corona versus low pressure plasma treatment: effect on surface properties and adhesion of polymers. *J Adhes* 42(1–2):91–102. doi:10.1080/00218469308026573
- [147] Pascual M, Sanchis R, Sánchez L, García D, Balart R (2008) Surface modification of low density polyethylene (LDPE) film using corona discharge plasma for technological applications. *J Adhes Sci Technol* 22(13):1425–1442. doi:10.1163/156856108X305723
- [148] Owens DK (1975) The mechanism of corona and ultraviolet light-induced self-adhesion of poly(ethylene terephthalate) film. *J Appl Polym Sci* 19(12):3315–3326. doi:10.1002/app.1975.070191216
- [149] Novák I, Chodák I (1998) Adhesion of poly(propylene) modified by corona discharge. *Angew Makromol Chem* 260:47–51
- [150] Lynch JB, Spence PD, Baker DE, Postlethwaite TA (1999) Atmospheric pressure plasma treatment of polyethylene via a pulse dielectric barrier discharge: comparison using various gas compositions versus corona discharge in air. *J Appl Polym Sci* 71(2):319–331. doi:10.1002/(SICI)1097-4628(19990110)71:2<319:AID-APP16>3.0.CO;2-T
- [151] Bablyuk EB, Popov ON, Segueikin GI (1996) Adhesion properties of polyethylene terephthalate (PET) film treated with corona discharge. In: Anon (ed) Proceedings of the 1996 IS&T 49th annual conference, springfield, VA, United States, Minneapolis, MN, USA, 1996. *Soc Imaging Sci Technol*, pp 556–558
- [152] Sakata I, Morita M, Furuichi H, Kawaguchi Y (1991) Improvement of plybond strength of paperboard by corona treatment. *J Appl Polym Sci* 42(7):2099–2104. doi:10.1002/app.1991.070420738
- [153] Gaiolas C, Costa AP, Nunes M, Silva MJS, Belgacem MN (2008) Grafting of paper by silane coupling agents using cold-plasma discharges. *Plasma Processes Polym* 5(5):444–452. doi:10.1002/ppap.200700149
- [154] Berlioz S, Stinga C, Condoret J, Samain D (2008) SFGP 2007—investigation of a novel principle of chemical grafting for modification of cellulose fibers. *Int J Chem React Eng* 6(1):17
- [155] Freire CSR, Silvestre AJD, Neto CP, Belgacem MN, Gandini A (2006) Controlled heterogeneous modification of cellulose fibers with fatty acids: effect of reaction conditions on the extent of esterification and fiber properties. *J Appl Polym Sci* 100(2):1093–1102. doi:10.1002/app.23454
- [156] Singha AS, Rana RK (2010) Effect of pressure induced graft copolymerization on the physico-chemical properties of bio-fibers. *BioResources* 5(2):1055–1073
- [157] Antonsson S, Henriksson G, Lindstrom ME (2008) Adding lignin derivatives to decrease the effect of mechano-sorptive creep in linerboard. *Appita J* 61(6):468–471
- [158] Antonsson S (2008) Strategies for improving kraftliner pulp properties. Dissertation, Royal Institute of Technology, Stockholm
- [159] Antonsson S, Henriksson G, Johansson M, Lindström ME (2008) Low Mw-lignin fractions together with vegetable oils as available oligomers for novel paper-coating applications as hydrophobic barrier. *Ind Crops Prod* 27(1):98–103. doi:10.1016/j.indcrop.2007.08.006
- [160] Laurell Lyne A, Fellers C, Kolseth P (1996) The effect of filler on hygroexpansivity. *Nordic Pulp Pap Res J (Sweden)* 11(3):152–156
- [161] Figueiredo AB, Magina S, Evtuguin DV, Cardoso EF, Ferra JM, Cruz P (2016) Factors affecting the dimensional stability of decorative papers under moistening. *BioResources* 11(1):2020–2029
- [162] Li Z, Li K, Camm C, Chen Z (2009) Dimensional stability of paper made from mixtures of BCTMP and kraft fibres. *J Pulp Pap Sci* 35(3–4):123–129
- [163] Čabalová I, Kačík F, Geffert A, Kačíková D (2011) The effects of paper recycling and its environmental impact. In: Elzbieta Broniewicz (ed) *Environmental Management in Practice*. InTech, pp 329–350. doi:10.5772/23110
- [164] Fernandes Diniz JMB, Gil MH, Castro JAAM (2004) Hornification—its origin and interpretation in wood pulps. *Wood Sci Technol* 37(6):489–494. doi:10.1007/s00226-003-0216-2
- [165] Kato K, Cameron R (1999) A review of the relationship between thermally-accelerated ageing of paper and hornification. *Cellulose* 6(1):23–40. doi:10.1023/A:1009292120151
- [166] Racz I, Borsa J (1997) Swelling of carboxymethylated cellulose fibres. *Cellulose* 4(4):293–303. doi:10.1023/a:1018400226052
- [167] Müller Y, Tot I, Potthast A, Rosenau T, Zimmermann R, Eichhorn K-J, Nitschke C, Scherr G, Freudenberg U, Werner C (2010) The impact of esterification reactions on physical properties of cellulose thin films. *Soft Matter* 6(15):3680–3684. doi:10.1039/c0sm00005a

- [168] Swanson J (1950) The effects of natural beater additives on papermaking fibers. *Tappi* 33(9):451–462
- [169] Klipper W (1952) Schrumpfung und Dehnung der Papierbahn in der Papiermaschine [Shrinkage and extensibility of paper web in paper machine]. *Papier*
- [170] Laptew L, Kraft G (1967) Untersuchungen der Dimensionsstabilität von Papier und Karton mit einem neuen Prüfgerät [Investigations of dimensional stability of paper and paperboard by means of a new test apparatus]. *Zellst Pap* 16(1):11
- [171] Pulkkinen I, Fiskari J (2008) The use of fibre wall thickness data to predict handsheet properties of eucalypt pulp fibres. *O Papel* 69(5):71–85
- [172] Nielsen I, Priest D (1997) Dimensional stability of paper in relation to lining and drying procedures. *Pap Conserv* 21(1):26–36
- [173] Fahey DJ, Chilson W (1963) Mechanical treatments for improving dimensional stability of paper. *Rev Process Non-Ref (Other)* 46(7):393–399
- [174] Uesaka T, Kodaka I, Okushima S, Fukuchi R (1989) History-dependent dimensional stability of paper. *Rheol Acta* 28(3):238–245. doi:10.1007/BF01332856
- [175] Salmén L, Fellers C, Htun M (1987) The development and release of dried-in stresses in paper. *Nord Pulp Pap Res J* 2:44–48
- [176] Nanri Y (1995) Dimensional stability of superheated steam dried paper. Master thesis, Mc Gill University, Montreal
- [177] Yamamoto H (1999) A model of the anisotropic swelling and shrinking process of wood. Part 1. Generalization of Barber's wood fiber model. *Wood Sci Technol* 33(4):311–325
- [178] Barber N, Meylan B (1964) The anisotropic shrinkage of wood. A theoretical model. *Holzforschung Int J Biol Chem Phys Technol Wood* 18(5):146–156
- [179] Heyden S, Gustafsson P-J (2002) Modelling of hygroexpansion of paper. In: *Progress in paper physics seminar*, pp 76–80
- [180] Dorris GM, Gray DG (1981) Effect of relative humidity on the external area of paper. *J Chem Soc Faraday Trans 1 Phys Chem Condens Phases* 77(4):713–724. doi:10.1039/f19817700713
- [181] Axelsson M (2009) An evaluation of scale and noise sensitivity of fibre orientation estimation in volume images. In: Foggia P, Sansone C, Vento M (eds) *Image analysis and processing—ICIAP 2009: 15th International conference Vietri sul Mare, Italy, September 8–11, 2009 Proceedings*. Springer, Berlin, pp 975–984. doi:10.1007/978-3-642-04146-4_104
- [182] Erkkilä AL, Pakarinen P, Odell M (1998) Sheet forming studies using layered orientation analysis: can lead to a better understanding of the drainage process, vol 1. Southam, Don Mills
- [183] Bosco E, Bastawrous MV, Peerlings RHJ, Hoefnagels JPM, Geers MGD (2015) Bridging network properties to the effective hygro-expansivity of paper: experiments and modelling. *Phil Mag* 95(28–30):3385–3401. doi:10.1080/14786435.2015.1033487
- [184] Gates ER, Kenworthy IC (1963) Effects of drying shrinkage and fibre orientation on some physical properties of paper. *Pap Technol* 4(5):485–493
- [185] Lavrykov S, Ramarao B, Laurell Lyne Å (2004) The planar transient hygroexpansion of copy paper: experiments and analysis. *Nord Pulp Pap Res J* 19(2):183–190
- [186] Lindem PE, Tappi (1995) Biaxial hygroexpansion of newsprint paper. In: *1995 International paper physics conference*. Tappi Press, Atlanta
- [187] Lindner M (2016) Nutzung des elektrischen Oberflächenwiderstandes zur Abschätzung der Hygroexpansion, Substratrauheit und Gasbarriere von aufgedampften Aluminiumschichten auf Papier und Folie. Fraunhofer IVV, Freising
- [188] Sellén C, Isaksson P (2013) A mechanical model for dimensional instability in moisture-sensitive fiber networks. *Journal of Composite Materials* 48(3):0021998312470576. doi:10.1177/0021998312470576
- [189] Kulachenko A, Uesaka T (2007) The effect of fibre orientation streaks on out-of-plane instabilities in paper. In: *61st Appita annual conference and exhibition, Gold Coast, Australia 6–9 May 2007: Proceedings, 2007*. Appita Inc., p 255
- [190] Lipponen P, Leppänen T, Kouko J, Hämäläinen J (2008) Elasto-plastic approach for paper cockling phenomenon: on the importance of moisture gradient. *Int J Solids Struct* 45(11–12):3596–3609. doi:10.1016/j.ijsolstr.2008.02.017
- [191] Leppänen T (2007) Effect of fiber orientation on cockling of paper. University of Kuopio, Kuopio
- [192] Mao CQ, Kortschot M, Farnood R, Spelt J (2003) Local rewetting and distortion of paper. *Nord Pulp Pap Res J* 18(1):10–17
- [193] Erkkilä A-L, Leppänen T, Hämäläinen J, Tuovinen T (2015) Hygro-elasto-plastic model for planar orthotropic material. *Int J Solids Struct* 62:66–80. doi:10.1016/j.ijsolstr.2015.02.001
- [194] Marulier C, Dumont P, Orgéas L, Caillerie D, du Roscoat SR (2012) Towards 3D analysis of pulp fibre networks at the fibre and bond levels. *Nord Pulp Pap Res J* 27(2):245. doi:10.3183/NPPRJ-2012-27-02-p245-255
- [195] Strömbro J, Gudmundson P (2008) An anisotropic fibre-network model for mechano-sorptive creep in paper. *Int J Solids Struct* 45(22–23):5765–5787. doi:10.1016/j.ijsolstr.2008.06.010

- [196] Haslach HW (1996) A model for drying-induced micro-compressions in paper: buckling in the interfiber bonds. *Compos B Eng* 27(1):25–33. doi:10.1016/1359-8368(95)00003-8
- [197] Marulier C, Dumont PJJ, Orgeas L, du Roscoat SR, Cailierie D (2015) 3D analysis of paper microstructures at the scale of fibres and bonds. *Cellulose* 22(3):1517–1539. doi:10.1007/s10570-015-0610-6
- [198] Ganser C, Hirn U, Rohm S, Schennach R, Teichert C (2014) AFM nanoindentation of pulp fibers and thin cellulose films at varying relative humidity. *Holzforschung* 68(1):53–60. doi:10.1515/hf-2013-0014
- [199] Bo NJP, Christian G, Franz S, Christian T, Robert S, Eduard G, Ulrich H (2013) Adhesion of cellulose fibers in paper. *J Phys Condens Matter* 25(4):045002
- [200] Bosco E, Peerlings RHJ, Geers MGD (2015) Predicting hydro-elastic properties of paper sheets based on an idealized model of the underlying fibrous network. *Int J Solids Struct* 56–57:43–52. doi:10.1016/j.ijsolstr.2014.12.006
- [201] Uesaka T, Qi D (1994) Hygroexpansivity of paper: effects of fibre-to-fibre bonding. *J Pulp Pap Sci* 20(6):J175–J179
- [202] Dickerman GK, Savage RL (1960) Method of making printable coated paper. 2,949,382. USA Patent Office
- [203] DeMatte ML, Kelly ST (1999) Coated paper for inkjet printing. 5,985,424. USA Patent Office
- [204] Kuroyama Y, Ohmura T, Yamazaki Y, Nanri Y (1998) Cast-coated paper for ink jet recording and production method thereof. 5,755,929. USA Patent Office
- [205] Paunonen S (2010) Influence of moisture on the performance of polyethylene coated solid fiberboard and boxes. Dissertation, Norwegian University of Science and Technology, Trondheim
- [206] Hanhijärvi A (2000) Deformation properties of Finnish spruce and pine wood in tangential and radial directions in association to high temperature drying part IV. Modelling. *Holz als Roh- und Werkstoff* 58(4):211–216. doi:10.1007/s001070050415
- [207] Bogren KM, Gamstedt EK, Neagu RC, Akerholm M, Lindstrom M (2006) Dynamic-mechanical properties of wood-fiber reinforced polylactide: experimental characterization and micromechanical modeling. *J Thermoplast Compos Mater* 19(6):613–637. doi:10.1177/0892705706067480
- [208] Muszyński L (2006) Empirical data for modeling: methodological aspects in experimentation involving hygromechanical characteristics of wood. *Dry Technol* 24(9):1115–1120. doi:10.1080/07373930600778254
- [209] Mishnaevsky L Jr, Qing H (2008) Micromechanical modelling of mechanical behaviour and strength of wood: state-of-the-art review. *Comput Mater Sci* 44(2):363–370. doi:10.1016/j.commatsci.2008.03.043
- [210] Ebrahimzadeh PR, McQueen DH (1998) A model of the dynamic mechanical responses of wood, paper and some polymers to moisture changes. *J Mater Sci* 33(5):1201–1209. doi:10.1023/a:1004373525437
- [211] Thuvander F, Kifetew G, Berglund AL (2002) Modeling of cell wall drying stresses in wood. *Wood Sci Technol* 36(3):241–254. doi:10.1007/s00226-001-0134-0
- [212] Marklund E, Varna J (2009) Modeling the effect of helical fiber structure on wood fiber composite elastic properties. *Appl Compos Mater* 16(4):245–262. doi:10.1007/s10443-009-9091-9
- [213] Barber N (1968) A theoretical model of shrinking wood. *Holzforschung Int J Biol Chem Phys Technol Wood* 22(4):97–103
- [214] Almgren KM, Gamstedt EK (2010) Characterization of interfacial stress transfer ability by dynamic mechanical analysis of cellulose fiber based composite materials. *Compos Interfaces* 17(9):845–861. doi:10.1163/092764410x539235
- [215] Yamamoto H, Almèras T (2007) A mathematical verification of the reinforced-matrix hypothesis using the Moritani theory. *J Wood Sci* 53(6):505–509. doi:10.1007/s10086-007-0897-5
- [216] Cristian Neagu R, Kristofer Gamstedt E, Bardage SL, Lindström M (2006) Ultrastructural features affecting mechanical properties of wood fibres. *Wood Mat Sci Eng* 1(3–4):146–170
- [217] Joffe T (2014) Structure and mechanical behaviour of wood-fibre composites. Dissertation, Uppsala University, Uppsala
- [218] Saliklis EP, Kuskowski SJ (1998) Constitutive modeling of paper accounting for rate of load and transient relative humidity effects. *Tappi J* 81(2):181–188
- [219] Lu W, Carlsson L (2001) Influence of viscoelastic behavior on curl of paper. *Mech Time Depend Mater* 5(1):79–100. doi:10.1023/A:1009895419026
- [220] Tjahjanto DD, Giralanda O, Ostlund S (2015) Anisotropic viscoelastic–viscoplastic continuum model for high-density cellulose-based materials. *J Mech Phys Solids* 84:1–20. doi:10.1016/j.jmps.2015.07.002
- [221] Kulachenko A, Gradin P, Koivurova H (2007) Modelling the dynamical behaviour of a paper web. Part I. *Comput Struct* 85(3–4):131–147. doi:10.1016/j.compstruc.2006.09.006
- [222] Rahman AA, Urbanik TJ, Mahamid M (2006) FE analysis of creep and hygroexpansion response of a corrugated fiberboard to a moisture flow: a transient nonlinear analysis. *Wood Fiber Sci* 38(2):268–277

- [223] Kulachenko A, Uesaka T (2012) Direct simulations of fiber network deformation and failure. *Mech Mater* 51:1–14. doi:10.1016/j.mechmat.2012.03.010
- [224] Östlund S, Nygård M (2009) Through-thickness mechanical testing and computational modelling of paper and board for efficient materials design. In: Hannu Paulapuro symposium, March 20, 2009, Esbo, Finland, pp 69–82
- [225] Stååne K (2001) Modelling of stiffness and hygroexpansion of wood fibre composites. Licentiate dissertation, Div of Structural Mechanics, Lund University, Sweden
- [226] Erkkilä A-L (2015) Hygro-elasto-plastic behavior of planar orthotropic material. *Acta Universitatis Lappeenrantaensis*. Dissertation, Lappeenranta University of Technology, Lappeenranta
- [227] Bosco E, Peerlings R, Geers M (2015) Multi-scale modelling of paper hygro-mechanics. Poster. Materials Innovation Institute, Delft
- [228] Stååne K (2008) 3D Homogenisation of hygroscopic anisotropic fibre network composites. Report TVSM-7156, Div of Structural Mechanics, Lund University, Sweden
- [229] Nilsson T (2006) Micro mechanical modelling of natural fibres for composite materials.. Dissertation, Lund University, Lund
- [230] Marklund E (2007) Modeling the mechanical performance of natural fiber composites. Department of Applied Physics and Mechanical Engineering, Division of Polymer Engineering, Luleå University of Technology, Luleå
- [231] Shi SQ, Gardner DJ (2006) Hygroscopic thickness swelling rate of compression molded wood fiberboard and wood fiber/polymer composites. *Compos A Appl Sci Manuf* 37(9):1276–1285. doi:10.1016/j.compositesa.2005.08.015
- [232] Tam J-Q (2002) A state space formalism for anisotropic elasticity. Part I: rectilinear anisotropy. *Int J Solids Struct* 39(20):5143–5155. doi:10.1016/S0020-7683(02)00411-0
- [233] Tam J-Q (2002) A state space formalism for anisotropic elasticity: part II: cylindrical anisotropy. *Int J Solids Struct* 39(20):5157–5172. doi:10.1016/S0020-7683(02)00412-2
- [234] Dano M-L, Bourque J-P (2009) Deformation behaviour of paper and board subjected to moisture diffusion. *Int J Solids Struct* 46(6):1305–1316. doi:10.1016/j.ijsolstr.2008.10.035
- [235] Hämäläinen J, Hämäläinen T, Leppänen T, Niskanen H, Sorvari J (2014) Mathematics in paper—from fiber suspension fluid dynamics to solid state paper mechanics. *J Math Ind*. doi:10.1186/2190-5983-4-14
- [236] Gendron G, Dano ML, Cloutier A (2004) A numerical study of the hygro-mechanical deformation of two card-board layups. *Compos Sci Technol* 64(5):619–627. doi:10.1016/j.compscitech.2003.06.002
- [237] Bortolin G, Gutman PO, Nilsson B (2002) Modeling of out-of-plane hygroinstability of multi-ply paperboard. In: Proceedings of international symposium on mathematical theory of networks and systems, MTNS
- [238] Almgren KM (2010) Wood-fibre composites: stress transfer and hygroexpansion. Dissertation, KTH Royal Institute of Technology in Stockholm, Stockholm
- [239] Xue Y, Wang K (2008) Micromechanical simulations on hygro-mechanical properties of bio-fiber plastic composites. In: MRS proceedings, 2008. Cambridge Univ Press, pp 1097-GG1004-1020
- [240] Joffe T, Wernersson ELG, Miettinen A, Luengo Hendriks CL, Gamstedt EK (2013) Swelling of cellulose fibres in composite materials: constraint effects of the surrounding matrix. *Compos Sci Technol* 74:52–59. doi:10.1016/j.compscitech.2012.10.006
- [241] Marklund E, Varna J, Neagu RC, Gamstedt EK (2008) Stiffness of aligned wood fiber composites: effect of microstructure and phase properties. *J Compos Mater* 42(22):2377–2405. doi:10.1177/0021998308095886

3. Review:

Thickness measurement methods for physical vapor deposited aluminum coatings in packaging applications: A review

Typical systems used to determine the thickness of aluminum on polymer substrates are often based on indirect measurements and are therefore not straight forward to apply for aluminum thickness measurements on paper substrates. Such methods include the use of quartz microbalances (QCM), and the measurement of optical density (OD) or electrical resistance (ER; as the inverse value of conductance). They can be compared to direct measurements using methods such as atomic force microscopy (AFM) for the geometric thickness, and inductively coupled plasma mass spectrometry (ICP-MS) for determining the area density (i.e. mass thickness) by quantitative analysis of dissolved aluminum ions.

Mass thickness is measured in $\mu\text{g}/\text{cm}^2$ and is not altered by the coatings' micro structure or surface morphology. For calculations used to determine mass thickness (based on ICP-MS and QCM), all the aluminum in the sample is assumed to have properties equivalent to bulk aluminum. Defects or irregularities in the atomic lattice, or aluminum converted to aluminum oxide can thus not be detected.

Nanoscale materials can be assumed to show different chemical and mechanical behavior compared to ideal bulk material. These differences can affect the values derived from AFM, OD and ER measurements. Aluminum coatings may not be completely closed due to the presence of pores or defects in the coatings. Those defects may lead to significant variations in AFM readings, and may reduce the OD and increase the ER. This effect is apparent when aluminum coatings on polymer and paper surfaces are compared. This leads to higher sheet resistance. Accordingly, effective resistivities are approximately one order of magnitude higher on paper substrates compared to polymer substrates such as polyethylene terephthalate.

These observations indicate that **(i) the interpretation of measured and derived thickness values is critical, and (ii) electrical resistance and resistivity can be used to detect defects in aluminum coatings.**

Author contributions: Martina Lindner: original manuscript, outline, editing, revision, completion. Markus Schmid: outline, revision, completion, editing.



Review

Thickness Measurement Methods for Physical Vapor Deposited Aluminum Coatings in Packaging Applications: A Review

Martina Lindner ^{1,*} and Markus Schmid ^{1,2}

¹ Fraunhofer-Institute for Process Engineering and Packaging IVV, Giggenhauser Strasse 35, Freising 85354, Germany; markus.schmid@ivv.fraunhofer.de

² Chair for Food Packaging Technology, Technische Universität München, Weihenstephaner Steig 22, Freising 85354, Germany

* Correspondence: martina.lindner@ivv.fraunhofer.de; Tel.: +49-8161-491-536

Academic Editor: Massimo Innocenti

Received: 14 November 2016; Accepted: 27 December 2016; Published: 14 January 2017

Abstract: The production of barrier packaging materials, e.g., for food, by physical vapor deposition (PVD) of inorganic coatings such as aluminum on polymer substrates is an established and well understood functionalization technique today. In order to achieve a sufficient barrier against gases, a coating thickness of approximately 40 nm aluminum is necessary. This review provides a holistic overview of relevant methods commonly used in the packaging industry as well as in packaging research for determining the aluminum coating thickness. The theoretical background, explanation of methods, analysis and effects on measured values, limitations, and resolutions are provided. In industrial applications, quartz micro balances (QCM) and optical density (OD) are commonly used for monitoring thickness homogeneity. Additionally, AFM (atomic force microscopy), electrical conductivity, eddy current measurement, interference, and mass spectrometry (ICP-MS) are presented as more packaging research related methods. This work aims to be used as a guiding handbook regarding the thickness measurement of aluminum coatings for packaging technologists working in the field of metallization.

Keywords: PVD; aluminum; quartz micro balance; optical density; AFM; electrical conductivity; eddy current; interference; ICP-MS; metal coating; nano-scale coatings

1. Introduction

As early as 1994, researchers were looking for the absolute minimum of material usage for disposable packaging, pursuing the need for environmental protection. Additionally, mono materials are preferred due to easier recyclability [1]. However, pure polymeric materials often fail to fulfill the barrier requirements needed to sufficiently protect packed goods, e.g., food against light, moisture, oxygen, and other gases. In contrast to that, aluminum foil with a thickness of about 6 to 40 μm has extremely high barrier properties. Therefore it is predominantly used for the packaging of highly sensitive pharmaceutical products in flexible packaging or blister packs [2,3]. Yet, aluminum has a rather negative environmental impact, which is why we must strive to further reduce its amount [4]. In order to maintain the high barrier properties of aluminum while simultaneously minimizing material usage, nanometer-thin aluminum coatings are applied on polymers via PVD (vacuum evaporation). In this process, aluminum is heated until it evaporates in a vacuum chamber. The polymer substrate is moved across the aluminum gas cloud so that the metal condenses on the polymer surface. In this way, thicknesses of only a few nanometers can be realized. However, in order to reach suitable barrier properties, an approximate thickness of 40 nm of aluminum is commonly necessary. Apart from pure

aluminum, aluminum oxide and silicon oxide are common inorganic coating materials (ceramics). In the following review, we refer to aluminum only. The aluminum coating will be referred to as aluminum or coating. When writing about a single atomistic or molecular layer in the aluminum coating, this is referred to as a layer. The substrate polymer is named a substrate or polymer.

1.1. Deposition Techniques in Packaging Applications

In general, according to Seshan [5], all deposition techniques can be subdivided into evaporative methods (such as vacuum evaporation), glow-discharge processes combined with either sputtering or plasma processes, gas-phase chemical processes with either chemical vapor deposition or thermal forming processes, and liquid phase chemical techniques combined with either electro processes or mechanical techniques. Thin film application techniques are widely used in industries like microelectronics, photovoltaic devices, and optics. Apart from that, especially vacuum evaporation is used in the packaging industry. However, other methods find their way into the packaging market, such as CVD (chemical vapor deposition), PECVD (plasma-enhanced chemical vapor deposition), ALD (atomic layer deposition), magnetron sputtering and sol-gel coating. Apart from financial and production speed considerations, the decisive factor for choosing one of the methods will be the required characteristics of the coating. The most important task of the coating in the packaging industry is to achieve a suitable barrier against gases. Thus, the coating must be pure and not contain cracks or pores [5]. In the following, vacuum deposition and other coating methods that appear in the packaging industry are described.

During vacuum deposition, commonly only one inorganic material can be deposited. This happens by heating the coating material and the subsequent condensation on the substrate surface. However, if alloys are used, the heating of the target material might lead to a disintegration of the compound. Moreover, undercuts and roughness are difficult to coat. Furthermore, the process requires high-performance cooling and vacuum systems. The vacuum deposition process has the advantage that due to the vacuum the energy to melt the material is reduced, and furthermore, the incorporation of gaseous atoms into the coating is drastically reduced. The deposition rate is highly dependent on the gas pressure in the chamber. The flux distribution can be altered by the source geometry. In comparison to other methods, high deposition rates and extremely pure coatings can be obtained [6].

Sputtering is a process sometimes used in packaging applications, in which atoms from the target are attacked by accelerated ions, which transfer their momentum to the targeted atoms. Thus the targeted atoms are knocked out from the bulk, leave it in a cosine distribution, and then hit the substrate surface and adhere there. The magnetron sputtering technique has the advantage, that secondary electrons generated in the target are trapped so that they cannot hit the substrate surface. Sputtering has a high amount of materials usable for deposition and typically the coating has the same composition as the target material. However, if reactive gases are present in the chamber, they can react with the target and alter the composition. Moreover, the particles have a higher kinetic energy compared to thermally vaporized atoms. It is possible that temperature-sensitive substrates can be coated without excessive temperature impact [6].

In contrast to that, CVD offers the opportunity to introduce precursors into the process chamber, which then react with the metal to form, e.g., metal oxides, nitrides, carbides, borides and others. However, in this process, volatile and partially toxic gases may be produced, which have to be handled separately. At the same time, powerful vacuum pumps are not necessary like in vacuum deposition. As the impacting molecules or atoms have a high kinetic energy, this process might lead to an increase in the substrate temperature. Moreover, the interaction with precursor atoms may lead to a scattering of the evaporated atoms. This in turn can lead to a roughening of the surface, the penetration of atoms or molecules into the material, pinholes and chemical reactions with the rest gases. However, the achieved thicknesses can be up to centimeter scales. As the coating is not limited to line-of-sight areas, the process has the advantage that three dimensional structures, voids, and peaks can also be covered evenly [7].

ALD is a layer-by-layer process in which only one monomolecular layer is applied in each production cycle. It is based on alternate pulsing of the precursor gases onto the substrate surface, followed by the chemisorption or surface reaction [8]. The advantage is that the produced layers are perfectly dense and free of pinholes. Therefore, they offer extremely low gas permeabilities. Moreover, temperature and pressure conditions are less intense than in vacuum deposition [9]. Although lately a continuous operation mode was developed, the production speed is rather low and therefore costly.

One example for liquid phase chemical techniques in packaging applications is Ormocer[®], i.e., organically modified ceramics [10]. Those are applied via a sol-gel process in order to achieve a nanometer thin coating [11,12]. The very basic form of a sol-gel process is the draining and evaporation of the solvent, followed by condensation reactions [13]. This coating leads to smoothening of the surface of polymers. Like this, the negative impact of surface inhomogeneities on barrier performance can be reduced [14]. The advantage in comparison to other processes is the lower amount of required equipment and lower costs. Moreover similar to CVD it provides the possibility to tailor the microstructure of the coating [13].

1.2. Application of Aluminum via Vacuum Evaporation and Layer Growth

Physical vapor deposition is not only used for packaging materials, but also e.g., for capacitor films, holographic coatings, transparent conducting oxides, energy conservation windows, solar cells and absorbers, flexible circuits, or thin film batteries [15]. The basic construction for a vacuum evaporation deposition chamber is illustrated in Figure 1. The chamber is divided into two parts, where chamber (A) includes the unwinding (C) and rewinding (D) of the substrate web and holds a low pressure of about 1×10^{-3} mbar. The lower part (B) is set under a vacuum of about 1×10^{-5} mbar. There are lots of data available about aluminum vapor pressure curves, onset, offset and melting temperature as values change a lot depending on the exact metal composition [16]. However, it can be said that the vacuum reduces the evaporation temperature of aluminum from approximately 2742 °C at 1013 mbar to 813 °C at 1×10^{-5} mbar [17,18]. Moreover the vacuum avoids the scattering of aluminum atoms and their reaction with other gas atoms or molecules (e.g., with oxygen to aluminum oxide). The chilled process roll (I) together with the conductance rolls (E) separate the chamber into (A) and (B), leaving a small opening for the substrate to pass from one zone to the other. The process roll (I) is positioned above the evaporator (F). Two main principles are available for evaporation. The aluminum could either be fed as a wire onto a resistance heated boat, from where it evaporates. Otherwise the aluminum could be fed as granulate in a target and then be heated via an electron beam. In each case the aluminum evaporates and condenses on the surface of the substrate web, which is moved across the process roll (I). The thickness of the aluminum can be adjusted by the web speed or the evaporation rate. The evaporation rate is regulated via the energy input in the evaporator in combination and/or the speed of aluminum feed. The thickness is commonly monitored either by a quartz micro balance (QMB) right at the place of evaporation (G) or by the measurement of optical density (H) before rewinding [15].

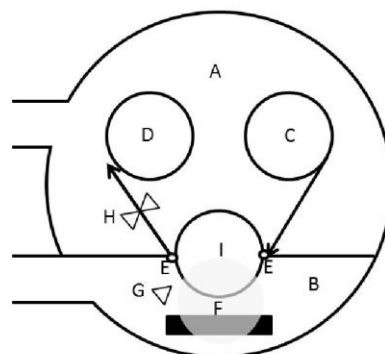


Figure 1. Basic construction of a vacuum deposition chamber (adapted from [1]).

The growing of condensed atoms to a closed coating and the developing micro structure are dependent on various parameters. The kind of substrate as well as its orientation, evaporation temperature and rate play an important role. Coating thickness, angle of deposition and the energy of condensed atoms or molecules also affect the material structure [19]. Apart from that, the substrate has a major effect on the formation of the coating. In case dust is present on the polymer surface, these particles might be coated with aluminum but then fall off after deposition. In this case, the particle leaves behind a non-coated pinhole, which reduces the gas barrier. One other issue is the substrate roughness. According to [15] and others, valleys in the surface will lead to preferential nucleation and epitaxy as these valleys are energetically favorable for aluminum atoms. Consequently, layer growth is not evenly distributed but rather inhomogeneous. One technique to overcome this problem is the biaxial orientation of polymeric substrates, which leads to the reduction of surface roughness due to the stretching and smoothening of polymeric chains for PET [20]. Generally it is assumed that by stretching the polymer chains align, so that the crystallinity of the material increases and the surface is smoothened [21]. Conversely, a roughening effect due to stretching was reported in [22]. The negative effect of substrate roughness on the gas barrier of inorganic coatings is described in [23,24]. Moreover, the attachment of atoms on the polymer surface depends on the surface tension of the substrate. Surface tension can be increased by plasma treatment, by which e.g., carbonyl, carboxyl, hydroxyl, peroxide, and other groups are introduced onto the polymer surface. There is a tendency that with higher surface tension, more atoms attach on the surface and thus increase the barrier [24]. Additionally, it was reported that plasma treatments can simultaneously alter the surface geometry, as low weight molecules migrate to the charged areas on the surface and consequently built peaks [25].

Layer growth starts with the first nuclei of condensed atoms, which define the subsequent layer structure. The arriving atoms can either deflect from the substrate or lose enough kinetic energy that they are loosely bound as adatoms on the surface. Those adatoms predominantly bind to existing material clusters or to other energetically favorable places. Those could be steps, edges or cavities in the surface topography. If the residual energy is high enough, the atoms further diffuse on the substrate surface. Like this, single adatoms can form stable or metal stable clusters [26,27].

Generally, three models are described, which cover a variety of possible interactions between substrate and adatoms of which model in Figure 2a,c are the two extremes and Figure 2b is a combination of both [26–29]. In the model of Frank van der Merwe (Figure 2a), the cohesion between the adatoms is weaker than the binding to the substrate. Then, a monolayer grows, which is first fully closed, before the next layers start to grow. In comparison to that, the Stranski-Krastanov model (Figure 2b) introduces the idea that first single layers grow like in (Figure 2a), on which islands then start to appear. The Volmer-Weber model (Figure 2c) goes to the other extreme and assumes that the interactions between adatoms are stronger than the interaction with the substrate. After the nucleation of small clusters, these grow to small three-dimensional islands. Only at high layer thicknesses can closed coating be achieved [29–32].

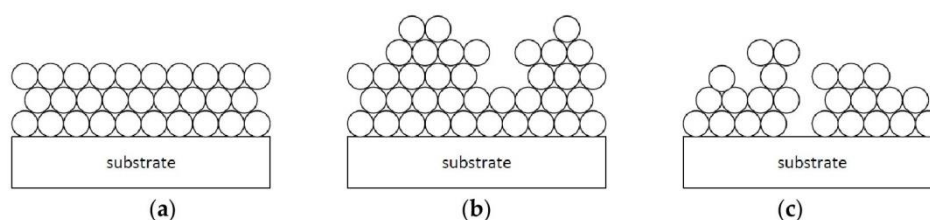


Figure 2. Models for layer growth: Frank van der Merwe (a); Stranski-Krastanov (b); Volmer-Weber (c) (adapted from [1,15]).

1.3. Pores and Defects

Normally, metals have a crystalline structure, i.e., a strictly periodical arrangement of atoms. Therefore, Bravais [33] introduced the concept of a space lattice, which equals a three-dimensional mathematical point pattern. Herein, each point can be imagined as the center of an atom. Metallic elements mostly crystallize in three lattice types [34]: cubic body centered, cubic face centered, and hexagonal. Aluminum typically crystallizes in a cubic face centered manner [35]. However, crystalline structures are never free of defects. Defects are subdivided into (i) blank spaces and interstitials; (ii) displacements; (iii) grain and phase limits [34,36] and can affect physical properties like barrier towards gases, electrical conductivity, and optical density.

Apart from the defects due to the lattice, additional macroscopic defects might appear due to contamination with dust prior to the deposition process. These dust particles might stick on the substrate surface, are then covered with aluminum and fall off the substrate afterwards as they are only loosely bound. In such a case, this leaves behind a defect in the coating. Additionally some films contain so-called anti-block particles on one side of the film. When the material is winded, the backside of the film touches the front side of the film. Consequently, the anti-block particles can injure the inorganic nano-scale aluminum coating [37].

1.4. Formation of Aluminum Oxide

Aluminum is a reactive metal that easily oxidizes when it is taken out of the vacuum chamber and set under atmospheric conditions. Hence it builds up a stable oxide layer that has an amorphous structure and protects the underlying metal from further corrosion and oxidation. Then the oxide layer is hydrated to aluminum oxide hydroxide or aluminum hydroxide [38,39]. The oxide layer has a thickness of 3 to 10 nm [39–42]. In [42] it was observed, that the oxide layer grows not only on the outer surface but also between the aluminum and the substrate web.

1.5. Permeation through Organic Substrates and Inorganic Coatings

A barrier is defined as the resistance against permeation, i.e., against the mass transfer of gaseous substances through a solid body. The process of permeation involves four main stages: adsorption, absorption, diffusion and desorption [43]. In the first step the molecules are adsorbed onto the substrate surface of the solid material and build up a thin molecule layer by adhesive power. Then, permeating molecules are absorbed and transported through the polymer. The permeation coefficient (P) of molecules is determined by two factors, (S) and (D) (Equation (3)). The solubility coefficient (S) describes the concentration (c) of dissolved molecules in the polymer in dependence of the partial pressure (p) (Equation (1)). The diffusion coefficient (D) describes how fast molecules permeate along the concentration gradient (Δc) using intermolecular and intramolecular spaces until a solution equilibrium is established. The diffusion flux (J) of molecules permeating through a homogenous polymer over a certain distance (Δd) along the concentration gradient is explained by Fick's first law of diffusion (Equation (2)). Finally molecules are desorbed from the polymer surface and evaporated or removed by other mechanisms. The overall permeability of a polymer (Q_{poly}) is then described by the permeation coefficient (P) and the thickness of the material (d) (Equation (4)).

$$c = S \times p \quad (1)$$

$$J = -D \times \frac{\Delta c}{\Delta d} \quad (2)$$

$$P = D \times S \quad (3)$$

$$Q_{\text{poly}} = \frac{P}{d} \quad (4)$$

The barrier of inorganic coatings is subjected to its chemical composition, the microstructure and homogeneity [19,26]. Although a thin evaporated inorganic coating clearly improves the barrier

properties of polymer substrates, it still shows a permeability that is several magnitudes higher than it would be for a perfectly crystalline material. This can be partially explained by the layer growth and the connected degree of imperfection. Moreover, contamination during the evaporation by other gases or dust, anti-block particles in the substrate, as well as mechanical tensions between the substrate and the inorganic coating play an important role. All these factors may lead to cracks or pores in the coating and thus increase the gas transmission of the polymer and coating ($Q_{\text{poly+coat}}$) [44,45]. In relation to the pore size, different mechanisms for permeation are presented in [46]. Nevertheless, the diffusion through macroscopic defects (100 nm) plays a major role [47]. Given such macroscopic defects, permeation continues as if there was no inorganic coating. According to the current state of the art, a completely defect free inorganic coating cannot be produced by vacuum deposition [48]. However, the determination of the amount and size of pores is rather complex and time-consuming. This is why the barrier improvement factor (*BIF*) is commonly used to describe the quality of the inorganic coating. This value sets into relation the permeabilities of the polymer with ($Q_{\text{poly+coat}}$) and without (Q_{poly}) the inorganic coating. It is affected by the amount and size of defects as well as the thickness of the underlying polymer substrate:

$$BIF = \frac{Q_{\text{poly}}}{Q_{\text{poly+coat}}} \quad (5)$$

Herein, the permeability of the polymer with inorganic coating ($Q_{\text{poly+coat}}$), actually consists of the transmission through all defects, assuming that the rest of the surface does not let pass any gas. Trying to describe the permeation through these defects, various models were developed. The first models were created by Prins and Hermans [44], based on which further ideas were presented by e.g., [49–53]. For technically relevant substrate thicknesses and defect sizes, the models can be rewritten approximately as in Equation (6). Herein it is visible, that the transmission $Q_{\text{poly+coat}}$ does not depend on the substrate thickness (within the range of validity), but only on the permeability coefficient (P) of the material, the amount of the defects per area (n_d) and the effective average of defect area (a) [37]:

$$Q_{\text{poly+coat}} \approx 2 \times P \times n_d \times \sqrt{a} \quad (6)$$

1.6. Importance of Coating Thickness for Barrier Properties

The thickness and consistency of nanodeposited layers (nanocoatings) have a high impact on their performance [54]. Several studies [37,50,55] showed that the permeability $Q_{\text{poly+coat}}$ negatively correlates with the increasing thickness of the inorganic coating until a certain point. Then, even for higher thicknesses, $Q_{\text{poly+coat}}$ stays almost constant. In [37] it was shown that only for thicknesses that are one to three magnitudes higher the permeability further decreases. It was concluded, that the idea of Volmer-Weber growth helps us to understand the steady decrease of permeability for low coating thicknesses. Nonetheless, the few existing investigations that have been made to analyze the coating structure rather indicate a Frank-van-der-Merwe growth.

Figure 2 raised the question of how the thickness of an inorganic coating should be defined. Does “thickness” take blank spaces or defects into account or not? Is “thickness” an average value over a broader surface or is it measured at a certain distinct point? Does “thickness” include aluminum oxide or only pure aluminum? Accordingly, when having a look at various publications [37,39,42,56–60], the thickness is measured by numerous different methods. Because the thickness of these aluminum coatings is much shorter than the wavelength of visible light, traditional microscopy is not usable for this application.

As stated by Mattox [61], these methods can be subdivided into mass, geometrical, and property thicknesses. Mass thickness is measured in $\mu\text{g}/\text{cm}^2$ (e.g., by mass spectroscopy) but does not take into account the density, micro structure, composition, or surface morphology. In contrast, the geometrical thickness is measured in μm , nm , or Å (e.g., AFM, profilometry). This value is affected by the surface morphology (e.g., roughness). Just like the mass thickness, geometrical thickness does not consider

composition, thickness, or microstructure. By measuring property thicknesses, a physical value is obtained (e.g., electrical resistance, optical density, interference) which is then mathematically related to the coating thickness (see Figure 3).

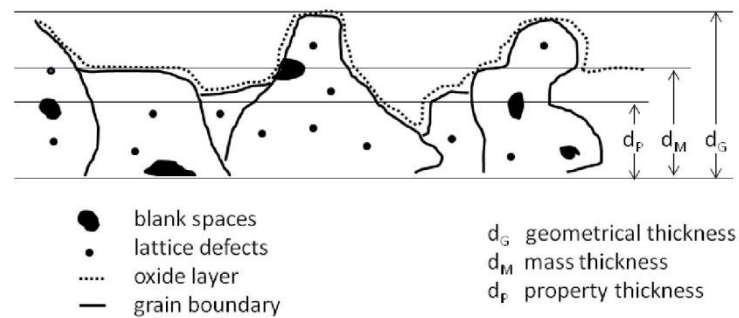


Figure 3. Mass, geometrical, and property thickness.

In the following sections, the quartz micro balance (QMB), mass spectroscopy (ICP-MS), atomic force microscopy (AFM), optical density (OD), interference, electrical surface resistance and eddy current measurements are presented as examples for the methods explained above.

For each technique the theoretical background, the method, and the analyses are explained. Limitations and especially parameters affecting the measured values are highlighted. Yet, especially concerning limitation values, equipment specifications will give more specialized information to the user. This work aims to be used as a guiding handbook for packaging technologists working in the field of metallization. For more detailed information, literature hints are provided for the interested reader.

2. Characterization Techniques

2.1. Mass Thickness

There are various measurement techniques available today, for determining mass thickness, such as X-ray fluorescence, ion probe, radioactivation analysis, chemical balance, micro balance, or torsional balance [62]. However, the most common method in the field of PVD is the quartz crystal micro balance (QCM), with which the evaporation rate is usually monitored [63]. Taking into account the coating speed and geometrical constraints under which the QCM, the evaporation source and the substrate are arranged, the coating thickness can be calculated in g/m^2 . The second method presented here is the analyses via ICP-MS, which is a certain kind of mass spectrometry. This, of course, can only be used when the sample is inserted as a liquid. Therefore, the evaporated aluminum needs to be dissolved from the substrate of distinct area before the amount of aluminum in the sample can be determined.

2.1.1. QCM

QCM: Theory

When alternating current (AC) is applied on to the gold electrodes, which are evaporated on a piezoelectric quartz crystal, the crystal starts to oscillate in its resonance frequency (see Figure 4). A quartz with a thickness of 3.317×10^{-4} has a resonance frequency of 5 MHz [64]. For doing so, the crystal needs ideally to be cut from a mono crystal at an angle of 35.1° toward the optical axis, so that it oscillates in thickness shear mode. The frequency of this oscillation depends on the geometry of the crystal and therefore drops when the thickness increases [65,66]. By monitoring the change

in frequency and relating it to the deposited mass, this effect is used to gain information about the amount of aluminum that is evaporated on the QCM [67].

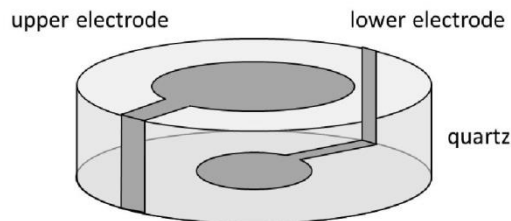


Figure 4. Typical QCM geometry, diameter ca. 10–30 mm, thickness ca. 0.3 mm (adapted from [64]).

The relation between frequency and mass is based on physical principles, as explained in the following. Commonly, the software will use mathematics to export data about the thickness.

Under the assumption, that the evaporated material (aluminum) behaves similar to the quartz and that the evaporated mass is small in comparison to the quartz (about 2%), the resonance frequency changes linearly with the mass increase. Resonance appears, when the thickness of the quartz (d) is half of the transversal wavelength (λ) (Equation (7)). The speed of sound (v_s) in quartz is a constant and dictates possible wavelengths (λ) and frequencies (f) (Equation (8)). Consequently, (d) and (f) always have the same proportion, as (v_s) is constant (Equation (9)). When the evaporated material arrives on the surface, the thickness and mass increase. Therefore, Sauerbrey [68] introduced the mass density (M_E) for the evaporated material and for the quartz material (M_Q) which is defined by the thickness (d) and density (δ) as in Equations (10) and (11). Accordingly, when the thickness (d) increases, also the mass density (M_E) increases. Consequently, the change in frequency (Δf) is related to the mass density (M_E) as in Equation (12). By combining Equations (8), (11) and (12), Equation (13) can be derived and it becomes obvious, that (Δf) directly relates to the mass density of aluminum (M_E), as (v_s), (δ_Q) and (f) are constant. This correlation was first mentioned by Sauerbrey [68] and is therefore denoted as the Sauerbrey-equation [66]. For further improvement of the mathematical model, the impedance values for each plane can be introduced when modeling them as coupled resonators from two planes. A precise overview is given in [65].

$$d = \frac{\lambda}{2} \quad (7)$$

$$v_s = \lambda \times f \quad (8)$$

$$\frac{\Delta d}{d} = -\frac{\Delta f}{f} \quad (9)$$

$$M_E = d_E \times \delta_E \quad (10)$$

$$M_Q = d_Q \times \delta_Q \quad (11)$$

$$\Delta f = -f \times \frac{\Delta M_E}{M_Q} \quad (12)$$

$$\Delta f = -2f^2 \times \frac{M_E}{\delta_Q \times v_s} \quad (13)$$

QCM: Method

The QCM is commonly integrated in the machine at some point close to the evaporation source and the process roll. It has to be taken into account, that at the place where the aluminum is deposited on the QCM, there is a shadowing effect so the aluminum will not reach the substrate surface. Additionally, the angle (α) and distance towards the evaporation source should be taken into account, as this might alter the measured results (see Figure 5).

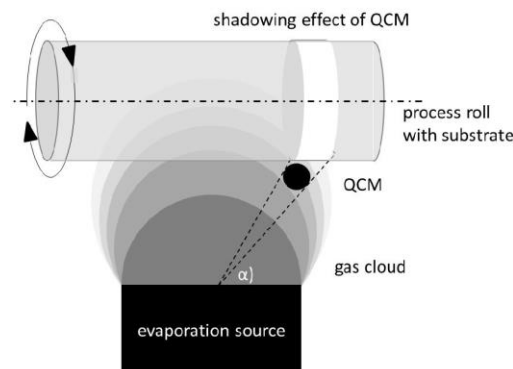


Figure 5. Arrangement of a QCM in the vacuum deposition unit.

QCM: Practical Aspects and Analyses

The software commonly needs the material density as input and its output will commonly be the deposition rate in $\text{\AA}/\text{s}$. The accuracy is about 2%. The accuracy decreases with increasing thickness, which is why there are a few methods to reduce this effect. One option is to use a shutter, which only lets aluminum pass on the QCM in a certain frequency. Or a filter could be used, which only lets a certain number of atoms pass through to the QCM. Like this, the actually arriving amount of aluminum can be extrapolated, while at the same time the layer thickness on the QCM is reduced. Of course, this will reduce the accuracy of the QCM [15,67,69]. It has to be taken into account that the value obtained is the deposition rate and has the unit $\text{\AA}/\text{s}$. The faster the material moves, the lower the coating thickness will be. The coating thickness (t) can be approximated by the following Equation (14), taking into account the deposition rate (x), the web speed (w) and the shutter width (y):

$$t = x \times \frac{w}{v} \quad (14)$$

2.1.2. ICP-MS

ICP-MS: Theory

ICP-MS (inductively coupled plasma mass spectrometry) is based on the chemical dissolution of the aluminum and the subsequent measurement of the concentration of aluminum in the dissolution. There are quite a few different ICP methods available for detecting unknown substances. The major concurring method that needs to be mentioned is ICP-OES (inductively coupled plasma optical emission spectrometry), in which electrons are excited, and the photons that are emitted when the electrons fall back to their ground state, are detected. In comparison, in ICP-MS, the plasma is used to ionize atoms and the ion charge is used to detect them. However, even for ICP-MS there are various equipment designs available today, of which three are outlined. An extensive overview is given in [70].

The ICP-MS basically consists of three main parts: the probe- and plasma unit, the cones, and the mass spectrometer. Firstly, the liquid probe is conveyed over the pump and the vaporizer into the spray chamber. The small droplets are then transferred into the plasma unit. The plasma unit involves an induction coil that produces a high-frequency electromagnetic field. Argon is inserted in this field and becomes plasma, which is "seeded" with electrons [70]. When the small gas droplets reach the plasma, they are dried, decomposed, atomized and ionized. Afterwards, the positively charged ions pass through two concentric quartz cylinders (sampling cone, skimmer cone) where non-ionized atoms are excluded. The cones also lead to a focusing of the ion beam (Figure 6).

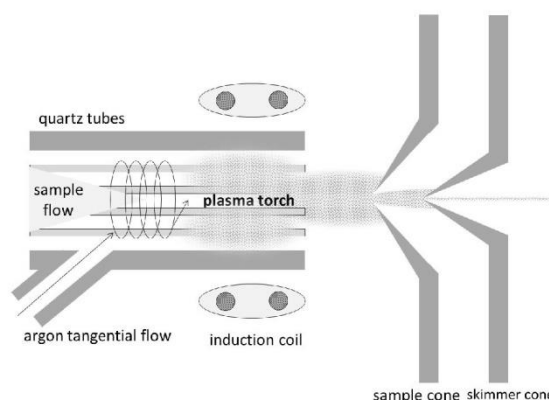


Figure 6. Plasma unit and torch in ICP-MS (adapted from [70–72]).

In a mass spectrometer, three basic principles are used, namely quadrupole filters, magnetic analyzers, and time-of-flight analyzers. In the first case, the ions pass a quadrupole or even octopole reaction system. This element consists of four or eight dipoles with opposite directions. On the opposing dipoles, a combination of DC and AC potentials is applied. A positively charged ion will be torn towards the negatively charged rod and discharged, unless the voltage changes before the collision. When the voltage changes before collision, the ion changes its direction. Like this, depending on their mass to charge ratio (m/z) ions start to oscillate and can only pass the quadrupole if they have a distinct m/z -value for a given frequency (Figure 7) [65,71]. All other ions will impact on the surface of the quadrupole or the sled wall and are discharged. Within one measurement, typically one mass is detected after another. Additionally, a helium collision mode is available. In this mode, helium is inserted in the quadrupole and leads to collisions with the sample ions. As molecular ions have bigger dimensions, they tend to collide more often with helium atoms and consequently lose kinetic energy (KED, kinetic energy discrimination). Like this, they are rather easily torn towards the quadrupole rods and can be excluded more easily while passing the magnetic field.

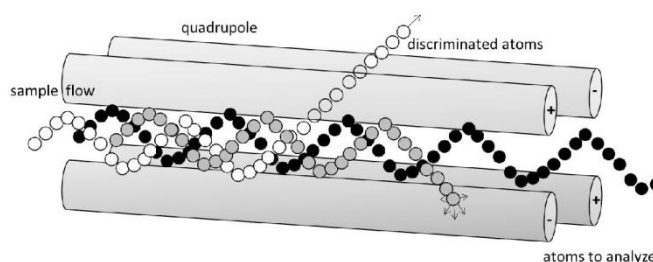


Figure 7. Quadrupole filter (adapted from [70–72]).

In a magnetic analyzer, the ions pass an electric field. When a particle, charged with the load (q) (Equation (15)) is accelerated in an electric field, its kinetic energy (E_k) and velocity (v) depend on the voltage (U) (Equation (16)). When this accelerated ion passes a magnetic field that is perpendicular to the trajectory, it is deflected and follows a circular path (Figure 8), on which the centrifugal force equals the magnetic force (Equation (17)). The magnetic force is defined by the magnetic field strength (B). By combining Equations (16) and (17), Equation (18) is deduced. It becomes obvious, that the radius (r) is related to the m/z -ratio and that by a local dissolution of impinging ions on the detector, the abundance of each m/z -specie can be observed [73].

$$q = z \times e \tag{15}$$

$$E_k = \frac{m \times v^2}{2} = q \times U \quad (16)$$

$$q \times v \times B = m \times \frac{v^2}{r} \quad (17)$$

$$r = \frac{\sqrt{2 \times m \times E_k}}{q \times B} \quad (18)$$

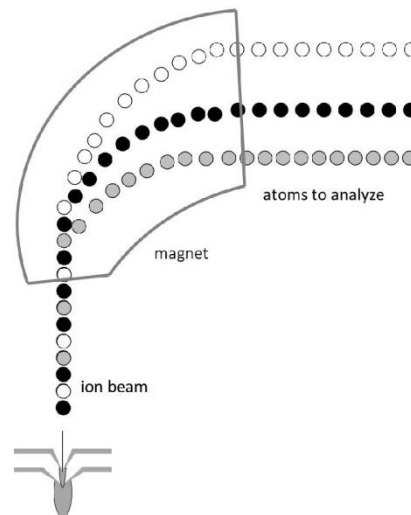


Figure 8. Magnetic analyzer (adapted from [70]).

In a time-of-flight measurement the ions are first accelerated in an electric field and then enter a field free region (Figure 9). As already revealed in Equation (16), the speed at the end of the electric field depends on the mass (m) and charge (q). As all ions have the same charge, the speed (v) is defined by the mass (m). For then passing a certain distance (L), the ions will need the time (t) at a given velocity (v) (Equation (19)). By combining Equations (15), (16) and (19), the time of flight (t) can be used to calculate the m/z -ratio of ions, when (L) and (U) are kept constant (Equation (20)) [71]. An overview of interferences between atoms with the same m/z -ratio is given in [74].

$$L = v \times t \quad (19)$$

$$t^2 = \frac{m \times L^2}{z \times e \times 2 \times U} \quad (20)$$

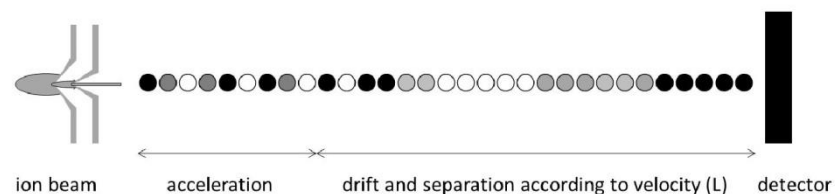


Figure 9. Time of flight measurement (adapted from [70]).

After the mass spectrometer, the ions need to be detected and quantified. As detection systems, three main working functions are available. Either the charge is directly measured (Faraday cup),

or the kinetic energy transfer (which depends on the mass and velocity of the ions) leads to secondary electrons which are detected. In each case, the impacting ions lead to an electric current that is proportional to the amount of ions that are counted per second. Correspondingly, the resulting value is CPS (count per second) [71].

A quantitative identification of atoms in a probe is possible by standard dissolutions, as there is a linear relationship between the signal intensities of the ions (counts per second, CPS) and the concentration of the element [72,73].

ICP-MS: Method

For calibration, an aluminum standard dissolution is used. This should be diluted with double distilled water to concentrations of, e.g., 0.25, 0.50, 1.00, 1.50, 2.00, and 3.00 mg/L aluminum. The software automatically calculates the counts per second (CPS), which is associated with the relating dilution and draws a standard graph (Figure 10).

For the analysis of the aluminum content of the samples, those should be cut to a defined surface (A), e.g., 10 cm². In the next step, the aluminum of each sample is dissolved by a defined factor (f_1) in 1 molar NaOH, e.g., 50 mL. After dissolving the aluminum for a certain time, the sample can again be diluted with double-distilled water by a factor (f_2). The concentration (c) in µg/L of this double diluted sample is then analyzed in the ICP-MS as counts per second (CPS) and then related to the concentration by the standard graph.

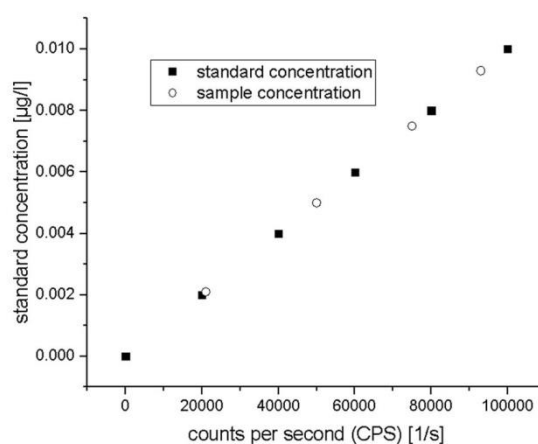


Figure 10. Example of a standard graph for correlation of CPS and standard concentrations.

In order to reach trustworthy results, the following needs are formulated in [70]:

- Complete dissolution;
- Highly pure reagents;
- No chemical interaction between equipment and reagents;
- No loss of analyte.

When it comes to the interpretation of the measured values, it needs to be considered that this value is related to a certain area of the tested material. Whereas the thickness determined via QCM is only valid for a certain location in relation to the evaporation source, the thickness determined via ICP-MS is more of an average value for a whole area. When the measurement area is taken from the same place, where the QCM is usually measuring, the values should be comparable. However, it cannot be compared to, e.g., the area right above the evaporation source, as the thickness will be higher there due to the cosine distribution.

ICP-MS: Practical Aspects and Analyses

Under consideration of the dilution factor (b_1) and (b_2), the sample surface (a_s) and the theoretical density (δ) of aluminum, the thickness (d) of the evaporated coating can be calculated according to Equation (21).

$$d = \frac{c \times b_1 \times b_2}{a_s \times \delta} \quad (21)$$

When using this value, it should be considered that this method determines all the aluminum in the sample: aluminum existing as oxide as well as the pure metal, which might explain the deviations from other methods [42]. Additionally, interferences between atoms with the same m/z -ratio might alter the results. An overview of those is given in [74]. Limits of detectable concentrations (c) for diverse elements are given in [71] and range from 0.001 to $>10 \mu\text{g/L}$. For aluminum, the range is 0.001–0.1 $\mu\text{g/L}$. This range can further be exploited by increasing or decreasing the dilution factors (b_1) and (b_2) or sample surface (a_s), as given in Equation (21).

2.2. Geometrical Thickness: AFM

AFM is a contact profilometry method. In contrast to contact profilometry, non-contact profilometry uses electrons or photons for scanning the surface and gathering information about the depth profile. Contact profilometry methods are mechanical stylus profilometers, AFM and STM (scanning tunneling microscopy). In the latter, a cantilever is brought in such a short distance to the surface, that electrons start to tunnel and the current is measurable. As the current is then proportional to the distance, a surface topography image can be obtained. The AFM is based on a mechanical scanning of surfaces with the help of a cantilever with a sharp probe on top. This probe is moved across the surface line by line. In consonance with the surface topography, the cantilever is deflected and the extent of bending can be measured with capacitive or optical sensors. This information is translated into a surface topography image.

2.2.1. AFM

AFM: Theory

When the probe approaches the surface, depending on the distance, different interaction forces superimpose. Van-der-Waals forces which are indirect proportional to $-(r^6)$, appear due to charge transfer and act attractive. At smaller distances, orbital overlaps produce repulsive forces. They are indirect proportional to r^{12} . When superimposing both potentials, the resulting Lenard-Jones-potential shows the dependency of attractive and repulsive forces of the distance between probe and surface (Figure 11). As the probe approaches the surface, the cantilever ideally shows no bending. Then a “snap in” occurs, when attractive forces start to dominate. At this point, the probe starts to touch the surface. When the cantilever is further pressed against the surface, it is deflected and the repulsive forces dominate. Due to this effect, not only the imaging of topography but even the resolution of single atom orbitals is possible. For operating the AFM two different procedures are possible, one of which is in the field of “attractive forces” and the other one in the area of “repulsive” forces [75].

AFM: Method

Basically, three different modes are available for AFM measurements: contact mode, non-contact mode, and intermitting mode. In the contact mode with constant height, the probe is moved so close to the surface that it is bent. According to the extent of bending (repulsive forces), the surface topography is imaged. However, in this mode, the surface and probe might be injured and hence the nature of the surface might affect the results.

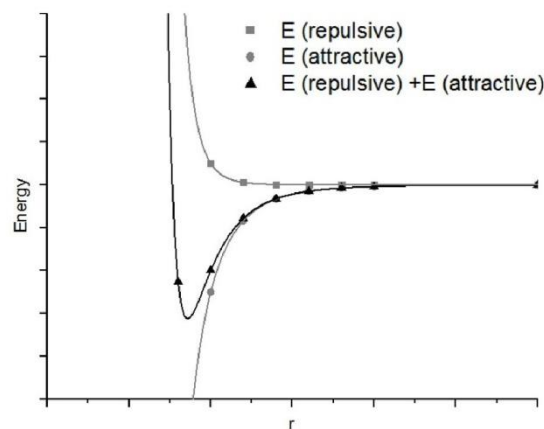


Figure 11. Lennard Jones potential (adapted from [76]).

In the contact mode with constant force, the deflection of the cantilever is adjusted permanently to a set point that is especially useful for soft matter. In order to optimize the outcome, the set point needs to be adjusted in dependence of the cantilever stiffness and the surface nature. Information about the topography can then be extracted from the adjusted height of the cantilever. The advantages of this mode are the high resolution and that the probe and surface are protected.

In the non-contact mode, the cantilever oscillates at its resonant frequency. As the cantilever comes near the surface, it interacts with the force field (attractive forces), which quenches the oscillation and affects frequency and amplitude. Based on the phase and amplitude shift, information about the surface topography is deduced.

In the intermittent mode, the cantilever oscillates just like in the non-contact mode. Still, the distance between probe and surface is continuously adjusted to a constant level by keeping the interaction steady [75]. The advantage is that, apart from topography, stiffness and adhesion can also be determined by separately capturing attractive and repulsive forces [77]. As stated by Eaton and West [75], more than 20 different modes of AFM are available today. Therefore only the basic principles are outlined in this review.

All modes use the same basic function, as explained in the following. The surface of the sample is scanned line by line. Therefore, either the sample or the cantilever can be moved. As described before, based on the interaction between cantilever and sample surface the cantilever is deflected vertically. While the probe moves across the surface, the bending of the cantilever is measured by optical sensors (Figure 12). In this optical sensor a laser beam impinges on the backside of the reflective cantilever and the movement of the reflected light spot is measured by a photodetector. Thus when the probe touches the surface, the light spot moves and the feedback control reacts by increasing the voltage output. Following the increase of voltage, a piezoelectric device will expand and lets the probe move away from the surface (approximately 0.1 nm per applied volt). The voltage used to move the piezo element in the z-direction is monitored and the height topography can be imaged accordingly [75,77,78].

The resolution power of the AFM is limited by the geometry of the cantilever. Due to the respective geometries there is a real and an imaginary point of contact between probe and surface during scanning. Mathematically speaking, the measurement is a convolution between probe geometry and the surface (Figure 13). Consequently, elevations are depicted larger (Figure 13c,d) and indentations are represented smaller (Figure 13a,b) than they really are. Thus the geometry of the probe is critical to the quality of the images measured with an AFM [75].

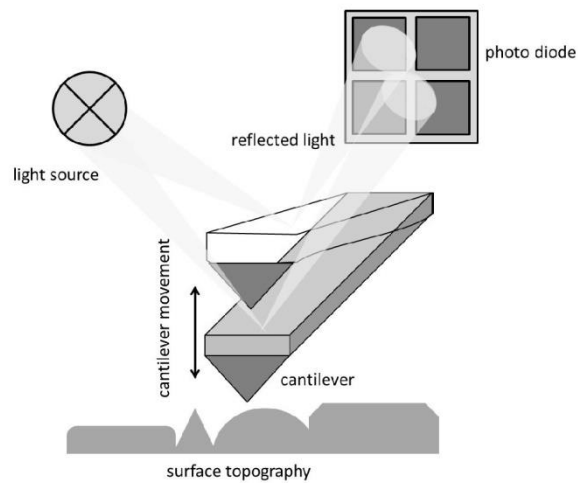


Figure 12. AFM equipment (adapted from [77]).

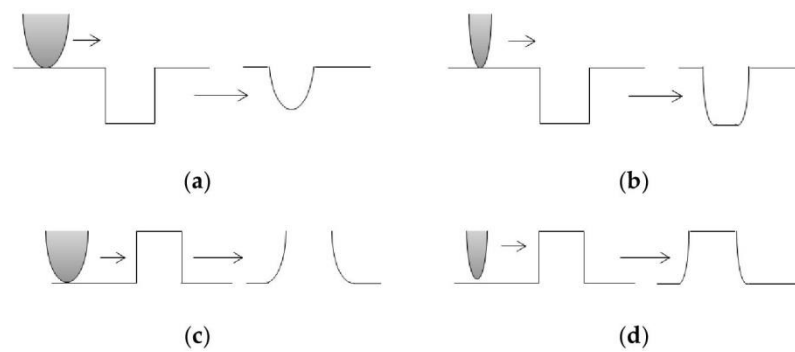


Figure 13. AFM operation (adapted from [75]) (a,b) smaller representation of indentations and (c,d) larger representation of elevations.

The cantilever with the nm-scale probe on top is usually produced by MEMS (Micro-Electro-Mechanical Systems) technology. The materials used are commonly Si_3N_4 or Si which show a diamond-like structure. Whereas SiN_4 cantilevers tend to bend due to residual stress, Si probes have a tendency to chip while contacting the surface [75].

For measuring the thickness of evaporated aluminum, an adhesion tape needs to be applied on the surface before evaporation (Figure 14). Afterwards, the adhesion tape is removed and a clear edge between the aluminum coated surface and the area, that was covered by the adhesive tape, appears. In this area, the measurements can be done by AFM. The measurement area can be adjusted between a few μm to up to $100 \mu\text{m} \times 100 \mu\text{m}$.

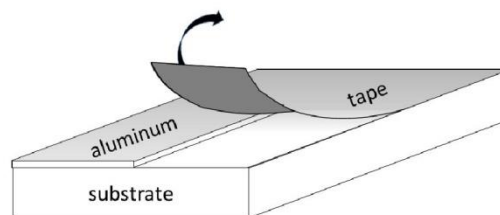


Figure 14. AFM measurement surface.

AFM: Practical Aspects and Analyses

Based on the measured topography (Figure 15) cross sections perpendicular to the edge are drawn and height profiles are extracted (Figure 16). The coating thickness can now be calculated by the height difference between the surface with and without aluminum. The peak in the middle of the graph in Figure 16 is a result of the tearing of the adhesive tape. By tearing, the aluminum is slightly lifted on the edges. Therefore, the peak area must not be considered. Moreover, the base line might not be as ideally horizontal as in Figure 16. In this case, the extracted height profile must be transcribed into an Excel file. Here, the data points from the base line of the substrate can be used to approximate a linear curve. Then the intercept of the curve is moved up so that the base line for the substrate plus coating can be fitted. By using a cosine function, a perpendicular can be dropped between the two baselines in order to calculate the distance between them.

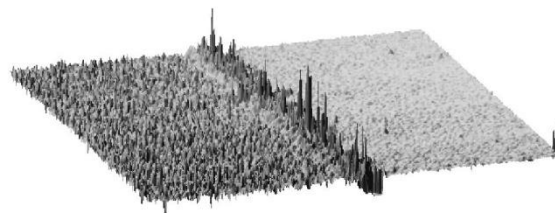


Figure 15. Example of a surface topography.

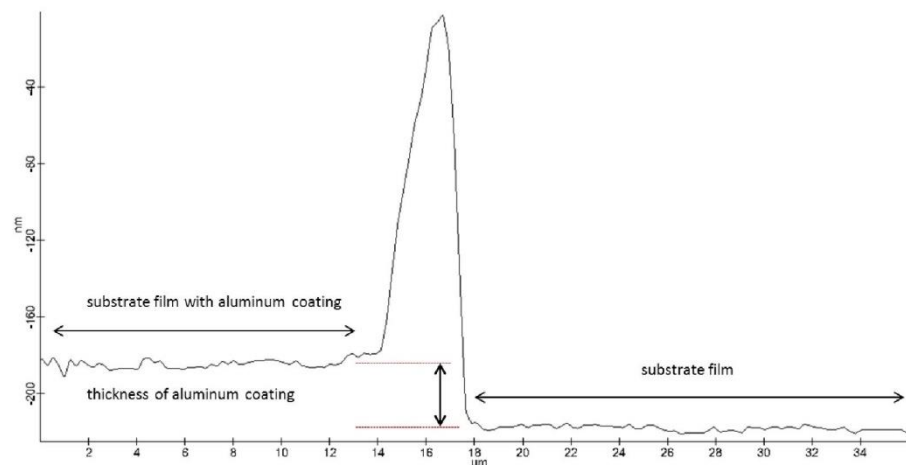


Figure 16. Example of an extracted profile.

What has to be taken into account when using this method is that that aluminum oxide is not captured separately but is included in the measured value. Additionally, inclusions, blank spaces, voids, etc. are not recorded either. The measurement is quite punctual, because it is not practical to make measurements on areas greater than about $100 \mu\text{m} \times 100 \mu\text{m}$. Scanning larger areas would lead to long scanning times in the range of a few hours. However, the resolution is extremely high and apart from height information, knowledge about the single molecule interactions between surface and cantilever (e.g., surface tension) can be gathered [75]. As displayed in Figure 13, the image that is acquired is strongly affected by the cantilever that is used. This effect can be diminished, when profile information is not only gathered in one scan direction but in backward and forward measurement modes. That means that each unevenness is captured from both sides. The resolution of AFM is commonly greater than 100 nm, reaching up to atomistic scales. Commercial specimens for Z calibrations are even available to a size of 2 nm [75].

2.3. Property Thickness

Whereas the last two chapters described the geometrical and mass thickness of thin coatings, this chapter focuses on the so-called property thickness. This denomination originates from the fact, that not the material itself, but the interaction with another physical phenomenon, e.g., ions, neutral particles, electrical field, or thermal energy, is monitored. In the present case, the interaction with photons (optical density, interference) and electrons (electrical surface resistance, eddy current measurement) is used to further describe thin aluminum coatings [65]. Other methods that can be counted as property thickness measurements are the Hall voltage measurement, interference spectra, polarization analysis, beta backscattering, X-ray fluorescence, X-ray emission, energy dispersive X-ray spectroscopy (EDX), and others [65].

2.3.1. Optical Density

Any optical phenomenon is connected with the reaction of light with matter. Light can generally be considered as a superposition of electromagnetic waves, which interact with the substrate so that amplitude, wave length, angular frequency, intensity, polarization, and propagation direction changes. For all optical methods, one or more of these characteristics is observed and then related to the material features [79]. Examples are: total reflection X-ray fluorescence analysis (TXRF), energy-dispersive X-ray spectroscopy (EDXS), grazing incidence X-ray, glow discharge optical emission spectroscopy (GD-OES), reflection absorption IR spectroscopy (RAIRS), surface-enhanced Raman scattering (SERS), and UV-Vis-IR ellipsometry (ELL) [65,80]. When the correspondent signals are analyzed, one will usually achieve information about the surface of the probe and/or about the material itself. However, especially when thin coatings are analyzed, both effects superimpose. This problem is often solved by building mathematical models that incorporate both phenomena. Then the model is fitted to the measured values. Like this, information about both (geometry and material) can be derived. Though for doing so, a minimum knowledge about the materials (e.g., refractive indices, absorption coefficients, approximate thicknesses, etc.) in the probe is necessary before fitting the measurement with the mathematical model [79]. The method of measuring the optical density uses the intensity of light as a characteristic feature. The material specific property that has to be known for this kind of analyses is the absorption coefficient (α), as explained in the following.

Optical Density: Theory

When light impacts a surface, it will partially be reflected (R), absorbed (A), scattered (S), and transmitted (T). Because of the conservation of energy, the sum of all parts is always 1 (Equation (22)). By knowing three of them, the fourth one can easily be calculated. However, reflection (R) and transmission (T) are rather easy to capture. Consequently, (A) and (S) are often summarized to the optical loss (L), as they are rather hard to define (Equation (22)). Commonly, the parts of reflected, absorbed, scattered, and transmitted light are defined by their relation to the initial intensity of the light beam (Equation (23)) [79,81].

$$R + A + S + T = 1 = R + L + T \quad (22)$$

$$R \equiv \frac{I_R}{I_0} \quad S \equiv \frac{I_S}{I_0} \quad A \equiv \frac{I_A}{I_0} \quad T \equiv \frac{I_T}{I_0} \quad (23)$$

Apart from that, Lambert and Beer introduced a mathematical law concerning absorption, which is commonly used in biology and chemistry to find the amount of dispersed particles in a liquid. They found that the intensity of transmitted light correlates with the absorption coefficient of the particles (α) and the distance (l) that light travels through the dispersion according to Equation (24).

The absorption coefficient (α) in turn is linked to the frequency (ω), speed of light (c) and extinction coefficient (K), as illustrated in Equation (27) [79].

$$I_T = I_0 \times e^{-\alpha l} \quad (24)$$

$$\alpha = 2 \times \frac{\omega}{c} \times K(\omega) \quad (25)$$

This means that according to the Lambert Beer law, absorbance (A') is defined as the part of the light that is not transmitted (Equation (26)). This definition of "absorbance" does not equal the definition given at the beginning of the paragraph but is rather defined by absorption (A), scattering (S), and reflectance (R), as becomes obvious in Equation (27). Nevertheless, the optical density (OD) (Equation (27)) is derived from Equation (24) and is used to characterize the thickness of thin coatings. That means a coating having an optical density of 1, 2 or 3 lets pass 10%, 1% and 0.1% of light, respectively. Consequently, when using the concept of optical density, one needs to be aware that scattering, reflectance and absorption might alter the measured value although the originally defined absorbance might have kept constant. Additionally all four values are subjected to the wavelength, material, and the material's structure [79,81,82].

$$T = 1 - A' \quad (26)$$

$$\alpha l = -\log \frac{I_T}{I_0} = -\log(1 - A - S - R) = OD \quad (27)$$

Optical Density: Method

Because of the above-mentioned simplification, only the transmittance is measured for optical density [39]. Some simpler or rather sophisticated methods are commercially available. They all have in common that, for measuring the transmittance, the object is placed under a focused light source and transmittance is measured by a photo diode on the backside of the material. Depending on the equipment, one single wave length or a whole range can be measured (e.g., with FTIR). As evaporated coatings are typically applied on polyethyleneterephthalate or polypropylene substrates, the optical density of the pure substrate should also be captured and subtracted from the measured value.

Optical Density: Practical Aspects and Analyses

Weiss [83] showed in his work a linear correlation between optical density and thickness in the range of optical density of 0.3 to 3.5 (this means a transmission of 50% to 0.03%, respectively). However, the thickness suddenly increases at optical thicknesses <3.5. Similarly Hertlein [81] declares that OD is not useful for values >3.2. Apart from that, Copeland and Astbury [39] showed, that the optical density decreases over time, as the light-absorbing aluminum reacts to the transparent aluminum oxide. Therefore, the acquired value only takes into account the metallic part of the coating.

Apart from that, the challenge while calculating the thickness of the coating based on the optical density is the definition of the absorption coefficient (α), and the extinction coefficient (K). As mentioned before, these parameters are highly susceptible on material, wavelength, and structure. It was calculated for various other evaporated substances in [84–88]. The interrelation of optical density or transmittance with process conditions, coating thickness and wavelength was evaluated by [42,89,90]. According to Schulz [91], the absorption coefficient for aluminum has a value of approximately 4–9 for wavelengths of 0.4–0.9 μm . As stated by Lehmuskero and Kuittinen [89] the coefficient had a value of 3–21 for a wavelength of 0.3–2 μm . Heavens [92] gave an overview of coefficients determined by various sources. Here, the extinction coefficient attained values of 0–12 in the region of 0.1–100 μm wavelength. Moreover, Lehmuskero and Kuittinen [89] found that the values for atomic layer deposited aluminum were higher than for physical vapor deposited aluminum. This was explained by the higher grain size for evaporated coatings, which leads to a reduced scattering of electrons, which in turn

increases the absorption coefficient. Apart from that, the coating thickness showed an effect over the whole range of wave lengths without showing a clear trend. One way to explain this effect was to take into account the aluminum oxide. Depending on the overall thickness, the oxide layer might occupy different portions of this thickness and might therefore have different impacts on the optical density. However, this was not evaluated further. As a conclusion, Lehmuskero and Kuittinen [89] recommended, not to use literature values for extinction and absorption coefficients, as these might lead to deviations of approximately 20% but rather identify them for each new process and process equipment. Consequently, the method can be used as a fast way of obtaining approximate thickness evaluations, especially when the process conditions are kept constant. However, the coefficients need to be clearly determined when very accurate values shall be obtained. In this case, the identification of these values might be extremely time consuming.

2.3.2. Interference (Tolansky Method)

In 1827 the physicist Jacques Babinet proposed the idea of using the wavelength of light as a measure of length, which is basically done in interferometry [93]. As elucidated previously, the interaction of light with matter alters the amplitude, wave-length, angular frequency, intensity, polarization, and/or propagation direction [79]. The interference method uses the reflectance (R) of surfaces as well as the intensity (I) of light.

Interference is the superimposition of rays, which can be non-destructive or destructive in the case of coherent waves, and a phase shift of a half wavelength. If rays are reflected on a surface and superimpose with itself at a phase shift of a half wavelength, then the intensity becomes zero. This effect is visible as bright and dark lines (interference pattern) and can therefore be used to measure coating thicknesses, as is demonstrated in the following Section [93].

For thin coating analyses, a huge number of measurements based on interference is available, which are principally divided into single and multiple beam interferometry. The latter has the advantage that the intensity at each interference band is an accumulated intensity of each reflection and therefore the bands are rather sharp and easy to identify. Further examples are the Michelson interferometry, Fourier spectroscopy, and Fabry-Perot Interferometry.

Interference (Tolansky Method): Theory

The thickness of a deposited aluminum coating can be determined by the light interference method according to Tolansky [94], which is based on Newtonian interference bands. Knowledge about material density, electrical conductivity, etc. is not necessary [95]. The prerequisite for this method is access to an edge on the substrate, as illustrated in Figure 14. Additionally, both surfaces (aluminum and underlying polymer) should have a high (ideally identical) reflection. If this is not the case, an additional nano meter thin coating of e.g., gold should be sputtered on both surfaces. For creating an interferable system, a semitransparent reference glass is positioned on the sample surface under a small angle (α). Rays will pass through the glass, impact on the probe surface, and be reflected by it with a phase shift of 180° . Incoming and reflected rays will then interfere. For doing so, these rays need to have a minimum distance. This is achieved by a small distance between the glass and the surface as well as a small angle between both. When the distance between the substrate surface and the reference glass is a multiple of 0.5λ , waves superimpose in a destructive way and interference bands appear in a defined distance (a). Due to the small angle and low distance, interference bands are highly contrasting with a step loss in intensity. They will appear very thin compared to their distances (a) and are therefore usable for an evaluation [96]. Because of the step due to the aluminum coating, there is an offset (a') between the interference bands caused by the polymer surface and the bands caused by the aluminum surface. The higher the aluminum thickness (d), the bigger the offset (a') (Figure 17) [94,95,97]. A mathematical description of the dependencies based on simple trigonometric

relations allows for deriving Equations (28) and (29). By combining both, the thickness (d) is then calculated like in Equation (30) [98,99].

$$\tan \alpha = \frac{d}{a'} \tag{28}$$

$$\tan \alpha = \frac{\lambda/2}{a} \tag{29}$$

$$d = \frac{\lambda \times a'}{2 \times a} \tag{30}$$

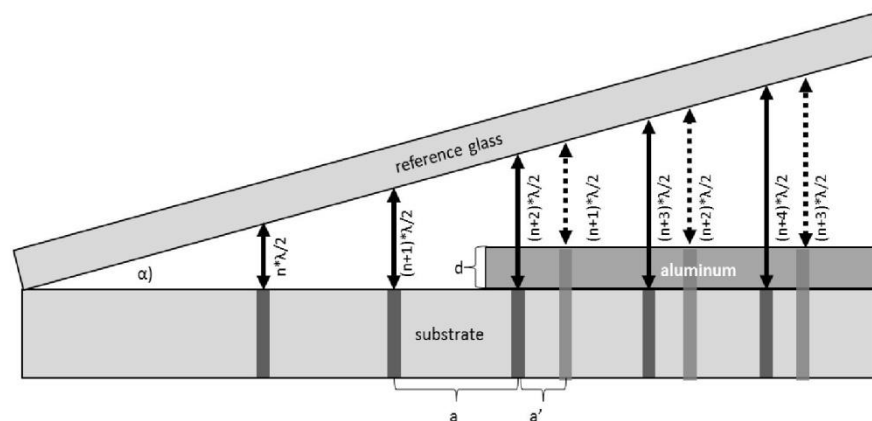


Figure 17. Appearance of interference bands on the semitransparent reflecting coating.

Interference (Tolansky Method): Method

According to the theory described before, only the wavelength (λ) as well as the distance (a) and offset (a') need to be known/measured, for calculating the coating thickness (d). Ideally, both surfaces should have the same refractive index. This is why an additional sputtered coating is often applied on both the polymer and the aluminum. For generating the interference bands, a Tolansky objective is applied on the light microscope and a filter is added for adjusting the light to monochromatic rays of 550 nm. The microscopic objectives that are necessary for interference measurements are commercially available. They are working on the basic principle depicted in Figure 18. Light is emitted and condensed by a lens, then filtered by a monochrome filter to a wave-length of typically 550 nm. Condensed by a second lens and mirrored towards the reference glass, the step between the aluminum and the substrate triggers interference bands, which are then visible and ready to be evaluated by microscope software. The interference bands should be perpendicular to the direction of the coating edge. Once the resolution is adjusted, (a) and (a') is measured and (d) is calculated as in Equation (30).

Interference (Tolansky Method): Practical Aspects and Analyses

Figure 19 shows typical interference bands of an aluminum coating on a PET surface. Care needs to be taken to correctly identify (a) and (a'). One possibility to facilitate this was presented by Hanszen [95], who explained that, due to the different phase shifts of monochromatic light on the substrate and coating, both should be covered with an additional, highly reflective 10 nm coating (e.g., gold or silver). This is especially important, when the thickness of the transparent aluminum oxide layer should be included in the measured value. However, roughness, blank spaces between aluminum coating, and sputtered coating, as well as gaps in the sputtered coating, still have an effect. Thus, if the surface to measure is rough, the actually measured coating thickness is not the average height (d), but a certain factor higher than (d). Only if the roughness of the substrate and the coating are the same is this effect negligible. Gaps in the sputtered coating appear due to island growth (see Figure 19).

When this happens, light is partially reflected on the sputtered island and partially on the coating. This might lead to deviations in the measured value of the coating thickness. Moreover, even this sputtered coating might show different growth behavior, which might again manipulate the results. Piegari and Masetti [59] followed that, in order to avoid deviations, the sputtered coating should be applied in a high vacuum at low condensation temperatures. However, the accuracy is reported to be approximately 1%.

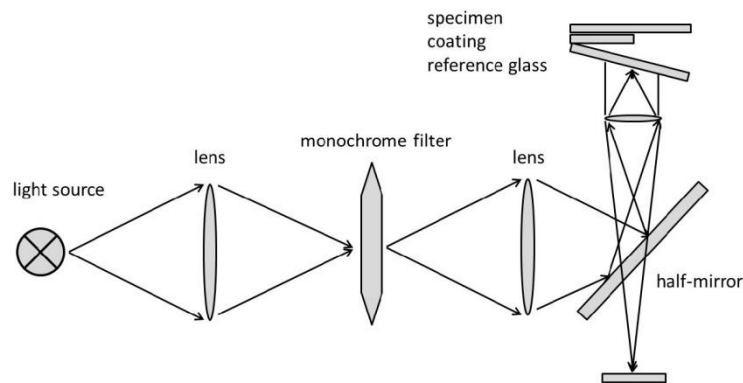


Figure 18. Set up for interference measurement.

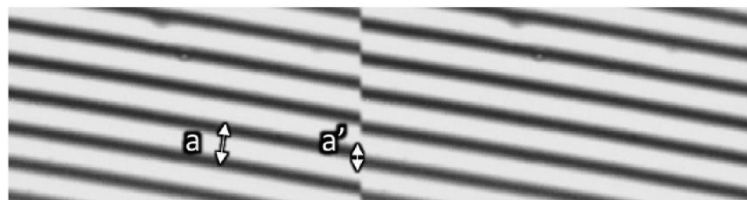


Figure 19. Microscopic image of interference bands.

2.3.3. Electrical Surface Resistance

Electrical Surface Resistance: Theory

Electrical resistivity (R) is the property of a current carrying conductor to inhibit the current flow. It is inhibited by collisions with lattice defects and impurities as well as oscillations of the crystal lattice atoms [100]. It is defined as the relation of voltage (U) to current (I). The inverse value represents the conductivity (G) (Equation (31)) [75]. The electrical resistivity depends on the geometry and material characteristics of the current carrying conductor. With the help of the specific electrical resistivity (ρ), length (l), width (b) and thickness (d) of the conductor, the expected resistivity (R) can be calculated (Equation (32)). If length (l) and width (b) are equal, both can be deducted from the formula which leads to the value of the so called surface resistivity (R_{\blacksquare}) (Equation (33)). As this resistivity is measured in a squarish setup, it is often indexed with a small square (R_{\blacksquare}). The advantage is now, that by using a defined construction (with $l = b$) for measuring the resistance, the coating thickness (d) can easily be calculated from Equation (33).

$$R = \frac{U}{I} \quad G = \frac{1}{R} = \frac{I}{U} \quad (31)$$

$$R = \rho \times \frac{l}{A} = \frac{\rho \times l}{d \times b} \quad (32)$$

$$R_{\blacksquare} = \frac{\rho \times l}{d \times b} = \frac{\rho}{d} \quad (\text{with } l = b) \quad (33)$$

Pursuant to the Drude-Lorentz-Sommerfeld theory, the conductivity of metals is subjected to the density of the free electrons in the metal (n), the electron charge (e), the mean free path of the conducting electrons (l), the effective mass of an electron (m), and the average speed of free electrons (v_F), like in Equation (34). However, the mean free path (a) is related to the amount of imperfections and defects as well as the structure of the conductor as electrons are scattered on these lattice imperfections [100]. Kinds of imperfections are revealed in [34]. For small amounts of impurities, the effective resistivity is a sum of the bulk resistivity ($\rho_b(T)$) in dependence of the temperature (T) and the resistivity of the defects ($\rho_d(c)$) in dependence of the defect concentration (c) [100]. According to Matthiessen's rule for thin metal coatings, an additional term for the scattering at the boundary surfaces ($\rho_h(h)$) can be added, which correlates with the thickness (d) of the thin coating [100]:

$$\rho_0 = \frac{m \times v_F}{n \times e^2 \times a} \quad (34)$$

$$\rho_0 = \rho_b(T) + \rho_d(c) + \rho_d(d) \quad (35)$$

Electrical Surface Resistance: Method

In order to eliminate (b) and (l) from Equation (33), a defined geometry of the measured surface needs to be ensured where $b = l$. For accuracy reasons, usually 4 point set ups are used which are depicted in Figure 20. Therefore, electrodes might either be arranged in a linear or in a squarish way (van-der-Pauw method). In each case, the current is introduced between point (A) and (B) and the decrease in voltage is determined via (C) and (D).

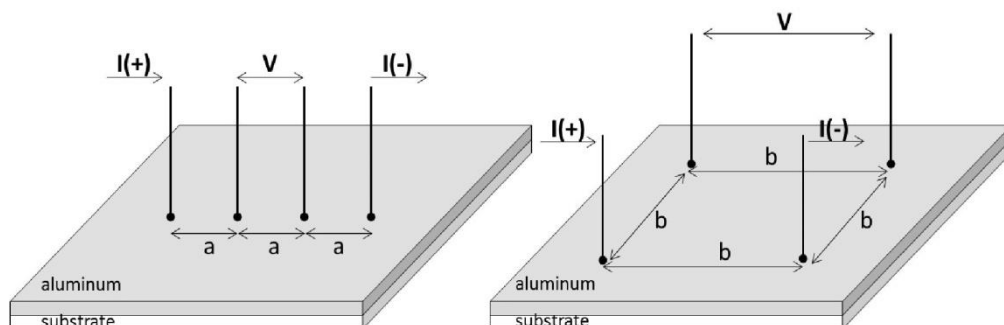


Figure 20. Common arrangements for measurement of surface resistance.

Electrical Surface Resistance: Practical Aspects and Analyses

Especially for nanometer thin coatings, the gravitational pressure of the tool might already cause cracks in the material. To reduce the influence of the pressure of the measurement setup on the thin coating, the electrodes are sometimes spring loaded. Moreover, oxide layers (which can have a resistivity 20-fold higher than the pure metal) can increase the determined value. Once the surface resistivity (R_{\square}) is measured, the coating thickness (h) can easily be calculated. However, some more effects should be taken into account, when interpreting this value.

Aluminum oxide has a resistivity of 10^{18} ($\Omega \cdot \text{mm}^2$)/m, which is 20-fold higher than aluminum. Consequently, the thickness of aluminum oxide is not captured in the measured value.

Another factor is the effect of electron scattering on surfaces and grain boundaries, of surface roughness and of island growth on electrical conductivity for different other metals such as copper, silver or gold were evaluated by [101–119] and fitted to models of Fuchs [120], Sondheimer [121], Soffer [122], Namba [107], Mayadas, and Shatzkes [123,124].

Rider and Foxon [125] quantified the dislocation density in cold-worked and partially annealed aluminum. They found that the dislocation resistivity was independent of dislocation density and

arrangement. Additionally, Mayadas and Feder [126] measured the resistivity of thin aluminum coatings in the range of 700 to 10,000 Å and modeled the effect of electron scattering on surfaces as well as on grain boundaries. However, the fitting of the curves to the Fuchs theory was not successful. However, Mayadas and Shatzkes [123] showed that if the grain size increases with coating thickness, then a distinct effect on the resistivity exists. In [124] the resistivity of a thin aluminum coating is modeled, taking into account the background scattering of phonons and point defects, grain boundaries, and scattering on external surfaces. The conclusions were that the effect of thickness on resistivity is due to the grain-boundary scattering and the Fuchs size effect. The grain-boundary reflection coefficient in aluminum was found to be ≈ 0.15 . Apart from that, in [127] results are presented, where the effect of pore size, its volume fraction, and direction on the electrical resistivity was measured, modeled, and simulated.

The methods limitation is mainly fixed by the set ups measurement range. Especially when aluminum coatings are thin and the distance between single atoms or clusters is large, no current can flow. Consequently, the resistivity of the aluminum coating is high and the measured value will principally be that of the substrate and therefore probably not detectable. This effect has been experimentally and theoretically investigated by [103,106,128,129].

2.3.4. Eddy Current Measurement

Just like with the setup for the electrical surface resistance, the eddy current technology is used to measure the resistivity—or in this case the conductivity—of the aluminum surface. The eddy current measurement is extendable to the impedance spectroscopy by varying the inserted frequency of the current (I), which allows for extracting some more information about Ohmic and capacitive resistivities (as e.g., in [130]).

Eddy Current Measurement: Theory

Just like surface resistance measurement, the eddy current measurement is an electrical method. However, it can be applied for non-destructive material testing, which is especially used for defining quality characteristics like coating thickness, resistivity, material homogeneity, and other physical changes in the material. By applying an alternating voltage (100 kHz to some MHz) on the induction coil, an electromagnetic field (primary field) is generated. If a conducting sample is placed in this electromagnetic field, eddy currents are triggered in the sample. The notation “eddy current” is based on the movement of the current carriers on circular paths. This eddy current then leads to a secondary electromagnetic field, which impinges on the primary field. This impingement can be measured and related to the thickness of the coating [65]. The basic physical principles are outlined in the following. However, the exact mathematical description of the interaction of coil and a flat metal sheet can be found in [131].

The aluminum coating is characterized by the thickness (d), the electrical conductivity ($1/R$), and the magnetic permeability (μ_r) [65]. When an alternating current passes a coil, this leads to the development of an electromagnetic field (Figure 21), defined by the magnetic flux density (B_1) and electric flux density (E), which leads to the movement of current carriers with the velocity (v) in a flat metal sheet supposed to the field. The three vectors (B), (E), and (v) are perpendicular to each other (Lorentz rule) (Equation (38)) and lead to the circular movement of the current carriers in the aluminum (eddy current). The magnetic flux density (B_1) is triggered depending on the electrical current (I) passing through the coil, the length of the coil (l), its coil number (N), and the magnetic constant (μ_0) (Equation (36)). These eddy currents trigger a secondary magnetic field (B_2), which is opposite directed and alters the primary field (B_1). Pursuant to the rule of Lenz, the secondary field superimposes the first one and reduces it to the value of (B_1'). The relation of (B_1') to (B_1) is denoted as the permeability (μ_r). In a nutshell, the eddy currents will be higher when the aluminum coating is thicker, and the inductance in the coil will be lower [65,132,133]. This energy loss consists of three parts: the hysteresis loss (W_h), the classical loss (W_{cl}), and the excess loss (W_{exc}) (see Equation (42)).

Herein the classical loss (W_{cl}) depends on the thickness as in Equation (43). Here, (σ) is the conductivity, (d) is the material thickness, (J_p) is the peak polarization, (f) is the frequency, and (δ) is the material density [134].

$$B = \mu_0 \times I \times \frac{N}{l} \quad (36)$$

$$F_M = Q \times v \times B \quad (37)$$

$$F_L = Q \times v \times B + Q \times E \quad (38)$$

$$\mu_r = \frac{B}{B_0} \quad (39)$$

$$\mu = \mu_0 \times \mu_r \quad (40)$$

$$Z = \frac{U_{eff}}{I_{eff}} \quad (41)$$

$$W = W_h + W_{cl} + W_{exc} \quad (42)$$

$$W_{cl} = \frac{\pi^2}{6} \times \frac{\sigma d^2 J_p^2 f}{\delta} \quad (43)$$

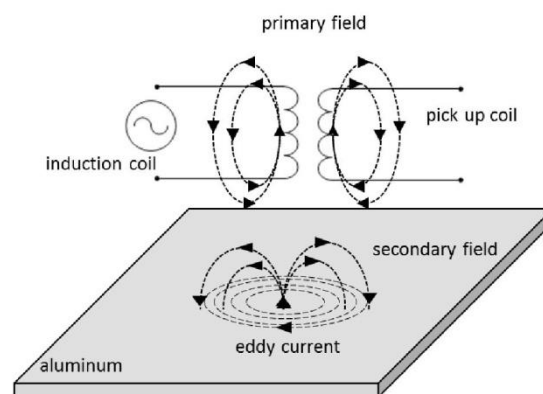


Figure 21. Schematic representation of eddy current (adapted from [133]).

Eddy Current Measurement: Method

Basically, two different methods are used for eddy current measurements: the surface and transmission technique. In the first case, the sending coil is also the receiving coil and the specimen is placed at a defined distance to it. In the second case, the specimen is placed between two coils: the first one triggers the electromagnetic field; in the second coil the electromagnetic field leads to a current in the coil. The second method has the advantage that misalignments as well as the distance between coil and specimen only have a minor effect on test results [135]. Various different methods and setups are reviewed in [136].

In order to reveal the shift of inductance, a circuit can be used, as in Figure 22. This consists of a power supply (U_0), the coil with inductance (L), the coils' resistivity (r), a capacitor (C), and an external resistor (R). Because of the shift of energy between the coil and the capacitor, the circuit oscillates and shows a typical resonance frequency, which can be monitored via the LC circuit voltage (U_{LC}). When the sample is introduced to the system, the coils inductivity (L) changes and the resonance voltage (U_{LC}) shifts away. The change of (U_{LC}) is amplified and related to the samples' surface resistivity (R_{\blacksquare}). Further variations in the eddy current measurements are described in [130,131,135,137–141].

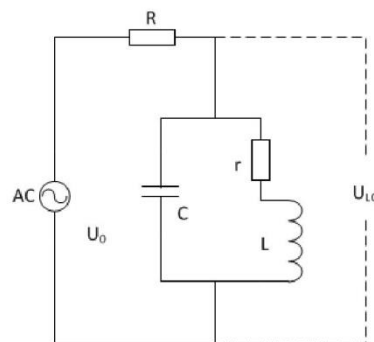


Figure 22. Resonant circuit used of eddy current measurements (adapted from [142]).

Eddy Current Measurement: Practical Aspects and Analyses

Once the surface resistance (R_{\square}) is measured, the material thickness (d) can then be calculated from Equation (33). New systems exist, that automatically or semi-automatically measure the surface resistance in a raster of e.g., 1 cm squares. Although eddy current measurements are a rather punctual method, this offers the opportunity to gain an average value which characterizes a whole material area. In [143] simulations have been carried out that show a clear relationship between bulk resistivity of the specimens and the eddy current induced in the thin conductor metals. Measurement setups are available e.g., in the range of 0.001–3000 Ω/sq , that equals of an ideal aluminum coating thickness of approximately 26 μm –0.01 nm [133]. Just like in the electrical surface resistance measurement, aluminum oxide is not captured in the measured value because of the extremely high resistivity.

However, several factors might affect the results. Heuer and Hillmann [139] stated, that subjected to the frequency, the depth where eddy currents are triggered might vary. Therefore, for thicker materials, a lower frequency is necessary to ensure the full penetration of the material.

Qu, Zhao [142] varied the coil resistance, its capacity, and induction in the LC circuit and found that, by reducing the resistance by using multi strand of wires for the coil the sensitivity increases. The maximum sensitivity reached was 2 mV/nm. The importance of sensitivity was also emphasized by Angani, Ramos [141]. Moulder, Uzal [140] determined the effect of the coil size to specimen thickness ratio on the sensitivity of the instrument. They found that for thin specimens only one feature (thickness or conductivity) can be measured when the other one is known. This effect is also comprehensively explained in [135], where a solution is presented as to avoid this problem by choosing the right frequency. Similar to Moulder, Uzal [140], Rajotte [138] also recommended, that the specimen should be at least 1.5 times larger than the outside diameter of the spiral coil.

Hillmann, Klein [135] evaluated the effect of sensor-to-sensor distances and material thickness on the deviation from expected values and found a non-linear behavior. The deviation was small (approximately 0.25 to 1.5 nm) and showed a further decrease for thicknesses below 20 nm. However, the deviation was much higher (approximately 0.5 to 4.0 nm) but still showed a decrease for thicknesses of ≥ 50 nm. A smaller distance between the two sensors (6 cm, 4 cm and 2 cm were tested) seemed to reduce the deviation.

Heuer, Hillmann [139] and Hillmann, Klein [135] even stated that the kind of material in mono and multilayers, the depth profile, thicknesses, and hardnesses as well as microstructure properties can be revealed. However, they were partially working in a thickness range of several micrometers and it is not mentioned which method was used to apply the coating. Concerning the differentiation of materials, Hillmann, Klein [135] emphasized the importance of choosing the right frequency, in order to properly distinguish between different materials with different conductivities and thicknesses. Angani, Ramos [141] proposed using this method to evaluate the corrosion of metals.

3. Methods Overview and Conclusions

As illustrated before, each method has its challenges when it comes to the interpretation of the measured values. No measurement is the “wrong” or the “right” one, but they need to be interpreted based on the characteristic that is actually acquired. Only in accordance with the scope of application, can the “most suitable” system be chosen. Table 1 gives an overview that provides indications for choosing the most suitable method for different purposes. The indications are denoted as follows.

Table 1. Overview over methods.

Characteristic	Mass Thickness		Geometrical Thickness	Property Thickness				
	QCM	ICP-MS	AFM	Eddy Current Measurement	Electrical Resistivity Linear	Electrical Resistivity Squarish	Optical Density	Interference
Measurement range	++	+++	++	+++	+++	+++	+	++
Time needed for one measurement	+	+++	++	+	+	+	+	++
Non destructive	✓	✗	✗	✓	✗	✗	✓	✗
Punctual measurement	(✓)	✗	✓	✓	✗	✗	✓	✓
Measurement within multilayer is possible	✗	✓	(✓)	✓	✗	✗	✗	✗
Impact of pores and defects	✗	✗	++	+++	+++	+++	++	++
Is only metallic aluminum detected?	✓	✗	✗	✓	✓	✓	✓	✓
Usable as inline measurement	✓	✗	✗	✓	✗	✗	✓	✗
Financial invest	+	+++	+++	++	+	+	+	++

+++/++/+: big/intermediate/small; ✓/✗: yes/no; (): with restrictions.

From this overview it can be concluded, that a higher financial investment does not necessarily lead to shorter measuring times or higher measurement ranges. Whereas ICP-MS, AFM, and interference seem to be more interesting methods for science related questions, especially QCM, eddy current, electrical resistivity, and optical density are commonly used in packaging material producing industries. QCM and optical density are widely used as inline measurement method, as they are also non-destructive.

When it comes to the correlation of thickness values with barrier effects against water vapor and oxygen, the awareness about the subdivision into mass, geometrical, and property thickness is useful. As permeation appears mainly through areas where the aluminum coating is not yet closed or is defective, the interpretation of measured and derived thickness values is critical.

For the calculation of mass thickness measurements, it is assumed that all the aluminum in the sample is arranged in a perfectly crystalline manner on the substrate surface. It is not taken into account that there might be defects or irregularities in the atomic lattice or aluminum that reacted to aluminum oxide and might influence the gas barrier.

In contrast to that, the geometrical measurement based on AFM is a very punctual measurement. The measured thickness consists of both the pure aluminum and also of aluminum oxide. Here one needs to be aware that the molar volume of aluminum oxide is higher (values depending on the exact composition) than that of pure aluminum. Additionally, the measurement should be repeated at different areas of the sample as it cannot be excluded that one measurement is done on a defect or an area with extraordinarily high or thin aluminum coverage.

REVIEW:

THICKNESS MEASUREMENT METHODS FOR PHYSICAL VAPOR DEPOSITED ALUMINUM
COATINGS IN PACKAGING APPLICATIONS: A REVIEW

Coatings 2017, 7, 9

27 of 32

As the name suggests, property thickness measurements measure a certain property of the aluminum, the thickness of which is then calculated based on the assumption that the nanometer thin coating behaves like an ideal bulk material. However, it is known, that nanometer materials behave differently from bulk material. Imagine a thick coating, full of pores and defects. These pores and defects might lead to increased electrical resistivity. Thus, a thickness would be calculated, that is thinner than it actually is (compare Equation (33)). For the case of optical density, an increasing relative amount of aluminum oxide decreases the measured value for the optical density. The amount of aluminum oxide is in turn affected by the residual oxygen in the recipient.

From this overview it becomes obvious, that the thickness can be measured rather quickly; however, a full characterization of the coating can only be done by the combination of the above mentioned methods.

Acknowledgments: This work was supported by the German Research Foundation (DFG) and the Technical University of Munich (TUM) in the framework of the Open Access Publishing Program. Therefore the authors thank the DFG and TUM for their support. Moreover, the authors thank Horst-Christian Langowski and Florian Höflsauer for their support.

Author Contributions: Martina Lindner wrote the manuscript and was in charge of the overall outline and editing of the manuscript. She was involved in the revision and completion of the work. Markus Schmid contributed to the outline as well as to the revision, completion, and editing of the manuscript.

Conflicts of Interest: The authors declare no conflict of interest.

References

1. Bichler, C.; Langowski, H.C.; Moosheimer, U.; Bischoff, M. Transparente Aufdampfschichten aus Oxiden von Si, Al und Mg für Barrierepackstoffe. Available online: <https://www.mysciencework.com/publication/show/430561f397d6f9ad469136be1369ee3b> (accessed on 29 December 2016).
2. Pilchik, R. Pharmaceutical blister packaging, Part I. *Pharm. Technol.* **2000**, *24*, 68–78.
3. Dean, D.A.; Evans, E.R.; Hall, I.H. *Pharmaceutical Packaging Technology*; Taylor & Francis: London, UK, 2005.
4. Huang, C.C.; Ma, H.W. A multidimensional environmental evaluation of packaging materials. *Sci. Total Environ.* **2004**, *324*, 161–172. [CrossRef] [PubMed]
5. Seshan, K. *Handbook of Thin Film Deposition Processes and Techniques*; William Andrew: Norwich, NY, USA, 2002.
6. Mattox, D.M. Physical vapor deposition (PVD) processes. *Metal Finish.* **2001**, *99*, 409–423. [CrossRef]
7. Pierson, H.O. *Handbook of Chemical Vapor Deposition: Principles, Technology and Applications*; William Andrew: Norwich, NY, USA, 1999.
8. Leskelä, M.; Ritala, M. Atomic layer deposition (ALD): From precursors to thin film structures. *Thin Solid Films* **2002**, *409*, 138–146. [CrossRef]
9. Hirvikorpi, T.; Vähä-Nissi, M.; Mustonen, T.; Harlin, A.; Iiskola, E.; Karppinen, M. Thin inorganic barrier coatings for packaging materials. In Proceedings of the PLACE 2010 Conference, Albuquerque, NM, USA, 18–21 April 2010.
10. Mackenzie, J.D.; Bescher, E.P. Physical properties of sol-gel coatings. *J. Sol-Gel Sci. Technol.* **2000**, *19*, 23–29. [CrossRef]
11. Logothetidis, S.; Laskarakis, A.; Georgiou, D.; Amberg-Schwab, S.; Weber, U.; Noller, K.; Schmidt, M.; Kuecukpinar-Niarchos, E.; Lohwasser, W. Ultra high barrier materials for encapsulation of flexible organic electronics. *Eur. Phys. J. Appl. Phys.* **2010**, *51*, 33203. [CrossRef]
12. Noller, K.; Mikula, M.; Amberg-Schwab, S.; Weber, U. Multilayer coatings for flexible high-barrier materials. *Open Phys.* **2009**, *7*, 371–378.
13. Brinker, C.J.; Frye, G.C.; Hurd, A.J.; Ashley, C.S. Fundamentals of sol-gel dip coating. *Thin Solid Films* **1991**, *201*, 97–108. [CrossRef]
14. Schultrich, B. Physikalische dampfphasenabscheidung: Bedampfen. In Proceedings of the Surface Engineering und Nanotechnologie SENT, Dresden, Germany, 5–7 December 2006.
15. Bishop, C.A. *Vacuum Deposition onto Webs, Films and Foils*, 2nd ed.; Elsevier: Amsterdam, The Netherlands, 2011.
16. Mondolfo, L.F. *Aluminum Alloys: Structure and Properties*; Elsevier: Amsterdam, The Netherlands, 2013.
17. Ans, J.; Lax, E.; Synowietz, C. *Taschenbuch für Chemiker und Physiker*; Springer: Berlin/Heidelberg, Germany, 1967.

REVIEW:

THICKNESS MEASUREMENT METHODS FOR PHYSICAL VAPOR DEPOSITED ALUMINUM
COATINGS IN PACKAGING APPLICATIONS: A REVIEW

Coatings **2017**, *7*, 9

28 of 32

18. Hatch, J.E.; Association, A.; Metals, A.S. *Aluminum: Properties and Physical Metallurgy*; American Society for Metals: Geauga County, OH, USA, 1984.
19. Kaßmann, M. *Grundlagen der Verpackung: Leitfaden für die Fächerübergreifende Verpackungsausbildung*; Beuth Verlag: Berlin, Germany, 2014.
20. Iwakura, K.; Wang, Y.D.; Cakmak, M. Effect of Biaxial Stretching on Thickness Uniformity and Surface Roughness of PET and PPS Films. *Int. Polym. Process.* **1992**, *7*, 327–333. [[CrossRef](#)]
21. Cakmak, M.; Wang, Y.; Simhambhatla, M. Processing characteristics, structure development, and properties of uni and biaxially stretched poly (ethylene 2,6 naphthalate)(PEN) films. *Polym. Eng. Sci.* **1990**, *30*, 721–733. [[CrossRef](#)]
22. Lin, Y.J.; Dias, P.; Chum, S.; Hiltner, A.; Baer, E. Surface roughness and light transmission of biaxially oriented polypropylene films. *Polym. Eng. Sci.* **2007**, *47*, 1658–1665. [[CrossRef](#)]
23. Müller, K.; Schönweitz, C.; Langowski, H.C. Thin Laminate Films for Barrier Packaging Application—Influence of Down Gauging and Substrate Surface Properties on the Permeation Properties. *Packag. Technol. Sci.* **2012**, *25*, 137–148. [[CrossRef](#)]
24. Utz, H. Barriereigenschaften Aluminiumbedampfter Kunststoffolien. Ph.D. Thesis, Technische Universität, Fakultät für Brauwesen, Lebensmitteltechnologie und Milchwissenschaft, Berlin, Germany, 1995. (In German)
25. Kim, C.; Goring, D. Surface morphology of polyethylene after treatment in a corona discharge. *J. Appl. Polym. Sci.* **1971**, *15*, 1357–1364. [[CrossRef](#)]
26. Neugebauer, A. Condensation, nucleation, and growth of thin films. In *Handbook of Thin Film Technology*; Maissel, L.I., Glang, R., Eds.; McGraw-Hill: New York, NY, USA, 1970.
27. Haefer, R.A. *Oberflächen- und Dünnschicht-Technologie*; Springer: Berlin, Germany, 1987.
28. Jacobs, K. H. Frey, G. Kienel. *Dünnschichttechnologie*. VDI-Verlag GmbH, Düsseldorf 1987. 691 + XVIII pages, numerous figures and tables, 395.00 DM, ISBN 3-18-400670-0. *Cryst. Res. Technol.* **1989**, *24*, 1232. [[CrossRef](#)]
29. Vook, R.W. Structure and growth of thin films. *Int. Met. Rev.* **1982**, *27*, 209–245. [[CrossRef](#)]
30. Reichelt, K.; Jiang, X. The preparation of thin films by physical vapour deposition methods. *Thin Solid Films* **1990**, *191*, 91–126. [[CrossRef](#)]
31. Kern, R.; Metois, G.L. Basic mechanisms in the early stage of epitaxy. *Curr. Top. Mater. Sci.* **1979**, *3*, 135–419.
32. Stoyanov, S. Nucleation theory for high and low supersaturations. *Curr. Top. Mater. Sci.* **1979**, *3*, 421–462.
33. Bravais, A. *Abhandlung über Die Systeme von Regelmässig auf Einer Ebene Oder Raum Vertheilten Punkten*; Wilhelm Engelmann: Leipzig, Germany, 1897. (In German)
34. Gottstein, G. *Materialwissenschaft und Werkstofftechnik: Physikalische Grundlagen*; Springer: Berlin, Germany, 2014.
35. Weitze, M.D.; Berger, C. Strukturen und Eigenschaften. In *Werkstoffe: Unsichtbar, Aber Unverzichtbar*; Springer: Berlin, Germany, 2013; pp. 9–66.
36. Bollmann, W. *Crystal Defects and Crystalline Interfaces*; Springer Science & Business Media: Berlin, Germany, 2012.
37. Miesbauer, O.; Schmidt, M.; Langowski, H.C. Stofftransport durch Schichtsysteme aus Polymeren und dünnen anorganischen Schichten. *Vak. Forsch. Prax.* **2008**, *20*, 32–40. [[CrossRef](#)]
38. Barker, C.P.; Kochem, K.-H.; Revell, K.M.; Kelly, R.S.A.; Badyal, J.P.S. The Interfacial Chemistry of Metal Oxide Coated and Nanocomposite Coated Polymer Films. *Thin Solid Films* **1995**, *257*, 77–82. [[CrossRef](#)]
39. Copeland, N.J.; Astbury, R. Evaporated aluminium on polyester: Optical, Electrical, and Barrier Properties as a Function of Thickness and Time (Part I). In Proceedings of the AIMCAL Technical Conference, Myrtle Beach, SC, USA, 14 October 2010.
40. Hass, G.; Scott, N.W. On the structure and properties of some metal and metal oxide films. *J. Phys. Radium* **1950**, *11*, 394–402. [[CrossRef](#)]
41. McClure, D.; Struller, C.; Langowski, H.C. Evaporated Aluminium on Polypropylene: Oxide-Layer Thickness as a Function of Oxygen Plasma-Treatment Level. Available online: http://www.aimcal.org/uploads/4/6/6/9/46695933/mcclure_abs.pdf (accessed on 29 December 2016).
42. McClure, D.J.; Copeland, N. Evaporated Aluminium on Polyester: Optical, Electrical, and Barrier Properties as a Function of Thickness and Time (Part II). Available online: <http://dnn.convertquarterly.com/magazine/matteucci-awards/id/2420/evaporated-aluminum-on-polyester-optical-electrical-and-barrier-properties-as-a-function-of-thickness-and-time-part-1.aspx> (accessed on 29 December 2016).
43. Menges, G. *Werkstoffkunde der Kunststoffe*; Walter de Gruyter: Berlin, Germany, 1971; Volume 2620.

REVIEW:

THICKNESS MEASUREMENT METHODS FOR PHYSICAL VAPOR DEPOSITED ALUMINUM
COATINGS IN PACKAGING APPLICATIONS: A REVIEW

Coatings **2017**, *7*, 9

29 of 32

44. Prins, W.; Hermans, J.J. Theory of Permeation through Metal Coated Polymer Films. *J. Phys. Chem.* **1959**, *63*, 716–720. [[CrossRef](#)]
45. Langowski, H.C. Stofftransport durch polymere und anorganische Schichten Transport of Substances through Polymeric and Inorganic Layers. *Vak. Forsch. Prax.* **2005**, *17*, 6–13. [[CrossRef](#)]
46. Langowski, H.C.; Utz, H. Dünne anorganische Schichten für Barrierepackstoffe. *Int. Z. Lebensm. Technol. Mark. Verpack. Anal.* **2002**, *9*, 522.
47. Roberts, A.P.; Henry, B.M.; Sutton, A.P.; Grovenor, C.R.; Briggs, G.A.; Miyamoto, T.; Kano, M.; Tsukahara, Y.; Yanaka, M. Gas permeation in silicon oxide/polymer (SiO_x/PET) barrier films: Role of oxide lattice, nano-defects and macrodefects. *J. Membr. Sci.* **2002**, *208*, 75–88. [[CrossRef](#)]
48. Lohwasser, W. Not only for packaging. In Proceedings of the 43rd Annual Technical Conference of the Society of Vacuum Coaters, Denver, CO, USA, 23–28 April 2000.
49. Hanika, M.; Langowski, H.C.; Moosheimer, U.; Peukert, W. Inorganic layers on polymeric films—Influence of defects and morphology on barrier properties. *Chem. Eng. Technol.* **2003**, *26*, 605–614. [[CrossRef](#)]
50. Hanika, M. Zur Permeation Durch Aluminiumbedampfte Polypropylen-und Polyethylenterephthalatfolien. Ph.D. Thesis, Technical University of Munich, Munich, Germany, 2004.
51. Mueller, K.; Weisser, H. Numerical simulation of permeation through vacuum-coated laminate films. *Packag. Technol. Sci.* **2002**, *15*, 29–36. [[CrossRef](#)]
52. Rossi, G.; Nulman, M. Effect of local flaws in polymeric permeation reducing barriers. *J. Appl. Phys.* **1993**, *74*, 5471–5475. [[CrossRef](#)]
53. Jamieson, E.H.H.; Windle, A.H. Structure and oxygen-barrier properties of metallized polymer film. *J. Mater. Sci.* **1983**, *18*, 64–80. [[CrossRef](#)]
54. Bugnicourt, E.; Kehoe, T.; Latorre, M.; Serrano, C.; Philippe, S.; Schmid, M. Recent Prospects in the Inline Monitoring of Nanocomposites and Nanocoatings by Optical Technologies. *Nanomaterials* **2016**, *6*, 150. [[CrossRef](#)]
55. Utz, H. Barriereigenschaften Aluminiumbedampfter Kunststofffolien. Ph.D. Thesis, Technical University of Munich, Munich, Germany, 1995.
56. Kääriäinen, T.O.; Maydannik, P.; Cameron, D.C.; Lahtinen, K.; Johansson, P.; Kuusipalo, J. Atomic layer deposition on polymer based flexible packaging materials: Growth characteristics and diffusion barrier properties. *Thin Solid Films* **2011**, *519*, 3146–3154. [[CrossRef](#)]
57. McCrackin, F.L.; Passaglia, E.; Stromberg, R.R.; Steinberg, H.L. Measurement of the thickness and refractive index of very thin films and the optical properties of surfaces by ellipsometry. *J. Res. Natl. Bur. Stand. Phys. Chem. A* **1963**, *67*, 363–377. [[CrossRef](#)]
58. Chatham, H. Oxygen diffusion barrier properties of transparent oxide coatings on polymeric substrates. *Surf. Coat. Technol.* **1996**, *78*, 1–9. [[CrossRef](#)]
59. Piegari, A.; Masetti, E. Thin film thickness measurement: A comparison of various techniques. *Thin Solid Films* **1985**, *124*, 249–257. [[CrossRef](#)]
60. Pulker, H.K. Thickness measurement, rate control and automation in thin film coating technology. In Proceedings of the 1983 International Technical Conference, Geneva, Switzerland, 18 April 1983.
61. Mattox, D.M. Film characterization and some basic film properties. In *Handbook of Physical Vapor Deposition (PVD) Processing*; Mattox, D.M., Ed.; William Andrew Publishing: Westwood, NJ, USA, 1998; pp. 569–615.
62. Martin, P.M. *Handbook of Deposition Technologies for Films and Coatings: Science, Applications and Technology*; Elsevier: Amsterdam, The Netherlands, 2009.
63. Juzeliūnas, E. Quartz crystal microgravimetry—fifty years of application and new challenges. *Chemija* **2009**, *20*, 218–225.
64. Zeitvogel, J. Quarzkristallmikrowaage-QCM. Ph.D. Thesis, University of Erlangen-Nuremberg, Erlangen, Germany, 2009.
65. Frey, H.; Khan, H.R. *Handbook of Thin Film Technology*; Springer: Berlin, Germany, 2010.
66. Höpfner, M. Untersuchungen zur Anwendbarkeit der Quarzmikrowaage für Pharmazeutisch Analytische Fragestellungen. Ph.D. Thesis, Martin Luther University of Halle-Wittenberg, Halle, Germany, 2005.
67. MacLeod, H.A. *Thin-Film Optical Filters*, 3rd ed.; CRC Press: Cleveland, OH, USA, 2001.
68. Sauerbrey, G. Verwendung von Schwingquarzen zur Wägung dünner Schichten und zur Mikrowägung. *Z. Phys.* **1959**, *155*, 206–222. [[CrossRef](#)]

REVIEW:

THICKNESS MEASUREMENT METHODS FOR PHYSICAL VAPOR DEPOSITED ALUMINUM
COATINGS IN PACKAGING APPLICATIONS: A REVIEW

Coatings 2017, 7, 9

30 of 32

69. Lu, C.; Czanderna, A.W. *Applications of Piezoelectric Quartz Crystal Microbalances*; Elsevier: Amsterdam, The Netherlands, 2012.
70. Thomas, R. *Practical Guide to ICP-MS: A Tutorial for Beginners*, 2nd ed.; Taylor & Francis: London, UK, 2008.
71. De Hoffmann, E.; Stroobant, V. *Mass Spectrometry: Principles and Applications*; Wiley: New York, NY, USA, 2007.
72. Zoorob, G.K.; McKiernan, J.W.; Caruso, J.A. ICP-MS for elemental speciation studies. *Microchim. Acta* **1998**, *128*, 145–168. [[CrossRef](#)]
73. Broekaert, J.A.C. ICP-Massenspektrometrie. In *Analytiker-Taschenbuch*; Günzler, H., Bahadir, A.M., Danzer, K., Engewald, W., Fresenius, W., Galensa, R., Huber, W., Linscheid, M., Schwedt, G., Tölg, G., Eds.; Springer: Berlin/Heidelberg, Germany, 1988; pp. 127–163.
74. May, T.W.; Wiedmeyer, R.H. A table of polyatomic interferences in ICP-MS. *At. Spectrosc.* **1998**, *19*, 150–155.
75. Eaton, P.; West, P. *Atomic Force Microscopy*; Oxford University Press: Oxford, UK, 2010.
76. Voigtlaender, B. *Scanning Probe Microscopy: Atomic Force Microscopy and Scanning Tunneling Microscopy*; Springer: Berlin/Heidelberg, Germany, 2015.
77. Schieferdecker, H.G. *Bestimmung Mechanischer Eigenschaften von Polymeren Mittels Rasterkraftmikroskopie*; Fakultät für Naturwissenschaften, Universität Ulm: Ulm, Germany, 2005.
78. Meyer, G.; Amer, N.M. Simultaneous measurement of lateral and normal forces with an optical-beam-deflection atomic force microscope. *Appl. Phys. Lett.* **1990**, *57*, 2089–2091. [[CrossRef](#)]
79. Stenzel, O. *The Physics of Thin Film Optical Spectra*; Springer: Berlin, Germany, 2005.
80. Bubert, H.; Rivière, J.C.; Arlinghaus, H.F.; Hutter, H.; Jenett, H.; Bauer, P.; Palmetshofer, L.; Fabry, L.; Pahlke, S.; Quentmeier, A.; et al. *Surface and Thin-Film Analysis*; Wiley Online Library: New York, NY, USA, 2002.
81. Hertlein, J. *Untersuchungen über Veränderungen der Barriereigenschaften Metallisierter Kunststofffolien Beim Maschinellen Verarbeiten*; Utz, Wiss: München, Germany, 1998.
82. Miller, D.A. *Optical Properties of Solid Thin Films by Spectroscopic Reflectometry and Spectroscopic Ellipsometry*; ProQuest: Ann Arbor, MI, USA, 2008.
83. Weiss, J. Einflussfaktoren auf die Barriereigenschaften metallisierter Folien. *Verpak. Rundsch.* **1993**, *44*, 23–28.
84. Anna, C.; Cosslett, V.E. The optical density and thickness of evaporated carbon films. *Br. J. Appl. Phys.* **1957**, *8*, 374–376.
85. Deb, S.K. Optical and photoelectric properties and colour centres in thin films of tungsten oxide. *Philos. Mag.* **1973**, *27*, 801–822. [[CrossRef](#)]
86. Johnson, P.B.; Christy, R.W. Optical Constants of the Noble Metals. *Phys. Rev. B* **1972**, *6*, 4370–4379. [[CrossRef](#)]
87. Agar, A.W. The measurement of the thickness of thin carbon films. *Br. J. Appl. Phys.* **1957**, *8*, 35–36. [[CrossRef](#)]
88. Moss, T.S. Optical Properties of Tellurium in the Infra-Red. *Proc. Phys. Soc. Sec. B* **1952**, *65*, 62–66. [[CrossRef](#)]
89. Lehmuskero, A.; Kuittinen, M.; Vahimaa, P. Refractive index and extinction coefficient dependence of thin Al and Ir films on deposition technique and thickness. *Opt. Express* **2007**, *15*, 10744–10752. [[CrossRef](#)] [[PubMed](#)]
90. Hass, G.; Waylonis, J.E. Optical constants and reflectance and transmittance of evaporated aluminum in the visible and ultraviolet. *JOSA* **1961**, *51*, 719–722. [[CrossRef](#)]
91. Schulz, L.G. The Optical Constants of Silver, Gold, Copper, and Aluminum. I. The Absorption Coefficient k . *J. Opt. Soc. Am.* **1954**, *44*, 357–362. [[CrossRef](#)]
92. Heavens, O.S. Optical properties of thin films. *Rep. Prog. Phys.* **1960**, *23*, 1–65. [[CrossRef](#)]
93. McMillan, G.K.; Considine, D. *Process/Industrial Instruments and Controls Handbook*, 5th ed.; McGraw-Hill: New York, NY, USA, 1999.
94. Pulker, H.K. Einfaches Interferenz-Wechselobjektiv für Mikroskope zur Dickenmessung nach Fizeau-Tolansky. *Naturwissenschaften* **1966**, *53*, 224. [[CrossRef](#)] [[PubMed](#)]
95. Hanszen, K.J. Der Einfluss von Strukturunregelmäßigkeiten beim Zusammenwachsen zweier Aufdampfschichten auf das Schichtdickenmessverfahren mit Hilfe von Vielstrahl-Interferenzen. *Thin Solid Films* **1968**, *2*, 509–528. [[CrossRef](#)]
96. Großes Interferenzmikroskop. In *Vertriebsabteilung Feinmessgeräte*; Carl Zeiss Jena, Ed.; Druckerei Fortschritt: Jena, Germany, 1965.
97. Tippmann, H.; Schawohl, J.; Kups, T. *Schichtdickenmessung*; TU Ilmenau—Fakultät für Elektrotechnik und Informationstechnik Institut für Werkstofftechnik: Ilmenau, Germany, 2013.
98. Hammer, A.; Hammer, H.; Hammer, K. *Physikalische Formeln und Tabellen*; Lindauer: Munich, Germany, 1994.
99. Pitka, R. *Physik: Der Grundkurs*; Harri Deutsch Verlag: Frankfurt am Main, Germany, 1999.

REVIEW:

THICKNESS MEASUREMENT METHODS FOR PHYSICAL VAPOR DEPOSITED ALUMINUM
COATINGS IN PACKAGING APPLICATIONS: A REVIEW

Coatings **2017**, *7*, 9

31 of 32

100. Zhigal'skii, G.P.; Jones, B.K. *The Physical Properties of Thin Metal Films*; CRC Press: Cleveland, OH, USA, 2003; Volume 13.
101. Liu, H.D.; Zhao, Y.P.; Ramanath, G.; Murarka, S.P.; Wang, G.C. Thickness dependent electrical resistivity of ultrathin (<40 nm) Cu films. *Thin Solid Films* **2001**, *384*, 151–156.
102. Philipp, M. Electrical Transport and Scattering Mechanisms in Thin Silver Films for Thermally Insulating Glazing. Available online: http://www.qucosa.de/fileadmin/data/qucosa/documents/7092/Dissertation_Martin_Philipp.pdf (accessed on 29 December 2016).
103. Hoffmann, H.; Vancea, J. Critical-Assessment of Thickness-Dependent Conductivity of Thin Metal-Films. *Thin Solid Films* **1981**, *85*, 147–167. [[CrossRef](#)]
104. Leung, K.M. Electrical resistivity of metallic thin films with rough surfaces. *Phys. Rev. B* **1984**, *30*, 647–658. [[CrossRef](#)]
105. Ke, Y.; Zahid, F.; Timoshevskii, V.; Xia, K.; Gall, D.; Guo, H. Resistivity of thin Cu films with surface roughness. *Phys. Rev. B* **2009**, *79*, 155406. [[CrossRef](#)]
106. Borziak, P.G.; Kulyupin, Y.A.; Nepijko, S.A.; Shamonya, V.G. Electrical conductivity and electron emission from discontinuous metal films of homogeneous structure. *Thin Solid Films* **1980**, *76*, 359–378. [[CrossRef](#)]
107. Namba, Y. Resistivity and Temperature Coefficient of Thin Metal Films with Rough Surface. *Jpn. J. Appl. Phys.* **1970**, *9*, 1326–1329. [[CrossRef](#)]
108. Darevskii, A.S.; Zhdan, A.G. Real structure and electrical conductivity of island films of metals. *Sov. Microelectron.* **1978**, *7*, 356–359.
109. Bassewitz, A.V. Der Einfluß der Unterlage auf die Struktur und Leitfähigkeit metallischer Aufdampfschichten. *Z. Phys.* **1967**, *201*, 350–367. [[CrossRef](#)]
110. Jannesar, M.; Jafari, G.R.; Farahani, S.V.; Moradi, S. Thin film thickness measurement by the conductivity theory in the framework of born approximation. *Thin Solid Films* **2014**, *562*, 372–376. [[CrossRef](#)]
111. Palasantzas, G.; Zhao, Y.P.; Wang, G.C.; Lu, T.M.; Barnas, J.; De Hosson, J.T. Electrical conductivity and thin-film growth dynamics. *Phys. Rev. B* **2000**, *61*, 11109. [[CrossRef](#)]
112. Munoz, R.C.; Finger, R.; Arenas, C.; Kremer, G.; Moraga, L. Surface-induced resistivity of thin metallic films bounded by a rough fractal surface. *Phys. Rev. B* **2002**, *66*, 205401. [[CrossRef](#)]
113. Timalsina, Y.P.; Horning, A.; Spivey, R.F.; Lewis, K.M.; Kuan, T.S.; Wang, G.C.; Lu, T.M. Effects of nanoscale surface roughness on the resistivity of ultrathin epitaxial copper films. *Nanotechnology* **2015**, *26*, 075704. [[CrossRef](#)] [[PubMed](#)]
114. Ketenoglu, D.; Ünal, B. Influence of surface roughness on the electrical conductivity of semiconducting thin films. *Phys. A Stat. Mech. Appl.* **2013**, *392*, 3008–3017. [[CrossRef](#)]
115. Arenas, C.; Henriquez, R.; Moraga, L.; Muñoz, E.; Munoz, R.C. The effect of electron scattering from disordered grain boundaries on the resistivity of metallic nanostructures. *Appl. Surf. Sci.* **2015**, *329*, 184–196. [[CrossRef](#)]
116. Lim, J.W.; Mimura, K.; Isshiki, M. Thickness dependence of resistivity for Cu films deposited by ion beam deposition. *Appl. Surf. Sci.* **2003**, *217*, 95–99. [[CrossRef](#)]
117. Zhang, W.; Brongersma, S.H.; Richard, O.; Brijs, B.; Palmans, R.; Froyen, L.; Maex, K. Influence of the electron mean free path on the resistivity of thin metal films. *Microelectron. Eng.* **2004**, *76*, 146–152. [[CrossRef](#)]
118. Camacho, J.M.; Oliva, A.I. Surface and grain boundary contributions in the electrical resistivity of metallic nanofilms. *Thin Solid Films* **2006**, *515*, 1881–1885. [[CrossRef](#)]
119. Camacho, J.M.; Oliva, A.I. Morphology and electrical resistivity of metallic nanostructures. *Microelectron. J.* **2005**, *36*, 555–558. [[CrossRef](#)]
120. Fuchs, K. The conductivity of thin metallic films according to the electron theory of metals. *Math. Proc. Camb. Philos. Soc.* **1938**, *34*, 100–108. [[CrossRef](#)]
121. Sondheimer, E.H. The mean free path of electrons in metals. *Adv. Phys.* **1952**, *1*, 1–42. [[CrossRef](#)]
122. Soffer, S.B. Statistical Model for the Size Effect in Electrical Conduction. *J. Appl. Phys.* **1967**, *38*, 1710–1715. [[CrossRef](#)]
123. Mayadas, A.F.; Shatzkes, M.; Janak, J.F. Electrical resistivity model for polycrystalline films: The case of specular reflection at external surfaces. *Appl. Phys. Lett.* **1969**, *14*, 345–347. [[CrossRef](#)]
124. Mayadas, A.F.; Shatzkes, M. Electrical-Resistivity Model for Polycrystalline Films: The Case of Arbitrary Reflection at External Surfaces. *Phys. Rev. B* **1970**, *1*, 1382–1389. [[CrossRef](#)]

REVIEW:

THICKNESS MEASUREMENT METHODS FOR PHYSICAL VAPOR DEPOSITED ALUMINUM
COATINGS IN PACKAGING APPLICATIONS: A REVIEW

Coatings 2017, 7, 9

32 of 32

125. Rider, J.G.; Foxon, C.T.B. An experimental determination of electrical resistivity of dislocations in aluminium. *Philos. Mag.* **1966**, *13*, 289–303. [CrossRef]
126. Mayadas, A.F.; Feder, R.; Rosenberg, R. Resistivity and structure of evaporated aluminum films. *J. Vac. Sci. Technol.* **1969**, *6*, 690–693. [CrossRef]
127. Nakajima, H. *Porous Metals with Directional Pores*; Springer: Berlin, Germany, 2013.
128. Lux, F. Models proposed to explain the electrical conductivity of mixtures made of conductive and insulating materials. *J. Mater. Sci.* **1993**, *28*, 285–301. [CrossRef]
129. Siegel, A.C.; Phillips, S.T.; Dickey, M.D.; Lu, N.; Suo, Z.; Whitesides, G.M. Foldable printed circuit boards on paper substrates. *Adv. Funct. Mater.* **2010**, *20*, 28–35. [CrossRef]
130. Parfenov, E.V.; Yerokhin, A.L.; Matthews, A. Impedance spectroscopy characterisation of PEO process and coatings on aluminium. *Thin Solid Films* **2007**, *516*, 428–432. [CrossRef]
131. Dodd, C.V.; Deeds, W.E. Analytical Solutions to Eddy-Current Probe-Coil Problems. *J. Appl. Phys.* **1968**, *39*, 2829–2838. [CrossRef]
132. Hillmann, S.; Heuer, H.; Klein, M. Schichtdicken-Charakterisierung dünner, leitfähiger Schichtsysteme mittels Wirbelstromtechnik. In Proceedings of the DGZfP-Jahrestagung, Erfurt, Germany, 10–12 May 2010.
133. Suragus GmbH. EddyCus[®] TF Lab 4040. Available online: <https://www.suragus.com/en/products/thin-film-characterization/sheet-resistance/eddy-cus-tf-lab-4040/> (accessed on 29 December 2016).
134. Fiorillo, F. *Measurement and Characterization of Magnetic Materials*; Elsevier: Amsterdam, The Netherlands, 2004.
135. Hillmann, S.; Klein, M.; Heuer, H. In-line thin film characterization using eddy current techniques. *Stud. Appl. Electromagn. Mech.* **2011**, *35*, 330–338.
136. García-Martín, J.; Gómez-Gil, J.; Vázquez-Sánchez, E. Non-destructive techniques based on eddy current testing. *Sensors* **2011**, *11*, 2525–2565. [CrossRef] [PubMed]
137. Singh, S.K. *Industrial Instrumentation & Control*, 2nd ed.; McGraw-Hill Education: Noida, India, 2003.
138. Rajotte, R.J. Eddy-current method for measuring the electrical conductivity of metals. *Rev. Sci. Instrum.* **1975**, *46*, 743–745. [CrossRef]
139. Heuer, H.; Hillmann, S.; Roellig, M.; Schulze, M.H.; Wolter, K.J. Thin film characterization using high frequency eddy current spectroscopy. In Proceedings of the 9th IEEE Conference on Nanotechnology (2009 IEEE-NANO), Genoa, Italy, 26–30 July 2009.
140. Moulder, J.C.; Uzal, E.; Rose, J.H. Thickness and conductivity of metallic layers from eddy current measurements. *Rev. Sci. Instrum.* **1992**, *63*, 3455–3465. [CrossRef]
141. Angani, C.S.; Ramos, H.G.; Ribeiro, A.L.; Rocha, T.J.; Prashanth, B. Transient eddy current oscillations method for the inspection of thickness change in stainless steel. *Sens. Actuators A Phys.* **2015**, *233*, 217–223. [CrossRef]
142. Qu, Z.; Zhao, Q.; Meng, Y. Improvement of sensitivity of eddy current sensors for nano-scale thickness measurement of Cu films. *NDT E Int.* **2014**, *61*, 53–57. [CrossRef]
143. Mehrabad, M.J.; Ehsani, M.H. An Investigation of Eddy Current, Solid Loss, Induced Voltage and Magnetic Torque in Highly Pure Thin Conductors, Using Finite Element Method. *Procedia Mater. Sci.* **2015**, *11*, 412–417. [CrossRef]



© 2017 by the authors; licensee MDPI, Basel, Switzerland. This article is an open access article distributed under the terms and conditions of the Creative Commons Attribution (CC-BY) license (<http://creativecommons.org/licenses/by/4.0/>).

4. Research paper:

Comparison of thickness determination methods for physical-vapor-deposited aluminum coatings in packaging applications

Different methods used to determine the thickness of aluminum coatings do not necessarily agree on the same result. However, there are indications² that more information about the aluminum coating can be obtained by combining different thickness determination methods. Common methods include the determination of evaporation rates using a quartz crystal microbalance (QCM) and the quantitative analysis of dissolved aluminum ions by inductively-coupled plasma mass spectrometry (ICP-MS), which provide mass thickness values. Alternatively, atomic force microscopy (AFM) and interference provide geometrical values. Optical density (OD) and electrical resistance (ER) measure other properties.

The ability of these methods to determine the thickness of aluminum coatings applied to polyethylene terephthalate (PET) and paper by physical vapor deposition (PVD) was compared. When the aluminum was applied to paper, only the indirect mass thickness determination by ICP-MS generated reliable results. The observed differences between ICP-MS and other methods mainly resulted from the assumption that the relevant material constants are equal to their bulk values, but this is not the case: the microstructure of the deposited layer has an important effect and material constants depend on the film thickness. On polymer substrates, the electrical resistivity declines with increasing coating weight. But on paper substrates, the substrate porosity prevents the formation of a closed layer and introduces additional defects in the aluminum coatings. When ER is measured by eddy currents, such defects increase the ER and the effective resistivity by restricting the domains for eddy current formation. Accordingly, the measured effective resistivity of aluminum coatings on paper as reported here is approximately one order of magnitude higher than the same coatings on polymers due to the formed defects in the aluminum coating.

A **physical model** is needed to understand the relationship between substrate and resistivity and this offers the opportunity to **characterize the aluminum structure** in more detail. A particularly interesting question is how the resistivity is related to the substrate roughness, which **could reveal information about defects in the aluminum structure**.

² Lindner, M.; Schmid, M. Thickness measurement methods for physical vapor deposited aluminum coatings in packaging applications: A review. Coatings 2017.

RESEARCH PAPER:
COMPARISON OF THICKNESS DETERMINATION METHODS FOR PHYSICAL-VAPOR-DEPOSITED
ALUMINUM COATINGS IN PACKAGING APPLICATIONS

Author contributions: Martina Lindner: writing, supervision, design of experiments, data analysis. Florian Höflsauer and Julia Heider: experiments, data analysis. Matthias Reinelt and Horst-Christian Langowski: feedback concerning analysis and manuscript.

RESEARCH PAPER: COMPARISON OF THICKNESS DETERMINATION METHODS FOR PHYSICAL-VAPOR-DEPOSITED ALUMINUM COATINGS IN PACKAGING APPLICATIONS

Thin Solid Films 666 (2018) 6–14



Contents lists available at ScienceDirect

Thin Solid Films

journal homepage: www.elsevier.com/locate/tsf



Comparison of thickness determination methods for physical-vapor-deposited aluminum coatings in packaging applications



Martina Lindner^{a,b,*}, Florian Höflsauer^b, Julia Heider^{a,b}, Matthias Reinelt^b,
Horst-Christian Langowski^{a,b}

^a TUM School of Life Sciences, Chair for Food Packaging Technology, Technical University of Munich, Weihenstephaner Steig 22, 85354 Freising, Germany

^b Fraunhofer Institute for Process Engineering and Packaging IVV, Giggenhauser Straße 35, 85354 Freising, Germany

ARTICLE INFO

Keywords:

Thin film
Quartz crystal micro balance
Atomic force microscopy
Interference
Optical density
Electrical resistivity

ABSTRACT

Methods used to determine the aluminum coating thickness on polymer films may not measure the geometrical thickness directly but may instead measure the mass or other properties, thus leading to different thickness values. Common methods include the determination of evaporation rates using a quartz crystal microbalance (QCM) and the quantitative analysis of dissolved aluminum ions by inductively-coupled plasma mass spectrometry (ICP-MS), which provide mass thickness values. Alternatively, atomic force microscopy (AFM) and interference (INT) across the step of a partially removed aluminum layer yield geometrical values, and optical density (OD) and electrical resistance (ER) measure other properties. We compared the ability of these methods to determine the thickness of aluminum coatings applied to polyethylene terephthalate (PET) and paper by physical vapor deposition. We measured ER using four-point probes, five-point probes, and eddy currents. ER and OD achieved high precision but low accuracy, showing that the resistivity and absorption coefficients of thin aluminum layers can deviate from bulk constants. When the constant values were adjusted, both methods achieved higher accuracy. ICP-MS and QCM values were similar, when a geometrical model was applied, and in comparison AFM and INT showed low precision but high accuracy. When the aluminum was applied to paper instead of PET, only ICP-MS generated reliable results. In summary, the values derived using these different methods are only in agreement when method-specific constants such as absorption coefficients and resistivity are suitably modified.

1. Introduction

The thickness and consistency of aluminum coatings have a strong impact on performance. In packaging applications, performance may be defined as the effectiveness as a gas barrier or the optical impression of decorative aluminum coatings. Gas permeation has been shown to decrease with increasing aluminum thickness up to approximately 60 nm [1] and only decreases further when the coating is 1–3 orders of magnitude thicker [2,3]. However, when measuring the relationship between permeability and aluminum thickness, the values reported and the techniques used to measure the thickness of the aluminum layer varied widely [2,4–10].

Coating thickness can be measured using methods that determine mass, geometry and other properties based on parameters such as electrical conductivity, light transmission, or the quantity of aluminum ions [11], but it is unclear whether the different instruments generate equivalent values (Fig. 1). For each type of instrument, some of the

factors that influence the measurement are already known, and are summarized below. More detailed information can be found elsewhere [12].

Quartz crystal microbalances (QCMs) determine the “total mass thickness” of the deposited material based on the weight of the deposited aluminum, which includes both aluminum atoms and foreign atoms such as oxygen. This technique is accurate to within ~2%, but accuracy declines with increasing aluminum thickness [13–15]. Inductively-coupled plasma mass spectrometry (ICP-MS) similarly determines the “mass thickness” but in contrast to QCM only measures the pure aluminum. This is achieved by dissolving aluminum oxide and pure aluminum in sodium hydroxide before measuring the aluminum concentration [6]. The range of detectable concentrations is limited to approximately 0.001–0.1 µg/l for aluminum in aqueous solutions [16], and the results can be affected by interference between atoms with the same m/z ratio [17].

Atomic force microscopy (AFM) and interference (INT) determine

* Corresponding author at: Fraunhofer Institute for Process Engineering and Packaging IVV, Giggenhauser Straße 35, 85354 Freising, Germany.
E-mail address: martina.lindner@ivv.fraunhofer.de (M. Lindner).

<https://doi.org/10.1016/j.tsf.2018.09.032>

Received 4 April 2018; Received in revised form 10 September 2018; Accepted 12 September 2018

Available online 15 September 2018

0040-6090/© 2018 The Authors. Published by Elsevier B.V. This is an open access article under the CC BY-NC-ND license

(<http://creativecommons.org/licenses/by-nc-nd/4.0/>).

RESEARCH PAPER: COMPARISON OF THICKNESS DETERMINATION METHODS FOR PHYSICAL-VAPOR-DEPOSITED ALUMINUM COATINGS IN PACKAGING APPLICATIONS

M. Lindner et al.

Thin Solid Films 666 (2018) 6–14

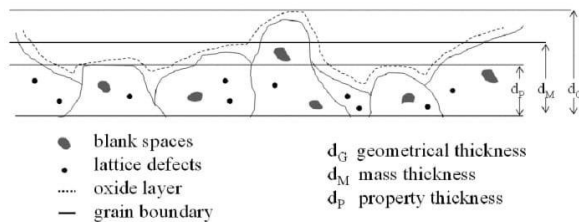


Fig. 1. Mass, geometrical and property thickness can vary widely because they are derived from diverse material characteristics such as light transmission, electrical resistance, or the quantity of metal ions.

the “geometrical thickness” of a sample. They capture the overall thickness of aluminum and aluminum oxide on a step produced by partial removal of the deposited aluminum layer. For INT measurements, both surfaces (substrate and aluminum) are covered with an additional 10-nm gold film to equalize the reflection characteristics. If the surface is rough, the reported thickness is higher than the average thickness of the layer [18]. Similarly, AFM does not separately record inclusions and voids, and the interaction between the AFM cantilever and the surface (topography and hardness) can affect the profile and the corresponding thickness values [19].

Finally, optical density (OD) and eddy current (EC) measure an indirect “property thickness”. When using the OD method, a minimum transmission of ~0.03% (OD = 3.5) is useful [20]. Although greater thicknesses can be distinguished by using more sensitive equipment, the error increases due to heterogeneities and defects. The OD also decreases over time because the light-absorbing aluminum reacts with oxygen to form transparent aluminum oxide [4]. Furthermore, the OD is defined by the absorption coefficient α and the related extinction coefficient k (see Eq. (5)), and these values are highly dependent on the process conditions, grain size, coating thickness, and wavelength of the incident light [6,21,22]. When four-point (4P) and five-point (5P) probes are used to measure the electrical resistance (ER), a variety of factors can increase the resulting values. First, the instrument’s electrical contacts may scratch the surface and cause cracks in the material. Second, oxide layers with a resistivity 20 orders of magnitude higher than the pure metal can act as an isolator between the aluminum and the contacts. Third, electrons can be scattered by the surface (particularly a rough surface) and by grain and island boundaries [23–30]. When the sheet resistance is measured by contactless EC methods, the values are influenced by the presence of aluminum oxide due to its extremely high resistivity. Furthermore, the sensitivity of EC measurements also depends on many other factors, such as the properties of the electromagnetic excitation field [31–33], the sensor-to-sensor distance, and the material thickness [34].

The aim of this study was to compare the thickness measurements produced by OD, electrical sheet resistance (4P, 5P and EC), QCM, ICP-MS, AFM and INT in order to determine whether the resulting values are similar, whether any differences can be explained and whether any of the methods are affected by the substrate beneath the aluminum layer, which in this study was either the polymer polyethylene terephthalate (PET) or paper. We use the data we obtained to draw conclusions about the structure of the aluminum layer.

These are important considerations because thickness and related parameters such as gas barrier efficiency, costs, and machine speeds are regularly compared using values derived using different methods. This can lead to misunderstandings and misinterpretations, and our findings will therefore be useful for researchers working on inorganic gas barrier coatings and industrial metallizers.

The data flow in this study is summarized in Fig. 2. The thickness determined by ICP-MS was used as a reference value for all the other methods. We then determined the material constants (absorption coefficient and resistivity) from OD, ER and ICP-MS reference values in

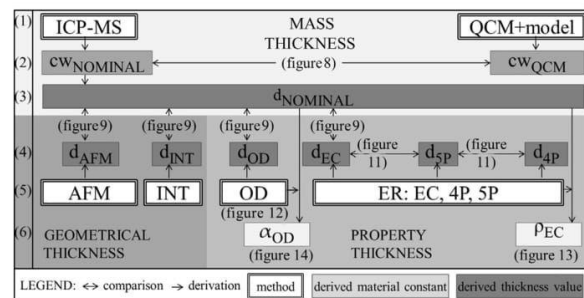


Fig. 2. Workflow for the experiments described in this article. Derivation of coating weight $cw_{NOMINAL}$ and cw_{QCM} from ICP-MS and QCM + model (1), comparison of both (2), derivation of a nominal thickness $d_{NOMINAL}$ from ICP-MS (3) and comparison of $d_{NOMINAL}$ with other methods (4,5), derivation of material constants (6) from $d_{NOMINAL}$ in combination with measured properties (5).

order to characterize the structure of the aluminum layer.

2. Materials and methods

2.1. Physical vapor deposition

The aluminum was applied by physical vapor deposition using an electron beam heater. The coating was applied in a 0.5 m × 1.0 m box coater (L560UV; Leybold Vacuum GmbH, Germany) at the Fraunhofer IVV (Fig. 3, right). This coater had been adapted for the roll-to-roll coating of polymer webs by adding winding equipment (deposition roll, unwinding, and rewinding; Lenze, Germany). The equipment was managed using L560 VAC Cluster Tool Controller (AIS Automation GmbH, Germany) software. The box coater was equipped with an E2M175 rotary vacuum pump (160 m³/h) and an EH500 roots pump (505 m³/h) both supplied by Edwards Ltd., UK, and a turbomolecular pump (850–1150 l/s, TMP 1000; Leybold Vacuum GmbH, Germany) to create a vacuum in the 10^{−4} Pa range. Remaining moisture in the chamber was extracted using a Meissner cold trap, and the deposition roll was water-cooled. The pressure was determined using a PPT-100 Pirani gauge and a HPT-100 hot cathode Bayard–Alpert–Pirani wide-range gauge, both from Pfeiffer GmbH, Germany. The EV M-10 electron beam source (270° configuration) was fitted with a Genius Carrera 10 kW high-voltage supply, all supplied by Ferrotec, Germany.

The aluminum was 99.98% pure and the coating thickness was varied by changing the web speed from 0.5 to 3.5 m/min in steps of 0.5 m/min at an evaporation rate of 4–4.5 nm/s. During the evaporation process, the pressure in the chamber was maintained at 5.6–7·10^{−4} Pa. The moisture content of paper substrates is typically approximately 5% under ambient conditions, thus making it difficult to achieve a high vacuum. Therefore, the paper (Metalkote 65 g/m²; Munksjö, Sweden) was dried at 50 °C for 4 days and then at 75 °C for 3 h in a Heratherm Oven (Thermo Fisher Scientific, USA) before the aluminum coating was applied. The polymer substrate was a 50- μ m polyethylene terephthalate (PET) sheet (Melinex 401; DuPont Teijin Films, UK). The evaporation rate was monitored with a QCM (008-010-G10; Inficon, USA). The positioning of the balance in the vacuum chamber is described in Section 2.2.

2.2. Model for gas cloud expansion and aluminum thickness distribution

The crucible from which the aluminum vapor expanded was positioned immediately below the roll. The thickness distribution in cross direction (CD) was estimated on the basis of geometrical assumptions by considering two factors: (a) the expected gas cloud expansion and resulting thickness distribution in CD (Fig. 3, left); and (b) the web

RESEARCH PAPER:
COMPARISON OF THICKNESS DETERMINATION METHODS FOR PHYSICAL-VAPOR-DEPOSITED ALUMINUM COATINGS IN PACKAGING APPLICATIONS

M. Lindner et al.

Thin Solid Films 666 (2018) 6–14

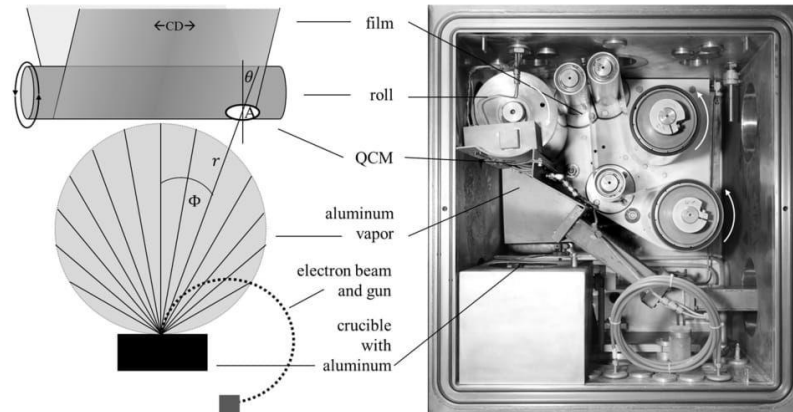


Fig. 3. Device schematic in CD (left) and an image of the evaporation chamber (right).

speed, which affects the time available for aluminum deposition in machine direction (MD) (Fig. 3, right). The aluminum thickness was related to the deposition rate, which was monitored in-line using the QCM, positioned on the right-hand side of the roll.

2.2.1. Gas cloud expansion and the resulting thickness distribution in cross direction

We assumed that the aluminum would disperse from the surface source with an angular distribution. Given that the electron beam produces a small pond of molten aluminum, the aluminum atoms are likely to originate from a small area at a constant mass evaporation rate M_e [g/s]. A certain fraction M_A would be deposited on the polymer web surface A [m²] at distance r [m] (Fig. 3). According to Lambert's Cosine Law [35] and Martin Knudsen [36] the number of atoms evaporated per second would depend on the angle Φ between the normal and line of sight, the cosine of the angle Θ between the observer's line of sight and the normal of surface A , and a factor n related to the electron beam energy input [37] and the crucible geometry [38]. Higher energy inputs and crucibles with smaller diameters or greater depths lead to more elliptical vapor clouds, and thus a more directional deposition profile with greater thickness variations in CD. Therefore, the number of atoms, i.e. the mass flow rate M_A condensing on the surface A , can be calculated as shown in Eq. (1):

$$\frac{M_A}{A} = \frac{M_e (n + 1) \cos^n \Phi \cdot \cos \Theta}{2\pi r^2}. \quad (1)$$

2.2.2. Web speed and deposition time

A slit blind shielded the substrate from evaporated aluminum atoms that would impact the surface at shallow angles. The slit blind width defines the distance s in MD over which the evaporated atoms hit the polymer's surface. For a given web speed v [m/s], the aluminum can condense on a web of length s [cm] only for a certain time t [s]. Thus, the final aluminum thickness can be calculated by considering the time t and aluminum density δ as follows:

$$d = \frac{M_A}{A \cdot \delta} \cdot \frac{s}{v} = \frac{M_A}{A \cdot \delta} \cdot t. \quad (2)$$

2.3. Chemical stripping and mass spectrometry

The sample surface, volume, and dilution factors were adjusted on the basis of the expected aluminum concentration: for each sample, with a surface A of 1.10 cm² or 1.15 cm² (samples cut along MD), the aluminum was stripped off using 50, 30, 20, 10 or 5 ml of 1.0 M sodium hydroxide (Chemsolute 1.0 mol/l; Th. Geyer GmbH, Germany). The

volume of 1.0 M sodium hydroxide was defined as the sample volume V . After 1 h, the liquid aluminumous samples were mixed in the tubes and then diluted with double-distilled water to a dilution factor f_d of 1:10 or 2:10. The amount of aluminum in the diluted samples was then determined by mass spectrometry using an Agilent 770 × ICP-MS (Agilent Technologies, USA). A standard aluminum solution (ICP multi-element standard solution IV 1.11355.0100; Merck, Germany) with an aluminum concentration of 1000 mg/l was used for calibration. This standard solution was diluted with double-distilled water to 0.10, 0.20, 0.25, 0.30, 0.50, 0.75, 1.00, 1.50, 2.00, 3.00 and 3.50 mg/l aluminum, and the calibration lines were used to correlate the given concentration with the signal intensity. This correlation was then used to calculate the concentration c [mg/l] of aluminum.

The aluminum layer thickness d_{NOMINAL} for the given stripped-off sample area A was calculated on the basis of the determined aluminum concentration and by assuming a literature bulk density ρ_L value of 2.7 g/cm³ [39]:

$$d_{\text{NOMINAL}} = \frac{c \cdot f_d \cdot V}{A \cdot \rho_L}, \quad (3)$$

and the coating weight cw [g/m²] was calculated as

$$cw = d_{\text{NOMINAL}} \cdot \rho_L. \quad (4)$$

Values derived from ICP-MS measurements are indexed with NOMINAL hereafter and are used as reference values in this article.

2.4. Atomic force microscopy

Adhesive strips were placed on the substrate film in CD over the whole web width with a spacing of 1 m. After the aluminum coating was applied, the adhesive strip was removed to obtain a clear edge between the coated and non-coated surface parts. The measurements were performed close to the positions used for EC and OD measurements (within 1 cm²). The measurement positions were chosen to cover a wide range of aluminum thicknesses. The accessible edge was scanned over an area of 60 μm × 60 μm with an alpha500 atomic force microscope (WITec GmbH, Germany) in pulsed force mode, with 256 points per line and 265 lines per image, with data acquired from forward and backward scans. Three height profiles were extracted for the surface at random positions perpendicular to the edge (Project Four software; WITec GmbH). The geometrical data were then exported to OriginPro (OriginLab Corporation, USA) for further calculations. The thickness of the evaporated aluminum layer was calculated from the difference in the height profiles of the coated and non-coated substrate films (Fig. 4). We ignored the peak in the middle of the profile caused when the removal of the adhesive strips lifted the aluminum layer. Two linear

RESEARCH PAPER: COMPARISON OF THICKNESS DETERMINATION METHODS FOR PHYSICAL-VAPOR-DEPOSITED ALUMINUM COATINGS IN PACKAGING APPLICATIONS

M. Lindner et al.

Thin Solid Films 666 (2018) 6–14

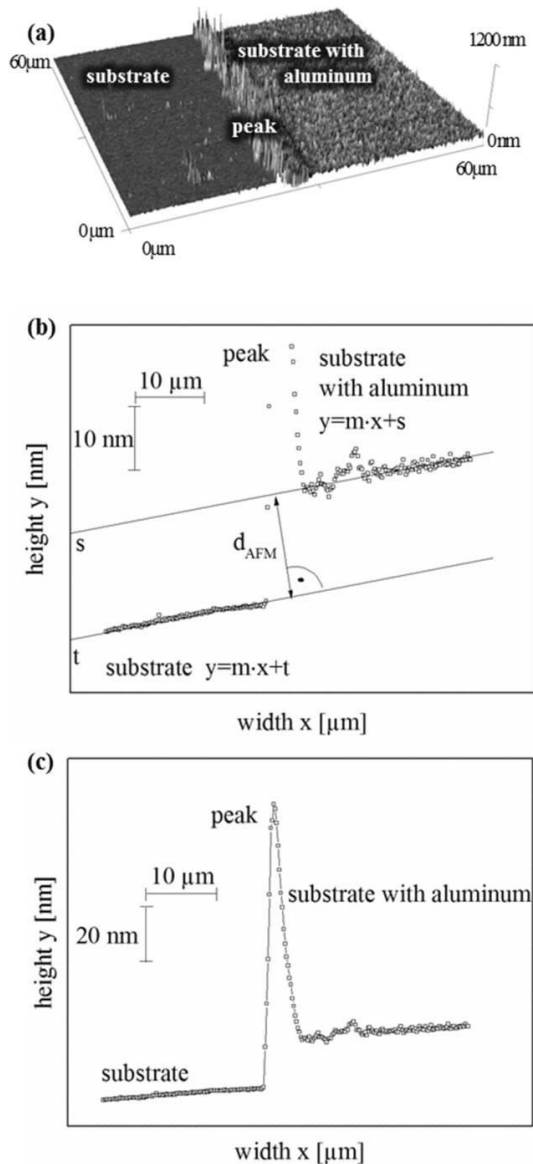


Fig. 4. Example of surface topography (a), profile extracted from it (b) and a magnified view showing the determination of d_{AFM} (c).

functions with the same slope were fitted to represent the “substrate” and “substrate with aluminum” surfaces (Fig. 3), and the thickness d_{AFM} was calculated from the normal distance between the two functions.

2.5. Optical density

The OD was measured six times within 1 cm^2 with a DDM 4 densitometer (Theimer, Germany), very close (within 1 cm^2) to the edge used for the AFM and INT measurements. For the paper substrates, the OD of the pure paper ($OD = 1$) was subtracted from the OD of the aluminum-coated paper. These measurements were taken under red light (absorption peak wavelength $\lambda = 615\text{ nm}$). An extinction coefficient for the deposited aluminum was assumed ($k_1 = 6.16$) based on the linear interpolation of the literature values for k and λ

($100\text{ nm} < \lambda < 900\text{ nm}$; $R^2 = 0.9894$) [21,40,41]. The thickness was calculated as follows:

$$d_{OD} = \frac{OD \cdot \lambda}{k_1 \cdot 4 \cdot \pi} \quad (5)$$

The real absorption coefficient α_r was calculated from the thickness deduced by mass spectrometry $d_{NOMINAL}$ as

$$\alpha_r = \frac{OD}{d_{NOMINAL}} \quad (6)$$

This was then used to calculate the real extinction coefficient k_r , given a light wavelength λ of 615 nm:

$$k_r = \frac{\alpha_r \cdot \lambda}{4 \cdot \pi} \quad (7)$$

2.6. Electrical resistance

The resistance of electrical conductors depends on their geometry and electrical resistivity, which can be influenced by side-effects such as electron scattering on surfaces and grain boundaries, surface roughness, and island growth. By measuring the resistance R of aluminum while knowing length l , width b , and resistivity ρ , the thickness d can be calculated as follows:

$$d = \frac{\rho \cdot l}{R \cdot b} = \frac{\rho}{R_{\square}} \quad (8)$$

In the 4P and 5P methods, l and b were equivalent due to the nature of the measurement setup, so they cancelled each other. The resulting resistance is called the electrical sheet resistance and is subscripted with a square (R_{\square}). The sheet resistance R_{\square} was also determined by EC. The literature bulk value of $\rho_1 = 0.027\ \Omega \cdot \text{mm}^2/\text{m}$ [39] was used to calculate the thickness.

2.6.1. Four-point probe

The experimental setup described previously [1] was used for the 4P measurements, which were carried out three times. Four copper plates were arranged (Fig. 5), and the contact areas were covered with gold. The length l and width b of the area between the inner contacts were both 10 cm. A known current was introduced over the two outer plates, and the potential difference and thus the resistance $R_{\square 4P}$ was measured over the two inner plates using a System Multimeter PM 2535 (Philips, Germany). This setup excludes the influence of the contact resistance. Values derived from 4P measurements are shown with a 4P subscript hereafter.

2.6.2. Five-point probe

The experimental setup shown in Fig. 6 was used for the 5P measurements. The distances l and b were both 10 cm. The electrode contacts were spring-loaded and covered with gold. The current was introduced via the central contact and the electrical potential, and thus the resistance R_{\square} , was measured by using a UT71E multimeter (TME,

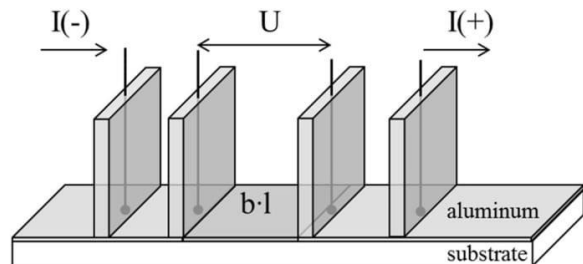


Fig. 5. Experimental setup for the four-point probe (4P).

RESEARCH PAPER: COMPARISON OF THICKNESS DETERMINATION METHODS FOR PHYSICAL-VAPOR-DEPOSITED ALUMINUM COATINGS IN PACKAGING APPLICATIONS

M. Lindner et al.

Thin Solid Films 666 (2018) 6–14

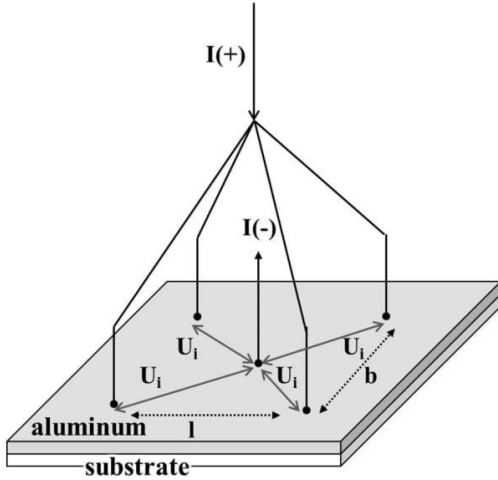


Fig. 6. Experimental setup for the five-point probe (5P).

Germany) at the outer contacts. These measurements were carried out three times. Values derived from 5P measurements are shown with a 5P subscript hereafter.

2.6.3. Eddy current

The EC measurements were performed using an EddyCus TF lab 4040 (Suragus, Germany), capturing an area of 4 mm × 5 mm. The ECs induced in the aluminum by a primary coil create a magnetic field and a current in a secondary coil, which was measured to determine the ER of the aluminum coating [12]. Values derived from EC measurements are shown with an EC subscript hereafter.

The measurements were carried out five times. For comparison with the 4P and 5P measurements, the same area of the surface was used for the EC measurements and 36 data points were acquired (Fig. 7).

The real material-specific resistivity ρ_r was calculated from the thickness d_{NOMINAL} deduced by ICP-MS and the measured electrical sheet resistance $R_{\text{■EC}}$:

$$\rho_r = d_{\text{NOMINAL}} \cdot R_{\text{■EC}} \quad (9)$$

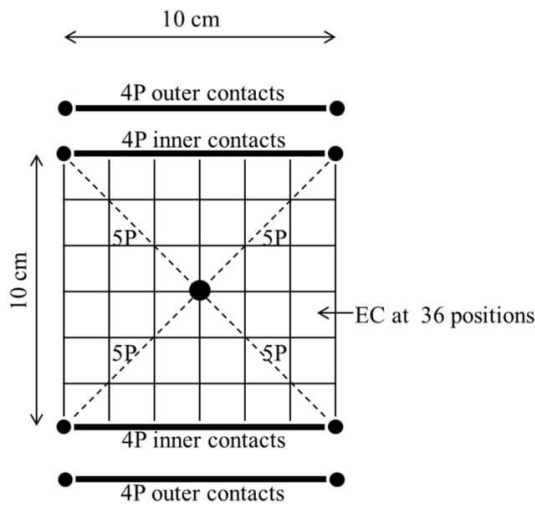


Fig. 7. Overview of the measurement area for the 4P, 5P and EC measurements.

2.7. Light interference

The INT measurements were performed as previously described [42,43] at a wavelength λ of 550 nm using a Leitz Diaplan microscope and a DFC295 digital color camera fitted with an Leitz Wetzlar F2246, 3.2/5/10 interference lens (all supplied by Leica GmbH, Germany). To achieve the same reflection and phase shift for both the aluminum coated and the non-metallized part of the PET substrate, a ~10-nm layer of gold was sputtered onto both surfaces using a Hummer JR Technics sputter system (Anatech, USA). The difference between the interference band distances a and the offset between the interference bands a' was used to calculate the aluminum thickness (d_{INT}) [nm] as follows:

$$d_{\text{INT}} = \frac{\lambda \cdot a'}{2 \cdot a} \quad (10)$$

The measurements were carried out three times on the same samples that were used for the AFM measurements. Values derived from INT measurements are shown with an INT subscript hereafter.

2.8. Statistical methods

All data were tested against a Gaussian distribution using the Kolmogorov–Smirnov and Anderson–Darling tests, and any significant differences were tested using t -tests ($\alpha = 0.05$). Outlier tests were performed as specified by Hampel using Visual XSel 13.0 (CRGraph, Germany). The statistical measures we used were the arithmetic mean and standard deviation.

3. Results and discussion

Among the methods we used, only AFM and INT provide geometrical thickness data, whereas the other methods derive the thickness from measurements such as the resistance, OD, or mass of deposited aluminum. We decided to use the ICP-MS values as a reference (d_{NOMINAL} , cw_{NOMINAL}) because this technique completely dissolves the aluminum layer and the values describe the amount of pure aluminum that is physically present on the substrate surface. We adapted the model for the aluminum thickness distribution (which includes the QCM data) to the ICP-MS results for comparison, allowing the analysis and interpretation of the results generated by all the other measurement techniques, including a comparison of the three electrical sheet resistance methods. Finally, we investigated the effect of the substrate material on the measured values and determined the material constants.

3.1. Model of the angular aluminum thickness distribution (QCM) and comparison with ICP-MS values

Fig. 8 shows the dependence of the ICP-MS results, including the aluminum coating weight cw_{NOMINAL} [g/m²] and thickness d [nm], on the web speed v and position f . The reproducibility of the thickness measurements obtained via ICP-MS by QCM was examined by inserting the QCM data into the geometrical model and using the parameter n as a fit factor. In Eq. (1), all factors other than n are fixed. To determine n , d_{NOMINAL} values were normalized and n was fitted to the normalized function, yielding a value of 1.6. M_A was then calculated from the deposition rate R [nm/s], QCM surface area A , and ideal density δ_{bulk} of aluminum [g/m³] as follows:

$$M_A = R \cdot A \cdot \delta_{\text{bulk}} \quad (11)$$

Finally, M_e was calculated by inserting the QCM values for M_A and A into Eq. (1), yielding a value of 0.0039 g/s.

The model accurately represents the angular distribution and the effect of the web speed, leading to the conclusion that the d_{NOMINAL} variation in CD can be calculated on the basis of simple geometric

RESEARCH PAPER: COMPARISON OF THICKNESS DETERMINATION METHODS FOR PHYSICAL-VAPOR-DEPOSITED ALUMINUM COATINGS IN PACKAGING APPLICATIONS

M. Lindner et al.

Thin Solid Films 666 (2018) 6–14

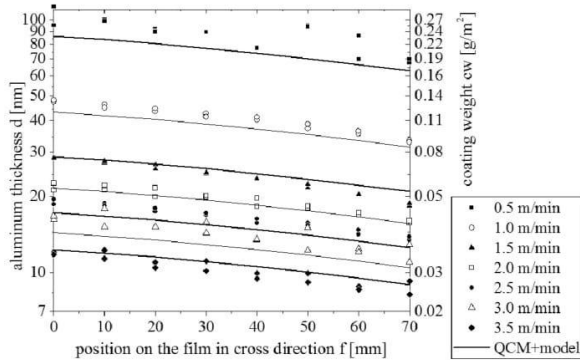


Fig. 8. Aluminum thickness comparison showing the modeled values with the factor $n = 1.6$ and ICP-MS values. ICP-MS values are well represented by the model assumptions.

assumptions and by using the QCM output values.

3.2. Comparison of the measurement techniques

Fig. 9 compares the thickness values determined using all the techniques (except 4P and 5P, which are discussed in the next section). The x-axis shows the coating weight $cw_{NOMINAL}$ and thickness $d_{NOMINAL}$ deduced from the ICP-MS measurements. Ideally, the correlation between coating weight and aluminum thickness should be linear, similar to that for $d_{NOMINAL}$. We found that d_{EC} and d_{OD} achieve high precision but low accuracy, whereas d_{AFM} and d_{INT} achieve low precision but better accuracy. Each technique is discussed in detail below.

Although neither the d_{AFM} nor the d_{INT} values were accurate, they reflected similar fluctuations and were thus internally consistent, and both measured the geometrical thickness precisely. However, the AFM values were always higher than the INT values, and this systematic difference appears to be method-dependent. We reasoned that AFM is more sensitive than INT to unevenness and peaks on the surface. The d_{INT} and d_{AFM} values fell within a range from 0.6 times lower to 1.5 times higher than $d_{NOMINAL}$. Such variations can be explained by three observations. First, both techniques are strongly affected by the

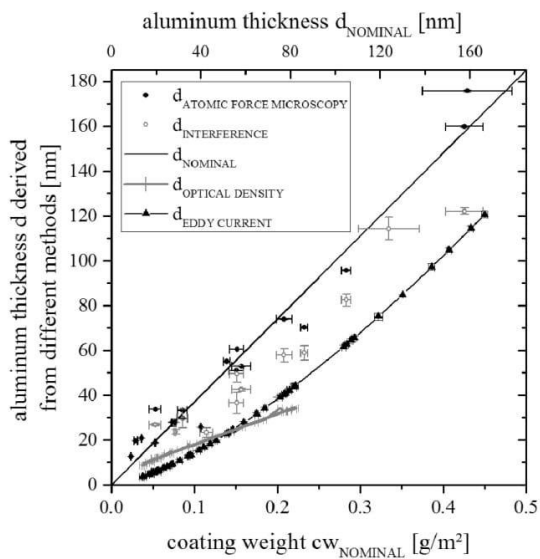


Fig. 9. Overview of the comparative results from all measurement techniques.

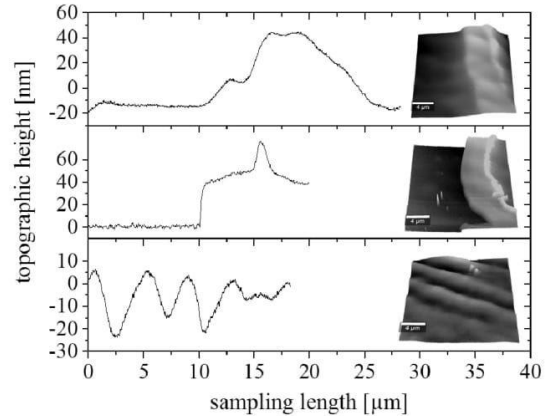


Fig. 10. Cross sections of uneven PET surface after removal of the adhesive tape.

aluminum surface. For the interference measurements, the surface was coated with a thin gold layer. However, the aluminum and aluminum oxide surface is not a perfectly crystalline material, hence surface roughness, gaps in the sputtered gold coating, and uneven gold layer growth all affect the recorded values [18]. Second, lower values can be explained by the proven remains of the adhesive tape on the polymer surface and waves in the polymer caused by tape removal (Fig. 10). These remains can reduce the measured geometrical thickness. Third, during the evaporation process, the deposition rate was not constant but varied by $\pm 8\%$ over the course of a few seconds. The ICP-MS value represented the mean value over a larger surface (10–15 cm^2), whereas AFM and INT generated very localized ($< 60 \mu m$) measurements that could vary with the evaporation rate.

In contrast, d_{OD} achieved very high precision. A coating weight of $0.25 g/m^2$ corresponds to an OD of ~ 3.5 , which is the upper measurement limit of the densitometer. At higher coating weights, the transmitted light intensity I_T becomes too low for the light sensor to measure accurately. This is why coating weights higher than $0.25 g/m^2$ could not be measured using this technique.

The d_{EC} values were up to four times lower than $d_{NOMINAL}$, but the error decreased with increasing coating weight. The error could be caused by the insulating character of the aluminum oxide and the porosity (voids, crystallinity) of the aluminum coating. This will be discussed in more detail in Sections 3.4 and 3.5.

3.3. Comparison of the electrical measurement methods

The ER of samples with different thicknesses of aluminum on PET were measured using three different methods (4P, 5P and EC), covering the same $100 cm^2$ surface in all cases (see Section 2.6). The thickness was calculated using Eq. (8). In Fig. 11, the y-axis shows the recorded values, whereas the x-axis shows the reference coating weight $cw_{NOMINAL}$ and thickness $d_{NOMINAL}$ deduced from the ICP-MS measurements. Ideally, the correlation between the coating weight and aluminum thickness should be linear. However, the nominal values ($d_{NOMINAL}$) were up to 3.8 times higher than the measured values on PET, although this error declined with increasing coating weight. A more detailed interpretation of this observation is provided in Section 3.5.1.

The values measured by 4P, 5P and EC were the same (significance $\alpha = 0.05$) up to a coating weight of $0.15 g/m^2$ on PET. At coating weights $> 0.15 g/m^2$, the EC values were 30–40% higher than for 4P or 5P. These differences may reflect the varying effect of material heterogeneity on the measuring method given that microstructures are known to alter EC, 4P and 5P readings [44,45]. However, the reason for

RESEARCH PAPER: COMPARISON OF THICKNESS DETERMINATION METHODS FOR PHYSICAL-VAPOR-DEPOSITED ALUMINUM COATINGS IN PACKAGING APPLICATIONS

M. Lindner et al.

Thin Solid Films 666 (2018) 6–14

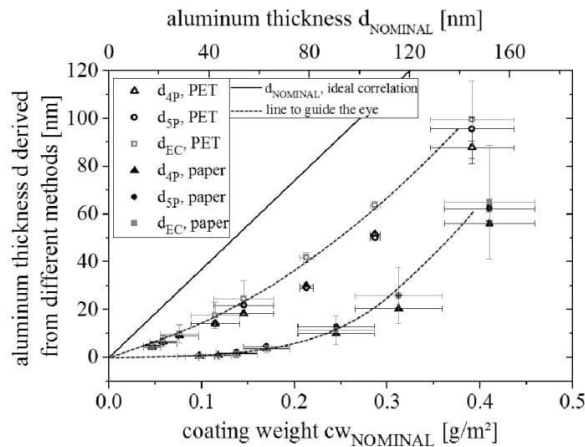


Fig. 11. Aluminum thicknesses on PET and paper as determined by 4P, 5P and EC measurements.

the differences we observed cannot be determined based on the data we collected.

3.4. Effect of the substrate material on the measured values

3.4.1. Electrical resistance

Fig. 11 shows the thickness values obtained by EC, 4P and 5P for two different substrate materials: PET and paper. The recorded values were up to 15 times higher on PET, indicating that the same measurement technique can lead to completely different values when used on different substrates. The reason for this can be found in the structure of the aluminum coating: the typical surface roughness of PET shows nanometer-scale variations, whereas the roughness of the paper shows variations in the micrometer range [46]. Given that nanometer-scale aluminum coatings cannot build a complete layer on such a rough surface, the coating is interrupted by voids and defects, thus leading to higher sheet resistance and lower values for aluminum thickness [47].

Surprisingly, the differences between the three measurement techniques were similar for both paper and PET, indicating that the aluminum microstructure (heterogeneity, voids and defects) cannot explain the difference between the contact and contact-free methods. Instead, the primary difference between the methods seems to be related to internal device resistances.

3.4.2. Optical density

The OD was measured for paper and PET films with various coating thicknesses as described in Section 2.5. At the same coating weight ($cw_{NOMINAL}$), the OD and thus the calculated aluminum thickness d_{OD} was up to four times higher on PET than on paper (Fig. 12). As discussed for the ER-based methods, the resulting values were dependent on the substrate or the substrate's effect on the aluminum coating structure. In this case, the micrometer-scale roughness of the paper led to defects in the aluminum coating that allowed more light to pass through, resulting in lower ODs and in turn lower derived thickness values. The uncoated paper presented a relatively high baseline ($OD = 1$) so the measurement limit of $OD = 3.5$ was reached at a lower $d_{NOMINAL}$. This explains why the OD curve for paper inclines at a lower coating weight of 0.1 g/m^2 .

3.5. Determination of material constants

In the previous sections, we showed that the substrate material affects the aluminum structure, which in turn influences the material characteristics (resistivity, absorption coefficient), measured values,

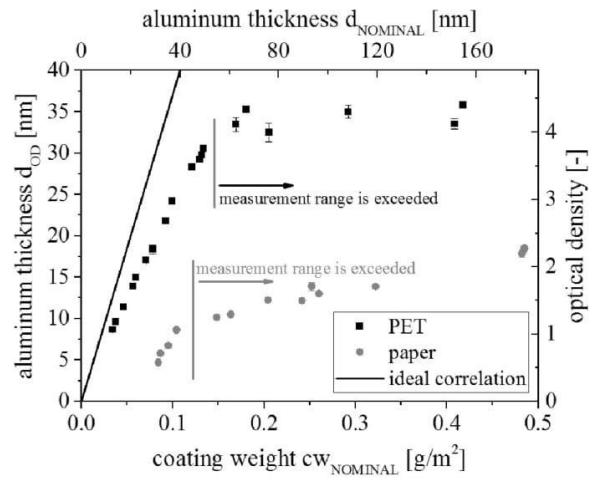


Fig. 12. Aluminum thicknesses for PET and paper substrates, from OD measurements.

and deduced aluminum coating thicknesses. This agrees with earlier reports describing how the material-specific properties of thin films can deviate from the bulk properties [38,48–50]. The next step was to calculate these material constants. In each case, $d_{NOMINAL}$ was used as the reference value because it describes the total amount of aluminum available. By combining this reference value with the corresponding measured sheet resistance R_{\square} and OD, we were able to calculate the equivalent resistivity ρ_r , absorption α_r , and extinction k_r coefficients (see Sections 2.5 and 2.6).

3.5.1. Electrical resistivity (on PET and paper)

The electrical resistivity ρ_r was calculated using Eq. (9). As shown in Fig. 13, the resistivity cannot be assumed to be constant when using this thickness determination technique. On PET, the resistivity declined with increasing coating weight, approaching a value of $\sim 5 \mu\Omega\text{-cm}$, which is twice the bulk value of $2.7 \mu\Omega\text{-cm}$ reported in the literature [51]. The higher resistivity can be caused by electrons being deflected at grain boundaries, the random arrangement of grains, and/or the limited number of connecting paths [52]. As the coating thickness

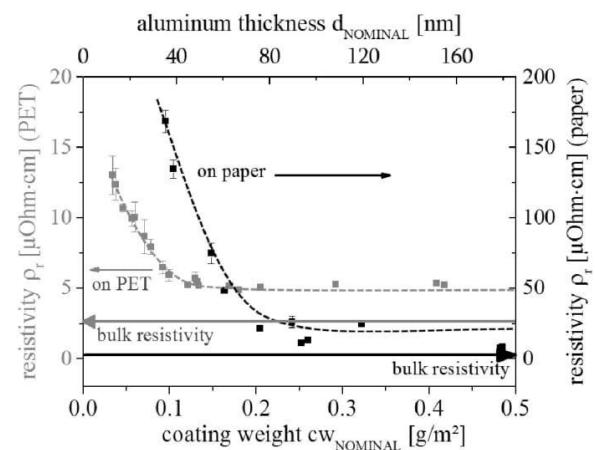


Fig. 13. Surface resistivity values for different coating weights on PET (left scale) and paper (right scale) in comparison to bulk resistivity [55]. Minimum resistivity on PET is approximately two times higher and on paper three times higher than bulk resistivity.

RESEARCH PAPER: COMPARISON OF THICKNESS DETERMINATION METHODS FOR PHYSICAL-VAPOR-DEPOSITED ALUMINUM COATINGS IN PACKAGING APPLICATIONS

M. Lindner et al.

Thin Solid Films 666 (2018) 6–14

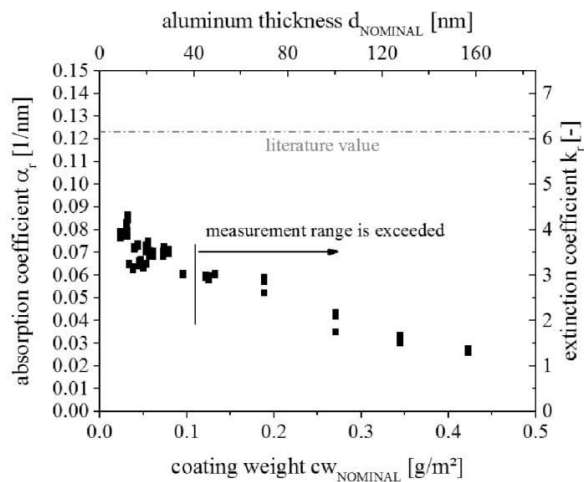


Fig. 14. Extinction and absorption coefficients for different coating weights on PET.

increases, the grain sizes increase, the connecting paths become more abundant, and there are fewer deflections, thus leading to a lower resistivity [53]. In our experiments, the minimum resistivity occurred at a coating weight of $\sim 0.12 \text{ g/m}^2$, and no further improvement was achieved at higher coating weights. On paper, the surface roughness prevented the formation of a complete layer and introduced additional defects, thus increasing the resistance and resistivity. Accordingly, the resistivity values were approximately one order of magnitude higher than on PET, and minimum resistivity values comparable to those recorded on PET were only achieved at 0.5 g/m^2 .

The resistivity was not constant on PET up to a thickness of 40 nm. However, 40 nm is typical for aluminum coatings that are applied in packaging applications to create gas barriers. Therefore, the use of ER to determine thickness can only be recommended if the user is aware of this error and can correct the resistivity values. Furthermore, the recorded values depend strongly on substrate roughness but can still be correctly interpreted if this factor is taken into account, e.g. by preparing calibration curves for each substrate material.

3.5.2. Extinction and absorption coefficients (on PET)

The extinction (k_r) and absorption (α_r) coefficients were calculated by introducing the measured OD and corresponding d_{NOMINAL} values (Fig. 14) into Eqs. (6) and (7). The literature provides the following extinction coefficients: 4–9 for wavelengths of 0.4–0.9 μm [40], 3–21 for wavelengths of 0.3–2 μm [21], and 0–12 for wavelengths of 0.1–100 μm [41]. Linear interpolation based on these values leads to an anticipated extinction coefficient of 6.16 for a wavelength of 615 nm. The actual values we recorded are lower presumably due to the formation of transparent aluminum oxide, which reduces the absorption, and are in agreement with the value of 0.07 determined previously [1]. The coefficient values were not constant but declined slightly with increasing aluminum thickness, consistent with earlier findings Anni Lehmuskero, Markku Kuittinen, Pasi Vahimaa [21] and justified by the mass attenuation coefficient [54]. These observations show that, as with the resistivity, the absorption coefficient deviates from the literature values and also decreases as the aluminum coating becomes thicker. These effects must be taken into account in order to correctly interpret the OD values.

4. Conclusions

Our comparison of thickness determination by QCM, AFM, OD, INT

and ER revealed that the methods cannot be considered redundant. The differences we observed mainly result from the assumption that the relevant material constants are equal to their literature bulk values, but this is not the case: the bulk material constants are not the same as those for thin films made from the same material because the microstructure of the deposited layer has an important effect. This means that the material constants depend on the film thickness. Furthermore, the material constants cannot even be assumed to converge on the literature values for very thick films because the layer will still include lattice defects (missing ions, foreign ions) due to the evaporation process conditions (residual oxygen, epitaxy). These conditions primarily affect the light absorption and electrical resistivity, and no general threshold thicknesses can be given where the conditions no longer have a significant effect on the measurement. The thresholds for OD, EC and AFM/INT depend on instrument sensitivity, substrate roughness, and evaporation process stability, respectively. Therefore, derived values such as material costs, gas permeation, and machine speeds can only be compared using these methods if the material-specific constants are adjusted accordingly and the values are interpreted with caution. Ideally, this should be performed for each individual process and substrate.

The AFM and INT values indicated significant thickness heterogeneity, which may be caused during sample preparation and process control management. In contrast, the EC and OD material constants (electrical resistivity and light absorption) can and must be adjusted, and this cannot be achieved simply by introducing a correction factor because resistivity in particular declines with increasing thickness and depends on the substrate. A more sophisticated model is needed to understand the relationships between substrate and resistivity and this would offer the opportunity to characterize the aluminum structure in more detail. A particularly interesting question would be how the resistivity is related to the substrate roughness, which could reveal information about defects in the aluminum structure and the anticipated gas barrier performance for packaging applications.

Author contributions

Martina Lindner wrote the paper, supervised the project, conceived and designed the experiments and analyzed the data. Florian Höflsauer and Julia Heider performed the experiments and analyzed the data. Matthias Reinelt and Horst-Christian Langowski provided critical feedback and helped shape the research, analysis and manuscript.

Conflicts of interest

The authors declare no conflicts of interest.

Funding

This research did not receive any specific grant from funding agencies in the public, commercial, or not-for-profit sectors.

Acknowledgements

The authors thank Brigitte Seifert, Daniel Schlemmer, Michael Stenger and Christine Neumeier for advice and support with the experimental work.

References

- [1] H. Utz, *Barriereigenschaften Aluminiumbedampfter Kunststofffolien*, Doctoral Thesis Technical University of Munich, 1995.
- [2] O. Miesbauer, M. Schmidt, H.-C. Langowski, *Stofftransport Durch Schichtsysteme Aus Polymeren Und Dünne Anorganischen Schichten*, *Vakuum Forschung Praxis* 20 (6) (2008) 32–40, <https://doi.org/10.1002/vipr.200800372>.
- [3] M. Hanika, *Zur Permeation Durch Aluminiumbedampfte Polypropylen-Und Polyethylenterephthalatfolien*, Doctoral Thesis Technical University of Munich,

RESEARCH PAPER: COMPARISON OF THICKNESS DETERMINATION METHODS FOR PHYSICAL-VAPOR-DEPOSITED ALUMINUM COATINGS IN PACKAGING APPLICATIONS

M. Lindner et al.

Thin Solid Films 666 (2018) 6–14

- 2004.
- [4] N.J. Copeland, R. Astbury, Evaporated aluminium on polyester: optical, electrical, and barrier properties as a function of thickness and time (part I), *Aimcal Technical Conference*, 2010 Myrtle Beach, USA <https://www.aimcal.org/2010-usa.html>.
 - [5] T.O. Kääriäinen, P. Maydannik, D.C. Cameron, K. Lahtinen, P. Johansson, J. Kuusipalo, Atomic layer deposition on polymer based Flexible packaging materials: growth characteristics and diffusion barrier properties, *Thin Solid Films* 519 (10) (2011) 3146–3154, <https://doi.org/10.1016/j.tsf.2010.12.171>.
 - [6] D.J. McClure, N. Copeland, Evaporated aluminium on polyester: optical, electrical, and barrier properties as a function of thickness and time (Part I I), *Aimcal Technical Conference*, 2010 Myrtle Beach, USA <https://www.aimcal.org/2010-usa.html>.
 - [7] F.L. McCrackin, E. Passaglia, R.R. Stromberg, H.L. Steinberg, Measurement of the thickness and refractive index of very thin films and the optical properties of surfaces by ellipsometry, *J. Res. Nat. Stan. Sec. A* 67 (4) (1963) 4 (363-377).
 - [8] H. Chatham, Oxygen Diffusion Barrier Properties of Transparent Oxide Coatings on Polymeric Substrates, *Surf. Coat. Technol.* 78 (1-3) (1996) 1-9, [https://doi.org/10.1016/0257-8972\(95\)02420-4](https://doi.org/10.1016/0257-8972(95)02420-4).
 - [9] A. Piegari, E. Masetti, Thin Film Thickness Measurement: a Comparison of various Techniques, *Thin Solid Films* 124 (3) (1985) 249–257, [https://doi.org/10.1016/0040-6090\(85\)90273-1](https://doi.org/10.1016/0040-6090(85)90273-1).
 - [10] H.K. Pulker, Thickness Measurement, Rate Control and Automation. In *Thin Film Coating Technology*, (1983), Geneva, Switzerland, DOI: <https://doi.org/10.1117/12.935508>.
 - [11] D.M. Mattox, Film Characterization and Some Basic Film Properties, chap. 10, *Film Characterization and Some Basic Film Properties*, 1st ed., William Andrew Publishing, 1998, pp. 569–615, <https://doi.org/10.1016/B978-081551422-0.50011-5>.
 - [12] M. Lindner, M. Schmid, Thickness Measurement Methods for Physical Vapor Deposited Aluminum Coatings in packaging applications: a Review, *CoatingsTech* 7 (1) (2017) 9, <https://doi.org/10.3390/coatings7010009>.
 - [13] H.A. MacLeod, *Thin-Film Optical Filters*, 3rd ed., CRC Press, 1986.
 - [14] C.A. Bishop, *Vacuum Deposition Onto Webs, Films And Foils*, 2nd ed., Elsevier, 2011, <https://doi.org/10.1016/B978-1-4377-7867-0.00001-5>.
 - [15] C. Lu, A.W. Czanderna, *Applications of Piezoelectric Quartz Crystal Microbalances*, Vol. 7 Elsevier Science, Amsterdam, 2012.
 - [16] E. de Hoffmann, V. Stroobant, *Mass spectrometry: principles and applications*, (2007), Wiley.
 - [17] T.W. May, R.H. Wiedmeyer, A table of polyatomic interferences in Icp-MS, *At. Spectrosc.* 19 (5) (1998) 150–155.
 - [18] K.-J. Hanszen, Der Einfluss Von Strukturunregelmäßigkeiten Beim Zusammenwachsen Zweier Aufdampfschichten Auf Das Schichtdickenmessverfahren Mit Hilfe Von Vielstrahl-Interferenzen, *Thin Solid Films* 2 (5) (1968) 509–528, [https://doi.org/10.1016/0040-6090\(68\)90064-3](https://doi.org/10.1016/0040-6090(68)90064-3).
 - [19] P. Eaton, P. West, *Atomic Force Microscopy*, Oxford Univ. Presstime (2010), <https://doi.org/10.1093/acprof:oso/9780199570454.001.0001>.
 - [20] J. Weiss, Einflussfaktoren Auf Die Barriereigenschaften Metallisierter Folien, 44(4) *Verpackungs-Rundschau*, 1993, pp. S 23–S 28.
 - [21] A. Lehmuskero, M. Kuittinen, P. Vahimaa, Refractive index and extinction coefficient dependence of thin Al and Ir films on deposition technique and thickness, *Opt. Express* 15 (17) (2007) 17 10744–10752 <https://doi.org/10.1364/OE.15.010744>.
 - [22] G. Hass, J.E. Waylonis, Optical Constants and Reflectance and Transmittance of Evaporated Aluminum in the Visible and Ultraviolet, *J. Opt. Soc. Am.* 51 (7) (1961) 719–722.
 - [23] H.D. Liu, Y.P. Zhao, G. Ramanath, S.P. Murarka, G.C. Wang, Thickness Dependent Electrical Resistivity of Ultrathin (< 40 Nm) Cu Films, *Thin Solid Films* 384 (1) (2001) 151–156, [https://doi.org/10.1016/S0040-6090\(00\)01818-6](https://doi.org/10.1016/S0040-6090(00)01818-6).
 - [24] H. Hoffmann, J. Vancea, Critical-Assessment of Thickness-Dependent Conductivity of Thin Metal-Films, *Thin Solid Films* 85 (2) (1981) 147–167, [https://doi.org/10.1016/0040-6090\(81\)90627-1](https://doi.org/10.1016/0040-6090(81)90627-1).
 - [25] Y. Ke, F. Zahid, V. Timoshevskii, K. Xia, D. Gall, H. Guo, Resistivity of Thin Cu Films with Surface Roughness, *Phys. Rev. B* 79 (15) (2009) 155406 155406-6-155406-1 <https://doi.org/10.1103/PhysRevB.79.155406>.
 - [26] A.S. Darevskii, A.G. Zhdan, Real Structure and Electrical Conductivity of Island Films of Metals, *Soviet Microelectronics* 7 (5) (1978) 356–359.
 - [27] K.M. Leung, Electrical Resistivity of Metallic Thin Films with Rough Surfaces, *Phys. Rev. B* 30 (2) (1984) 647–658, <https://doi.org/10.1103/PhysRevB.30.647>.
 - [28] J.W. Lim, K. Mimura, M. Ishiki, Thickness Dependence of Resistivity for Cu Films Deposited by Ion Beam Deposition, *Appl. Surf. Sci.* 217 (1–4) (2003) 95–99, [https://doi.org/10.1016/S0169-4332\(03\)00522-1](https://doi.org/10.1016/S0169-4332(03)00522-1).
 - [29] J.M. Camacho, A.I. Oliva, Surface and Grain Boundary Contributions in the Electrical Resistivity of Metallic Nanofilms, *Thin Solid Films* 515 (4) (2006) 1881–1885, <https://doi.org/10.1016/j.tsf.2006.07.024>.
 - [30] E.H. Sondheimer, The mean Free Path of Electrons in Metals, *Adv. Phys.* 1 (1) (1952) 1–42, <https://doi.org/10.1080/00018735200101151>.
 - [31] H. Heuer, S. Hillmann, M. Roellig, M.H. Schulze, K.-J. Wolter, Thin film characterization using high frequency eddy current spectroscopy, 18th IEEE International Conference on Nanotechnology, IEEE, 2009Genoa, Italy.
 - [32] Z. Qu, Q. Zhao, Y. Meng, Improvement of sensitivity of eddy current sensors for nano-scale thickness measurement of Cu films, *NDT&E International* 61 (2014) 53–57, <https://doi.org/10.1016/j.ndteint.2013.09.007>.
 - [33] J.C. Moulder, E. Uzal, J.H. Rose, Thickness and Conductivity of Metallic Layers from Eddy-Current Measurements, *Rev. Sci. Instrum.* 63 (6) (1992) 3455–3465, <https://doi.org/10.1063/1.1143749>.
 - [34] S. Hillmann, M. Klein, H. Heuer, In-Line Thin Film Characterization Using Eddy Current Techniques. in *Studies in Applied Electromagnetics and Mechanics*, STM Publishing House, Szczecin, Poland, 2011, pp. 330–338.
 - [35] J.H. Lambert, *Photometria, Sive De Mensura Et Gradibus Luminis, Colorum Et Umbrae*. Anding, Leipzig, Germany, W. Engelmann, 1892.
 - [36] M. Knudsen, Das Cosinusgesetz in Der Kinetischen Gastheorie, *Ann. Phys.* 353 (24) (1916) 1113–1121.
 - [37] D. Chaleix, P. Choquet, A. Bessaudou, L. Frugier, J. Machel, A spatial distribution study of a beam vapour emitted by electron-beam-heated evaporation sources, *J. Phys. D. Appl. Phys.* 29 (1) (1996) 218–224, <https://doi.org/10.1088/0022-3727/29/1/032>.
 - [38] M. Ohring, *The Materials Science of Thin Films*, 1st ed., Academic Press, 1992.
 - [39] G.E. Totten, D.S. MacKenzie, *Handbook of Aluminum: Vol. 1: Physical Metallurgy and Processes*, 1st ed., CRC Press, 2003.
 - [40] L.G. Schulz, The Optical Constants of Silver, Gold, Copper, and Aluminum. I. The Absorption Coefficient K, *J. Opt. Soc. Am.* 44 (5) (1954) 357–362, <https://doi.org/10.1364/JOSA.44.000357>.
 - [41] O.S. Heavens, Optical Properties of Thin Films, *Rep. Prog. Phys.* 23 (1) (1960) 374–376.
 - [42] C. Zeiss, *Großes Interferenzmikroskop, Vertriebsabteilung Feinmessgeräte* (1965) 1–20.
 - [43] H.K. Pulker, Einfaches Interferenz-Wechselobjektiv Für Mikroskope Zur Dickenmessung Nach Fizeau-Tolansky, *Naturwissenschaften* 53 (9) (1966) 224, <https://doi.org/10.1007/bf00633891>.
 - [44] S. Meyer, R. Gorges, G. Kreisel, Preparation and characterisation of titanium dioxide films for catalytic applications generated by anodic spark deposition, *Thin Solid Films* 450 (2) (2004) 276–281, <https://doi.org/10.1016/j.tsf.2003.11.168>.
 - [45] X. Ma, A.J. Peyton, Y.Y. Zhao, Eddy current measurements of electrical conductivity and magnetic permeability of porous metals, *NDT & E Int.* 39 (7) (2006) 562–568, <https://doi.org/10.1016/j.ndteint.2006.03.008>.
 - [46] M. Lindner, Factors affecting the hygroexpansion of paper, *J. Mater. Sci.* 53 (1) (2017) 1–26, <https://doi.org/10.1007/s10853-017-1358-1>.
 - [47] A.C. Siegel, S.T. Phillips, M.D. Dickey, N. Lu, Z. Suo, G.M. Whitesides, Foldable printed circuit boards on paper substrates, *Adv. Funct. Mater.* 20 (1) (2010) 28, <https://doi.org/10.1002/adfm.200901363>.
 - [48] D.A. Miller, *Optical Properties of Solid Thin Films by Spectroscopic Reflectometry and Spectroscopic Ellipsometry*, Doctoral Thesis City University of New York, 2008.
 - [49] O. Stenzel, *Springer, The Physics of Thin Film Optical Spectra*, 2nd ed., 2005, <https://doi.org/10.1007/978-3-319-21602-7>.
 - [50] K.-N. Tu, R. Rosenberg, *Preparation and Properties of Thin Films: Treatise on Materials Science and Technology*, 24 Elsevier, 1982.
 - [51] P.D. Desai, H. James, C.Y. Ho, Electrical resistivity of aluminum and manganese, *J. Phys. Chem. Ref. Data* 13 (4) (1984) 1131–1172, <https://doi.org/10.1063/1.555725>.
 - [52] F.M. Reicha, M.A. El Hiti, P.B. Barna, Electrical Properties of Thin Oxidized Aluminium Films, *J. Mater. Sci.* 26 (8) (1991) 2007–2014, <https://doi.org/10.1007/bf00549159>.
 - [53] G.P. Panta, D.P. Subedi, Electrical characterization of aluminium (Al) thin films measured by using four-point probe method, *Kathmandu Univ. J. Sci. Eng. Technol.* 8 (2) (2012) 31–36, <https://doi.org/10.3126/kuset.v8i2.7322>.
 - [54] J.H. Hubbell, Photon mass attenuation and energy-absorption coefficients from 1 Kev to 20 Mev, *Int. J. Appl. Radiat. Isot.* 33 (11) (1982) 1269–1290, [https://doi.org/10.1016/0020-708x\(82\)90248-4](https://doi.org/10.1016/0020-708x(82)90248-4).

5. Research paper:

Hygroexpansion and surface roughness cause defects and increase the electrical resistivity of physical vapor deposited aluminum coatings on paper

Previous reports³ showed that **substrate roughness seems to introduce defects** in the aluminum coating, which is reflected as an **increase in the effective resistivity** of the coating. However, it is unclear whether the effect of roughness and also **hygroexpansion** (see Sections 1.3.1 and 1.3.3) can be quantified by measuring resistivity. Therefore, the sheet resistance of aluminum coated onto four different rough paper surfaces was measured by the induction of eddy currents at different relative humidities (0–95%). The mass of aluminum per unit area was indirectly determined by inductively-coupled plasma mass spectrometry. The effective resistivity was calculated based on the measured resistance and aluminum mass per unit area, combined with a value for bulk aluminum density.

The effect of substrate roughness and aluminum thickness on electrical resistance and effective resistivity could be mathematically described. The substrate roughness showed a linear relationship with effective resistivity. Relative humidity correlated with the moisture content of the paper substrate according to the Guggenheim, Anderson and De Boer sorption isotherm, whereas the moisture content was proportional to hygroexpansion. When paper expands due to the uptake of water, the aluminum coating is stretched so that the effective resistivity increases. At relative humidities of up to ~50%, hygroexpansion was proportional to the increase in effective resistivity, which is related to the mechanical straining and deformation of aluminum. When humidity exceeded ~50%, the aluminum already started to crack at a relatively low hygroexpansion on rough substrates. When the substrate surface was smoother, aluminum started to crack at a relatively higher hygroexpansion. Hygroexpansion led to a lower increase in effective resistivity than substrate roughness did.

These findings highlight the need for information about substrate roughness, humidity, and hygroexpansion when we compare the results of eddy current measurements. Furthermore, the increase in effective resistivity can be used to learn more about the **development of defects and the underlying effects of roughness, hygroexpansion and aluminum thickness.**


³ Lindner, M. et al. Comparison of thickness determination methods for physical-vapor-deposited aluminum coatings in packaging applications. Thin Solid Films 2018.

RESEARCH PAPER:
HYGROEXPANSION AND SURFACE ROUGHNESS CAUSE DEFECTS AND INCREASE THE
ELECTRICAL RESISTIVITY OF PHYSICAL VAPOR DEPOSITED ALUMINUM COATINGS ON PAPER

Author Contributions: Martina Lindner: conceptualization, formal analysis, investigation, methodology, visualization, original draft. Julia Heider: data curation, formal analyses, methodology. Matthias Reinelt: supervision, review and editing. Horst Christian Langowski: supervision, review and editing.

Article

Hygroexpansion and Surface Roughness Cause Defects and Increase the Electrical Resistivity of Physical Vapor Deposited Aluminum Coatings on Paper

Martina Lindner ^{1,2,*} , Julia Heider ^{1,2}, Matthias Reinelt ² and Horst-Christian Langowski ^{1,2}

¹ Chair for Food Packaging Technology, TUM School of Life Sciences, Technical University of Munich, Weißenstephaner Steig 22, 85354 Freising, Germany; julia.heider@yahoo.de (J.H.); horst-christian.langowski@ivv.fraunhofer.de (H.-C.L.)

² Fraunhofer Institute for Process Engineering and Packaging IVV, Giggenhauser Strasse 35, 85354 Freising, Germany; matthias.reinelt@ivv.fraunhofer.de

* Correspondence: martina.lindner@ivv.fraunhofer.de; Tel.: +49-8161-491-536

Received: 21 November 2018; Accepted: 20 December 2018; Published: 8 January 2019



Abstract: Aluminum coatings, which are applied by physical vapor deposition (PVD), have to be virtually defect-free in barrier applications for the packaging industry. When aluminum is applied to paper, hygroexpansion and substrate roughness can impair the aluminum coating. Neither effect is easy to detect by microscopy, but both can manifest as an increase in electrical resistance. Here, we quantified the effect of substrate paper hygroexpansion and surface roughness on the effective resistivity ρ_{EFF} of aluminum coatings. The sheet resistance of aluminum coated onto four different rough paper surfaces was measured via eddy currents at different relative humidity (0%–95%). The mass of aluminum per unit area was determined by inductively-coupled plasma mass spectrometry (ICP–MS). We calculated ρ_{EFF} based on the measured resistance and aluminum mass per unit area, combined with a value for aluminum density from the literature. The substrate roughness was proportional to ρ_{EFF} . Relative humidity correlated with the moisture content of the paper substrate according to the Guggenheim, Anderson, and De Boer (GAB) equation, whereas the moisture content showed a linear correlation with hygroexpansion. At relative humidity of up to 50%, hygroexpansion was linearly correlated with the increase in ρ_{EFF} , which is related to the mechanical straining and deformation of aluminum. At higher humidity, aluminum started to crack first on rough substrates and later on smooth substrates. The increase in ρ_{EFF} was larger on rough substrates. The findings highlight the need for information about substrate roughness, humidity, and hygroexpansion when eddy current measurement results are compared, and will help to ensure that aluminum coatings, applied by PVD, are defect-free.

Keywords: electrical resistance; thin films; packaging; inductively-coupled plasma mass spectrometer; relative humidity

1. Introduction

Aluminum coatings are widely used for applications such as packaging, paper electronics, and wafer technology, and are usually applied by physical vapor deposition (PVD). Effective coatings must be virtually defect-free, and one challenge to be addressed is the surface roughness of the substrate. Often, such inorganic coatings are applied onto very smooth, partially biaxially oriented, stretched polymeric films, which have roughness scales in the nanometer range. However, this is not the case for

RESEARCH PAPER:

HYGROEXPANSION AND SURFACE ROUGHNESS CAUSE DEFECTS AND INCREASE THE ELECTRICAL RESISTIVITY OF PHYSICAL VAPOR DEPOSITED ALUMINUM COATINGS ON PAPER

Coatings 2019, 9, 33

2 of 18

paper substrates, because the surface roughness of paper is in the micrometer range. Roughness can lead to defects in the inorganic coating, as illustrated in Figure 1.

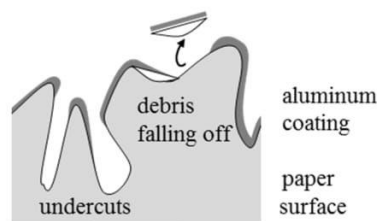


Figure 1. Defects appearing on rough surfaces.

A further challenge associated with the PVD coating of paper is hygroexpansion, which is the moisture-induced dimensional change of a material. The cellulose fibers in paper are hygroscopic and swell following the absorption of moisture from the surrounding atmosphere. However, the transverse expansion of the fibers is about 10 times greater than the longitudinal expansion, and because the fibers are aligned in machine direction (MD), most of the expansion in paper sheets occurs in cross direction (CD) [1,2]. When a closed aluminum coating is required, hygroexpansion is a challenge during PVD because the metallization of paper takes place under a high vacuum ($\sim 10^{-6}$ mbar) so the water evaporates and the paper shrinks. After metallization, the paper is transferred to humid air and subsequently expands as water enters from the uncoated side. Consequently, the aluminum coating is strained and eventually cracks [3].

Both hygroexpansion and defects formed due to substrate roughness therefore impair the aluminum coating. However, neither can be detected by light microscopy or scanning electron microscopy because the cracks are too small and too numerous, and therefore not clearly observed in the light transmittance or light reflectance modes. However, both effects manifest as an increase in electrical resistance [3–11]. Sheet resistance is commonly used to determine the thickness of nanometer-scale thin coatings, for example in film capacitors, holographic coatings, energy-saving windows, solar cells, absorbers, flexible circuits, thin film batteries, stretchable electronics, and packaging applications [12,13].

The effect of substrate expansion on sheet resistance has been reported for polymeric substrates. Resistance increase factors ($\Delta R/R_0$) of up to 2.2 were reported at a strain of 20% for copper coatings [14–17], with equivalent values of 3% at 20% strain for silver coatings [18] and 15,000 at 20% strain for aluminum coatings, depending on strain speed and aluminum thickness [19]. Moreover, this behavior was time dependent [19] and was influenced by the adhesion between the polymeric substrate and coating [14]. The fracture characteristics of such ductile materials must be carefully distinguished from those of brittle coatings such as silicon oxide or indium oxide [20]. To the best of our knowledge, the impact of hygroexpansion and roughness on the appearance of defects in aluminum coatings on paper substrates has not been investigated in detail, and it is unclear whether this can be monitored by measuring electrical resistance [21]. In this study, we therefore addressed the following questions:

- How does surface roughness correlate with the sheet resistance and effective resistivity of an aluminum coating?
- How does relative humidity (RH) affect the hygroexpansion of paper and how does it correlate with the sheet resistance and effective resistivity of the aluminum coating?
- Is there interdependency between substrate roughness and the sensitivity of aluminum coatings toward hygroexpansion?

The approach chosen to address these questions is summarized in Figure 2. For two papers, the roughness R_z , the sorption isotherm and the hygroexpansion were determined. Then, the respective four different paper surfaces (coated and non-coated sides of the two different papers) were PVD-coated

RESEARCH PAPER:

HYGROEXPANSION AND SURFACE ROUGHNESS CAUSE DEFECTS AND INCREASE THE ELECTRICAL RESISTIVITY OF PHYSICAL VAPOR DEPOSITED ALUMINUM COATINGS ON PAPER

Coatings 2019, 9, 33

3 of 18

with aluminum. The amount of aluminum (d_{NOMINAL}) was determined by inductively coupled plasma-mass spectrometry (ICP-MS) in combination with a value for aluminum density from the literature, and the resistance (R) of the coating was measured at different RH values. From d_{NOMINAL} and R , the effective resistivity ρ_{EFF} was derived. The increase of ρ_{EFF} was determined according to the RH.

Finally, the resistivity was then correlated with the surface roughness and the hygroexpansion of paper.

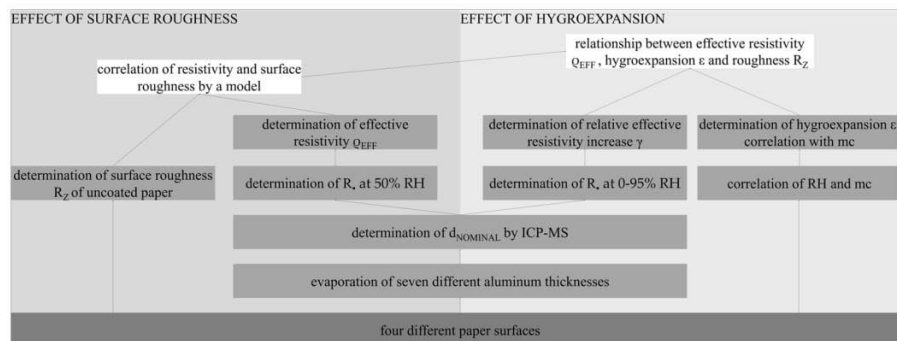


Figure 2. Details of the experimental procedures and work flow used in this study. Following abbreviations are used: RH: relative humidity; mc: moisture content; ICP-MS: inductively coupled plasma-mass spectrometry, and R_{\square} : sheet resistance.

2. Materials and Methods

2.1. Abbreviations

All non-generalized abbreviations used here are as follows: AC, aluminum coating, metallization; CC, side of the paper that is clay coated; CD, cross direction; COS, crack onset strain; MD, machine direction; mc, moisture content; PVD, physical vapor deposition; RH, relative humidity; without CC, side of the paper that is not clay coated.

2.2. PVD Coating of Aluminum on Paper

The paper substrates were Metalkote with a grammage of 65 g/m² (Ahlstrom-Munksjö Oyj, Stockholm, Sweden) and Nikla Select with a grammage of 70 g/m² (Brigl & Bergmeister, Niklasdorf, Austria). Paper samples were cut to a size of 105 × 148 mm². The samples were taped along all four edges onto a Metalkote paper carrier roll using thermally stable adhesive tape (Kapton, DuPont, Wilmington, DE, USA).

In order to achieve a high vacuum during PVD, it was necessary to reduce the moisture content (mc) of the paper substrate. Therefore, the carrier roll containing all the samples was dried at 70 °C for nine days in a Heratherm oven (Thermo Fisher Scientific, Waltham, MA, USA) prior to metallization.

The metallization was applied by PVD using the electron beam heating method. The coating process was performed in a L560UV 0.5 × 1.0 m² box coater (Leybold Vacuum, Cologne, Germany) at Fraunhofer IVV. This coater was adapted for the roll-to-roll coating of polymer webs by the introduction of deposition roll, un-winding and re-winding equipment (Lenze, Hameln, Germany). The equipment was controlled using VAC Cluster Tool Controller L560 (AIS Automation, Dresden, Germany). The box coater was equipped with a 160-m³/h, E2M175 rotary vacuum pump and a 505-m³/h EH500 roots pump (both from Edwards, UK), and a 850–1150-L/s TMP 1000 turbomolecular pump (Leybold Vacuum) to create a vacuum down to ~10⁻⁶ mbar. Remaining moisture in the chamber was extracted using a Meissner cold trap (nitrogen-cooled copper pipe) and the deposition roll was water cooled. The pressure was determined using a PPT 100 Pirani gauge and a HPT100 hot-cathode Bayard–Alpert–Pirani wide-range gauge (both from Pfeiffer, Aßlar, Germany). The EV M-10 electron

RESEARCH PAPER:

HYGROEXPANSION AND SURFACE ROUGHNESS CAUSE DEFECTS AND INCREASE THE ELECTRICAL RESISTIVITY OF PHYSICAL VAPOR DEPOSITED ALUMINUM COATINGS ON PAPER

Coatings 2019, 9, 33

4 of 18

beam source with a 270° configuration was combined with a 10-kW Genius Carrera high voltage supply (both from Ferrotec, Unterensingen, Germany). The aluminum we used had a purity of 99.98%. The coating thickness was varied by changing the web speed from 0.5 to 3.5 m/min at steps of 0.5 m/min and an evaporation rate of 2–3.5 nm/s. During the evaporation process, the pressure in the chamber ranged from 10⁻⁴ to 10⁻⁵ mbar, resulting in an approximate mean free path of 0.9–9 m [12].

After removing the rolls from the box coater, they were transferred to a 60-L HM-HDPE drum (Mauser-Werke, Brühl, Germany) containing 1 kg Perlform silica gel (orange, 2–5 mm, with indicator; Carl Roth, Karlsruhe, Germany) to reduce the RH to 0%. As such, the water uptake and hygroexpansion of the paper was kept to a minimum. The drum was then stored at 23 °C.

2.3. Determination of Sheet Resistance via Eddy Currents at Different RH Values

Prior to re-humidification of the aluminum-coated samples, rigid frames were produced onto which the samples were later loosely attached to avoid curling. This frame consisted of four Purell HP570M plastic strips (Lyondell Basell, Rotterdam, The Netherlands) fixed together using Shamrock adhesive tape (Scientific Specialty Systems, Waltham, MA, USA). Furthermore, paper towels were stapled to form pouches of 75 × 95 mm² and filled with 30 g silica gel. They were stored, together with the paper carrier roll, in the HDPE drum with silica gel.

In the next step, we placed the plastic frames, the silica pouches, a dish containing 500 g silica gel, a pair of scissors, pressure lock bags, adhesive tape (Scotch Magic), a testostor 175 hygrometer (Testo, Lenzkirch, Germany), and Fibox oxygen concentration measuring points (PreSens Precision Sensing, Regensburg, Germany) into a glove box (Mecaplex Metall, Grenchen, Switzerland). Finally, the roll with the aluminum-coated samples was placed into the glove box, which was immediately closed and flushed with pure nitrogen to remove moisture. Flushing was assumed to be complete when a constant, minimal RH value of < 3% (determined via the hygrometer) was reached. The paper samples were then removed from the carrier roll and attached to the frames with adhesive tape. The samples, together with the silica pouches, were transferred into the pressure log bags. After transferring all samples into these bags, the glove box was opened and the pressure log bags were placed in the plastic drum with fresh silica gel.

The samples were then taken one by one from the drum and the sheet resistance was measured at five predetermined points on each sample. The sheet resistance (R_{\blacksquare}) was measured using the eddy current method (EddyCus TF lab 4040, Suragus, Dresden, Germany). The skin depth with the applied set up was > 8 μm, which ensures the full penetration of the aluminum layer by the magnetic field. The area captured by the measurement was approximately 5 × 5 mm². The sheet resistance R_{\blacksquare} of a resistor with thickness d and resistivity ρ is defined as

$$R_{\blacksquare} = \frac{\rho}{d} \quad (1)$$

The effective resistivity ρ_{EFF} was then calculated from the thickness determined by ICP-MS (d_{NOMINAL}) and the measured sheet resistance (R_{\blacksquare}):

$$\rho_{\text{EFF}} = d_{\text{NOMINAL}} \cdot R_{\blacksquare} \quad (2)$$

After measurement, the samples were immediately transferred to a KBF720-230V climate chamber (Binder, Tuttlingen, Germany) set to 23 °C with RH values of 35%, 50%, 70%, 85%, and 95%. The samples were stored in each climate for 24 h prior to measurement of the sheet resistance. After each measurement, the samples were placed back into the climate chamber. Excessive air convection in the chamber was avoided by using additional plastic curtains placed inside the chamber. The relative effective resistivity increase (γ) was calculated based on the effective resistivity at a RH of 0% and at a given RH of $x\%$.

$$\gamma = \frac{\rho_{\text{EFF}}^{\text{RH}=x\%}}{\rho_{\text{EFF}}^{\text{RH}=0\%}} - 1 \quad (3)$$

2.4. Inductively-Coupled Plasma—Mass Spectrometry (ICP-MS)

The sample surface, volume, and dilution factors were adapted depending on the expected aluminum concentration. From each sample with a surface (A) of 10 cm² or 15 cm², the aluminum was stripped off using 50, 30, 20, 10, or 5 mL 1.0 M of sodium hydroxide solution (Chemsolute 1.0 mol/L, Th. Geyer GmbH, Renningen, Germany). The volume of 1.0 M sodium hydroxide used was taken as the sample volume (V). After 1 h, the samples were mixed within the tubes and the liquid aluminous sample was diluted with double-distilled water. The dilution factor (f) was 1:10 or 2:10. The amount of aluminum in these diluted samples was determined using an Agilent 770x ICP-MS (Agilent Technologies, Santa Clara, CA, USA). We used an aluminum standard solution for calibration (ICP-multi-element standard solution IV 1.11355.0100; Merck, Darmstadt, Germany). The aluminum concentration of the standard solution was 1000 mg/L. For calibration, this standard solution was diluted with double-distilled water to concentrations of 0.10, 0.20, 0.25, 0.30, 0.50, 0.75, 1.00, 1.50, 2.00, 3.00, and 3.50 mg/L aluminum. The calibration delivered the correlation for the given concentration with signal intensity. This correlation allowed us to calculate the concentration (c) [mg/L] of aluminum in each sample from the signal intensity.

Based on the stripped-off sample area A, the nominal thickness of the aluminum layer d_{NOMINAL} was calculated using the determined concentration of aluminum c and a bulk value for density (δ_{lit}) of 2.7 g/cm³ taken from the literature [22], as shown in Equation (4). The coating weight (cw_{NOMINAL}) [g/m²] was calculated according to Equation (5) [23].

$$d_{\text{NOMINAL}} = \frac{c \cdot f \cdot V}{A \cdot \delta_{\text{lit}}} \quad (4)$$

$$cw_{\text{NOMINAL}} = d_{\text{NOMINAL}} \cdot \delta_{\text{lit}} \quad (5)$$

2.5. Sorption Isotherm

Sorption isotherms of the paper substrates were recorded at 0%, 35%, 50%, 70%, 85%, and 95% RH (Sorptionprüfsystem SPSx-1 μ , ProUmid GmbH & Co. KG, Ulm, Germany). The temperature was set to 23 °C. For each humidity increase, the weight was measured until equilibrium was reached. The minimum time for each RH increase was set to 2 h, and the maximum to 48 h. The sorption isotherms between 35% and 95% RH were described using the Guggenheim, Anderson, and De Boer (GAB) equation, which is shown in Equation (6) [24]. In this model it is postulated that the state of sorbate molecules in the second layer is equal to those in superior layers, but different from those of the monolayer. Here, mc is the moisture content [–], M_0 [g/100 g fiber] the monolayer moisture content, RH the relative humidity, and h and c are constants. c is a measure of the strength of binding of water to the primary binding sites, whereas h is a correction factor, which corrects the properties of the multilayer molecules relative to the bulk liquid [25,26]. The equation was fitted to the data using OriginPro 2016 (OriginLab Corporation, Wellesley Hills, MA, USA) and the Levenberg–Marquardt algorithm.

$$mc = \frac{M_0 \cdot c \cdot h \cdot \text{RH}}{(1 - h \cdot \text{RH}) \cdot (1 - h \cdot \text{RH} + c \cdot h \cdot \text{RH})} \quad (6)$$

2.6. Hygroexpansion

The hygroexpansion measurement was carried out on three samples (288 × 200 mm²) from each paper. The samples were dried for 20 days in silica gel at 23 °C. Then, each was stored in the KBF720-230V climate chamber at 23 °C for 24 h, with sequentially increasing RH values of 35%, 50%, 70%, 85%, and 95%. The samples were taken one by one from the drum/climate chamber and scanned at a resolution of 1200 dpi (CanonScan LiDE 700F, Canon, Krefeld, Germany). Images were saved as a jpg file. Subsequently, the distance between certain measuring points ($l_{0,\text{CD}}$, $l_{0,\text{MD}}$) was measured using LAS v4.0 software (Leica Microsystems GmbH, Wetzlar, Germany). On each sample, we took three CD and three MD measurements. From these data, the percentage length increase ϵ at increasing

RH values was calculated by setting $l_{0,CD}$ and $l_{0,MD}$ in relation to the increased lengths l_{CD} and l_{MD} , as shown in Equation (7).

$$\epsilon_{CD} = \frac{l_{CD} - l_{0,CD}}{l_{0,CD}} \quad (7)$$

2.7. Surface Roughness

Roughness was determined using the mechanical profile method (Hommel Etamic W55, Jenoptik, Jena, Germany). Here, we use the roughness term R_z . In this method, the traversing length l_n is divided into five equal-sized subsections l_r , chosen according to DIN EN ISO 4288:1998 [27] and DIN EN ISO 3274:1998 [28] (in this case, 0.8 and 2.5 mm, respectively). In the single subsections, the single roughness Z_n was determined. The single roughness is the difference between the highest and lowest points in one subsection l_r [29]. From Z_n , R_z is determined as the arithmetic average.

2.8. Scanning Electron Microscopy (SEM)

Images were acquired using a JSM-7200F scanning electron microscope (Jeol, Peabody, MA, USA) at 4 kV. The working distance was maintained at 8.7–9.6 mm. Given that the samples were coated with aluminum, no additional gold sputtering was necessary.

2.9. Statistical Methods

Data points represent median values for resistances and average values for roughness. Statistical tests were carried out using OriginPro 2016 and Visual-XSel v12.0 (CRGRAPH, Starnberg, Germany). Statistically significant differences were determined using the Wilcoxon, Mann, and Whitney U-test ($\alpha = 0.05$).

3. Results

3.1. Surface Characterization via SEM and EDX

When considering substrate roughness, roughness parameters such as R_z are only used to describe certain features of a much more complex surface structure. To obtain a better visual impression, surface images were obtained by SEM (Figure 3).

Additional images obtained by energy dispersive X-ray spectroscopy did not reveal aluminum clusters or voids. This indicates that the sizes of the clusters and voids are in the nanometer range rather than the micrometer range.

RESEARCH PAPER:
HYGROEXPANSION AND SURFACE ROUGHNESS CAUSE DEFECTS AND INCREASE THE ELECTRICAL RESISTIVITY OF PHYSICAL VAPOR DEPOSITED ALUMINUM COATINGS ON PAPER

Coatings 2019, 9, 33

7 of 18

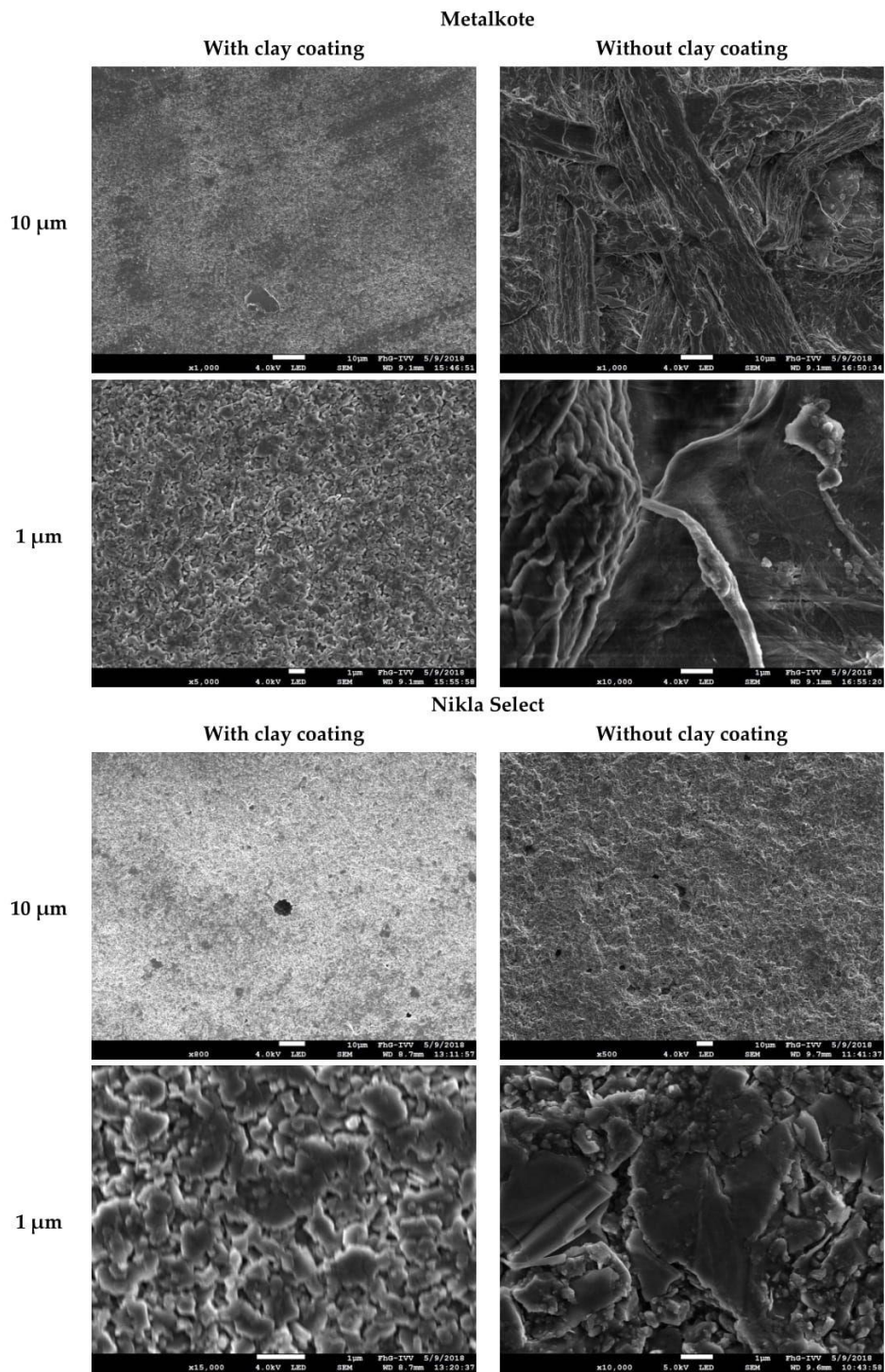


Figure 3. SEM images of the four paper surfaces that were PVD-coated with aluminum. Scale bars indicate 10 and 1 μm, respectively. The visible surface roughness induces defects in the aluminum coating and increases the electrical resistance.

3.2. Effect of Substrate Roughness on Sheet Resistance and Resistivity

Surface features, as shown in the previous section, manifest themselves as a change in electrical conductivity of the applied aluminum coatings. In Figure 4, the effect of d_{NOMINAL} on the sheet resistance is visible (for measurements at 50% RH). Apparently the sheet resistance (R_{\square}) inversely correlates with the aluminum thickness. This correlation is significantly different for different paper substrates, indicating that the resistivity is not the same on all paper substrates. Thus, the effective resistivity (ρ_{EFF}) is calculated from the measured sheet resistance (R_{\square}) and the thickness (d_{NOMINAL}) (Equation (2)).

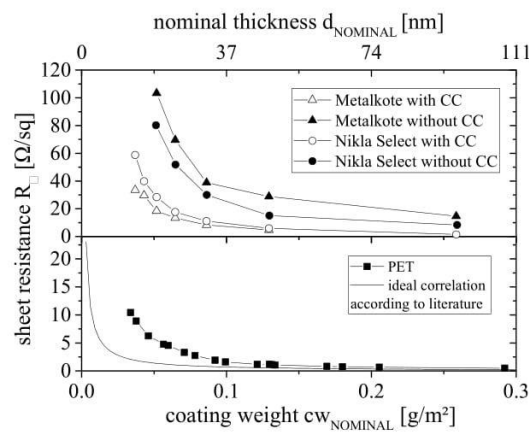


Figure 4. Correlation between sheet resistance and aluminum thickness (lines are included for visual clarity).

As shown in Figure 5, the effective resistivity ρ_{EFF} was neither constant nor close to the value reported in the literature. In detail, four observations can be made from this figure.

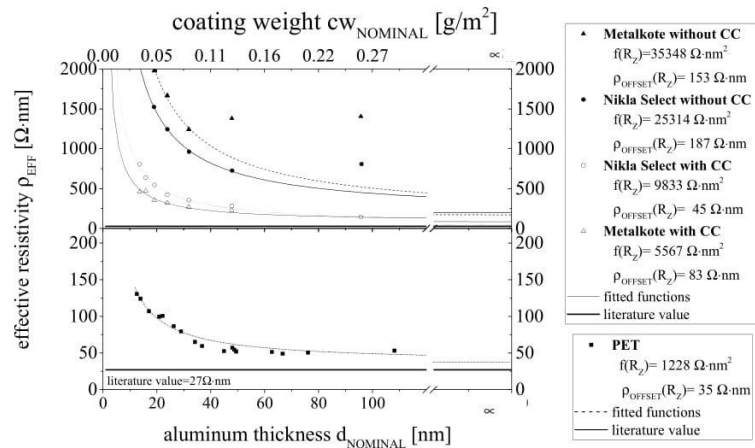


Figure 5. Correlation between aluminum thickness and resistivity; fitted black lines according to Equation (12).

All curves show a characteristic minimum resistivity value $\rho_{\text{OFFSET}} [\Omega \cdot \text{nm}]$ at high aluminum thickness, superimposed by a variable resistivity $\rho_n [\Omega \cdot \text{nm}]$ at lower thickness (Equation (8)).

$$\rho_{\text{EFF}} = \rho_{\text{OFFSET}} + \rho_n \tag{8}$$

Even for the thicker coatings, the minimum resistivity ρ_{OFFSET} would not achieve literature values for bulk aluminum ρ_{lit} . This can partially be explained as material properties are influenced by the PVD process conditions. Such process conditions include the residual oxygen and water vapor pressures, the kinetic energy of evaporated aluminum atoms, and the mean free path length. However, obviously a second factor affects the values, because the minimum resistivity ρ_{OFFSET} increases with substrate roughness (Equation (9)). This can be explained; as a low roughness leads to small defects which can easily become overgrown with aluminum. In comparison, defects on very rough papers are too large to become overgrown, thus increasing the resistance R and minimum resistivity ρ_{OFFSET} .

$$\rho_{\text{OFFSET}} \sim R_Z \quad (9)$$

Additionally, for thin coatings, the resistivity is higher on rough substrates. Thus, the variable resistivity ρ_n also depends on paper roughness R_Z (Equation (10)).

$$\rho_n \sim R_Z \quad (10)$$

Low thickness leads to a high resistivity, what can only partially be explained by electron scattering on aluminum grain boundaries [30]. Thus, it can be assumed that with decreasing thickness, less and less aluminum is available to overgrow the aforementioned defects. Thus, a thinner coating leads to more defects and to a higher variable resistivity ρ_n (Equation (11)).

$$\rho_n \sim 1/d_{\text{NOMINAL}} \quad (11)$$

The resistivity shows deviating behavior at thicknesses of 47 and 96 nm in the case of Metalkote without CC, and at 96 nm in the case of Nikla Select without CC. This indicates, that thicker coatings on rough substrates have a lower crack onset strain. The three data points mentioned above may therefore deviate due to this effect. This indicates a boundary condition for the application of the developed model. The data points are not considered explicitly in the following.

Observations (I)–(III) can be combined to the following very simple descriptive approach

$$\rho_{\text{EFF}} = f(R_Z) \cdot \frac{1}{d} + \rho_{\text{OFFSET}}(R_Z) \quad (12)$$

where $f(R_Z)$ and $\rho_{\text{OFFSET}}(R_Z)$ are functions of R_Z . The individual numbers for these functions can be obtained for each experimental curve in Figure 5 by fitting Equation (12) to the data points (least square method). However it is not yet clear what $f(R_Z)$ and $\rho_{\text{OFFSET}}(R_Z)$ actually are. To test this, the obtained numbers from the fit above are plotted versus R_Z (Figure 6) so that the scaling of these functions becomes clear: $f(R_Z)$ correlates linearly with a slope c of $2964 \Omega \cdot \text{nm}^2 / \mu\text{m}$ (Equation (13)). The scaling for $\rho_{\text{OFFSET}}(R_Z)$ is obtained similarly to be linear with a slope of $k = 0.5 / \mu\text{m}$. Additionally the linear plot intersects the y -axis and the respective y -value corresponds to ρ_{lit} (Figure 7, Equation (14)). The correlation in $\rho_{\text{OFFSET}}(R_Z)$ is less explicit. This may reflect the additional effects on ρ_{OFFSET} , such as the effect of foreign atoms.

$$f(R_Z) = R_Z \cdot c \quad (13)$$

$$\rho_{\text{OFFSET}}(R_Z) = \rho_{\text{lit}} \cdot (1 + R_Z \cdot k) \quad (14)$$

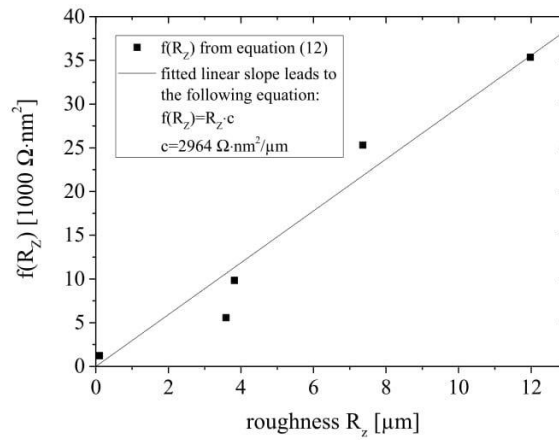


Figure 6. $f(R_z)$ describes the effect of R_z on the variable resistivity ρ_{it}

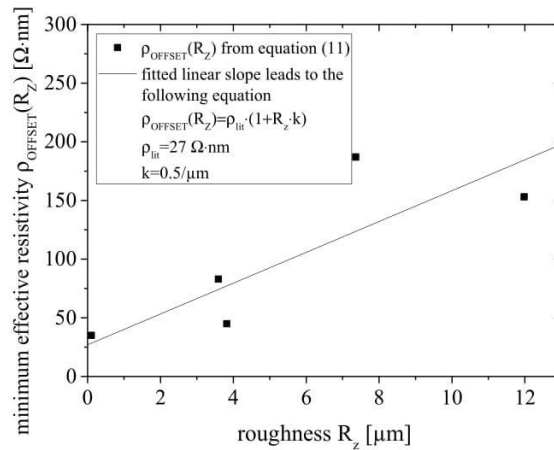


Figure 7. Effect of substrate roughness on minimum effective resistivity ρ_{OFFSET}

The combination of Equations (12)–(14) gives Equation (15), which was used to fit the three dimensional graph in Figure 8. This correlation fits well ($R^2 = 0.88$). The results show that the resistivity is not constant, but rather increases with decreasing thickness. Additionally, roughness increases the resistivity, and this effect is much more pronounced.

$$\rho_{\text{EFF}} = R_z \cdot c \cdot \frac{1}{d} + \rho_{\text{lit}} \cdot (1 + R_z \cdot k) \quad (15)$$

$\rho_{\text{lit}} = 27 \Omega \cdot \text{nm} \quad k = 0.5 / \mu\text{m} \quad c = 2964 \Omega \cdot \text{nm}^2 / \mu\text{m}$

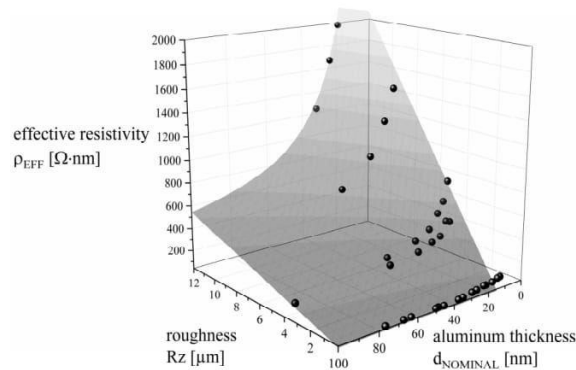


Figure 8. Correlation between substrate roughness R_Z , aluminum thickness $d_{NOMINAL}$, and effective resistivity ρ_{EFF} , as described by Equation (15).

3.3. Effect of Substrate Hygroexpansion on Resistivity

3.3.1. Sorption Isotherm

The relationship between mc and RH for the two paper samples is shown in Figure 9. Within the range 35%–90% RH , the curves were fitted to the GAB Equation (6). The fitted parameters for the GAB equation are shown in Table 1.

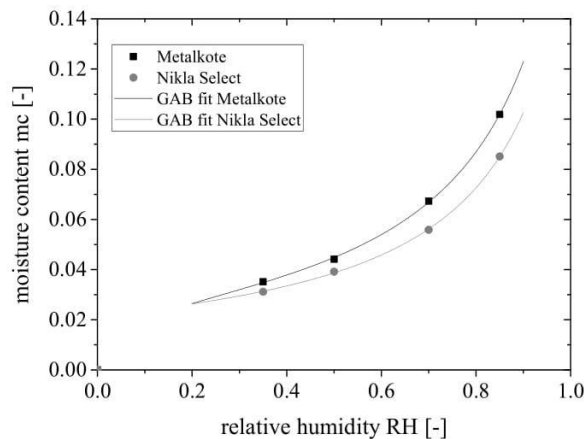


Figure 9. Effect of relative humidity on moisture content for Metalkote and Nikla Select.

Table 1. Fitted parameters for GAB equation.

Parameter	Metalkote	Nikla Select
M_0	0.02693	0.02177
C	20.2559	3382.55465
h	0.87096	0.87546

3.3.2. Moisture Content and Hygroexpansion

Fibers in paper expand when they take up moisture. This expansion is greater in the transverse fiber direction and therefore in CD owing to the molecular arrangement of cellulose, hemicellulose, and lignin [31]. In agreement with earlier reports [32,33], hygroexpansion in CD correlates linearly with mc (Figure 10). The relationship is fitted by a linear function with a as the fitting parameter (Equation (16)). In MD, the hygroexpansion appears to be almost constant because the values do not

vary significantly ($\alpha = 0.05$). As the expansion in MD is much lower than in CD, it is disregarded in the following sections.

$$\epsilon_{CD} = mc \cdot a \tag{16}$$

with $a_{\text{Metalkote}} = 10.4077\%$ and $a_{\text{Nikla Select}} = 10.9305\%$

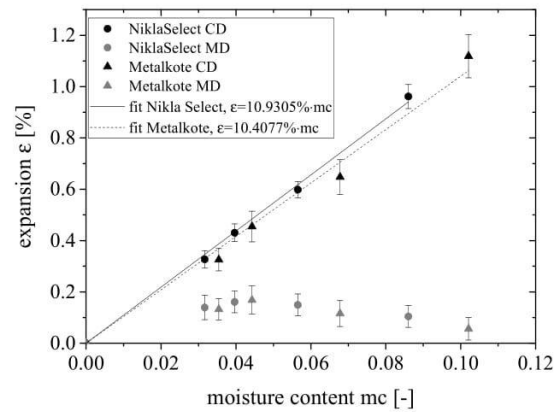


Figure 10. Effect of moisture content on hydroexpansion; whiskers indicate standard deviation.

3.3.3. Relative Humidity and Hydroexpansion

In CD, Metalkote expanded significantly ($\alpha = 0.05$) more than Nikla Select for the same RH value (Figure 11). By combining Equations (6) and (16) with the fitting parameters from Table 1, the relationship between hydroexpansion and RH was modeled, as shown in Equation (17).

$$\epsilon_{CD} = a \cdot \frac{M_0 \cdot c \cdot h \cdot RH}{(1 - h \cdot RH) \cdot (1 - h \cdot RH + c \cdot h \cdot RH)} \tag{17}$$

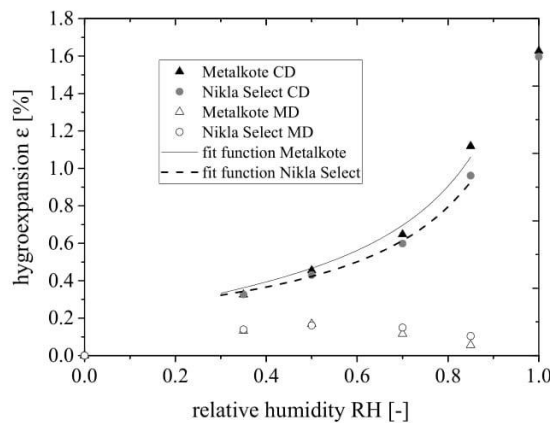


Figure 11. Effect of relative humidity on hydroexpansion in cross direction and machine direction.

3.4. Effect of Hydroexpansion on Effective Resistivity

As shown in Section 3.1, sheet resistance and resistivity are strongly dependent on substrate roughness and therefore differ significantly between the coated and non-coated sides of each substrate paper. Moreover, resistance and resistivity are affected by the hydroexpansion of the paper. In order to show the effect of hydroexpansion in isolation from the effect of roughness and thickness, the relative

RESEARCH PAPER:

HYGROEXPANSION AND SURFACE ROUGHNESS CAUSE DEFECTS AND INCREASE THE ELECTRICAL RESISTIVITY OF PHYSICAL VAPOR DEPOSITED ALUMINUM COATINGS ON PAPER

effective resistivity increase γ (rather than resistance or resistivity) is considered in Figures 12–14. This value sets the resistivity at a certain RH in relation to the resistivity at 0% RH or 0% hydroexpansion (Equation (3)). Moreover, the effect of aluminum thickness on γ is examined at RH values of 70%, 85%, and 95% (Figures 13 and 14).

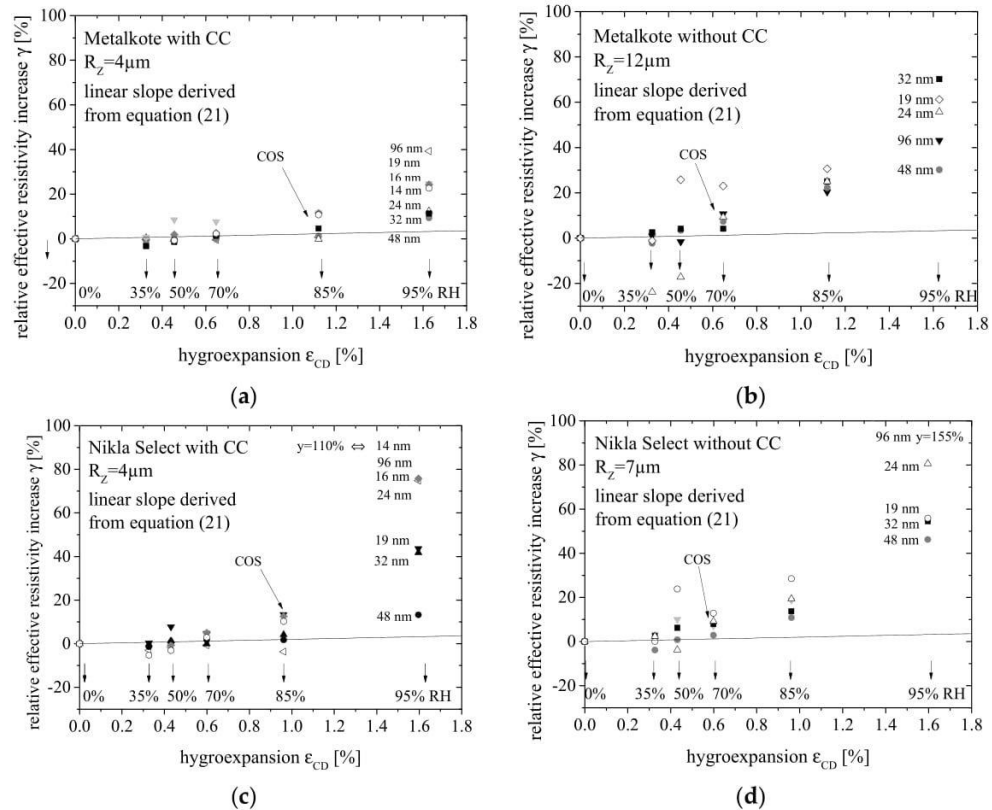


Figure 12. (a) Metalkote with clay coating; (b) Metalkote without clay coating; (c) Nikla Select with clay coating; (d) Nikla Select without clay coating. Correlation between the relative effective resistivity increase (γ) and CD hydroexpansion of Metalkote and Nikla Select on the sides of paper with and without clay coating (CC). γ sets the resistivity at a certain relative humidity (RH) in relation to the resistivity at 0% RH or 0% hydroexpansion, respectively. The linear slope represents the increase of resistivity due to the pure three-dimensional deformation, as described in Equations (20) and (21). Hydroexpansion, substrate roughness, and aluminum thickness affect γ and the crack onset strain (COS).

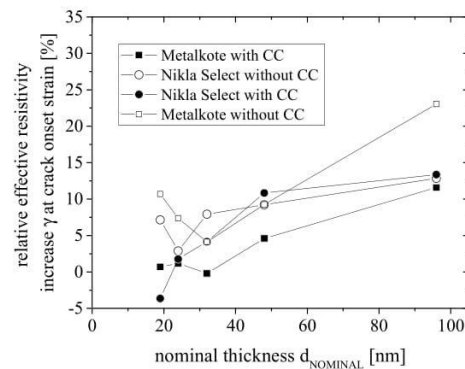


Figure 13. Relative effective resistivity increase (γ) at the crack onset strain (COS). This was at 85% relative humidity (RH) on Metalkote and Nikla Select with a clay coating (CC) and 70% RH on Metalkote and Nikla Select without a clay coating.

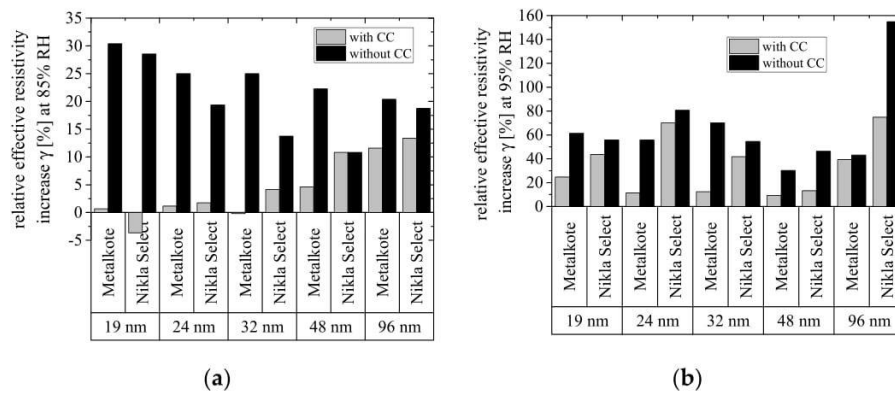


Figure 14. (a) Relative effective resistivity increase (γ) at 85% relative humidity (RH); (b) relative effective resistivity increase (γ) at 95% RH. Each for different aluminum thicknesses. No clear impact of thickness is visible. However, rougher surfaces led to greater γ (compare cases with and without clay coating [CC]).

We assumed that the aluminum coating forms cracks when the underlying paper expands, thus increasing the resistivity. Aluminum is considered a ductile material, and ductile thin coatings show a more complex fracture behavior than brittle materials. The mechanisms underlying this phenomenon have been extensively reviewed [34,35]. Two generic modes of ductile fracture are (a) failure by void coalescence and (b) failure by instability. In the first case, voids are already present or nucleate at inclusions; then they grow, form necks, and coalesce such that cracks and through thickness cracks appear. Finally, the material ruptures with a complete loss of stress-carrying capacity. In the second case, deformation is localized in thin shear bands arranged in a regular lattice, until the material fractures. In the current study, the first fracture mode is probably applicable because we assume that the paper roughness induces heterogeneity in the aluminum coating. Strain hardening of thin films is not expected because dislocations in metal films can escape due to the limited thickness constraint [15]. In comparison with free-standing films, the strain localization on the film could be suppressed by the substrate due to the geometrical constraint [14,15].

From Figures 12–14, the following observations and conclusions can be drawn:

- Increasing humidity and thus hygroexpansion leads to an increase in resistance and effective resistivity (Figure 12). This implies that aluminum is stretched due to the hygroexpansion of the underlying paper, and hence cracks appear. The values shown are similar to those reported

previously [3], where an increase in RH from 35% to 90% at 23 °C increased the resistance by about 40% for silver ink coatings.

- Initially, the increase in resistivity is almost linear with a strain with a small slope (Figure 12). The initial increase in resistivity follows the theoretical calculation according to Equation (20) [14]. This equation is based on the assumption that the volume of aluminum (cross section $A \times$ length l) is constant under tension ϵ , namely $A \cdot l = A_0 \cdot l_0$. Under tension, the material thins out and thus A decreases and l increases due to plastic deformation. From that assumption Equations (18) to (20) are derived. Based on this correlation and Equation (17), γ can be calculated from the RH, as in Equation (21).

$$\frac{R}{R_0} = \left(\frac{l}{l_0}\right)^2 \quad (18)$$

$$\frac{\rho}{\rho_0} = \left(\frac{l}{l_0}\right)^2 = (1 + \epsilon)^2 \quad (19)$$

$$\gamma = \frac{\rho}{\rho_0} - 1 = (1 + \epsilon)^2 - 1 \quad (20)$$

$$\gamma = \left(1 + a \cdot \frac{M_0 \cdot c \cdot h \cdot \text{RH}}{(1 - h \cdot \text{RH}) \cdot (1 - h \cdot \text{RH} + c \cdot h \cdot \text{RH})}\right)^2 - 1 \quad (21)$$

- Higher substrate roughness leads to more imperfections and thus a lower crack onset strain (COS) (Figure 12). The COS is the strain where γ deviates from the linear region, according to Equations (21) and (20). The COS indicates the appearance of defects in the shapes of necks and cracks in the aluminum. These cracks strongly increase the resistance and thus the nominal resistivity [15]. The COS is reached at RH values of ~70% ($\epsilon_{\text{CD}} \approx 0.6\%$) on paper surfaces without CC, but ~85% ($\epsilon_{\text{CD}} \approx 1.2\%$) on paper surfaces with CC. This indicates that the COS is lower for rougher surfaces (paper without CC), because higher roughness induces a heterogeneous thickness distribution and thus the appearance of defects. Defects can lead to local necks, which can cause further intense localized deformation, resulting in fast rupture [15].
- Higher substrate roughness leads to more cracks and a higher γ (Figure 14). γ on the rough side of the paper (without CC) is higher than that on the smooth side of the paper (with CC). As described in the previous observation, this leads to more defects, which consequently cause more voids and lead to a higher γ .
- The effect of aluminum thickness on γ cannot be defined (Figure 14). As the influence of roughness is much more pronounced than the effect of aluminum thickness, no clear correlation between aluminum thickness and γ can be observed. This is in line with the comparably low impact of thickness, as seen in Figure 8.

4. Conclusions

The following conclusions were drawn from the experimental results presented above.

- Substrate roughness and hygroexpansion both increase the resistance and effective resistivity of aluminum coatings.
- Hygroexpansion increased the resistivity less than substrate roughness. When aluminum thickness is determined via eddy currents, these factors should either be taken into account or a standard material representing each process/substrate combination should initially be fully characterized, so that each new measurement can be related to the standard material.
- The effect of substrate roughness and aluminum thickness on resistance and effective resistivity can be mathematically modeled. The effect of substrate roughness becomes more pronounced for thinner coatings.
- When paper expands due to the uptake of water, the applied aluminum is stretched so that the effective resistivity increases. For low RH values, the relative effective resistivity increase

RESEARCH PAPER:

HYGROEXPANSION AND SURFACE ROUGHNESS CAUSE DEFECTS AND INCREASE THE ELECTRICAL RESISTIVITY OF PHYSICAL VAPOR DEPOSITED ALUMINUM COATINGS ON PAPER

Coatings **2019**, *9*, 33

16 of 18

γ correlates linearly with hygroexpansion and can thus easily be linked to RH via basic physical assumptions.

- γ is higher for rougher substrates. Moreover, aluminum has a lower crack onset strain on rough substrates.
- The effect of aluminum thickness on the relative effective resistivity increase is low and most probably superimposed by roughness and hygroexpansion.

Various models have been presented to describe phenomena as the effect of hygroexpansion and roughness, such as the model according to the Effective Medium Theory [36,37], Maxwell [38], Maxwell–Garnet [39], Hamilton [40], power law approximation [41], Taylor series [42], percolation models [43,44], bond site models [45,46], and others [20]. However, more data are needed to enable the rational selection and interpretation of such models, which would be desirable for further research.

Moreover, in packaging applications, aluminum coatings are applied as gas barrier coatings. The gas barrier becomes less reliable as the number of defects increases. For such applications, it would be desirable to correlate the effective resistivity with the gas barrier of such coatings.

Author Contributions: Conceptualization, M.L.; Data Curation, J.H.; Formal Analysis, M.L. and J.H.; Investigation, M.L. and J.H.; Methodology, M.L. and J.H.; Supervision, M.R. and H.-C.L.; Visualization, M.L.; Writing—Original Draft, M.L.; Writing—Review and Editing, M.R. and H.-C.L.

Funding: This research received no external funding.

Acknowledgments: The authors gratefully thank Daniel Schlemmer, Michael Stenger, Dieter Bauer and Christine Neumeier for supporting experimental work and for advice.

Conflicts of Interest: The authors declare no conflict of interest.

References

1. Kirwan, M.J. *Handbook of Paper and Paperboard Packaging Technology*; Wiley-Blackwell: Oxford, UK, 2012.
2. Joffre, T.; Isaksson, P.; Dumont, P.J.J.; Roscoat, S.R.d.; Sticko, S.; Orgéas, L.; Gamstedt, E.K. A method to measure moisture induced swelling properties of a single wood cell. *Exp. Mech.* **2016**, *56*, 723–733. [[CrossRef](#)]
3. Wood, L.K.; Hrehorova, E.; Joyce, T.W.; Fleming, P.D.; Joyce, M.; Pekarovicova, A.; Bliznyuk, V. Paper substrates and inks for printed electronics. In Proceedings of the PIRA Ink on Paper Conference, London, UK, 1–3 November 2005.
4. Mueller, K.; Schoenweitz, C.; Langowski, H.-C. Thin laminate films for barrier packaging application—Influence of down gauging and substrate surface properties on the permeation properties. *Packag. Technol. Sci.* **2012**, *25*, 137–148. [[CrossRef](#)]
5. Kavčič, U.; Pavlovič, L.; Pivar, M.; Đokić, M.; Batagelj, B.; Muck, T. Printed electronics on recycled paper and cardboards. *Inf. MIDEM* **2013**, *43*, 50–57.
6. Siegel, A.C.; Phillips, S.T.; Dickey, M.D.; Lu, N.; Suo, Z.; Whitesides, G.M. Foldable printed circuit boards on paper substrates. *Adv. Funct. Mater.* **2010**, *20*, 28–35. [[CrossRef](#)]
7. Kattumenu, R.; Rebros, M.; Joyce, M.; Fleming, P.D.; Neelgund, G. Effect of substrate properties on conductive traces printed with silver-based flexographic ink. *Nordic Pulp Pap. Res. J.* **2009**, *24*, 101–106. [[CrossRef](#)]
8. Reinwand, D. *Dynamisches Magnetron-Sputterverfahren zur Vorderseitenmetallisierung Kristalliner Silicium-Solarzellen*; Shaker: Aachen, Germany, 2012. (In German)
9. Tobjörk, D.; Österbacka, R. Paper electronics. *Adv. Mater.* **2011**, *23*, 1935–1961. [[CrossRef](#)]
10. Trnovec, B.; Stanel, M.; Hahn, U.; Hübler, A.; Kempa, H.; Sangl, R.; Forster, M. Coated paper for printed electronics. *Prof. Papermak.* **2009**, *104*, 48–51.
11. Denneulin, A.; Blayo, A.; Bras, J.; Neuman, C. PEDOT: PSS coating on specialty papers: Process optimization and effects of surface properties on electrical performances. *Prog. Org. Coat.* **2008**, *63*, 87–91. [[CrossRef](#)]
12. Bishop, C.A. *Vacuum Deposition onto Webs, Films and Foils*, 2nd ed.; Elsevier: Amsterdam, The Netherlands, 2011.
13. Rogers, J.A.; Someya, T.; Huang, Y. Materials and mechanics for stretchable electronics. *Science* **2010**, *327*, 1603–1607. [[CrossRef](#)]
14. Lu, N.; Wang, X.; Suo, Z.; Vlassak, J. Metal films on polymer substrates stretched beyond 50%. *Appl. Phys. Lett.* **2007**, *91*, 221909. [[CrossRef](#)]

RESEARCH PAPER:

HYGROEXPANSION AND SURFACE ROUGHNESS CAUSE DEFECTS AND INCREASE THE ELECTRICAL RESISTIVITY OF PHYSICAL VAPOR DEPOSITED ALUMINUM COATINGS ON PAPER

Coatings **2019**, *9*, 33

17 of 18

15. Niu, R.; Liu, G.; Wang, C.; Zhang, G.; Ding, X.; Sun, J. Thickness dependent critical strain in submicron Cu films adherent to polymer substrate. *Appl. Phys. Lett.* **2007**, *90*, 161907. [[CrossRef](#)]
16. Berger, J.; Glushko, O.; Marx, V.M.; Kirchlechner, C.; Cordill, M.J. Effect of microstructure on the electro-mechanical behaviour of Cu films on polyimide. *J. Miner. Met. Mater. Soc.* **2016**, *68*, 1640–1646. [[CrossRef](#)]
17. Glushko, O.; Cordill, M. Electrical resistance of metal films on polymer substrates under tension. *Exp. Tech.* **2016**, *40*, 303–310. [[CrossRef](#)]
18. Polywka, A.; Stegers, L.; Krauledat, O.; Riedl, T.; Jakob, T.; Görrn, P. Controlled mechanical cracking of metal films deposited on polydimethylsiloxane (PDMS). *Nanomaterials* **2016**, *6*, 168. [[CrossRef](#)] [[PubMed](#)]
19. Hamasha, M.M.; Alzoubi, K.; Switzer, J.C.; Lu, S.; Desu, S.B.; Poliks, M. A study on crack propagation and electrical resistance change of sputtered aluminum thin film on poly ethylene terephthalate substrate under stretching. *Thin Solid Films* **2011**, *519*, 7918–7924. [[CrossRef](#)]
20. Cairns, D.R.; Witte, R.P.; Sparacin, D.K.; Sachsman, S.M.; Paine, D.C.; Crawford, G.P.; Newton, R. Strain-dependent electrical resistance of tin-doped indium oxide on polymer substrates. *Appl. Phys. Lett.* **2000**, *76*, 1425–1427. [[CrossRef](#)]
21. Torvinen, K.; Sievänen, J.; Hjelt, T.; Hellén, E. Smooth and flexible filler-nanocellulose composite structure for printed electronics applications. *Cellulose* **2012**, *19*, 821–829. [[CrossRef](#)]
22. Totten, G.E.; MacKenzie, D.S. *Handbook of Aluminum: Vol. 1: Physical Metallurgy and Processes*; Dekker: New York, NY, USA, 2003.
23. Lindner, M.; Schmid, M. Thickness measurement methods for physical vapor deposited aluminum coatings in packaging applications: A review. *Coatings* **2017**, *7*, 9. [[CrossRef](#)]
24. Parker, M.E.; Bronlund, J.E.; Mawson, A.J. Moisture sorption isotherms for paper and paperboard in food chain conditions. *Packag. Technol. Sci.* **2006**, *19*, 193–209. [[CrossRef](#)]
25. Everett, D.H. Adsorption hysteresis. *Solid-Gas Interface* **1967**, *2*, 1055–1113.
26. Quirijns, E.J.; Van Boxtel, A.J.; van Loon, W.K.; Van Straten, G. Sorption isotherms, gab parameters and isosteric heat of sorption. *J. Sci. Food Agric.* **2005**, *85*, 1805–1814. [[CrossRef](#)]
27. *Geometrical Product Specifications (GPS)—Surface Texture: Profile Method—Rules and Procedures for the Assessment of Surface Texture (ISO 4288:1996)*; German Version EN ISO 4288:1997; German Institute for Standardization: Berlin, Germany, 1998. (In German)
28. *Geometrical Product Specifications (GPS)—Surface Texture: Profile Method—Nominal Characteristics of Contact (Stylus) Instruments (ISO 3274:1996)*; German Version EN ISO 3274:1997; German Institute for Standardization: Berlin, Germany, 1998. (In German)
29. Sorg, H. *Praxis der Rauheitsmessung und Oberflächenbeurteilung*; Hanser: Munich, Germany, 1995. (In German)
30. Liu, H.D.; Zhao, Y.P.; Ramanath, G.; Murarka, S.P.; Wang, G.C. Thickness dependent electrical resistivity of ultrathin (<40 nm) Cu films. *Thin Solid Films* **2001**, *384*, 151–156.
31. Lindner, M. Factors affecting the hygroexpansion of paper. *J. Mater. Sci.* **2017**, *53*, 1–26. [[CrossRef](#)]
32. Larsson, P. Hygro-and Hydroexpansion of Paper. Ph.D. Thesis, KTH Royal Institute of Technology, Stockholm, Sweden, 2010.
33. Lavrykov, S.A.; Ramarao, B.V.; Lyne, O.L. The planar transient hygroexpansion of copy paper: Experiments and analysis. *Nordic Pulp Pap. Res. J.* **2004**, *19*, 183–190. [[CrossRef](#)]
34. Pineau, A.; Amine Benzerga, A.; Pardoën, T. Failure of metals iii: Fracture and fatigue of nanostructured metallic materials. *Acta Mater.* **2016**, *107*, 508–544. [[CrossRef](#)]
35. Pineau, A.; Benzerga, A.A.; Pardoën, T. Failure of metals i: Brittle and ductile fracture. *Acta Mater.* **2016**, *107*, 424–483. [[CrossRef](#)]
36. Bruggeman, V.D. Berechnung verschiedener physikalischer konstanten von heterogenen substanzen. I. Dielektrizitätskonstanten und leitfähigkeiten der mischkörper aus isotropen substanzen. *Ann. Phys.* **1935**, *416*, 636–664. (In German) [[CrossRef](#)]
37. Landauer, R. The electrical resistance of binary metallic mixtures. *J. Appl. Phys.* **1952**, *23*, 779–784. [[CrossRef](#)]
38. Levin, M.; Miller, M. Maxwell a treatise on electricity and magnetism. *Uspekhi Fizicheskikh Nauk* **1981**, *135*, 425–440. [[CrossRef](#)]

RESEARCH PAPER:

HYGROEXPANSION AND SURFACE ROUGHNESS CAUSE DEFECTS AND INCREASE THE ELECTRICAL RESISTIVITY OF PHYSICAL VAPOR DEPOSITED ALUMINUM COATINGS ON PAPER

Coatings **2019**, *9*, 33

18 of 18

39. Landauer, R. Electrical transport and optical properties of inhomogeneous media. In Proceedings of the First Conference on the Electrical Transport and Optical Properties of Inhomogeneous Media, American Institute of Physics Conference Proceedings, Columbus, OH, USA, 7–9 September 1977; Garland, J.C., Tanner, D.B., Eds.; American Institute of Physics: New York, NY, USA, 1978.
40. Hamilton, R.L.; Crosser, O. Thermal conductivity of heterogeneous two-component systems. *Ind. Eng. Chem. Fundam.* **1962**, *1*, 187–191. [[CrossRef](#)]
41. Nakajima, H. Fabrication, properties, and applications of porous metals with directional pores. *Proc. Jpn. Acad. Ser. B* **2010**, *86*, 884–899. [[CrossRef](#)]
42. Kraker, P.T.; Glushko, O.; Cordill, M.J. Relationship between cracking and resistance increase in polymer-supported metal films under mechanical load. Presented at Materials Science and Engineering Conference, Darmstadt, Germany, 27–29 September 2016.
43. Krcho, S. Electron percolation in copper infiltrated carbon. *Int. J. Electr. Eng.* **2015**, *66*, 339–343.
44. Feng, Y.; Zheng, H.; Zhu, Z.; Zu, F. The microstructure and electrical conductivity of aluminum alloy foams. *Mater. Chem. Phys.* **2003**, *78*, 196–201. [[CrossRef](#)]
45. Cox, H.L. The elasticity and strength of paper and other fibrous materials. *Br. J. Appl. Phys.* **1952**, *3*, 72. [[CrossRef](#)]
46. Panek, J.C. Fragmentation of Brittle Polymeric Toner Line Caused by Swelling of Paper Substrate during Immersion in Water. Ph.D. Thesis, Michigan Technological University, Houghton, MI, USA, 1999.



© 2019 by the authors. Licensee MDPI, Basel, Switzerland. This article is an open access article distributed under the terms and conditions of the Creative Commons Attribution (CC BY) license (<http://creativecommons.org/licenses/by/4.0/>).

6. Research paper:

Hygroexpansion, surface roughness and porosity affect the electrical resistance of EVOH-aluminum-coated paper

When aluminum is applied to paper by physical vapor deposition, substrate roughness contributes to the defect density and hygroexpansion can cause defects that impair the aluminum coating. Both effects can manifest as an increase in electrical resistance. The effect of substrate paper hygroexpansion (0–95% relative humidity) and paper surface roughness on the effective resistivity (ρ_{EFF}) of aluminum coatings was quantified. To create different degrees of roughness, five different papers were used. Each of them had one pigment coated side and one side without pigment coating. These different rough paper surfaces were pre-coated with ethylene vinyl alcohol co-polymer (EVOH).

It was shown that lacquer coating weights were higher when the lacquer was applied on paper surfaces, which were not pigment coated. This probably reflected the porous surface of the paper and its microchannels, which let the lacquer flow into and fill up pores and microchannels. This effect also promoted hygroexpansion, because the lacquer occupied the space that otherwise could be filled by expanding fibers.

When pure paper or paper covered with lacquer was coated with aluminum via PVD, the effective resistivity increased with the roughness, hygroexpansion and the thinness of the aluminum layer. The crack onset point decreased with increasing substrate roughness and aluminum thinness. The **relative effective resistivity increase only depended on aluminum thickness when the substrate was smooth** and free of pores. Regardless of the substrate, it was found that an **aluminum thickness of >35 nm did not further improve the mechanical stability** of the aluminum coatings under hygroexpansion-induced tension. For practical applications, this means that ~35 nm is the aluminum thickness that achieves the greatest avoidance of roughness induced defects and hygroexpansion induced defects while using the minimum amount of coating material. However, cracked aluminum barrier coatings did not regain their initial resistivity during re-contraction. This means it is critical to avoid hygroexpansion-induced defects.

Author Contributions: Martina Lindner: conceptualization, methodology, formal analysis, data curation, visualization, original draft preparation, review and editing.

RESEARCH PAPER:
HYGROEXPANSION, SURFACE ROUGHNESS AND POROSITY AFFECT THE ELECTRICAL
RESISTANCE OF EVOH-ALUMINUM-COATED PAPER

Matthias Reinelt: review and editing. Tobias Gilch: investigation, original draft preparation.

Horst-Christian Langowski: review and editing.

Article

Hygroexpansion, Surface Roughness and Porosity Affect the Electrical Resistance of EVOH-Aluminum-Coated Paper

Martina Lindner ^{1,2,*}, Matthias Reinelt ², Tobias Gilch ^{2,3} and Horst-Christian Langowski ^{1,2}

¹ TUM School of Life Sciences Weihenstephan, Technical University of Munich, Weihenstephaner Steig 22, 85354 Freising, Germany; horst-christian.langowski@ivv.fraunhofer.de

² Fraunhofer-Institute for Process Engineering and Packaging IVV, Giggenhauser Strasse 35, 85354 Freising, Germany; matthias.reinelt@ivv.fraunhofer.de (M.R.); tobias.gilch@ivv.fraunhofer.de (T.G.)

³ Munich University of Applied Sciences, Lothstraße 35, 80335 Munich, Germany

* Correspondence: martina.lindner@ivv.fraunhofer.de; Tel.: +49-8161-491-536

Received: 1 April 2019; Accepted: 26 April 2019; Published: 30 April 2019



Abstract: When aluminum is applied to paper by physical vapor deposition, substrate roughness contributes to the defect density and hygroexpansion can cause defects that impair the aluminum coating. Both effects can manifest as an increase in electrical resistance. We quantified the effect of substrate paper hygroexpansion (0–95% relative humidity) and paper surface roughness on the effective resistivity (ρ_{EFF}) of aluminum coatings. To create different degrees of roughness, five different papers were used. Each of them had one pigment coated side and one side without pigment coating. These different rough paper surfaces were pre-coated with ethylene vinyl alcohol co-polymer (EVOH). Hygroexpansion was promoted by pre-coating and increased more when the coating was applied on rough and porous surfaces. Simultaneously, the pre-coating reduced surface roughness; especially porosity. The reduction of porosity decreased effective resistivity (ρ_{EFF}). Based on these results, an aluminum thickness of ≥ 35 nm is recommended to ensure maximum mechanical stability during hygroexpansion in combination with minimum material usage. Moreover, the resistivity did not regain its initial value when the paper substrate shrank during re-drying.

Keywords: resistivity; physical vapor deposition; sheet resistance; ethylene vinyl alcohol; paper coating; penetration; porosity; sorption; humidity

1. Introduction

When nanometer thin coatings of aluminum are deposited on paper substrates, the substrate roughness determines its electrical resistance; and hygroexpansion manifests as an increase in electrical resistance and resistivity (compared to bulk aluminum) [1]. These phenomena reflect the greater number of defects in the aluminum layer. Defects triggered by hygroexpansion and roughness are relevant in various applications, such as packaging, paper electronics and flexible electronics.

In the case of packaging, aluminum coatings are used to create high gas barriers on polymer substrates. However, it is not yet possible, to achieve such gas barriers on paper substrates, because the aluminum coatings contain defects, which let gas permeate. In the case of paper electronics, such defects increase the resistance of the aluminum conductor coating. Although in the case of packaging applications, the effect of aluminum defects is a higher gas permeability, in both cases—packaging and paper electronics—defects can manifest as an increase in electrical resistance and resistivity. Two known reasons for such defects are substrate hygroexpansion and substrate roughness [1,2]. Hygroexpansion is the moisture-induced swelling of paper. Hygroexpansion and paper roughness can be altered by various methods during [3–10] or after [11–14] paper production. In the present case, the effect of

a polymer coating on both parameters—roughness and hygroexpansion—was evaluated. Previous studies [1,2] have shown that the effective resistivity ρ_{EFF} (defined by the measured resistance, coating weight of aluminum and ideal density; compare Equations (2)–(4) of such thin aluminum layers is not constant but decreases with increasing thickness (d) and decreasing substrate roughness (R_Z) [15,16]. The correlation can be described using Equation (1), which includes two fit factors (k and c) and the literature resistance value for bulk aluminum (ρ_{lit}) [1].

$$\rho_{EFF} = R_Z \cdot c \cdot \frac{1}{d} + \rho_{lit} \cdot (1 + R_Z \cdot k) \quad (1)$$

$$\rho_{lit} = 27 \Omega \cdot nm \quad k = 0.5 / \mu m \quad c = 2964 \Omega \cdot nm^2 / \mu m$$

Even though the relationship between roughness and resistivity can be well described, as in Equation (1), this is not yet the case for hygroexpansion and resistivity. The effect of hygroexpansion on electrical resistivity is much more complex, because the effect of hygroexpansion itself is also affected by the substrate roughness. As both processes are relevant for packaging and paper electronic applications, the current study investigates in depth the effect of substrate roughness on the increase in electrical resistivity during hygroexpansion. Different degrees of roughness were created by using different substrate papers with different rough back and front surfaces, either with a pigment coating (PC) or without (noPC), and by pre-coating the surfaces with ethylene vinyl alcohol co-polymer (EVOH) before aluminum deposition. The electrical resistivity of the aluminum coatings was then determined at different levels of relative humidity (RH). The aluminum thickness was varied to define the influence of this parameter.

2. Materials and Methods

2.1. Used Papers

The paper substrates were chosen as they are typically applied for metallization processes in the packaging industry. They are listed in Table 1. Each of the papers had one side, which is pigment coated (PC) and one side, which has not been pigment coated (noPC).

Table 1. Paper and polymer substrates.

Product Name	Grammage [g/m ²]	Supplier
Metalkote	65	Ahlstrom-Munksjö
Algro Finesse T	70	Sappi Europe SA
Adicar WS HGM	80	Cham Paper Group
Adicar 2	80	Cham Paper Group
Labelcar MTS	65	Cham Paper Group

2.2. Preparation of Aqueous EVOH Solutions

EVOH is known to be a water sensitive polymer and is often used to reduce the oxygen permeability of coated papers [17]. The required amount (15% w/w) of EVOH granulate (AQ4104, Kuraray, Frankfurt am Main, Germany) was mixed with the required amount of deionized water in a high-performance disperser (Thermomix TM 31, Vorwerk Deutschland, Wuppertal, Germany) at low stirring speed (40 rpm) for 15 min. Then, the disperser was set to 100 rpm for 90 min, heating up continually to 90 °C. Afterward the solution was stirred at 40 rpm for 120 min, while cooling to room temperature. The solution was then filtered and filled into a glass bottle, which was sonicated at 37 kHz and 10 °C for 10 min to remove air bubbles. The ethylene content of this EVOH grade was ~8 mol% [18].

2.3. Laboratory-Scale EVOH Coating

The paper types Adicar 2, Adicar WS HGM, Algro Finesse T and Labelcar MTS were only available as sheets, and were, therefore, coated using laboratory-scale equipment (CUF 5, Sumet Systems GmbH,

Denklingen, Germany). Each paper was coated once on PC and once on noPC (Figure 1). The substrate sheet was fixed with a clamp on a horizontal slide and a wired rod—with a theoretical wet coating thickness of 19 μm —was positioned on the top of the sheet and forced onto the sheet by applying a force of 40 N. Approximately 5 mL of the EVOH solution was applied with a syringe into the gap between the rod and the substrate across the width of the sheet. The slide was then moved horizontally below the rod (40 mm/s) to ensure even distribution across the paper sheet. The slide was then passed through a drying section to dry the coated paper by air convection at 85 $^{\circ}\text{C}$ for 90 s.

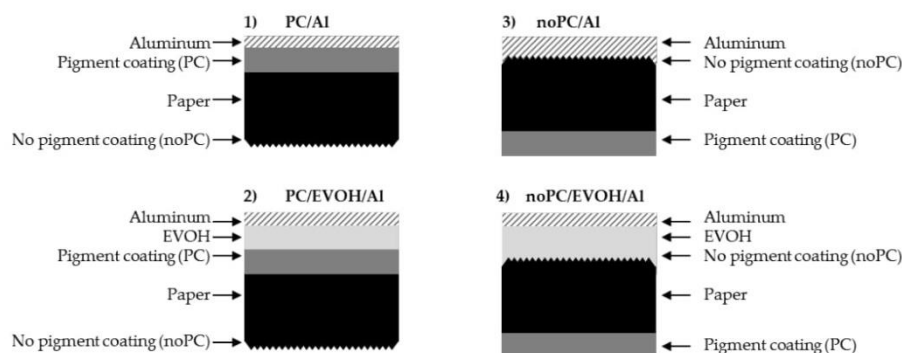


Figure 1. A schematic description of the samples that were produced, as described in the previous enumeration.

2.4. Pilot-Scale EVOH Coating

Metalkote paper was coated in a reel-to-reel process using the lacquering and lamination plant at Fraunhofer IVV. It was coated once on PC and once on noPC. The coating width was 210 mm at a web speed of 5 m/min, with an anilox ceramic roll (40 lines/cm, 45 $^{\circ}$ pattern, theoretical pick-up volume 45 mL/m 2) and a convective air drying temperature of 85 $^{\circ}\text{C}$, with an air flow rate of 8000 m 3 /h.

2.5. EVOH Coating Weight Determination

Samples were stored at 23 $^{\circ}\text{C}$, 50% RH for 48 h. Then, five circles with an area of 50 cm 2 were cut from the EVOH-coated and non-coated papers. Subsequently, the weight of the samples was determined (Mettler AT261 DeltaRange, Mettler-Toledo, Gießen, Germany). The coating weight was determined as the weight difference between EVOH-coated and non-coated papers, normalized to an area of 1 m 2 .

2.6. Physical Vapor Deposited (PVD) Aluminum Coating

The following samples were produced by PVD coating (Figure 1).

1. PC/AI: Aluminum was deposited on the paper side, that has been pigment coated;
2. PC/EVOH/AI: The paper was first coated with EVOH on the paper side, that has been pigment coated, and then aluminum was deposited on top of the EVOH;
3. noPC/AI: Aluminum was deposited on the paper side, which has not been pigment coated;
4. noPC/EVOH/AI: The paper was first coated with EVOH on the paper side, that has not been clay coated, then aluminum deposited was on top of the EVOH.

Paper samples were cut to 105 \times 148 mm 2 sheets and taped along all four edges onto a paper carrier roll using thermally stable adhesive tape (Kapton, DuPont, Neu-Isenburg, Germany). In order to achieve a high vacuum during PVD, it was necessary to reduce the moisture content (*mc*) of the paper substrate. Therefore, the carrier roll containing all the samples was dried at 70 $^{\circ}\text{C}$ for 9 days in a Heratherm oven (Thermo Fisher Scientific, Munich, Germany) prior to metallization, which is not an industrial process but necessary in pilot plant scale.

PVD was carried out using the electron beam heating method. Moisture remaining in the chamber was extracted using a Meissner cold trap and the deposition roll was water cooled. The aluminum was 99.98% pure (K135 from Drahtwerk Elisental W. Erdmann GmbH & Co., Neuenrade, Germany). The coating thickness was varied by changing the web speed from 0.5 to 3.5 m/min at steps of 0.5 m/min at an evaporation rate of 2–3.5 nm/s. Further process details can be found elsewhere [19].

Following their removal from the box coater, the rolls were transferred to a polyethylene drum containing 1 kg Perlform silica gel (orange, 2–5 mm, with an indicator; Carl Roth, Karlsruhe, Germany) to reduce the *RH* to 0%. As such, the unwanted water uptake and hygroexpansion of the paper before the experiments was kept to a minimum. The drum was then stored at 23 °C.

2.7. Aluminum Coating Weight Determination

The coating weight ($cw_{NOMINAL}$) and thickness ($d_{NOMINAL}$) of aluminum applied to the surface of each sample was calculated based on a previously described model [19]. Both values are linked by the literature value for aluminum density (δ_{LIT}) as shown in Equation (2).

$$cw_{NOMINAL} = d_{NOMINAL} \cdot \delta_{LIT}. \quad (2)$$

2.8. Scanning Electron Microscopy (SEM)

Images were acquired using a JSM-7200F scanning electron microscope (Jeol, Peabody, MA, USA) at 1–4 kV. The working distance was maintained at 9.1–10.0 mm. The samples were sputtered with gold.

2.9. Determination of Sheet Resistance via Eddy Currents at Different Relative Humidities

Prior to re-humidification of the aluminum-coated samples, rigid frames were produced to which the samples were loosely attached to avoid curling. In the next step, the plastic frames, the silica pouches, a dish containing 500 g silica gel, a pair of scissors, pressure lock bags, adhesive tape, a testostor 175 hygrometer (Testo SE & Co. KGaA, Lenzkirch, Germany), and Fibox oxygen concentration measuring points (PreSens Precision Sensing, Regensburg, Germany) were placed into a glove box (Mecaplex Metall, Grenchen, Switzerland). Finally, the roll with the aluminum-coated samples was placed into the glove box, which was immediately closed and flushed with pure nitrogen to remove moisture. Flushing was assumed to be complete when a constant, minimal *RH* value of <3% (determined using the hygrometer) was reached. The paper samples were then removed from the carrier roll and attached to the frames with adhesive tape. The samples were transferred into the pressure lock bags. After transferring all samples into these bags, the glove box was opened and the pressure lock bags were placed in the plastic drum with fresh silica gel.

The samples were then taken one by one from the drum and the sheet resistance was measured at five predetermined points on each sample. After this first measurement at 0% *RH*, the samples were immediately transferred to a KBF720-230V climate chamber (Binder, Tuttlingen, Germany) set to 23 °C, with humidity values of 35%, 50%, 70%, 85% and 95% *RH*. The samples were stored in each climate for 24 h before the next measurement of sheet resistance. After each measurement, the samples were placed back into the climate chamber. Excessive air convection in the chamber was avoided by using additional plastic curtains placed inside the chamber.

The sheet resistance (R_{\blacksquare}) was measured using the eddy current method (EddyCus TF lab 4040, Suragus, Dresden, Germany). The skin depth was $>8 \mu\text{m}$ [20,21], which ensured full penetration of the aluminum layer by the magnetic field. The area captured by the measurement was approximately $5 \times 5 \text{ mm}^2$. The sheet resistance (R_{\blacksquare}) of a resistor with thickness d and resistivity ρ is defined as shown in Equation (3).

$$R_{\blacksquare} = \frac{\rho}{d} \quad (3)$$

RESEARCH PAPER:

HYGROEXPANSION, SURFACE ROUGHNESS AND POROSITY AFFECT THE ELECTRICAL RESISTANCE OF EVOH-ALUMINUM-COATED PAPER

Coatings 2019, 9, 295

5 of 14

The effective resistivity (ρ_{EFF}) was then calculated from the thickness ($d_{NOMINAL}$) and the measured sheet resistance (R_{\blacksquare}) as shown in Equation (4).

$$\rho_{EFF} = d_{NOMINAL} \cdot R_{\blacksquare} \quad (4)$$

The relative effective resistivity increase (γ) was calculated from the effective resistivity at an RH of 0% and at a given RH of $x\%$, where $x = 35\%, 50\%, 70\%, 85\%$ or 95% RH, as shown in Equation (5).

$$\gamma = \frac{\rho_{EFF}^{RH=x}}{\rho_{EFF}^{RH=0\%}} - 1 \quad (5)$$

The theoretical increase in resistivity γ due to the mono-axial expansion of aluminum without any damaging effect can be estimated by the following assumption: The volume of aluminum (cross-section $A \times$ length L) is constant under strain ε , namely $A \cdot L = A_0 \cdot L_0$. Under strain, the material expands in length but also thins. Thus, A decreases and L increases due to plastic deformation. Based on that assumption, Equations (6)–(8) can be derived [22].

$$\frac{R_{\blacksquare}}{R_{\blacksquare 0}} = \left(\frac{L}{L_0}\right)^2 \quad (6)$$

$$\frac{\rho_{EFF}}{\rho_{EFF,0}} = \left(\frac{L}{L_0}\right)^2 = (1 + \varepsilon)^2 \quad (7)$$

$$\gamma = \frac{\rho_{EFF}}{\rho_{EFF,0}} - 1 = (1 + \varepsilon)^2 - 1 \quad (8)$$

2.10. Sorption Isotherm

Sorption isotherms for the paper substrates were recorded at 0%, 35%, 50%, 70%, 85% and 95% RH using SPSx-1 μ (ProUmid GmbH & Co. KG, Ulm, Germany). The temperature was set to 23 °C. For each humidity increase, the weight was measured until equilibrium was reached. The minimum time for each RH increase was set to 2 h, and the maximum to 48 h. The measurements were done once on the pure papers and twice on the EVOH-coated papers.

2.11. Hygroexpansion

The hygroexpansion measurement was carried out on three samples (288 \times 200 mm²) from each paper. The samples were dried for 20 days in silica gel at 23 °C. Then, each was stored in the KBF720-230V climate chamber (Binder, Tuttlingen, Germany) at 23 °C for 24 h, with sequentially increasing humidity values of 35%, 50%, 70%, 85% and 95% RH. The samples were taken one by one from the drum/climate chamber and their size was scanned at a resolution of 1200 dpi (CanonScan LiDE 700F, Canon, Nürnberg, Germany). Images were saved as jpg files. Subsequently, the distance ($L_{0,CD}$) between certain reference points in CD (cross direction) was measured threefold, using LAS v4.0 software (Leica Microsystems GmbH). Measurements were only performed in CD because hygroexpansion is dominant in this direction. From these data, the percentage length increase ε at increasing RH values was calculated by setting $L_{0,CD}$ in relation to the increased lengths L_{CD} as shown in Equation (9).

$$\varepsilon_{CD} = \frac{L_{CD} - L_{0,CD}}{L_{0,CD}} \quad (9)$$

2.12. Surface Roughness

The roughness was determined five-fold using the mechanical profile method (Hommel Etamic W55, Jenoptik, Jena, Germany). The roughness term R_Z was taken according to DIN EN ISO

4288:1998 [16] and DIN EN ISO 3274:1998 [15]: The traversing length L_N is divided into five equal-sized subsections L_R (in this case, $L_N = 4$ and $L_N = 12.5$, respectively). In the single subsections, the single roughness (Z_N) was determined. The single roughness is the difference between the highest and lowest points in one subsection L_R [23]. From Z_N , R_Z is determined as their arithmetic average. The value R_Z was used, as the graphs do not significantly change when other roughness values such as R_a and R_q are used. The usage of R_{p_c} was evaluated but was found to lead to inconsistent results because of the necessary adaption of the counting threshold.

2.13. Statistical Methods

The data points represent median values for resistances and average values for roughness. The statistical differences were evaluated with a u-test from Wilcoxon, Mann and Whitney, with the level considered significant when equal to 5%. Graphs were designed using OriginPro 2016 (version 2018.b) and statistical evaluations were carried out with Visual-XSel (CRGRAPH) (version 12.0).

3. Results and Discussion

3.1. Effect of Polymer Coatings on Paper Hygroexpansion

In the first set of experiments, we determined the effect of EVOH coatings on paper hygroexpansion and water absorption using five different papers, which were EVOH coated either on the side with pigment or without pigment coating (PC vs noPC). Initially, we measured the coating weight. Although in each case the same EVOH coating and the same rod was used, the coating weight of the EVOH coating was higher on noPC paper (Figure 2). This reflected the fact that noPC paper is rougher and more porous, so the EVOH could penetrate into the paper more easily (Figure 3) [24–27]. However, the coating weight did not show a linear correlation with roughness (R_Z), probably because the roughness value does not sufficiently describe the porosity of the paper sample.

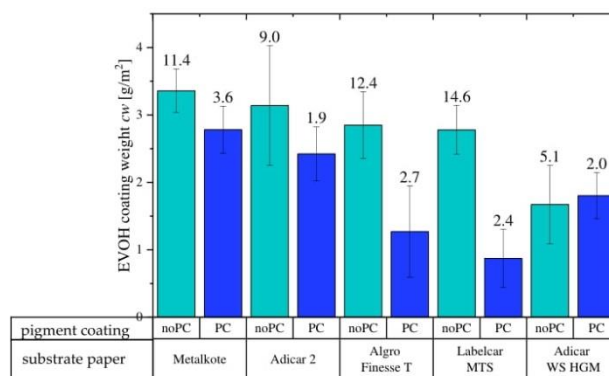


Figure 2. Coating weight at 50% relative humidity. Although in each case the same EVOH coating and the same rod was used, the weight of the EVOH coating was higher on the rougher noPC surface. Roughness values R_Z before EVOH coating are shown as numbers above the columns. PC/noPC = paper surface with/without pigment coating. EVOH = ethylene vinyl alcohol lacquer.

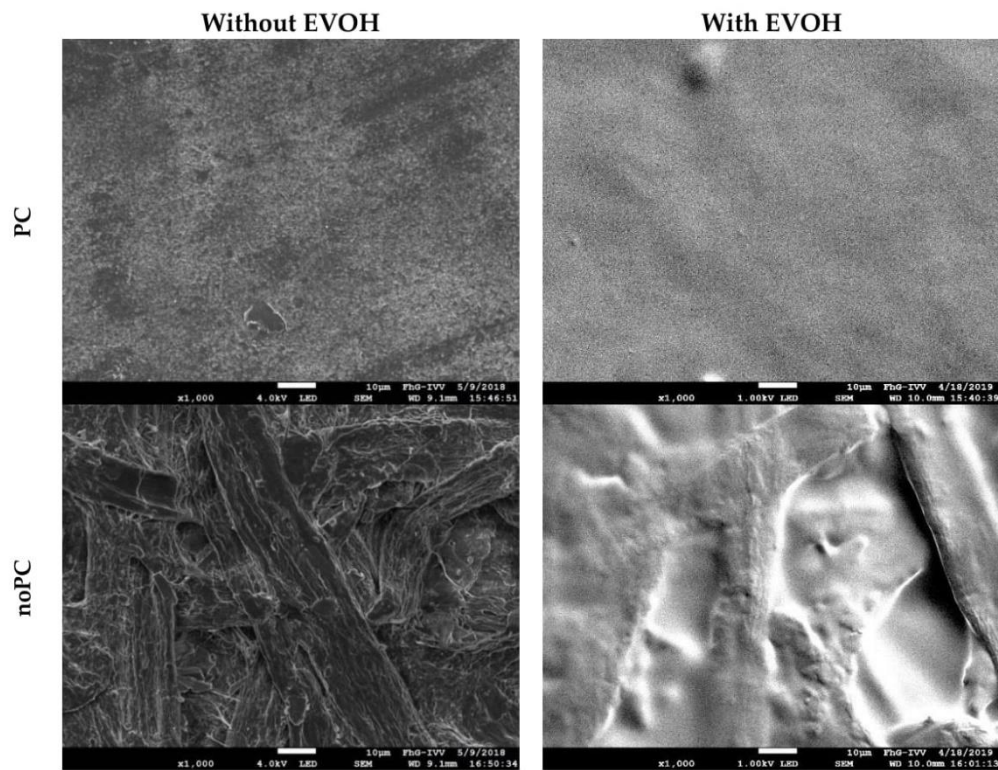


Figure 3. Scanning electron microscope images at 1000 times magnification of Metalkote paper. The EVOH-coated paper shows lower roughness and lower porosity.

Next, we measured the moisture sorption and hygroexpansion of the coated and non-coated papers. We found that EVOH increased the water absorption (Figure 4, left column) compared to the pure paper (—■—) but the absorption was the same regardless of the side of the paper to which the EVOH was applied (PC—▼— or noPC—◆—). This reflected the relatively low coating weight ($\sim 1\text{--}3\text{ g/m}^2$) compared to the paper grammage ($65\text{--}80\text{ g/m}^2$). In contrast, hygroexpansion (Figure 4, right column) was strongly affected by the side to which the EVOH was applied. The effect was not visible in the case of Adicar WSHGM, as the differences in roughness and coating weight between noPC and PC was low. The hygroexpansion was higher for the EVOH-coated papers than for the pure paper, but highest when EVOH was applied to the noPC side (—◆—). This indicated that the EVOH penetrated further into the noPC side of the paper because the surface contained more pores and channels (see images presented in [1]). EVOH thus fills the voids in the noPC paper and occupies space that the fibers would otherwise fill during expansion. This interpretation is supported by reference [28]. Because this space between the fibers is now occupied by EVOH, the paper expands further, particularly on the noPC side where more EVOH has penetrated between the fibers. This is because EVOH does not prevent water molecules from permeating towards the fibers, but it allows water molecules to permeate towards the fibers, which leads to fiber hygroexpansion. Moreover, the EVOH itself absorbs water and swells, which further intensifies the effect (lacquer hygroexpansion of $\sim 5\%$ and moisture content of 30% at $100\% RH$ at $23\text{ }^\circ\text{C}$).

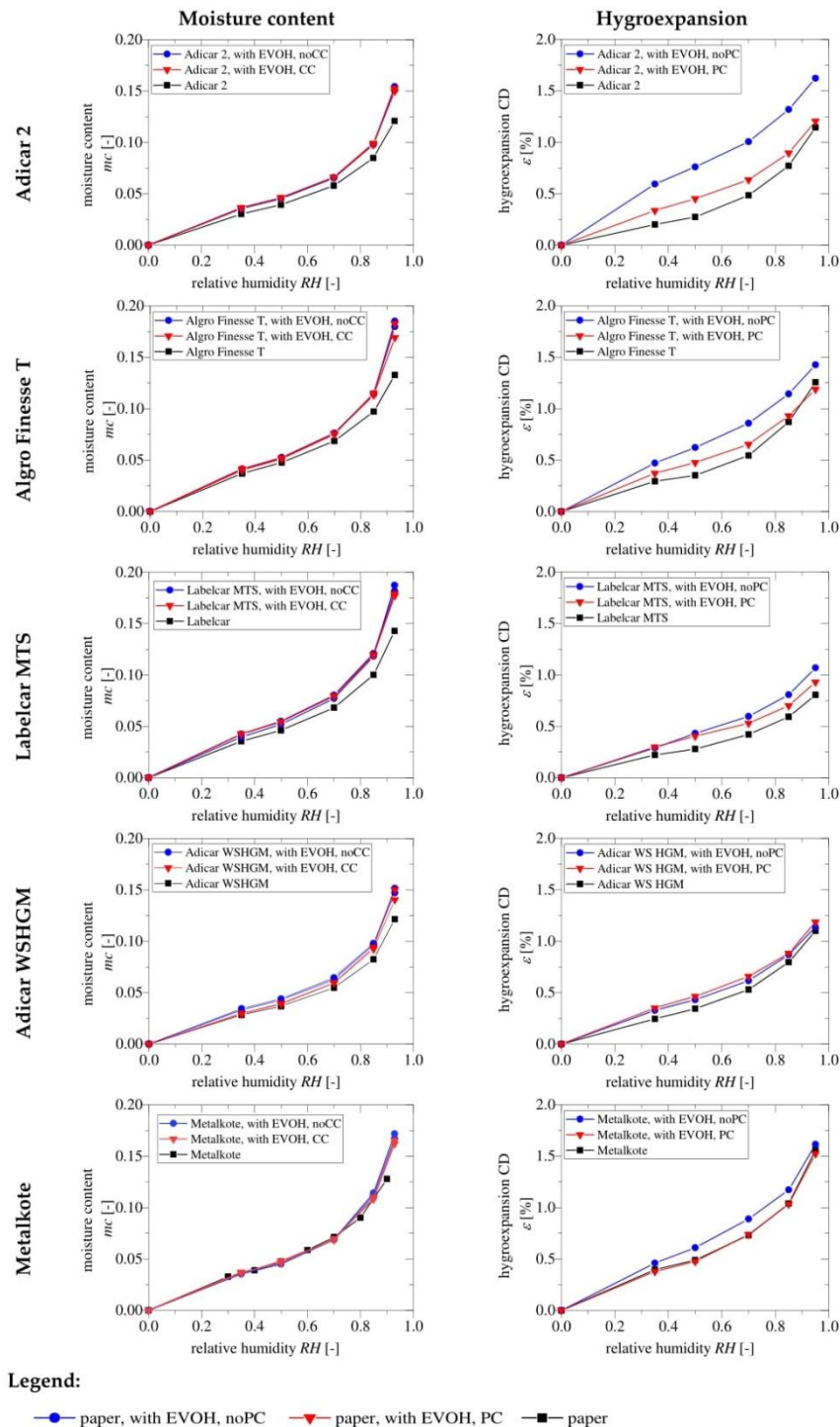


Figure 4. Moisture content (mc) and hygroexpansion (ϵ) increase with relative humidity (RH). The EVOH coating increased moisture content and hygroexpansion. Hygroexpansion increased more when the EVOH was applied to the noPC surface. PC/noPC = paper surface with/without pigment coating. EVOH = ethylene vinyl alcohol lacquer.

3.2. Effect of EVOH Pre-coating on Effective Resistivity of the Aluminum Coating

As we previously reported in reference [1], the effective resistivity ρ_{EFF} decreased with aluminum thickness and increased with substrate roughness, which was also confirmed in Figure 5. There, we found that curves—as in Figure 5—showed a characteristic minimum resistivity value ρ_{OFFSET} [$\Omega \cdot \text{nm}$] when the aluminum layer was thickest, overlaid by a variable resistivity ρ_n [$\Omega \cdot \text{nm}$] when the layer was thinner. Even for the thicker coatings, the minimum resistivity ρ_{OFFSET} would not achieve the literature values for bulk aluminum ρ_{lit} . In the same previous study [1], this minimum resistivity ρ_{OFFSET} decreased with decreasing substrate roughness, possibly because less roughness led to smaller defects, which were easily filled with aluminum. In comparison, defects on very rough papers were too large to be filled, thus increasing the resistance R and minimum resistivity ρ_{OFFSET} . For thin coatings, the resistivity was higher on rough substrates, and the variable resistivity ρ_n , therefore, also depended on paper roughness R_Z . Moreover, thinner coatings led to higher variable resistivity ρ_n because less aluminum was available to fill the defects. These observations have been combined with the simple descriptive approach shown in Equation (1).

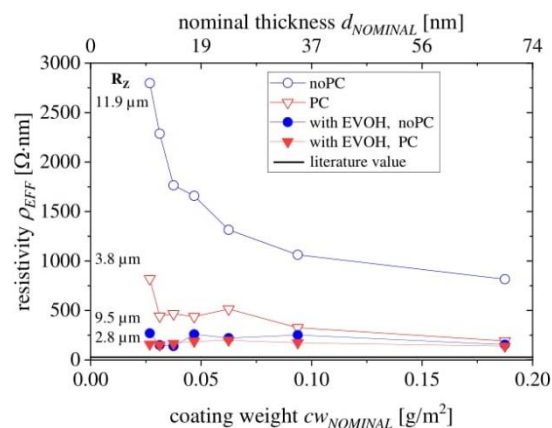


Figure 5. Increasing roughness increased the effective resistivity at 0% relative humidity (RH) due to defects in the aluminum coating. Although EVOH coating only had a minor impact on roughness (R_Z) values, the resistivity decreased massively due to the reduction of the areal density of micropores and channels. Results were generated on Metalkote paper. PC/noPC = paper surface with/without pigment coating. EVOH = ethylene vinyl alcohol lacquer.

However, the present study shows that substrate roughness cannot be the only influencing factor and the following conclusions can be drawn from Figure 5:

1. The resistivity of aluminum applied to EVOH-coated surfaces was lower than on surfaces without EVOH. This supports the observation described previously [1];
2. However, the roughness of noPC with EVOH (\bullet , $R_Z = 9.5 \mu\text{m}$) was much higher than PC (∇ , $R_Z = 3.8 \mu\text{m}$). Nevertheless, noPC with EVOH (\bullet) had a lower resistivity than PC (∇);
3. This indicates that, not only the roughness, but also the precise morphology—including pores and microchannels—were decisive factors. EVOH coatings may fill up pores and microchannels, but they did not affect the micrometer-scale roughness significantly (compare Figure 3);
4. This filling up of voids facilitated the formation of a closed aluminum layer because it reduced the severity of defects in the aluminum coating. As shown in Section 3.1, the filling up of voids promoted hygroexpansion and EVOH should, therefore, be applied on the PC side of the paper.

3.3. Effect of EVOH Pre-Coating on the Increase in Resistivity during Hygroexpansion

It is likely that the aluminum coating forms cracks when the underlying paper expands, thus increasing the resistivity, and that greater substrate roughness leads to more cracks and thus to a higher increase in effective resistivity (γ). In order to show the effect of hygroexpansion and roughness in isolation from the effect of aluminum thickness, the relative effective resistivity increase γ (rather than resistance R_{\square} or effective resistivity ρ_{EFF}) was considered, as shown in Figure 6.

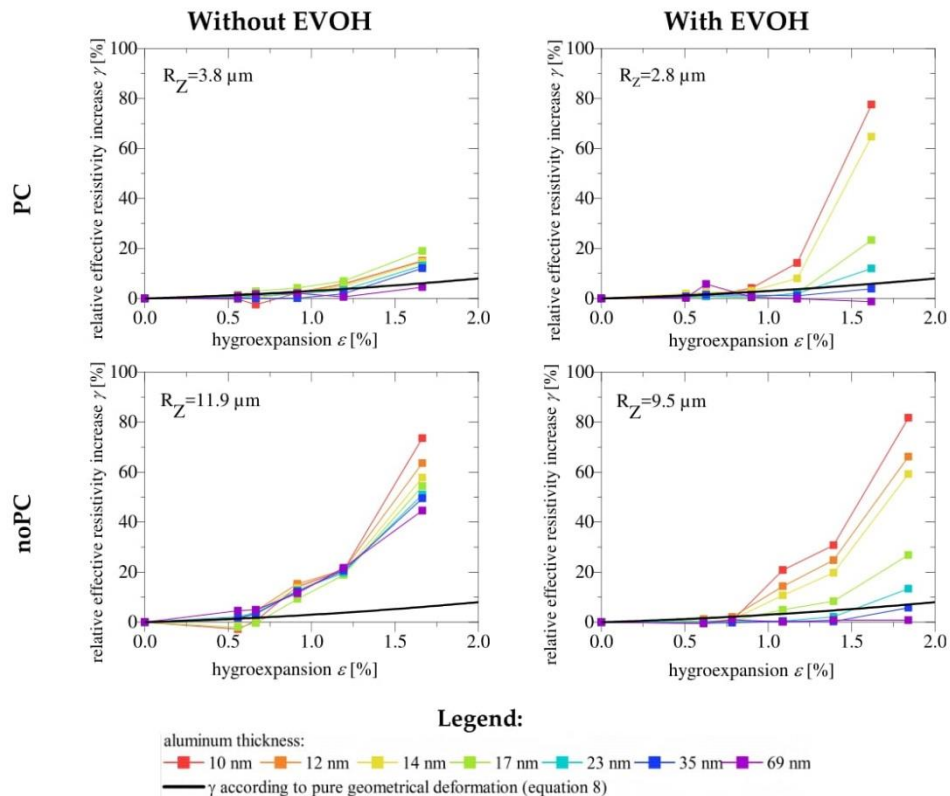


Figure 6. Increasing roughness R_Z and porosity of the substrate paper Metalkote increased the effective resistivity ρ_{EFF} due to defects in the aluminum coating. Although the EVOH coating only had a minor impact on roughness values R_Z , the resistivity was lower due to the lower porosity. PC/noPC = paper surface with/without pigment coating. EVOH = ethylene vinyl alcohol lacquer.

We found that the difference between the EVOH-coated and non-coated surfaces subsequently affects the relative effective resistivity increase γ during hygroexpansion. The increase in resistivity for PC and noPC paper surfaces with and without EVOH, and with aluminum layers differing in thicknesses, is summarized in Figure 6. The comparison of the different samples allows the following conclusions to be drawn:

1. The relative effective resistivity increase γ correlated with hygroexpansion ϵ ;
2. The maximum relative effective resistivity increase γ_{max} at 95% RH was partially higher on EVOH-coated surfaces (Figure 6). This was because the initial effective resistivity values ρ_{EFF} (Figure 5) were much lower; probably due to fewer initial defects. Therefore, the addition of only a few more defects increased the resistivity by a much greater degree. This means that γ_{max} also depended on the initial ρ_{EFF} before hygroexpansion, which was higher on rough and porous surfaces;

3. In the ideal case (smooth substrate surface, low hygroexpansion, and thick coatings) γ was equal to the value expected, according to the geometrical deformation model in Equation (8). This indicated that no additional defects occurred during hygroexpansion and that no additional defects should be expected in the case of smooth substrates and thick coatings (>35 nm);
4. On EVOH-coated surfaces, the effect of the aluminum thickness (d) was more explicit. Thinner coatings (<35 nm) led to a higher relative effective resistivity increase γ . Coatings >35 nm are, therefore, recommended;
5. On surfaces without EVOH, the effect of the aluminum thickness was less explicit. On non-EVOH coated surfaces, the effect of aluminum thickness on the increase in γ was lower because the aluminum already contained many defects before hygroexpansion, due to its roughness and porosity (Figure 3). Hence the additional defects due to hygroexpansion did not significantly affect the resistivity value. The EVOH decreased the roughness (R_z) and the areal density of pores and microchannels. For practical applications, this means that even by applying thicker aluminum coatings, the negative effect of roughness and pores during hygroexpansion cannot be reduced. Thus, a polymer pre-coating such as EVOH is indispensable;
6. The effect of aluminum thickness on the maximum relative effective resistivity increase γ_{max} (at 95% RH) is shown in Figure 7. When the paper was coated with EVOH, γ is affected to a greater degree by aluminum thickness. When the aluminum thickness was approximately 30–40 nm on EVOH-coated surfaces, γ_{max} did not decrease any further. For practical applications, this means that the maximum resistance against hygroexpansion was reached at this thickness;
7. Accordingly, the crack onset strain (COS) increased with aluminum thickness and decreasing substrate roughness;
8. Although the hygroexpansion was higher in the presence of EVOH than in its absence, γ_{max} on EVOH coated paper was only a little higher. The increase in hygroexpansion due to the EVOH coating was, therefore, not a major hindrance to the production of flexible and closed aluminum coatings.

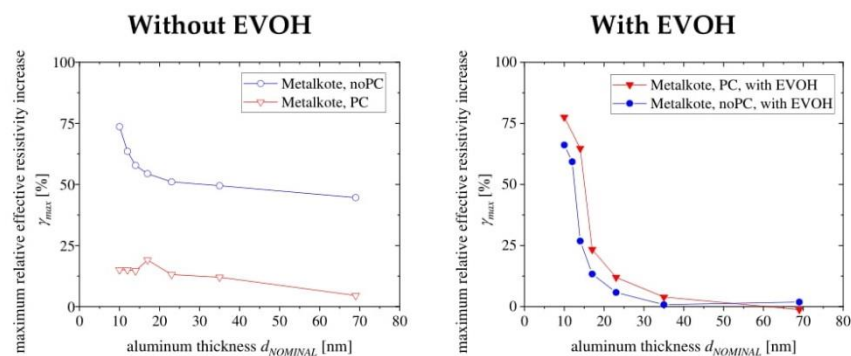


Figure 7. When the Metalkote paper was coated with EVOH, the maximum relative effective resistivity increase γ_{max} was much more dependent on aluminum thickness. PC/noPC = paper surface with/without pigment coating. EVOH = ethylene vinyl alcohol lacquer.

3.4. Effect of Drying Contraction on Electrical Resistivity

Inorganic brittle coatings can recover a part of their characteristic properties, such as conductivity after relaxation, when the applied strain or hygroexpansion, respectively, is removed [29]. In order to determine whether aluminum on paper behaves in a similar manner, the electrical resistivity was compared before and after humidification at 95% RH. Before and after humidification, the relative humidity was set to 50% (Figure 8).

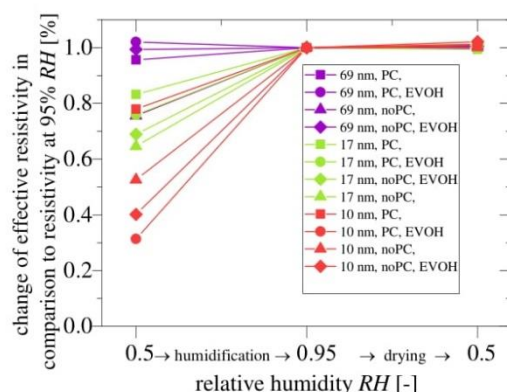


Figure 8. After humidification and subsequent drying, the differently coated Metalkote paper samples did not regain their initial resistivity values. PC/noPC = paper surface with/without pigment coating. EVOH = ethylene vinyl alcohol co-polymer lacquer coating as basis for aluminum coating.

The resistivity values were compared by assigning a reference value (=1) at 95% RH. We found that the resistivity after drying did not recover its original value, regardless of the substrate roughness, polymer coating or aluminum thickness. We, therefore, anticipate that the gas barrier performance would not be regained once the aluminum has cracked due to moisture uptake and hygroexpansion.

4. Conclusions

In this study, we showed that lacquer coating weights were higher when the lacquer was applied on paper surfaces, which were not pigment coated. This probably reflected the porous surface of the paper and its microchannels, which let the lacquer flow into and fill up pores and microchannels. This promoted hygroexpansion, because the lacquer occupied the space that otherwise could be filled by expanding fibers. Alternatively, hygroexpansion could be avoided by using wet-strength paper, which is hydrophobized and where fibers are cross-linked.

When pure paper or paper covered with lacquer was coated with aluminum via PVD, the effective resistivity increased with the roughness, hygroexpansion and the thinness of the aluminum layer. The crack onset point (COS) decreased with increasing substrate roughness and aluminum thinness. The relative effective resistivity increase only depended on aluminum thickness when the substrate was smooth and free of pores. Regardless of the substrate, we found that an aluminum thickness of >35 nm did not further improve the mechanical stability of the aluminum coatings under hygroexpansion-induced tension. For practical applications, this means that ~35 nm is the aluminum thickness that achieves the greatest avoidance of hygroexpansion and roughness induced defects while using the minimum amount of coating material. However, cracked aluminum barrier coatings did not regain their initial resistivity during re-contraction. This means it is critical to avoid hygroexpansion-induced defects.

Author Contributions: Conceptualization, M.L.; methodology, M.L.; formal analysis, M.L.; investigation, T.G.; data curation, M.L.; writing—original draft preparation, M.L. and T.G.; writing—review and editing, M.L., M.R., H.-C.L.; visualization, M.L.

Funding: This research received no external funding.

Acknowledgments: We acknowledge the support of Daniel Schlemmer, Michael Stenger and Brigitte Seifert.

Conflicts of Interest: The authors declare no conflict of interest.

RESEARCH PAPER: HYGROEXPANSION, SURFACE ROUGHNESS AND POROSITY AFFECT THE ELECTRICAL RESISTANCE OF EVOH-ALUMINUM-COATED PAPER

Coatings 2019, 9, 295

13 of 14

References

1. Lindner, M.; Heider, J.; Reinelt, M.; Langowski, H.-C. Hygroexpansion and surface roughness cause defects and increase the electrical resistivity of physical vapor deposited aluminum coatings on paper. *Coatings* **2019**, *9*, 33. [[CrossRef](#)]
2. Lindner, M.; Schmid, M. Thickness measurement methods for physical vapor deposited Aluminum Coatings in Packaging Applications: A Review. *Coatings* **2017**, *7*, 9. [[CrossRef](#)]
3. Kijima, T.; Yamakawa, I. Effect of beating condition on shrinkage during drying. *Jpn. Tappi J.* **1978**, *32*, 722–727. [[CrossRef](#)]
4. Salmén, L.; Boman, R.; Fellers, C.; Htun, M. The implications of fiber and sheet structure for the hygroexpansivity of paper [curl, shrinkage, beating, fines]. *Nord. Pulp Pap. Res. J. (Sweden)* **1987**, *4*, 127. [[CrossRef](#)]
5. Antonsson, S.; Mäkelä, P.; Fellers, C.; Lindström, M.E. Comparison of the physical properties between hardwood and softwood pulps. *Nord. Pulp Pap. Res. J.* **2009**, *24*, 409–414. [[CrossRef](#)]
6. Mendes, A.H.T.; Kim, H.Y.; Ferreira, P.J.T.; Park, S.W. The importance of the measurement of paper differential CD shrinkage. *O PAPEL* **2012**, *73*, 45–50.
7. Fahey, D.J.; Chilson, W. Mechanical treatments for improving dimensional stability of paper. *Rev. Process. Non-Refereed (Other)* **1963**, *46*, 393–399.
8. Sampson, W.W.; Yamamoto, J. The drying shrinkage of cellulosic fibres and isotropic paper sheets. *J. Mater. Sci.* **2011**, *46*, 541–547. [[CrossRef](#)]
9. Lif, J.O. Hygro-viscoelastic stress analysis in paper web offset printing. *Finite Elem. Anal. Des.* **2006**, *42*, 341–366. [[CrossRef](#)]
10. Alfthan, J. The Effect of Humidity Cycle Amplitude on Accelerated Tensile Creep of Paper. *Mech. Time-Depend. Mater.* **2004**, *8*, 289–302. [[CrossRef](#)]
11. Dickerman, G.K.; Savage, R.L. Method of Making Printable Coated Paper. U.S. Patent 2949382, 28 February 1960.
12. DeMatte, M.L.; Kelly, S.T. Coated Paper for Inkjet Printing. U.S. Patent 5985424A, 16 November 1999.
13. Kuroyama, Y.; Ohmura, T.; Yamazaki, Y.; Nanri, Y. Cast-Coated Paper for Ink Jet Recording and Production Method Thereof. U.S. Patent 5755929, 26 May 1998.
14. Paunonen, S. Influence of Moisture on the Performance of Polyethylene Coated Solid Fiberboard and Boxes. Ph.D. Thesis, Norwegian University of Science and Technology, Trondheim, Norway, October 2010.
15. DIN EN ISO 3274:1998-04. Geometrical Product Specifications (GPS)—Surface Texture: Profile method—Nominal Characteristics of Contact (stylus) Instruments (ISO 3274:1996), German version EN ISO 3274:1997; Beuth: Berlin, Germany, 1998.
16. DIN EN ISO 4288:1998-04. Geometrical Product Specifications (GPS)—Surface Texture: Profile method—Rules and Procedures for the Assessment of Surface Texture (ISO 4288:1996), German version EN ISO 4288:1997; Beuth: Berlin, Germany, 1998.
17. Zhang, Z.; Britt, I.J.; Tung, M.A. Permeation of oxygen and water vapor through EVOH films as influenced by relative humidity. *J. Appl. Polym. Sci.* **2001**, *82*, 1866–1872. [[CrossRef](#)]
18. Johansson, C.; Clegg, F. Hydrophobically modified poly (vinyl alcohol) and bentonite nanocomposites thereof: Barrier, mechanical, and aesthetic properties. *J. Appl. Polym. Sci.* **2015**, *132*, 41737. [[CrossRef](#)]
19. Lindner, M.; Höflsauer, F.; Heider, J.; Reinelt, M.; Langowski, H.-C. Comparison of thickness determination methods for physical-vapor-deposited aluminum coatings in packaging applications. *Thin Solid Film.* **2018**, *666*, 6–14. [[CrossRef](#)]
20. Kaden, H. *Wirbelströme und Schirmung in der Nachrichtentechnik*; Springer: Heidelberg, Germany, 2007.
21. Küpfmüller, K.; Mathis, W.; Reibiger, A. *Theoretische Elektrotechnik: Eine Einführung*; Springer: Heidelberg, Germany, 2006.
22. Lu, N.; Wang, X.; Suo, Z.; Vlassak, J. Metal films on polymer substrates stretched beyond 50%. *Appl. Phys. Lett.* **2007**, *91*, 221909. [[CrossRef](#)]
23. Sorg, H. *Praxis der Rauheitsmessung und Oberflächenbeurteilung*; Hanser: Munich, Germany, 1995.
24. Ridgway, C.J.; Gane, P.A. Bulk density measurement and coating porosity calculation for coated paper samples. *Nord. Pulp Pap. Res. J.* **2003**, *18*, 24–31. [[CrossRef](#)]

RESEARCH PAPER:

HYGROEXPANSION, SURFACE ROUGHNESS AND POROSITY AFFECT THE ELECTRICAL
RESISTANCE OF EVOH-ALUMINUM-COATED PAPER

Coatings **2019**, *9*, 295

14 of 14

25. Oliver, J.; Agbezuge, L.; Woodcock, K. A diffusion approach for modelling penetration of aqueous liquids into paper. *Colloids Surf. A Physicochem. Eng. Asp.* **1994**, *89*, 213–226. [[CrossRef](#)]
26. Roberts, R.J. Liquid Penetration into Paper. Ph.D. Thesis, Australian National University September, Canberra, Australia, September 2010.
27. Hyväluoma, J.; Raiskinmäki, P.; Jäsberg, A.; Koponen, A.; Kataja, M.; Timonen, J. Simulation of liquid penetration in paper. *Phys. Rev. E* **2006**, *73*, 036705. [[CrossRef](#)] [[PubMed](#)]
28. Viguie, J.; Dumont, P.J.J.; Mauret, E.; du Roscoat, S.R.; Vacher, P.; Desloges, I.; Bloch, J.F. Analysis of the hygroexpansion of a lignocellulosic fibrous material by digital correlation of images obtained by X-ray synchrotron microtomography: application to a folding box board. *J. Mater. Sci.* **2011**, *46*, 4756–4769. [[CrossRef](#)]
29. Polywka, A.; Stegers, L.; Krauledat, O.; Riedl, T.; Jakob, T.; Görrn, P. Controlled Mechanical Cracking of Metal Films Deposited on Polydimethylsiloxane (PDMS). *Nanomaterials* **2016**, *6*, 168. [[CrossRef](#)] [[PubMed](#)]



© 2019 by the authors. Licensee MDPI, Basel, Switzerland. This article is an open access article distributed under the terms and conditions of the Creative Commons Attribution (CC BY) license (<http://creativecommons.org/licenses/by/4.0/>).

7. Discussion, outlook and conclusion

Gas barrier improvement is not achieved when applying a coating to paper by PVD. Reasons for the lack of barrier performance of PVD inorganic coatings on paper had yet to be investigated in detail, in order to find suitable approaches for overcoming this challenge.

The area number density of defects in aluminum coatings is a key parameter because it affects the gas barrier properties of a physical vapor deposited (PVD) coating. The area number density of defects is affected by the aluminum thickness, hygroexpansion, and substrate roughness. As it is currently not possible to directly measure the area number density of defects in aluminum coating on paper by simple means, the observation of defects was done by using the aluminums' electrical resistance as a surrogate parameter.

Answers and explanation to the scientific questions in Section 1.2 were given in the previous sections 2-6. In the following, the relevant information from those chapters is summarized.

7.1. Factors leading to defects in aluminum coatings

The first scientific question addressed in this thesis was to determine which factors might lead to defects in the aluminum coating (Section 1.2, p. 2). The results indicated that paper roughness, aluminum thickness and hygroexpansion are decisive factors that affect the area number density of defects in aluminum coatings applied by PVD (Figure 10, p. 124).

An **aluminum thickness** of >35 nm was found to confer sufficient mechanical stability to prevent additional cracking during hygroexpansion (Figure 6, p. 118). A critical thickness, above which mechanical stability declines again, was not observed. However, reducing the aluminum thickness increased the effective resistivity, indicating an increase in the area number density of defects (Figure 13, p. 84; Figure 4-5, p. 96; Figure 5, p. 117).

In addition to **substrate roughness**, the **substrate porosity** was also included in Figure 10 because this was found to have an even more decisive impact, leading to defects in the aluminum coating (Figure 3, p. 115; Figure 6, p. 118). However, substrate porosity can only be measured indirectly (e.g. via air permeability [1]) and partially with high technical effort (optical coherence tomography [2]).

Paper hygroexpansion itself was also shown to be influenced by **polymer pre-coating** (Figure 4; p. 116). In the present study, the chosen coating was ethylene vinyl alcohol

co-polymer (EVOH) with 8% ethylene, because it possesses a high surface tension and is water soluble making it suitable for paper recycling processes. A more hydrophobic coating may help to reduce hygroexpansion, but this would limit the surface tension and may be incompatible with paper recycling and adhesion of aluminum on the coating.

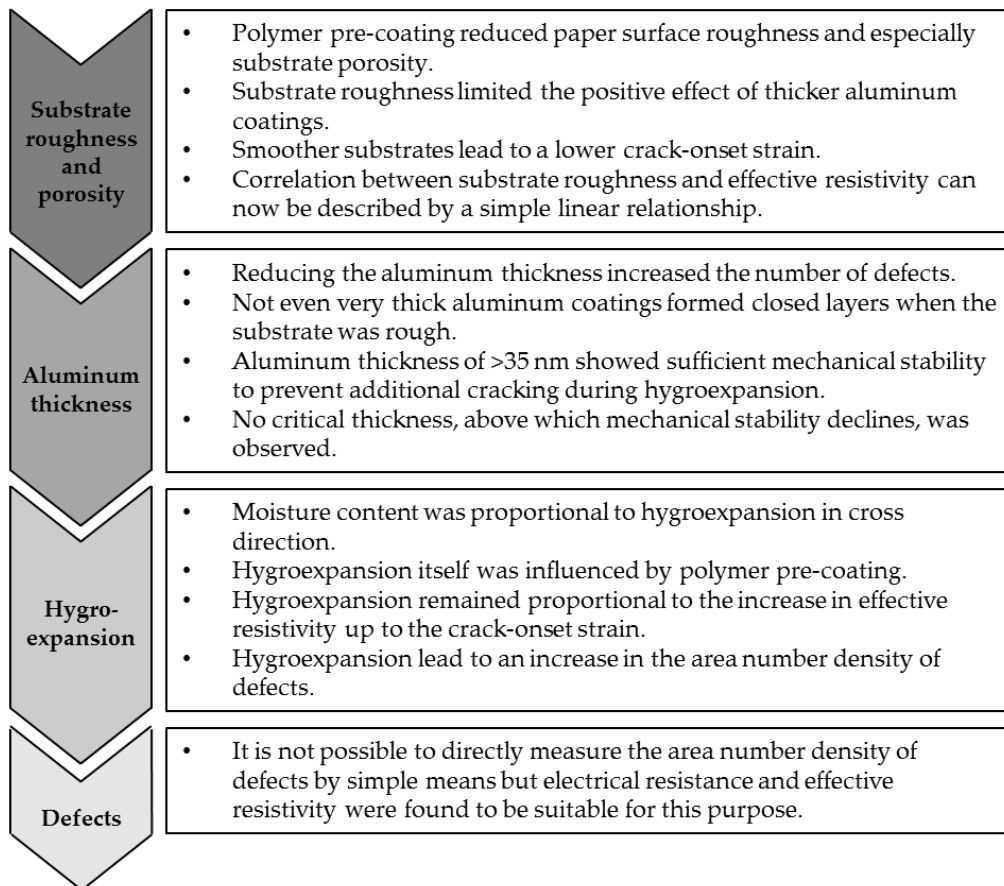


Figure 10. Interplay between the effects that appear during the PVD coating of paper. Compared to the preliminary diagram (Figure 2) additional found explanations have been included.

7.2. Detection of defects via electrical resistivity

The second scientific question addressed in this thesis was how to measure defects in aluminum coatings (Section 1.2, p. 2) on paper substrates. It is currently not possible to directly measure the area number density of defects that arise due to substrate roughness and hygroexpansion by simple means. However, electrical resistance was found to be suitable for this purpose. The electrical resistance of an aluminum coating is typically used to determine its thickness because there is an inverse relationship between these parameters. However, the electrical resistance was also found to increase in a monotonic, non-linear manner with substrate roughness, which is assumed to lead to defects in the aluminum

coating. Therefore, the electrical resistance and effective resistivity were used as an indication for the area number density of defects (Equation 2, p. 92) and the area mass density of aluminum applied to the surface (Equation 3-4, p. 80) was used as a reference.

Although the effective resistivity reveals information about the appearance of defects, the correlation of effective resistivity **with a definitive value for the area number density of defects** underlies even more influencing factors, such as the geometry of defects and the properties of the applied electromagnetic field. The same applies for the correlation between **effective resistivity and oxygen transmission**. These complex interrelations are not yet clarified and should be the subject of further research.

7.3. Reduction of defect-triggering factors and their interactions

The third scientific question addressed in this thesis was to determine how defect generating factors or their effects can be reduced, and the fourth was to understand the effect of different combinations of aluminum thickness, hygroexpansion and paper roughness on the area density of defects and electrical resistance of aluminum coatings (Section 1.2).

Roughness of paper substrates can be reduced by an additional polymer coating, and that aluminum thickness can easily be adjusted during PVD. This allowed both parameters to be tested to determine their effect on the area number density of defects in aluminum coatings (Sections 7.3.2–7.3.4). However, factors that influence hygroexpansion were only partially understood, and it was therefore necessary to review these factors to conclude how to reduce hygroexpansion (Section 7.3.1).

7.3.1. Modification of paper hygroexpansion

Hygroexpansion was anticipated to increase the area number density of defects in aluminum coatings and was therefore reviewed in order to understand its impact. However the main factors found in literature to influence the hygroexpansion of the substrate were single-fiber hygroexpansion and the inter-fiber contacts, which can only be controlled during paper manufacturing (Figure 9, p. 32).

The influence of a polymer pre coating – applied on the paper surface after paper manufacturing and before PVD coating – on hygroexpansion has only been evaluated once [3]. When now paper was pre-coated with the polymer EVOH, hygroexpansion (and thus the

external stress) increased, particularly when the coating was applied to rough and porous surfaces (Figure 4; p. 116). The explanation could be that fibers expand into the inter-fiber-voids during hygroexpansion, but those voids are not accessible when they are already filled with a polymer coating, thus increasing the degree of hygroexpansion.

The polymer coating used in this study was EVOH with a high content of polyvinyl alcohol (~92 mol%), which absorbs moisture and thus acts like a flexible matrix. In contrast to the hydrophilic EVOH coating used herein, a polyethylene coating used elsewhere was found to reduce paper hygroexpansion by ~25% [3]. In this case, polyethylene may provide a stable hydrophobic matrix that limits the expansion of fibers. Therefore, one future option would be to use EVOH grades with increasing proportions of ethylene, in order to achieve a suitable balance between low hygroexpansion and high surface tension. Low surface tension leads to poor adhesion but this could be partially overcome by corona treatment.

7.3.2. Effect of substrate hygroexpansion on electrical resistance of aluminum

The relative humidity was found to correlate with the moisture content of the paper substrate according to the Guggenheim, Anderson and De Boer sorption isotherm (Equation 6, p. 93; Figure 9, p. 99). Furthermore, the moisture content was proportional to hygroexpansion in cross direction (Figure 10, p. 100). When paper expands due to the uptake of water, an increase in effective resistivity was observed, indicating that defects in the aluminum coating are formed (Figure 12, p. 101). The increase in effective resistivity remained proportional to hygroexpansion up to the crack-onset strain. At higher degrees of hygroexpansion/humidity, a sudden increase in resistivity indicated that the aluminum started to crack. When paper contracted during drying, the effective resistivity did not fall to its original levels, indicating that the aluminum does not reform a closed layer (Figure 8, p. 120). The effect of hygroexpansion on the effective resistivity increase is also affected by substrate roughness and aluminum thickness, so those factors were also examined.

7.3.3. Reduction of substrate surface roughness and substrate porosity

Both substrate roughness and substrate porosity were anticipated to affect the integrity of the aluminum coating because they induce imperfections that reduce the

mechanical stability of the coating during hygroexpansion. Due to these built-in defects in the aluminum coating, the intrinsic stress is presumably much higher on paper substrates.

A polymer pre-coating was found to reduce paper surface roughness and especially substrate porosity (Figure 3, p. 115), with particularly the latter causing a lower effective resistivity indicating and lower area number density of defects in the aluminum coating (Figure 5, p. 117). Smooth substrates were therefore anticipated to reduce the intrinsic stress and increase mechanical stability. Moreover, the substrate roughness limits the positive effect of thicker aluminum coatings. Only on very smooth substrates can thick aluminum coatings achieve higher mechanical stability, as indicated by a lower increase in effective resistivity (Figure 7, p. 119). Smoother substrates presumably lead to a lower crack-onset strain, as indicated by a sudden increase in effective resistivity. However, it remains unclear whether preferential nucleation in valleys, self-shadowing by nuclei, or shadowing by surface roughness is the most important determinant.

The correlation between substrate roughness and effective resistivity can now be described by a simple linear relationship (Figure 7, p. 98; Equation 15, p. 98). However, the effect of roughness on the relative increase in effective resistivity during hygroexpansion cannot yet be described by such a simple mathematical model. This is due to additional complex effects in the case of hygroexpansion, which cannot yet be entirely overviewed. This is for example the appearance of new breaking edges in the aluminum during hygroexpansion, which are then prone to oxidation. Such additional aluminum oxide layers could further increase the effective resistivity. This should be the subject of future research.

7.3.4. Effect of increasing aluminum thickness on the area number density of defects in aluminum coatings

Thicker aluminum coatings were anticipated to show greater mechanical resistance towards external stresses, but also to trigger intrinsic stresses and might therefore lead to more defects in the aluminum coating. Indeed, thicker aluminum coatings were shown to partially overcome hygroexpansion, with no further raise in resistivity for aluminum coatings >35 nm thick when they were applied to polymer pre-coated, pore-free paper substrates (Figure 6, p. 118). This indicates that aluminum on pre-coated paper confers mechanical resistance during hygroexpansion, but even very thick aluminum coatings will

not form closed layers when the substrate is rough (Figure 5, p. 117). Because thick aluminum coatings did seemingly not crack on smooth substrates, a critical aluminum thickness leading to extremely high intrinsic strains was not yet reached, even at the maximum applied thickness of 69 nm (Figure 6, p. 118).

One further option for further research is the testing of **corona treatment** as a means to increase adhesion between the pre-coated polymer and aluminum layer. The scientific question would be to determine whether the **recommended coating thickness of 35 nm could be reduced any further due to increasing corona dosages**.

7.4. Conclusion: Main factor leading to defects in aluminum coatings

The final scientific question addressed in this thesis was to determine the main factor leading to defects in aluminum coatings (Section 1.2), which were indirectly described via electrical resistance measurements. The results indicated that all of the evaluated factors affect each other. To determine the most important factor it was therefore necessary to compare the effective resistivity under a range of selected conditions. In each condition, the effect of **one single factor is considered in isolation** (Table 3, p. 129):

- Condition 1) Isolated consideration of aluminum thickness: Thin aluminum coating that leads to a higher resistivity compared to thicker coatings (but no hygroexpansion and low substrate roughness);
- Condition 2) Isolated consideration of hygroexpansion: High degree of hygroexpansion that increases resistivity (but thicker aluminum coating and low substrate roughness);
- Condition 3) Isolated consideration of substrate roughness: High substrate roughness that leads to a higher resistivity compared to smoother substrates (but thicker aluminum coating and no hygroexpansion).

Table 3 summarizes the effective resistivity (column 2) achieved under the named conditions (column 1, column 4-6). This table of course can only give an overview within the tested conditions, namely an aluminum thickness of 10–69 nm, hygroexpansion of 0–1.6% and a substrate roughness of 0–11.9 μm . From Table 3 it can be seen, that the minimum reached resistivity value on PET (50 $\Omega\cdot\text{nm}$) is twice as high as the literature value for bulk

aluminum (27 $\Omega\cdot\text{nm}$). Thus, the value on PET is the best achievable value with the equipment used in this study.

Assuming, that a higher effective resistivity indicates a higher area number density of defects, the importance of each factor can now be estimated by taking the effective resistivity on PET (50 $\Omega\cdot\text{nm}$) as a reference value and by taking the effective resistivity caused by a high substrate roughness, hygroexpansion and thin aluminum coatings as multiples of the PET-value.

Within the evaluated boundaries, the overview shows that substrate roughness has the highest impact (higher resistivity by a factor of 16.3 compared to the lowest reached value on PET), hygroexpansion has a medium impact (higher resistivity by a factor of 3.3 compared to the lowest reached value on PET) and aluminum thickness the lowest (higher resistivity by a factor of 2.5 compared to the lowest reached value on PET).

Table 3: Overview over the effect of aluminum thickness, hygroexpansion and substrate roughness on effective resistivity under isolated conditions.

Selected conditions with focus on factor:	Effective resistivity	Factor *	Nominal aluminum thickness	Hygro-expansion	Substrate roughness	Graph
	$[\Omega\cdot\text{nm}]$ $[\mu\Omega\cdot\text{cm}]$	[-]	[nm]	[%]	$[\mu\text{m}]$	[Figure; page]
3: Substrate roughness	816 81.6	16.3	>35	0	<u>11.9</u>	Fig. 5, p. 117
2: Hygroexpansion	**166 **16.6	3.3	35	<u>1.6</u>	2.8	Fig. 5, p. 117 Fig. 6, p. 118
1: Nominal aluminum thickness	125 12.5	2.5	<u>10</u>	0	0	Fig. 13, p. 84
Minimum reached effective resistivity on PET	50 5.0	1.0	160	0	0	Fig. 13, p. 84
Bulk material	27 2.7	0.5	∞	0	0	Bulk material

* Factor: effective resistivity ρ_{EFF} as a multiple of the minimum effective resistivity reached on PET, which is set as reference value (=1)

** 166 $\Omega\cdot\text{nm}$ calculated from A) Fig. 5, p. 117, PC, with EVOH, hygroexpansion $\varepsilon=1.6\%$, 35 nm aluminum: maximum relative effective resistivity increase $\gamma=4\%$; and B) Fig. 6, p. 118, PC, EVOH, RH=0%; 35 nm aluminum: effective resistivity $\rho_{\text{EFF}}=160\ \Omega\cdot\text{nm}$. The combination of A) and B) leads to $160\ \Omega\cdot\text{nm}\cdot(1+4\%)=166\ \Omega\cdot\text{nm}=16.6\ \mu\Omega\cdot\text{cm}$.

7.5. Chapter bibliography

1. Butters, D. *Measurement of Paper Porosity*. Beiträge zur Tabakforschung 1970, 5.
2. Alarousu, E.; Krehut, L.; Prykäri, T.; Myllylä, R. *Study on the use of optical coherence tomography in measurements of paper properties*. Measurement Science and Technology 2005, 16, 1131.
3. Paunonen, S. *Influence of moisture on the performance of polyethylene coated solid fiberboard and boxes*. Dissertation, Norwegian University of Science and Technology, Trondheim, 10.2010.

8. Summary

As fossil based resources decline, renewable materials are gaining more importance in the packaging industry and oil-derived polymers could partially be replaced with paper. Packaging materials require an effective gas barrier. One possibility to enhance the gas barrier of packaging materials is the application of nanometer-scale aluminum layers by physical vapor deposition (PVD). However, gas barrier improvement is not achieved when applying a PVD coating to paper. Reasons for the lack of barrier performance of PVD inorganic coatings on paper had yet to be investigated in detail, in order to find suitable approaches for overcoming this challenge. Therefore, the following scientific questions were addressed:

1) Which key factors influence the extent of defects in the inorganic coating?

Low aluminum thickness, large paper hygroexpansion and large paper roughness were found as main factors to increase the area number density of defects.

2) How can such defects in an aluminum coating be detected?

Defects cannot be detected directly with a simple method. However, it was shown that various methods currently used (quartz micro balances, optical density, electrical resistance, atomic force microscopy and mass spectrometry) to determine the thickness of aluminum coatings are at least partially affected by the material morphology. This was particularly noticeable in the case of electrical resistance which is highly sensitive to the area number density of defects in aluminum coatings as shown on reference coatings on PET. The effective resistivity can be determined to gain indirect evidence for the appearance of defects.

3) How can factors that cause defects in an aluminum coating be influenced?

Substrate roughness can be reduced by applying a polymeric pre-coating and aluminum thickness can be controlled during PVD. Hygroexpansion in cross direction was proportional to the moisture content, which in turn correlated with humidity. Hygroexpansion behavior is mainly influenced by processing and chemical and morphological structure of the paper, which can be adjusted during paper production. However, the present study was limited to parameters that can be changed during converting processes following paper production, such as polymer pre-coating. Hygroexpansion was found to be promoted by polymer pre-coating and increased more when the coating was applied to rough and porous surfaces.

4) What is the effect of different combinations of aluminum thickness, hygroexpansion and paper roughness on the area number density of defects and electrical resistance of aluminum coatings?

The relationship between substrate roughness, aluminum thickness and effective resistivity was described using a mathematical equation. When the substrate paper expanded due to the uptake of moisture, the aluminum coating was more prone to cracking, as indicated by an increase in effective resistivity. Hygroexpansion was proportional to the increase in effective resistivity up to the crack-onset strain. This was related to the mechanical straining and deformation of the aluminum layer. The aluminum started to crack at higher strains and humidity, as reflected by a sudden increase in effective resistivity. These cracks seem to appear at lower degrees of hygroexpansion (~0.5%) when the substrate is rougher, because substrate roughness and substrate porosity presumably trigger defects in the aluminum. A polymer pre-coating reduced the roughness (e.g. from 11.9 to 9.5 μm) and especially the porosity of the paper surface, thus reducing the area number density of defects in the aluminum. This confirms that smooth substrates increase the mechanical stability of aluminum. Thick coatings achieved a higher mechanical stability but only on very smooth and non-porous substrates. On such smooth substrates, aluminum coatings >35 nm thick did not undergo further cracking during hygroexpansion. Furthermore, coatings up to 69 nm thick were not observed to lead to a critical degree of intrinsic strain. Aluminum coatings will not build closed layers even at thicknesses of ~100 nm when the substrate is rough (minimum applied paper roughness was $R_z=2.8 \mu\text{m}$).

5) What is the main factor leading to defects in the inorganic coating?

Within the range of conditions tested in this investigation, substrate roughness had the greatest impact on effective resistivity and thus on the appearance of defects in the aluminum coating (higher resistivity by a factor of 16.3 compared to the lowest reached value on PET), hygroexpansion had a medium impact (factor of ~3.3), and aluminum thickness has the lowest impact (factor of ~2.5). Further research has to correlate electrical resistance with a definitive value for the area number density of defects and with the oxygen transmission through such defects.

Curriculum vitae

Angaben zur Person

Name	Martina Lindner
Geburtsdatum	18. Januar 1988
Geburtsort	Pegnitz
Familienstand	ledig

Akademische Laufbahn / Studium

seit 11.2013	Wissenschaftliche Mitarbeiterin Fraunhofer Institut für Verfahrenstechnik und Verpackung IVV Freising, Abteilung Materialentwicklung
seit 09.2014	Anfertigung der vorliegenden Doktorarbeit Lehrstuhl für Lebensmittelverpackungstechnik Prof. Dr. H.-C. Langowski Fakultät WZW der TU München
03.2012 – 11.2013	Studium Milch- und Verpackungswirtschaft, M.Eng. (Note: 1,3) Hochschule Hannover Masterthesis bei Winpak Heat Seal Packaging Inc., Montreal, Kanada zum Thema „Simulation von Tiefziehprozessen für Aluminium-Blister“
09.2011– 02.2012	Nachweis über Zusatzleistungen, Hochschule Hannover Schwerpunkt: Milchtechnologie, Analytik
10.2007 – 08.2010	Studium Verpackungstechnik Hochschule der Medien, Stuttgart, Abschluss: B. Eng. (Note:1,6) Bachelorthesis bei Sanofi-Aventis Deutschland GmbH, Frankfurt zum Thema „Glasbruch“

Nebenberufliche Tätigkeiten

Seit 09.2017	Dozentin für „Verpackungstechnik“ (4 SWS) Hochschule Lemgo
04.2015 – 09.2015	Dozentin für „Lebensmittelverfahrens- und Prozesstechnik“ (2 SWS) Hochschule Fulda

Seit 11.2014	Dozentin für „Chemisch-technologische Grundlagen der Lebensmittel“ (4 SWS) Hochschule Kempten
06.2011 – 08.2011	Mitarbeit Packmittelkonstruktion Hertel & Co. GmbH, Bayreuth
11.2010 – 04.2011	Mitarbeit im Vertrieb AayurMed Biotech P. Limited, Mumbai (Indien)
07.2007 – 09.2007	Freiwilliger sozialer Dienst Dai Boro Gé Primary School, Grootfontein, Namibia

Stipendien

04.2014 – 04.2016	Stipendium Fraunhofer „Talenta“ Förder- und Entwicklungsprogramm zum Entwickeln von Wissenschaftlerinnen
11.2010 – 04.2011	Stipendium der GIZ (ehemals InWEnt)
04.2013 – 10.2013	Stipendium „Hin-und-Weg“ (DAAD)

Auszeichnungen

2010	Nachwuchs Award 2011 der Medienversicherung a.G.
2007	Ehrung durch die Deutsche Physikalische Gesellschaft für Leistungen im Fach Physik